Numerical Modeling of Piston Secondary Motion and Skirt Lubrication in Internal Combustion Engines

by

Fiona McClure

M.Eng., Mechanical Engineering
McGill University, 2002

and

B.Eng., Mechanical Engineering
B.S., Applied Mathematics
The University of Melbourne, 2000

Submitted to the Department of Mechanical Engineering in Partial Fulfillment of the Requirements for the Degree of Doctor of Philosophy in Mechanical Engineering

at the

Massachusetts Institute of Technology

September 2007

Signature of Author ....
Department of Mechanical Engineering
August 21, 2007

Certified by ....
Tian Tian
Principal Research Scientist, Department of Mechanical Engineering
Thesis Supervisor

Certified by ....
John B. Heywood
Sun Jae Professor of Mechanical Engineering
Thesis Supervisor

Accepted by ....
Lallit Anand
Chairman, Department Committee on Graduate Studies
Department of Mechanical Engineering

Numerical Modeling of Piston Secondary Motion and Skirt Lubrication in Internal Combustion Engines

by

Fiona McClure

Submitted to the Department of Mechanical Engineering
on August 21, 2007 in Partial Fulfillment of the Requirements for the
Degree of Doctor of Philosophy in Mechanical Engineering

Abstract

Internal combustion engines dominate transportation of people and goods, contributing significantly to air pollution, and requiring large amounts of fossil fuels. With increasing public concern about the environment and the reliability of oil supplies, automotive companies are pushed to improve engine design in order to reduce engine emissions and fuel consumption.

This project aims to develop a numerical model of piston dynamics and lubrication in internal combustion engines, enabling prediction of friction generation at the piston - cylinder bore interface, and oil transport in the power cylinder system. It is currently estimated that the piston – cylinder bore friction accounts for up to 25% of the power loss in a typical engine, while oil transported to the combustion chamber by the piston and ring-pack contributes significantly to engine emissions.

A dry piston model was first developed to allow fast calculation of approximate piston dynamics. An elastohydrodynamic lubrication model was then developed to allow direct numerical simulation of the effect of piston tooling marks, and comparison with results obtained using an Average Reynolds equation with flow factors. The lubrication model was incorporated into the piston dynamics model, enabling more accurate evaluation of friction and oil transport. Comparison between the dry and lubricated model results demonstrate the effect of oil film thickness on piston lateral motion, tilt, friction generation and oil transport.

Thesis Supervisors:

Tian Tian
Principal Research Scientist, Department of Mechanical Engineering

John B. Heywood
Sun Jae Professor of Mechanical Engineering

Acknowledgements

There are many people who I would like to thank for their contributions to this research, and to my time at MIT. In particular I would like to thank my supervisors, Dr. Tian Tian and Prof. John Heywood, for their support and guidance throughout my PhD. Their depth of knowledge and experience has significantly contributed to this research and to my learning experience at MIT. I would also like to thank the members of my thesis committee, Prof. Rohan Abeyaratne and Prof. Gareth McKinley for their encouragement, constructive advice, and interest in our research.

I would like to take this opportunity to thank our research sponsors, Mahle GmBh, AB Volvo, Peugeot PSA, Renault SA, and Dana Corporation for their financial support, and more specifically, their representatives, Rolf-Gerhard Fiedler, Eduardo Tomanik, Bengt Olson, Fredrick Stromstedt, Sebastien Messe, Gabriel Cavallaro, Randy Lunsford and Remi Rabute for their continued encouragement over the years, and for sharing their extensive experience with me. Our regular meetings provided not only a motivation for completing work, but also an invaluable opportunity to share knowledge and obtain constructive feedback. Without their help and guidance this research would not be possible.

I would also like to thank the members of the Sloan Automotive Laboratory for their support and friendship. In particular I would like to thank Liang Liu and Yong Li for their repeated help and guidance with my work, and the significant contributions they have made to this research, and the other students of the Lubrication Consortium, Steve Preszmitzki, Eric Senzer and Haijie Chen, for making the stressful times more fun. I would also like to thank Nancy Cook and Janet Maslow, not only for the great job they do as administrators, but also for providing a kind and supportive ear whenever it was needed, and for the many laughs we have had.

Finally, I would like to thank my friends and family for their love and support, which has provided me with so much comfort and strength.

Table of Contents

List of Figures

List of Tables

1. Introduction

1.1. Project Motivation

Internal combustion engines dominate transportation of people and goods, contributing significantly to air pollution, and requiring large amounts of fossil fuels. As concern for the environment, and the effects of global warning, increase, governments continue to introduce more stringent emissions criteria. Additionally, increasing political concern regarding dependence on foreign oil and political instability in the middle east, and corresponding increases in fuel prices, push for increased mileage per gallon. These two concerns, in parallel, are motivating automotive companies to improve engine design in order to reduce engine emissions and fuel consumption, while maintaining at least the current standards of noise, performance and maintenance requirements. An improved understanding of interactions within the engine is therefore required.

It is useful to separate engine emissions into emissions due to fuel and those due to oil consumption. Fuel consumption and engine emissions due to fuel can be reduced through improvements in combustion, fuel delivery and friction reduction. Current engine designs tend to have overall efficiencies of 38-41%, with 4-15% of the energy being lost to mechanical friction. It is estimated that 40-55% of the friction losses are due to the power cylinder system, made up of the piston (25-47%), ring-pack (28-45%) and connecting-rod bearings (18-33%) [1]. Friction generated in the power cylinder system therefore represents a significant proportion of the energy loss in the engine, and a corresponding opportunity for improvement in engine efficiency.

In order to better understand friction generation on the piston, we first must accurately model piston dynamics, which also significantly impact ring pack dynamics and friction generated within the ring pack. The piston dynamics are predominantly driven by the pressure load and connecting-rod angle, and constrained by the piston's interaction with the cylinder bore. Ideally, the piston has only one degree of freedom, allowing a reciprocating motion along the cylinder axis, which is commonly referred to as its primary motion. More realistically, the piston has six degrees of freedom, with the range of allowable motion in each direction varying significantly. The secondary motion of the piston is made up of translation perpendicular to the cylinder and piston pin axes, and rotation about the piston pin axis. This motion allows the piston to collide with the cylinder bore, a phenomenon referred to as piston slap. In a typical car engine the displacements in the axial direction are of the order of 100 mm, while the displacements involved in the secondary motion of the piston are of the order of 100 μm [2-4], and the piston tilts are of the order of 0.001 rad [3]. The piston's motion due to the remaining three degrees of freedom is currently believed to be significantly smaller than both its primary and secondary motions and is neglected for the purposes of this project.

Piston slap is initiated when the connecting-rod side force changes direction either due to changes in the connecting-rod angle, or the connecting-rod force (from compression to tension or vice versa). The piston's impact against the cylinder bore is a significant source of noise, vibration and energy loss, and can lead to cavitation wear on the cooling side of the liner, while its motion along the cylinder bore generates friction and transports oil, thereby affecting wear of the piston, rings and liner, and contributing to oil consumption.

Piston skirt lubrication is provided by lubrication oil, which is, in general, picked up from the oil sump and thrown onto the cylinder bore by the motion of the crankshaft. In some engines, lubrication oil is also sprayed onto the underside of the piston or other locations within the power cylinder system. The lubrication oil is then transported along the cylinder bore by the motion of the piston and piston rings, and by gravity. Lubrication oil is also transported around the system when it is entrained in blow-by gases. The lubrication oil leaves the cylinder bore in three ways: oil returns to the sump; oil entrained in the blow-by gas leaves the system via the crank case; or oil is consumed in the combustion chamber. The last two options create a significant source of engine emissions due to oil consumption.

Due to the complex nature of oil transport within this system, and the inaccessibility for experimental observation, it is often impossible to accurately predict the location and thickness of oil films within the system. Previous research, both experimental and computational, indicates average oil film thicknesses in the range 1-100μm [2, 4-8]. Depending on the amount of oil present, the side load and the sliding speed, regions of boundary, mixed and elastohydrodynamic lubrication may all be present simultaneously on the piston skirt throughout the cycle. On the lower end, oil film thicknesses of around 1 μm, which is significantly smaller than typically piston tooling mark wave heights, will result in boundary lubrication with significant solid-solid contact and friction generation. Significantly thicker oil film thicknesses, such as 100 μm may be sufficient to support the side load via elastohydrodynamic lubrication, eliminating solid-solid contact and wear. A detailed model of the piston – cylinder bore interface and oil film distribution is required for estimating lubrication conditions, friction generation and oil transport on the piston.

1.2. Introduction to Power Cylinder System

The Power Cylinder System can be considered to be made up of 6 components, each with a separate role:

1. Ring Pack
2. Piston
3. Wrist-Pin

4. Connecting-Rod
5. Crankshaft
6. Cylinder Bore

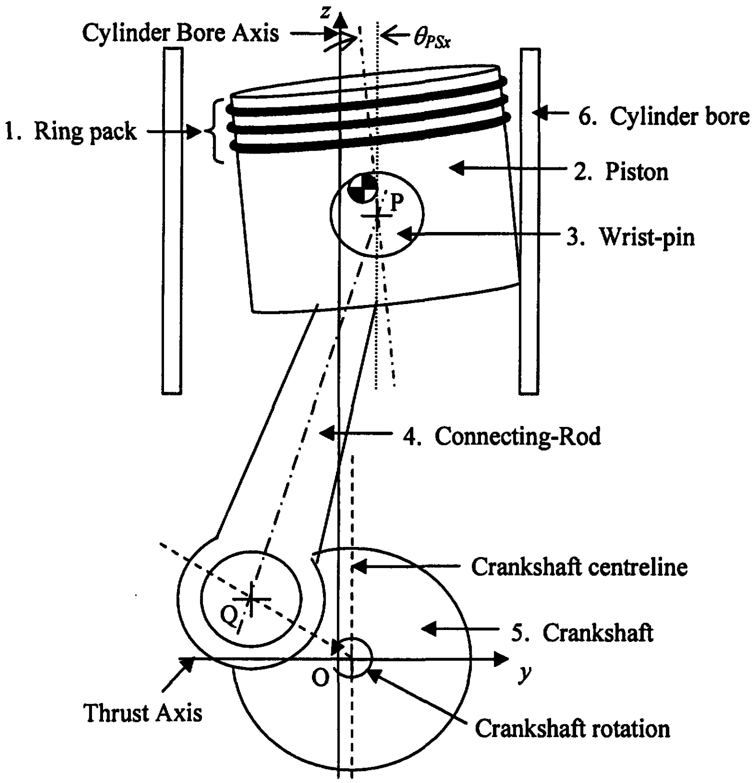

Figure 1.1: Power Cylinder System

The chemical energy in the fuel is converted to kinetic energy during combustion and transmitted from the combustion chamber, through the piston, pin and connecting-rod to the crankshaft. The geometric arrangement of the power cylinder system allows the linear motion of the piston to be converted into the rotational motion of the crankshaft. The angle of the connecting-rod causes lateral motion of the piston, and interaction with the bore, combined with the lateral motion and friction at the wrist-pin bearing tends to causes piston tilt.

1.2.1. Ring Pack

The Ring Pack plays two roles within the power cylinder system:

1. Seals the gases in the combustion chamber, both during compression and combustion, minimizing energy losses and emissions due to blow-by.
2. Transport oil along the cylinder bore, balancing conflicting criteria of providing oil to reduce friction, while reducing oil consumption.

A typical ring pack is made up of two or three rings, with the top one or two rings focusing on sealing the combustion chamber, and the lower ring acting as an oil control ring. Significant research has been completed in the areas of ring pack dynamics, friction generation and oil transport [5,6]. In terms of interactions between the piston and ring pack:

- The piston dynamics significant impact the ring pack, and an accurate model of piston motion is required as an input for ring pack analysis.
- Normal and friction forces generated between the piston and rings, while significant for the purposes of determining ring motion, are not significant in determining piston dynamics. The ring pack is therefore neglected for the purposes of this project.

1.2.2. Piston

The main role of the piston is to transmit the pressure force generated during combustion through the pin and connecting-rod to the crankshaft, thereby converting the energy of the expanding gases to the essentially linear kinetic energy of the piston, and finally to the rotational kinetic energy of the crankshaft. While ideally the piston travels in the axial direction only, in reality the connecting-rod angle results in significant side forces being transmitted through the piston, causing lateral motion. The resulting motion, often referred to as piston slap, occurs:

- when the connecting-rod angle changes sign, which is determined by engine geometry, and for an engine design with no crankshaft offset occurs at 0, 180, 360 and 540 °CA, and
- when the connecting-rod force changes sign, that is, from compression to tension, or vice versa, which is essentially a function of the pressure trace and component axial inertias, and typically occurs during the intake and exhaust strokes around mid-stroke.

In general, the outer surface of a piston is specified by a nominal radius, cold profile and ovality. There is also significant design of the internal structure of the piston, thereby influencing the:

- mass and weight distribution,
- heat transfer, and therefore temperature distribution and thermal expansion, and
- structural response to pressure, inertia and skirt loads

Design criteria for a piston are often conflicting in nature:

1. Piston – Bore Clearance: In order to minimize frictional losses, a smaller piston diameter is desired, allowing increased clearance between the piston and bore, while in order to reduce noise and impact losses, a large piston diameter is desired, with decreased clearances reducing lateral movement.
2. Piston structural stiffness: The piston must be structurally strong enough to withstand the large forces transmitted both axially and laterally, requiring stiffness around the pin bore where forces are transmitted to the wrist-pin, and

sufficient stiffness in the skirt, while a flexible skirt is more desirable for noise reduction and minimizing local contact pressures. Similarly there is an optimal flexibility for the skirt in terms of friction reduction.

3. Piston Mass: Decreased piston mass reduces the loss of energy to piston inertia, but sufficient mass must be provided for the required structural stiffness.
4. Piston profile: Significantly affects pressure generation, oil transport and friction generation at the piston-cylinder interface. As the piston slides axially along the liner, pressure tends to be generated by the converging gap at the leading edge of the piston which also acts to scrape oil along the cylinder bore, thereby altering the oil film thickness.

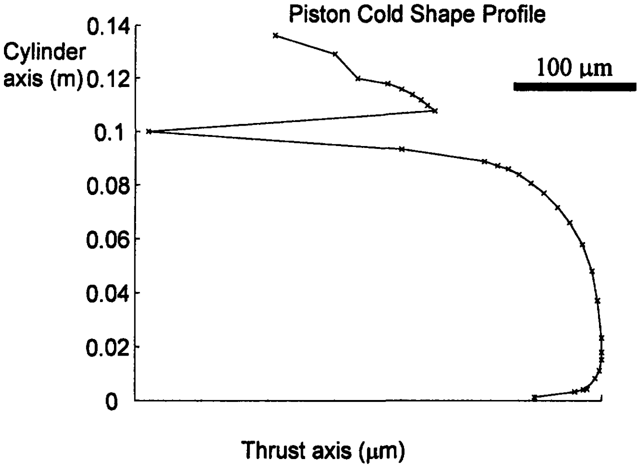

Figure 1.2: Piston profile

5. Piston ovality: With increased ovality the pressure generated at the piston-cylinder bore interface is centralized, thereby supporting the side load more efficiently, and the portion of the skirt that is fully flooded is reduced, thereby decreasing hydrodynamic friction, but also decreasing pressure generation for a given surface separation. Increased beyond an optimal value, the ovality will result in solid-solid contact due to decreased surface separation, and a significant rise in contact friction.

1.2.3. Wrist-Pin

The wrist-pin transmits forces between the piston and connecting-rod while allowing the piston and connecting-rod to rotate relatively independently of each other. At high loads, however, particularly around combustion TDC, significant torque is transmitted from the connecting-rod to the piston, even for small friction coefficients, thereby influencing the piston tilt. At these high loads, it is expected that there will be significant bending of the pin, but for the purposes of this work the pin is assumed to be rigid.

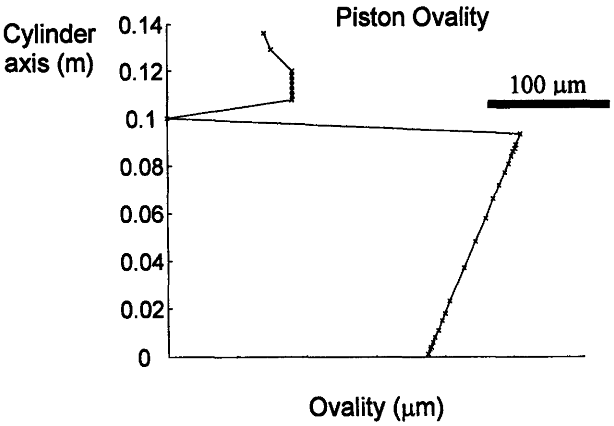

Figure 1.3: Piston ovality

1.2.4. Connecting-Rod

The connecting-rod transmits force from the wrist-pin to the crankshaft. The loads transmitted by the crankshaft are typically of the order of 100 kN, generating moments of 5 kNm. The small end of the connecting-rod connects to the wrist-pin, carrying out axial motion equal to twice the crankshaft radius (~ 100 mm), and lateral motion of the order of 100 µm. The large end of the connecting-rod connects to the crankshaft and rotates in a circular motion at the crankshaft radius. The longer the connecting-rod, the smaller the connecting-rod angle and the corresponding side force and bending moments, but the less compact the engine design, and the larger the connecting-rod mass and resulting energy loss due to component inertia. The connecting-rod must be sufficiently strong to transmit these loads without significant bending, and is assumed to be rigid for the purposes of this model.

1.2.5. Crankshaft

The crankshaft helps to convert the piston motion into a continuous rotation of the drive train and wheels with its large rotational inertia and rigid structure smoothing out the combustion pressure impulses. The connecting-rod - crankshaft joint represents the end of the power cylinder system for the purposes of this project. It is assumed that the connecting-rod – crankshaft bearing can be modeled as a frictionless pin joint, and that the crankshaft's motion is purely rotational.

1.2.6. Cylinder Bore

The cylinder bore acts to create the combustion chamber, and constrain piston motion. There are many different engine block designs including cylinder liners, coolant passages, bolt configurations, reinforcements etc. which significantly affect the heat transfer, temperature and thermal deformation distributions, mechanical deformations, and structural stiffness. There are also a wide range of surface finishing methods which impact the surface roughness and bore distortion.

For the purposes of this project, we are solely interested in the geometry of the internal surface of the cylinder, which is typically provided by a nominal radius, cold bore distortion and thermal deformation profiles. The deformation of the cylinder bore, due to interactions with the piston are neglected, as is the effect of the axial temperature distribution on oil viscosity.

1.3. Previous Research

A significant amount of research into piston motion has been carried out over the past four decades, initially focusing on investigating piston slap as a significant source of engine noise and then gradually developing to predicting piston secondary motion, friction generation and oil transport. There is still much to be learnt about this system though, and while simulation programs already exist, reports from industry suggest that there continue to be problems of instability, long running times, and inflexibility, and therefore that they do not currently meet the needs of industrial research facilities.

Early work in this area [9-13] was focused on reducing engine noise and vibration, and began with rigid body, frictionless models of the piston-cylinder system based on idealized joint constraints and a variety of additional simplifications. These models were initially used to solve for the crank angles at which the lateral force on the piston is reversed, causing piston slap to occur, and to develop an idea of which parameters were likely to affect piston motion. They were later developed into more sophisticated models that were used to investigate the effect of variations in piston-cylinder bore clearance and wrist-pin offset. Experimental results obtained by Griffiths and Skorecki [9] confirmed that piston slap is a significant source of engine noise, particularly in the range of 2000 to 4000 Hz, and were used both to confirm the trends predicted by the model simulations and to investigate the effect of varying lubrication conditions on piston slap.

In the early 1980's, focus shifted to minimizing piston assembly friction and models of hydrodynamic lubrication based on the Reynold's equation were developed for this system by Knoll and Peeken [14], and then combined with a rigid body model with idealized joint constraints by Li, Rohde and Ezzat [15]. The addition of thermal and elastic deformations by Oh, Li and Goenka [16], thereby extending the lubrication model to elastohydrodynamic lubrication, further improved the accuracy of these models.

More recent work has increasingly focused on modeling of the oil film. The average Reynolds equation developed by Patir and Cheng [17] was used by Zhu et al [18-19] to take into account surface roughness and waviness, and models have been extended from essentially two-dimensional kinematic models to quasi-three-dimensional models which make use of the two-dimensional Reynolds equation, which was applied over a variable circumferential extent by Dursunkaya, Keribar and Ganapathy [20]. Boundary conditions for the oil film were initially modeled as fully-flooded and the pressure distribution was simply restricted to being non-negative, but increasingly efforts have been made to accurately model oil starvation [21-22], and Duyar et al [23] make use of a finite volume solution to correctly satisfy mass and momentum conservation in the oil film.

There has been a significant amount of research completed on the effect of surface roughness on lubrication flows, and several average flow models have been developed. The Average Reynolds equation developed by Patir and Cheng [17] was expanded by Tripp [24] to include general roughness distributions, and by Harp and Salant [25] to include inter-asperity cavitation. Prat et al [26] and Bayada et al [27] have also developed more rigorous approaches to average flows. As a starting point, we have chosen to compare direction numerical simulation results with the baseline Patir and Cheng flow factor method.

1.4. Project Objectives

The overall aim of this research is to develop an accurate numerical model of piston secondary motion, and to improve understanding of piston dynamics, skirt lubrication, friction generation and oil transport. In order to achieve this, the project was broken into several objectives:

- To develop a fast, quasi-dry model of piston secondary motion.
- To develop an elastohydrodynamic lubrication model to investigate piston skirt lubrication.
- To develop a detailed, lubricated model of piston secondary motion.
- To develop a piston oil transport model.

One of the major challenges of this research is to provide a practical set of piston analysis tools that are sufficiently accurate and numerically robust, but also fast enough to be practically useful. Currently available lubricated piston models can take days to run, whereas a dry model can run in a matter of minutes or hours. It is also critical that the model is flexible, able to be applied to range of engine designs and data formats, well documented, and modular in design to allow for future improvements.

The first step in this process, the development of a fast, quasi-dry model of piston secondary motion allowed the overall program architecture, inputs and outputs to be established, and an understanding of the components dynamics and force generation and transmission to be developed. It also provides a significantly faster running analysis tool, than the lubricated model, and comparison with the lubricated model results allows an estimate of the dry model's accuracy and limitations to be established. The quasi-dry model can be used to investigate the affect of many system parameters on component dynamics and force generation, and to assess the degree to which current uncertainties in the system, such as wrist-pin friction, can influence these results. The governing equations for component dynamics and force generation due to both component interactions and external influences are presented in Chapter 2, while the user specifications of the power cylinder system are outlined in Chapter 3.

Results of the dry model, including discussion of component dynamics, particularly piston secondary motion, and the affect of system parameters and uncertainties are presented in Chapter 4. Experimental results obtained and processed by our sponsors, and corresponding input files for modeling the same engine, enabled comparisons to be made between the simulated and experimental piston dynamics, over a range of operating conditions. These comparisons are included in Chapter 4.

A set of lubrication flow models were then developed, beginning with a quasi-steady hydrodynamic lubrication flow model, based on the Universal Reynolds equation to allow for partial film regions while maintaining conservation of oil mass. The quasi-steady lubrication model was used to investigate the effects of piston skirt tooling marks on pressure and friction generation in sliding flow, as predicted by different surface representations.

The unsteady term and surface deformation were added in steps, resulting in an unsteady hydrodynamic lubrication model and finally unsteady elastohydrodynamic lubrication model. Each of these models provides a useful stand-alone tool for investigating different lubrication flow behaviors, independent of piston dynamics, and enabling more detailed analysis of surface texture effects within reasonable calculation times. Numerical solution of unsteady elastohydrodynamic lubrication presents a significant challenge due to the complicated geometries of the piston – cylinder bore interface, combined with rapidly varying side loads, including impacts and squeezing throughout the cycle, and the corresponding structural deformations that are the same order of magnitude as the nominal piston – cylinder bore clearance. This model is further complicated by the lack of information regarding oil supply conditions which are expected to vary significantly, resulting in regions of boundary, mixed and elastohydrodynamic lubrication.

In parallel, a set of lubrication flow models using an Average Universal Reynolds equation, based on the flow factor methods introduced by Patir and Cheng [17], were developed in order to assess the degree to which these methods can provide a sufficiently accurate representation of the effect of piston skirt tooling marks. The development of each of the lubrication flow models and their results are presented in Chapter 5.

Combining the unsteady elastohydrodynamic lubrication model with the dry piston dynamics model led to the creation a lubricated piston dynamics model. The addition of oil reservoirs at the top and base of the piston skirt, and the development of simple rules for the filling and emptying of these reservoirs form the basis of the piston oil transport model, as described in Chapter 5.

Results of the lubricated piston dynamics model are presented in Chapter 6. A range of inlet oil film thickness were investigated and the effect of oil film thickness on piston dynamics and friction generation described. Different surface representations were then compared and evaluated, demonstrating clear differences between the accuracy required for prediction of piston dynamics and that required for accurate evaluation of friction. The piston skirt oil transport model was then used to investigate a range oil supply configurations.

The development of these models, and the preliminary analysis presented in this thesis are just the first steps in achieving a better understanding of piston motion and lubrication behavior. It is hoped that as our knowledge of this system increases, it will be possible to improve this complex system, leading in the longer term to reductions in engine emissions and fuel consumption.

2. System Dynamics and Dry Piston Model

This chapter aims to:

- Introduce the power cylinder system, and define its components as represented by the model.
- Provide the equations of motion governing component dynamics.
- Provide the equations governing interface and external force generation.
- Outline the numerical algorithm used to solve for component dynamics.
- Outline the numerical algorithm used to solve for the dry piston – cylinder bore interface force and corresponding piston deformation.

2.1. System Definition, Solution Outline and Nomenclature

The power cylinder system is made up of the crankshaft, connecting-rod, wrist-pin, piston, ring pack and cylinder bore, as shown in Figure 2.1.

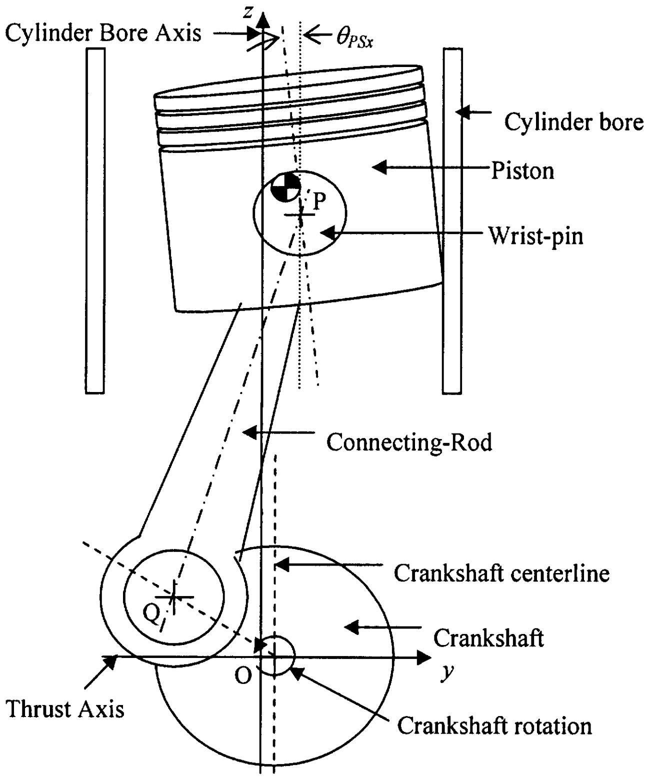

Figure 2.1: Power Cylinder System

For a given crankshaft speed and engine geometry, the ideal axial motions of the connecting-rod, wrist-pin and piston are defined by:

$$\mathbf{r}_{Q/O} = \left[-r_{CS}\sin(\theta_{CA}) + y_{CSO}\right]\mathbf{j} + r_{CS}\cos(\theta_{CA})\mathbf{k}$$

$$\mathbf{r}_{P/O} = \left[r_{CS}\cos(\theta_{CA}) + l_{CR}\cos(\phi_{CR})\right]\mathbf{k}$$

$$\phi_{CR} = \arcsin\left[\frac{y_{CSO}}{l_{CR}} - \frac{r_{CS}}{l_{CR}}\sin(\theta_{CA})\right]$$

In this project we aim to solve for piston secondary motion, that is, the lateral motion (in the y-direction) of the piston, x_{Py}, and its rotation about the pin-bore axis, ϕ_{PS}. The resulting motion of the power cylinder system is then defined by:

$$\mathbf{r}_{P/O} = x_{Py}\mathbf{j} + \left[r_{CS}\cos(\theta_{CA}) + l_{CR}\cos(\phi_{CR})\right]\mathbf{k}$$

$$\phi_{CR} = \arcsin\left[\frac{y_{CSO}}{l_{CR}} - \frac{r_{CS}}{l_{CR}}\sin(\theta_{CA}) - \frac{x_{Py}}{l_{CR}}\right]$$

This solution is obtained iteratively, as explained in more detail in Section 2.5, by:

- estimating the lateral motion, x_{Py}, and piston tilt, ϕ_{PS},
- applying axial force balances on the piston and wrist-pin to calculate the axial force transmitted to the connecting-rod
- applying a moment balance, on the connecting-rod, about the x-axis at point Q, to obtain the lateral force and friction torque at the connecting-rod small end bearing,
- applying a lateral force balance on the wrist-pin to determine the lateral force transmitted to the piston,
- checking to see whether the lateral force balance on the piston, and x-moment balance on the piston and wrist-pin are satisfied,
- improving the estimated lateral motion, x_{Py}, and piston tilt, ϕ_{PS}, until convergence is achieved.

In order to achieve this solution, we must first define:

- the dynamics of the each of the components,
- the force and moment balances that govern their motion, and
- the equations governing interface and external force generation.

For the purposes of this project, our system is defined by the following assumptions:

- The crankshaft is rigid, and carries out purely rotational motion.
- The crankshaft – connecting-rod bearing is an ideal frictionless pin joint, allowing relative rotational motion of the two components without friction generation or relative displacement at point Q.
- The connecting-rod is rigid, with a distributed mass.

- The connecting-rod – wrist-pin and wrist-pin – piston bearings are defined by a simple bearing model which generates a friction force acting perpendicular to their normal load, and corresponding friction moment, as described in Section 2.3.2. While there are significant clearances in each of these bearings, for the purposes of this project it is assumed that the connecting-rod small end, wrist-pin and piston have no relative displacement at point P.
- The wrist-pin is rigid, with a distributed mass.
- The piston is rigid, with a distributed mass, for the purposes of describing the motion of its centre of gravity. Structural deformations of the piston skirt and lands, due to interaction with the cylinder bore, are considered when determining the forces generated at the piston – cylinder-bore interface, as described in Section 2.3.3, and are of the order of 100 μm. Any variations in the moment of inertia or position of the centre of gravity, due to these deformations are considered to be negligible.
- The ring pack is neglected for the purposes of this project as the forces between the ring pack and piston are small compared to the other forces acting on the piston.
- The cylinder bore is assumed to be stationary and rigid. Depending on the combination of materials, cylinder bore deformation can be as significant as piston deformation, however, as a starting point, for the purposes of this project, cylinder bore deformation is neglected.

Given the large number of equations contained in this chapter, and the repetitive nature of the symbols used, it is convenient to define some general guidelines for nomenclature, which are assumed to apply unless otherwise specified.

Location	**Symbol**	**Explanation of Variable**
Main text		
	$\mathbf{a}$	Vector acceleration
	$\mathbf{F}$	Vector force
	F	Scalar force, direction usually specified by subscript
	$\mathbf{g}$	Gravity vector
	$\mathbf{i}$	Unit vector in the x-direction
	$\mathbf{j}$	Unit vector in the y-direction
	$\mathbf{k}$	Unit vector in the z-direction
	l	Length
	$\mathbf{M}$	Vector moment
	M	Scalar moment
	m	Mass
	p	Pressure
	$\mathbf{r}$	Vector position
	r	Radius
	t	Time
	$\boldsymbol{x}$	Vector position
	x	Scalar position, direction usually specified by subscript, otherwise, in x-direction
	y	Scalar position in y-direction
	y_{CSO}	Crankshaft offset
	z	Scale position in z-direction

	$\phi, \dot{\phi}$, $\ddot{\phi}$	Angular position, velocity and acceleration
	$\theta_{CA}, \dot{\theta}_{CA}$, $\ddot{\theta}_{CA}$	Crankshaft angle, speed and acceleration
	τ	Scalar torque or moment
	ω_{CA}	Crankshaft speed (angular)
	°*CA*	Degrees of crankshaft angle
Subscript		
	i/j	Dynamics: Pertaining to *i*, relative to *j*. Forces and Moments: Due to component *i*, acting on component *j*.
	0	Referring to an initial configuration or geometric specification
	/A	With respect to reference frame A
	ANG	Pertaining to angular momentum
	/B	With respect to reference frame B
	B	Pertaining to the bearing model
	bore	Pertaining to, or relative to the Cylinder Bore
	CB	Pertaining to, or relative to the Cylinder Bore
	CG	Pertaining to the component's centre of gravity
	CR	Pertaining to, or relative to the Connecting-Rod
	CS	Pertaining to, or relative to the Crankshaft
	ext	External
	F	Friction component
	N	Normal component (generally acting radially)
	O	Pertaining to, or relative to the point *O*, located at the ideal centre of the crankshaft.
	P	Pertaining to, or relative to the point *O*, located at the ideal centre of the wrist-pin, pin boss and connecting-rod small end bearing.
	P	Pertaining to the combustion chamber pressure.
	PS	Pertaining to, or relative to the Piston
	Q	Pertaining to, or relative to the point *O*, located at the ideal centre of the connecting-rod large end bearing.
	WP	Pertaining to, or relative to the Wrist-Pin
	x, X	Component in the *x*-direction
	XX	Relative to the *x*-axis (Moment of Inertia)
	y, Y	Component in the *y*-direction
	z, Z	Component in the *z*-direction

Table 2.1: Nomenclature Guidelines

2.2. Component Dynamics and Equations of Motion

This section contains a summary of the equations defining the component dynamics, and the force and moment balances governing their motion. A more detailed derivation of these equations is provided in Appendix 1.

2.2.1. Crankshaft Dynamics

It is assumed that the crankshaft has no linear motion, and rotates about its axis with a given angular speed, $\omega_{CA}(t)$. The motion of the centre of the connecting-rod large end bearing, point Q, as a function of crankshaft angle, $\theta_{CA}(t)$, relative to reference frame A, is therefore given by:

$$\mathbf{r}_{Q/O} = \left[-r_{CS}\sin(\theta_{CA}) + y_{CSO}\right]\mathbf{j} + r_{CS}\cos(\theta_{CA})\mathbf{k}$$

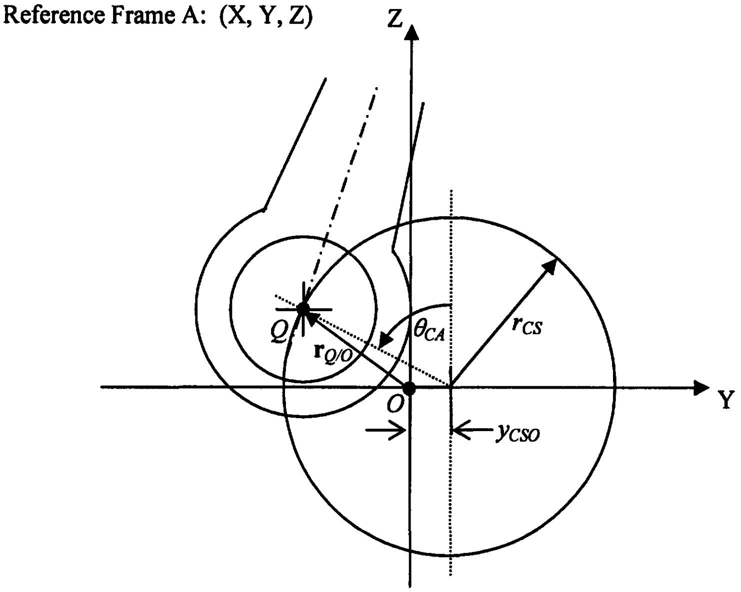

Figure 2.2: Crankshaft Dynamics

2.2.2. Connecting-Rod Dynamics and Equations of Motion

The connecting-rod connects the wrist-pin to the crankshaft, helping to convert the linear motion of the piston into the angular motion of the crankshaft. It is assumed that:

- There is no relative displacement between the centre of the large end of the connecting-rod and the corresponding point on the crankshaft, Q.
- The large end of the connecting-rod is attached to the crankshaft via bearings which are assumed to be frictionless, and therefore provide no moment to the connecting-rod.
- The connecting-rod is considered to be rigid for the purposes of this work.
- There is no relative displacement between the small end of the connecting-rod, the wrist-pin and piston at point P.

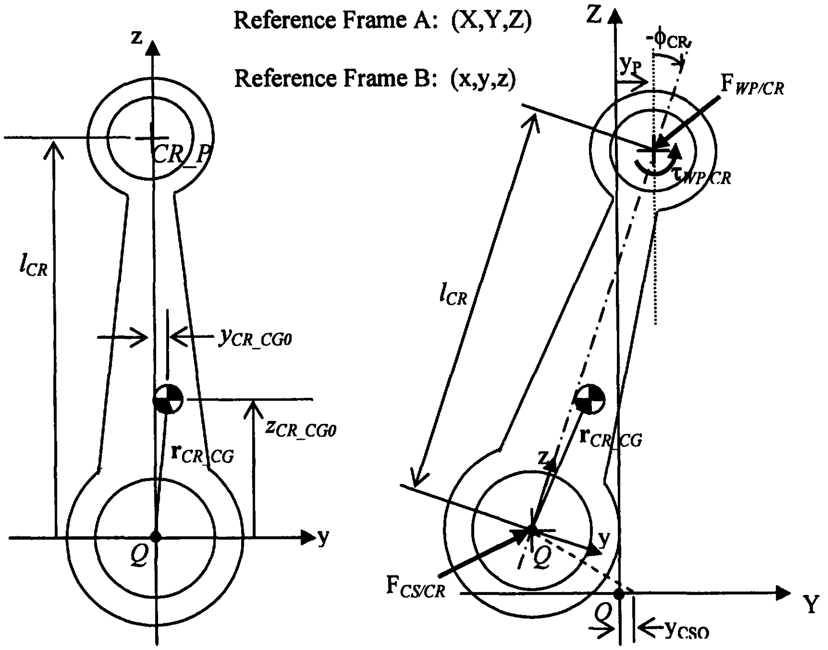

Figure 2.3: Connecting Rod Geometry and Dynamics

The connecting-rod angle, ϕ_{CR}, is defined by:

$$\phi_{CR} = \arcsin\left[\frac{y_{CSO}}{l_{CR}} - \frac{r_{CS}}{l_{CR}}\sin(\theta_{CA}) - \frac{x_{Py}}{l_{CR}}\right]$$

The lateral motion of point P does not significantly impact the connecting-rod angle, but the resulting changes to the connecting-rod angular acceleration, and the corresponding connecting-rod, wrist-pin and piston inertia terms, are important.

The motion of the centre of gravity of the connecting-rod can be expressed in terms of the crankshaft motion and engine geometry:

$$\begin{aligned}\mathbf{r}_{CR\_CG/O} &= \mathbf{r}_{Q/O} + \mathbf{r}_{CR\_CG/Q} \\ &= \left[-r_{CS}\sin(\theta_{CA}) + y_{CSO}\right]\mathbf{j} + r_{CS}\cos(\theta_{CA})\mathbf{k} + \mathbf{r}_{CR\_CG/Q}\end{aligned}$$

$$\begin{aligned}\mathbf{a}_{CR\_CG/A} &= \mathbf{a}_{Q/A} + \left[\left(\ddot{\phi}_{CR}\mathbf{i}\right)\times \mathbf{r}_{CR\_CG/Q}\right] + \left(\dot{\phi}_{CR}\mathbf{i}\right)\times\left[\left(\dot{\phi}_{CR}\mathbf{i}\right)\times \mathbf{r}_{CR\_CG/Q}\right] \\ &= \left[-\ddot{\theta}_{CA}r_{CS}\cos(\theta_{CA}) + \dot{\theta}_{CA}^{\,2}r_{CS}\sin(\theta_{CA})\right]\mathbf{j} - \left[\ddot{\theta}_{CA}r_{CS}\sin(\theta_{CA}) + \dot{\theta}_{CA}^{\,2}r_{CS}\cos(\theta_{CA})\right]\mathbf{k} \\ &\quad + \left[\left(\ddot{\phi}_{CR}\mathbf{i}\right)\times \mathbf{r}_{CR\_CG/Q}\right] + \left(\dot{\phi}_{CR}\mathbf{i}\right)\times\left[\left(\dot{\phi}_{CR}\mathbf{i}\right)\times \mathbf{r}_{CR\_CG/Q}\right]\end{aligned}$$

where the position of the centre of gravity, of the connecting-rod, relative to point Q, $\mathbf{r}_{CR\_CG/Q}$, is defined as:

$$\mathbf{r}_{CR\_CG/Q} = x_{CR\_CG0}\mathbf{i} + \left[\cos(\phi_{CR}) - z_{CR\_CG0}\sin(\phi_{CR})\right]\mathbf{j} + \left[y_{CR\_CG0}\sin(\phi_{CR}) + z_{CR\_CG0}\cos(\phi_{CR})\right]\mathbf{k}$$

As shown in Figure 2.3, the connecting-rod is subject to external forces from the interfaces it shares with the crankshaft and wrist-pin, $\mathbf{F}_{CS/CR}$ and $\mathbf{F}_{WP/CR}$ respectively, and due to gravity. The calculation of these forces is described in Sections 2.3 and 2.4. Conservation of linear momentum for the connecting-rod yields the following equation:

$$\mathbf{F}_{CS/CR} + \mathbf{F}_{WP/CR} + m_{CR}\mathbf{g} = m_{CR}\mathbf{a}_{CR\_CG/A}$$

Assuming that the motion of the connecting-rod is two-dimensional, conservation of angular momentum for the connecting-rod, about the point *Q*, yields the following equation:

$$\begin{aligned} I_{CR\_XX}\ddot{\phi}_{CR} = {} & \tau_{WP/CRX} + r_{CR\_P/Q_Y}F_{WP/CRZ} - r_{CR\_P/Q_Z}F_{WP/CRY} + r_{CR\_CG/Q_Y}m_{CR}g_Z \\ & - r_{CR\_CG/Q_Z}m_{CR}g_Y - r_{CR\_CG/Q_Y}m_{CR}a_{CR\_CG/A_Z} + r_{CR\_CG/Q_Z}m_{CR}a_{CR\_CG/A_Y} \end{aligned}$$

Rearranging this equation, we can express that angular motion of the connecting-rod in terms of known quantities, and the three unknown forces and moments acting at the connecting-rod – wrist-pin interface, $F_{WP/CR\,Z}$, $F_{WP/CR\,Y}$, and $\tau_{WP/CR\,X}$:

$$F_{WP/CRY} = \frac{\tau_{WP/CRX}}{r_{CR\_P/Q_Z}} + \frac{1}{r_{CR\_P/Q_Z}}\begin{bmatrix} r_{CR\_P/Q_Y}F_{WP/CRZ} + r_{CR\_CG/Q_Y}m_{CR}g_Z - r_{CR\_CG/Q_Z}m_{CR}g_Y \\ - r_{CR\_CG/Q_Y}m_{CR}a_{CR\_CG/A_Z} + r_{CR\_CG/Q_Z}m_{CR}a_{CR\_CG/A_Y} - I_{CR\_XX}\ddot{\phi}_{CR} \end{bmatrix}$$

The axial force acting at the connecting-rod – wrist-pin interface can be defined by axial force balances on the piston and wrist-pin, leaving the lateral force and moment to be solved for simultaneously from the above equation and the simple bearing model described in Section 2.3.2.

2.2.3. Wrist-Pin Dynamics and Equations of Motion

The wrist-pin connects the connecting-rod to the piston, allowing the piston to rotate relative to the connecting-rod. It can be fixed to the connecting-rod, fixed to the piston, or able to rotate independently of both the connecting-rod and piston (floating pin). For the purposes of this project we assume that the wrist-pin is rigid, and that there is no relative displacement between the wrist-pin, piston and small end of the connecting-rod at point *P*.

The motion of the centre of gravity of the wrist-pin can be expressed as:

$$\begin{aligned} \mathbf{r}_{WP\_CG/O} &= \mathbf{r}_{WP\_P/O} + \mathbf{r}_{WP\_CG/WP\_P} \\ &= x_{P_Y}\mathbf{j} + \left[r_{CS}\cos(\theta_{CA}) + l_{CR}\cos(\phi_{CR})\right]\mathbf{k} + \mathbf{r}_{WP\_CG/WP\_P} \end{aligned}$$

$$\begin{aligned}\mathbf{a}_{WP\_CG/A} &= \mathbf{a}_{WP\_P/A} + \left[(\ddot{\phi}_{WP}\mathbf{i}) \times \mathbf{r}_{WP\_CG/WP\_P}\right] + (\dot{\phi}_{WP}\mathbf{i}) \times \left[(\dot{\phi}_{WP}\mathbf{i}) \times \mathbf{r}_{WP\_CG/WP\_P}\right] \\ &= \ddot{x}_{Py}\mathbf{j} - \left[\ddot{\theta}_{CA} r_{CS} \sin(\theta_{CA}) + \dot{\theta}_{CA}{}^2 r_{CS} \cos(\theta_{CA}) + \ddot{\phi}_{CR} l_{CR} \sin(\phi_{CR}) + \dot{\phi}_{CR}{}^2 l_{CR} \cos(\phi_{CR})\right]\mathbf{k} \\ &\quad + \left[(\ddot{\phi}_{WP}\mathbf{i}) \times \mathbf{r}_{WP\_CG/WP\_P}\right] + (\dot{\phi}_{WP}\mathbf{i}) \times \left[(\dot{\phi}_{WP}\mathbf{i}) \times \mathbf{r}_{WP\_CG/WP\_P}\right]\end{aligned}$$

where the position of the centre of gravity, of the wrist-pin, relative to point *WP_P*, $\mathbf{r}_{WP\_CG/WP\_P}$, is defined as:

$$\begin{aligned}\mathbf{r}_{WP\_CG/WP\_P} &= x_{WP\_CG0}\mathbf{i} + \left[y_{WP\_CG0} \cos(\phi_{WP}) - z_{WP\_CG0} \sin(\phi_{WP})\right]\mathbf{j} \\ &\quad + \left[y_{WP\_CG0} \sin(\phi_{WP}) + z_{WP\_CG0} \cos(\phi_{WP})\right]\mathbf{k}\end{aligned}$$

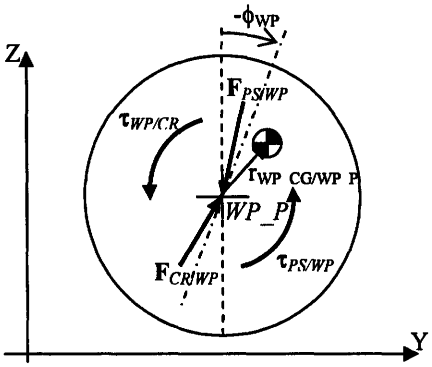

Figure 2.4: Wrist-Pin Dynamics

The wrist-pin is subject to external forces from the interfaces it shares with the connecting-rod and piston, $\mathbf{F}_{CR/WP}$ and $\mathbf{F}_{PS/WP}$ respectively, and due to gravity. The calculation of these forces is described in Sections 2.3 and 2.4. Conservation of linear momentum for the wrist-pin yields the following equation:

$$\mathbf{F}_{PS/WP} + \mathbf{F}_{CR/WP} + m_{WP}\mathbf{g} = m_{WP}\mathbf{a}_{WP\_CG/A}$$

Assuming that the motion of the wrist-pin is two-dimensional, conservation of angular momentum for the wrist-pin, about point *P*, yields the following equation:

$$\begin{aligned}I_{WP\_XX}\ddot{\phi}_{WP} &= \tau_{PS/WPX} + \tau_{CR/WPX} + r_{WP\_CG/WP\_P_Y} \times m_{WP} g_Z - r_{WP\_CG/WP\_P_Z} \times m_{WP} g_Y \\ &\quad - r_{WP\_CG/WP\_P_Y} \times m_{WP} a_{WP\_CG/A_Z} + r_{WP\_CG/WP\_P_Z} \times m_{WP} a_{WP\_CG/A_Y}\end{aligned}$$

2.2.4. Piston Dynamics and Equations of Motion

The piston is connected to the wrist-pin and constrained by the cylinder bore. During combustion the pressure force pushes the piston along the cylinder bore, thereby converting the chemical energy in the fuel into kinetic energy. The piston also carries the ring pack, which act to seal the combustion gases and control the transport of lubricating oil along the cylinder bore. The piston rotates relative to the wrist-pin, but it is assumed for the purposes of this model that there is no relative displacement between the two components at point *P*.

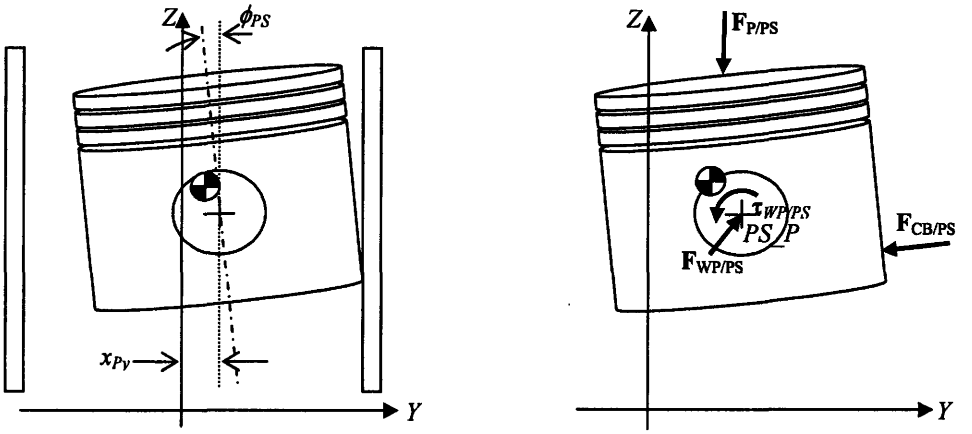

Figure 2.5: Piston Geometry and Dynamics

The motion of the centre of gravity of the piston can be expressed as:

$$\begin{aligned}\mathbf{r}_{PS\_CG/O} &= \mathbf{r}_{PS\_P/O} + \mathbf{r}_{PS\_CG/PS\_P}\\ &= x_{Py}\mathbf{j} + \left[r_{CS}\cos(\theta_{CA}) + l_{CR}\cos(\phi_{CR})\right]\mathbf{k} + \mathbf{r}_{PS\_CG/PS\_P}\end{aligned}$$

$$\begin{aligned}\mathbf{a}_{PS\_CG/A} &= \mathbf{a}_{PS\_P/A} + \left[\left(\ddot{\phi}_{PS}\mathbf{i}\right)\times \mathbf{r}_{PS\_CG/PS\_P}\right] + \left(\dot{\phi}_{PS}\mathbf{i}\right)\times\left[\left(\dot{\phi}_{PS}\mathbf{i}\right)\times \mathbf{r}_{PS\_CG/PS\_P}\right]\\ &= \ddot{x}_{Py}\mathbf{j} - \left[\ddot{\theta}_{CA}r_{CS}\sin(\theta_{CA}) + \dot{\theta}_{CA}{}^{2}r_{CS}\cos(\theta_{CA}) + \ddot{\phi}_{CR}l_{CR}\sin(\phi_{CR}) + \dot{\phi}_{CR}{}^{2}l_{CR}\cos(\phi_{CR})\right]\mathbf{k}\\ &\quad + \left[\left(\ddot{\phi}_{PS}\mathbf{i}\right)\times \mathbf{r}_{PS\_CG/PS\_P}\right] + \left(\dot{\phi}_{PS}\mathbf{i}\right)\times\left[\left(\dot{\phi}_{PS}\mathbf{i}\right)\times \mathbf{r}_{PS\_CG/PS\_P}\right]\end{aligned}$$

where the position of the centre of gravity, of the piston, relative to point *PS_P*, $\mathbf{r}_{PS\_CG/PS\_P}$, is defined as:

$$\begin{aligned}\mathbf{r}_{PS\_CG/PS\_P} &= x_{PS\_CG0}\mathbf{i} + \left[y_{PS\_CG0}\cos(\phi_{PS}) - z_{PS\_CG0}\sin(\phi_{PS})\right]\mathbf{j}\\ &\quad + \left[y_{PS\_CG0}\sin(\phi_{PS}) + z_{PS\_CG0}\cos(\phi_{PS})\right]\mathbf{k}\end{aligned}$$

The piston is subject to external forces from the interfaces it shares with wrist-pin and cylinder bore, $\mathbf{F}_{WP/PS}$ and $\mathbf{F}_{CB/PS}$ respectively, and due to combustion chamber pressure, $\mathbf{F}_{P/PS}$, and gravity. The calculation of these forces is described in Sections 2.3 and 2.4. Conservation of linear momentum for the piston yields the following equation:

$$\mathbf{F}_{WP/PS} + \mathbf{F}_{CB/PS} + \mathbf{F}_{P/PS} + m_{PS}\mathbf{g} = m_{PS}\mathbf{a}_{PS\_CG/A}$$

Assuming that the motion of the piston is two-dimensional, conservation of angular momentum for the piston, about the ideal centre of the pin bore, point *P*, yields the following equation:

$$I_{PS\_XX}\ddot{\phi}_{PS} = \tau_{WP/PSX} + \left\{\begin{aligned}&\mathbf{r}_{CB/PS\_P}\times\mathbf{F}_{CB/PS} + \mathbf{r}_{P/PS\_P}\times\mathbf{F}_{P/PS}\\ &+\mathbf{r}_{PS\_CG/PS\_P}\times m_{PS}\mathbf{g} - \mathbf{r}_{PS\_CG/PS\_P}\times m_{PS}\mathbf{a}_{PS\_CG/A}\end{aligned}\right\}_X$$

2.3. Component Interface Models

2.3.1. Crankshaft – Connecting-Rod Interface:

The Crankshaft – Connecting-Rod interface is assumed to be an idealized frictionless pin-joint with no relative displacement between the two components at point *Q*. The forces transmitted at this joint are not considered in this analysis, apart from assuming that no moment is generated at the joint.

2.3.2. Connecting-Rod – Wrist-Pin and Wrist-Pin – Piston Interfaces:

Depending on the engine design, the Wrist-Pin may be fixed to Connecting-Rod, fixed to the Piston, or float freely between the two. Cold wrist-pin – piston clearances are generally of the order of 5-25 μm, expanding with speed and load to around 80μm [28, 29]. Previous hydrodynamic modeling results [28] indicate that most of the wrist-pin motion, relative to the piston, is in the axial direction, with relative lateral motions of about one quarter of the operating clearance. Taking these motions into account would require a significantly more complicated wrist-pin bearing model, and corresponding increase in computational time. As a starting point it is assumed that there is no relative displacement between these three components at point *P*, but that the Wrist-Pin rotates independently of the other two, generating a friction moment, and that we must solve for this angular motion.

The Connecting-Rod – Wrist-Pin and Wrist-Pin – Piston interfaces can be considered as lubricated bearings whenever there is relative angular motion between the two components. The load supported by the bearing is considered to be made up of two components as shown in Figure 2.6:

- **F_N**: A normal force, which acts radially to the ideal bearing centre.
- **F_F**: A friction force, which acts circumferentially to the ideal bearing centre, at the same location as the normal force, in order to resist relative rotation of the two components.

The magnitude of the friction force is assumed to be related to the magnitude of the normal force by a friction coefficient function of the form:

$$f = a_1 \left(\frac{\mu R L \Delta \dot{\phi}}{|F|} \right)^{a_2} \left(\frac{R}{c} \right)^{a_3}$$

$$|F_F| = f |F_N|$$

where f is the friction coefficient, a_1, a_2, and a_3 are user supplied constants describing the wrist-pin bearing's friction behavior, μ is the viscosity of the lubrication oil in the bearing, R is the bearing radius, L is the bearing length, c is the bearing clearance, F is the load on the bearing, F_N is the normal load on the bearing, F_F is the friction force, and $\Delta\dot{\phi}$ is the relative angular velocity of component 1 with respect to component 2.

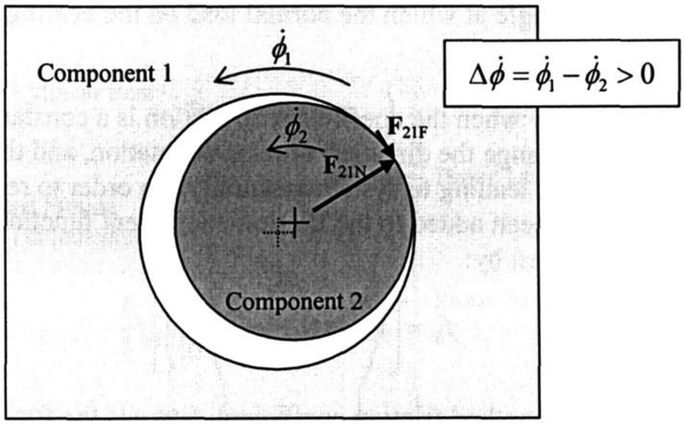

Figure 2.6: Bearing Forces Acting on Component 1

Many different correlations are available for bearing friction. Petroff's law [30] is one of the simplest of these:

$$f = 2\pi\left(\frac{\mu RL\Delta\dot{\phi}}{|F|}\right)\left(\frac{R}{c}\right) = 2\pi^2\left(\frac{\mu N}{P}\right)\left(\frac{R}{c}\right)$$

$$a_1 = 2\pi, a_2 = 1, a_3 = 1$$

where N = relative rotational speed in rev/s, P = pressure

The friction coefficient is a constant, a_1, when a_2 and a_3 are set equal to zero. Previous research [29] provides experimentally obtained friction coefficient values of 0.005 to 0.1 throughout the region around combustion TDC, with lower values (0.02-0.04) during peak loads. The oil temperature during these experiments was 140-150°C.

The direction of the friction force is determined by the angle at which the normal force acts, and the sign of the relative rotational speed of the components.

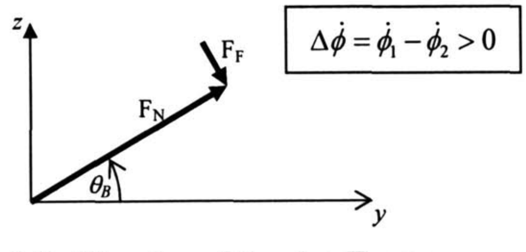

Figure 2.7: Direction of Bearing Forces

$$\theta_B = \arctan\left(\frac{F_{N_z}}{F_{N_y}}\right)$$

$$\mathbf{F}_F = -\mathrm{sign}(\Delta\dot{\phi}) f |F_N| [-\sin(\theta_B)\mathbf{j} + \cos(\theta_B)\mathbf{k}]$$

where θ_B is the angle at which the normal load on the bearing acts, as defined in Figure 2.7.

In some case, particularly when the coefficient of friction is a constant, small changes in rotational speeds may change the direction of relative rotation, and thereby significantly change the friction force, leading to system instability. In order to reduce this effect, a smoothing function has been added to the friction coefficient function. The smoothed friction coefficient is given by:

$$f_S = \left[1 - \exp\left(-\left|\frac{\Delta\dot{\phi}}{0.1 \times a}\right|\right)\right] f$$

where f_S is the smoothed friction coefficient, and a is the friction coefficient bandwidth.

The resulting equation governing bearing friction force is:

$$\mathbf{F}_F = -\mathrm{sign}(\Delta\dot{\phi}) f_S |F_N| [-\sin(\theta_B)\mathbf{j} + \cos(\theta_B)\mathbf{k}]$$

Combining the friction and normal components, the total force acting on the bearing is given by:

$$\mathbf{F}_B = |F_N| \{\cos(\theta_B) + \mathrm{sign}(\Delta\dot{\phi}) f_S \sin(\theta_B)\}\mathbf{j} + |F_N| \{\sin(\theta_B) - \mathrm{sign}(\Delta\dot{\phi}) f_S \cos(\theta_B)\}\mathbf{k}$$

The normal force is assumed to act radially, and therefore generate no moment. The moment generated by the friction force, about the ideal centre of the bearing, is given by:

$$\mathbf{M}_B = -\mathrm{sign}(\Delta\dot{\phi}) f_S |F_N| R\mathbf{i}$$

2.3.3. Piston – Cylinder Bore Interface:

The piston – cylinder bore interface is essentially made up of three components:

1. The deformed piston surface geometry, taking into account piston motion.
2. The cylinder bore geometry, which is considered to be stationary and rigid for the purposes of this project.
3. The oil film thickness distribution, which is neglected for the purposes of the dry piston model, but included in the lubricated piston model, as discussed in Chapter 5.

Piston – cylinder bore clearances are typically in the range of 0-100 μm. The variations in bore geometry are significant and lead to a height distribution which varies in time, relative to the piston. The combined surface roughness is of the order of 0.5 μm [31]. When piston tooling marks are present, they tend to have surface gradients of the order of 1/30, and are expected to dominate over any surface roughness effects.

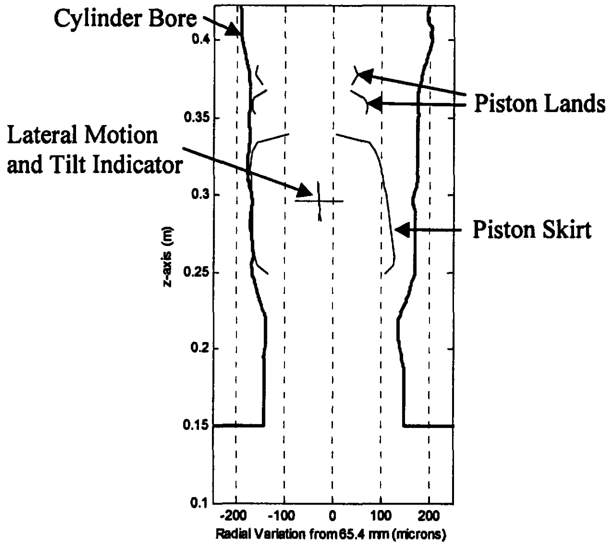

Figure 2.8: Diagram of Piston – Cylinder Bore Interface

The piston's axial sliding velocity ranges from 0-10 m/s. There is significant lateral motion of the piston both during piston slap events, and throughout the rest of the cycle due to the applied side load. Peak lateral velocities are expected to be around 0.01 m/s. In the absence of oil, the side load is supported by solid-solid contact between the piston and cylinder bore, generating significant friction.

The elasticity of the piston, as described by a compliance matrix, leads to structural deformations of the piston skirt and lands due to combustion chamber pressure, axial inertia, and pressure generated at the piston – cylinder bore interface. These deformations significantly alter profile of the piston, and resulting piston – cylinder bore clearance distribution.

The piston - cylinder bore interface model can be considered to be made up of four sub-models:

- Contact model: Determines pressure generation as a function of surface overlap.
- Contact friction model: Determines friction force as a function of normal force and relative surface velocity.
- Fluid model: Determines hydrodynamic pressure generation, shear stress and oil flow as a function of surface motion and oil film thickness.
- Compliance matrix: Determines piston surface deformation as a function of normal force.

These sub-models form a highly non-linear system which must be solved iteratively, using the algorithms described in Sections 2.6 and 5.5, to determine:

- net forces and moments acting on the piston,
- hydrodynamic and contact pressure distributions,
- shear stress and contact friction distributions,
- piston deformation, and
- oil film thickness distribution and oil transport by the piston skirt.

2.3.3.1 Contact Model:

A contact model describes the way in which pressure is generated by solid-solid contact as two surfaces approach each other, as shown in Figure 2.9. We assume that the pressure generation can be described by three constants, C_1, C_2, and h_{asp}, and a function of the form:

$$p_{asp} = \begin{cases} C_1 (h_{asp} - h)^{C_2}, & h \leq h_{asp} \\ 0, & h > h_{asp} \end{cases}$$

where p_{asp} is the average asperity contact pressure, h is the local gap height between the mean surface lines, h_{asp} is a measure of asperity or tooling mark height, as appropriate, and C_1 and C_2 are the corresponding user supplied constants.

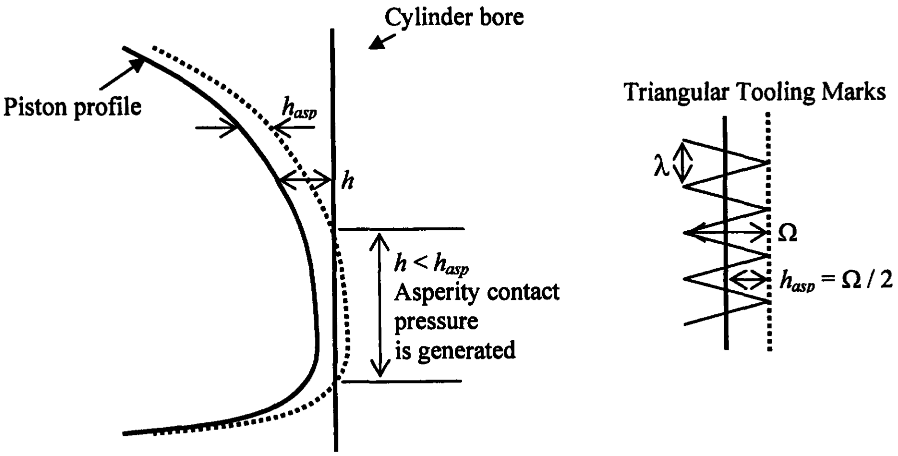

Figure 2.9: Contact Model Representations

When the piston skirt has tooling marks, their geometry dominates the generation of contact pressure. For triangular tooling marks, the analytical solution for a blunt wedge against a flat plane [32,18] provides an appropriate description of the relationship between contact pressure and surface separation:

$$\frac{\Omega}{2}-h=\left(\frac{\lambda p_{asp}}{E^*}\right)\left[0.6366\left(\ln\left(\frac{2\Omega}{\lambda}\right)-\ln\left(\frac{\lambda p_{asp}}{E^*}\right)\right)+1.0779\right],\quad h\leq\frac{\Omega}{2}$$

$$E^*=\left[\frac{1-\nu_1^2}{E_1}+\frac{1-\nu_2^2}{E_2}\right]^{-1}$$

where λ is the wavelength of the tooling marks, Ω is the peak to valley waveheight of the tooling marks, E_i is the Young's Modulus of surface *i,* and ν_i is the Poisson's Ratio of the surface *i.*

For a given set of surface properties, curve-fitting over an appropriate range of δ results in an expression of the form assumed above.

$$\left.\begin{array}{l}\lambda=250\,\mu\text{m}\\ \Omega=7\,\mu\text{m}\\ E^*=47\text{ GPa}\end{array}\right\}\quad p_{asp}=4.9065\times10^{13}\left(\frac{\Omega}{2}-h\right)^{1.0652}$$

$$\left.\begin{array}{l}\lambda=640\,\mu\text{m}\\ \Omega=20\,\mu\text{m}\\ E^*=47\text{ GPa}\end{array}\right\}\quad p_{asp}=2.013\times10^{13}\left(\frac{\Omega}{2}-h\right)^{1.069}$$

A detailed derivation of the analytical solution and numerical integrals is provided in Appendix 1.

When there are no tooling marks, or the waveheight is of the same order as the surface roughness, an asperity contact model is more appropriate. Greenwood and Tripp's model of contact pressure generated by two nominally flat surfaces [33] has been widely used to describe the relationship between contact pressure and surface overlap for both the piston – cylinder bore and ring-pack – cylinder bore interfaces [5, 6, 20, 23, 34]. A convenient formula for this model was proposed by Hu et al [34]:

$$p_{asp}=\begin{cases}A(4.0\sigma-h)^{6.804} & h\leq4.0\sigma\\ 0 & h>4.0\sigma\end{cases}$$

$$A=4.4068\times10^{-5}\times\frac{16\sqrt{2}}{15}\pi\frac{(N\beta'\sigma)^2}{\sigma}\sqrt{\frac{\sigma}{\beta'}}\frac{1}{\frac{1-\nu_1^2}{E_1}+\frac{1-\nu_2^2}{E_2}}$$

$$A=2.0884\times10^{-4}\frac{(N\beta'\sigma)^2}{\sqrt{\sigma\beta'}}E^*$$

$$(N\beta'\sigma) \sim 0.03 - 0.06$$

$$\sqrt{\frac{\sigma}{\beta'}} \sim 0.001 - 0.3$$

$$E^* \sim 7\times10^{10} - 9\times10^{10} \qquad [31, 33, 34]$$

where N is the number of asperities per unit contact area, β' is the asperity radius of curvature, and σ is the variance of the composite surface roughness.

2.3.3.2 Contact Friction Model:

A simple friction model is used to describe the contact friction force generated as the piston slides along the cylinder bore, as a function of contact force and a constant coefficient of friction:

$$\mathbf{F}_F = -sign(\Delta\dot{x}_z) f F_N \mathbf{k}$$

where f is the coefficient of friction, F_N is the contact force generated at the surface, and $\Delta\dot{x}_z$ is the axial velocity of the piston, relative to the cylinder bore.

2.3.3.3 Fluid Model:

An elastohydrodynamic lubrication model is included in the lubricated piston model, as described in detail in Chapter 5. It describes the way in which pressure and shear stress are generated within the oil film between the piston and cylinder bore, and the way in which the oil is transported. In the dry model, the effect of lubricant is neglected.

2.3.3.4 Compliance Matrix:

The compliance matrix is used to describe the radial mechanical deformation of the piston due to the combined loading of the contact and fluid pressures acting normal to the surface of the piston skirt and lands. The piston has a complicated structure with varying wall thicknesses ranging from a few millimeters to the full diameter of the piston, reinforcing struts, bearing surfaces, wear resistant inserts, and other variations in material. There are many different ways of generating such a matrix, and some of these are discussed in more detail in Section 3.4.4. For the purposes of this project, it is assumed that the user supplies a suitable compliance matrix, generated using an FEA program. This matrix is then used to calculate the radial deformation of the piston due to the normal forces generated due to the combined loading of the contact and fluid pressures.

$$\{\text{Radial Deformation}\} = [\text{Compliance Matrix}]\{\text{Normal Force}\}$$

2.4. Externally Applied Forces and Inertia Terms

2.4.1. Combustion Chamber Pressure Force:

The pressure force applied to the piston is assumed to act at a specified position in the plane perpendicular to the cylinder axis, at a specified height from the wrist-pin, as shown in Figure 2.10. Typically the pressure force is assumed to act at the ideal centre of the cylinder bore.

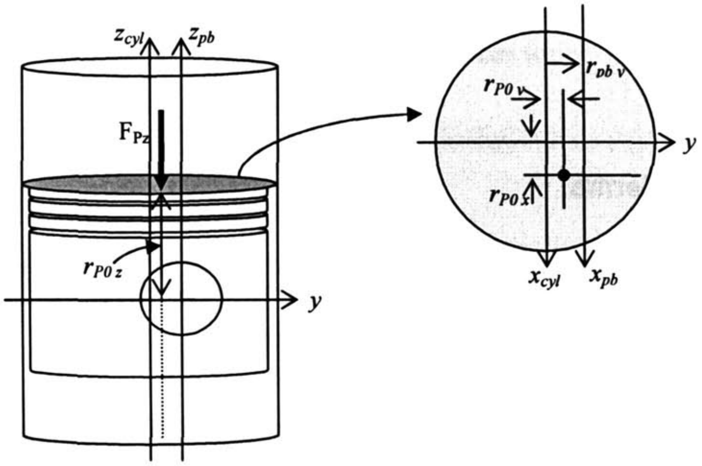

Figure 2.10: Combustion Pressure Force and Moment

When the piston tilts, the magnitude of the axial component of the pressure force is unchanged as it is assumed that the rings and piston combined still block the cylinder bore and transmit the same total force to the piston, therefore the projected area in the axial direction is constant. In the lateral direction though, the projected area over which pressure acts changes significantly. The projected areas and corresponding pressure forces are given by:

$$A_Z = \pi r_{bore}^2$$
$$A_Y = \pi r_{bore}^2 \tan(-\phi_{PS})$$
$$F_{PZ} = -pA_Z$$
$$F_{PY} = -pA_Y$$

The force radius, relative to the wrist-pin, must be adjusted to take into account the piston's lateral motion, resulting in the following definition for the pressure moment:

$$r_{PX} = r_{P0X}$$
$$r_{PY} = r_{P0Y} - r_{pbY} - x_{PSY}$$
$$r_{PZ} = r_{P0Z}$$
$$M_{PX} = \{\mathbf{r}_P \times \mathbf{F}_P\}_X = (r_{P0Y} - r_{pbY} - x_{PSY})F_{PZ} - r_{P0Z}F_{PY}$$

2.4.2. Gravity Force:

The gravity force for each component is given by the product of the components mass and the gravitational vector specified by the user:

$$\mathbf{F}_G = m\mathbf{g}$$

The moment generated by the gravity force, about a point, *P*, is given by the cross product of the position of the centre of gravity, relative to *P* and the gravity force.

$$\mathbf{M}_G = \mathbf{r}_{P\_CG} \times \mathbf{F}_G$$

2.4.3. Inertia Terms:

The general component equations of motion, described in detail in Section 2.2, are of the form:

$$\sum \mathbf{F}_{ext} = m\mathbf{a}_{CG/A}$$

$$\sum \mathbf{M}_{ext/P} = \frac{d\mathbf{H}_{CG}}{dt} + \mathbf{r}_{CG/P} \times m\mathbf{a}_{CG/A}$$

The terms on the right-hand side of these equations are usually referred to as inertia terms and describe the component's resistance to changes in motion. We can consider the inertia terms to be "forces" or "moments", as appropriate, and place them on the left hand side of the equations, resulting in the following governing equations:

$$\sum \mathbf{F}_{ext} + \mathbf{F}_I = 0$$

$$\sum \mathbf{M}_{ext/P} + \mathbf{M}_{ANG} + \mathbf{M}_I = 0$$

$$\text{where } \mathbf{F}_I = -m\mathbf{a}_{CG/A},\ \mathbf{M}_{ANG} = -\frac{d\mathbf{H}_{CG}}{dt},\ \mathbf{M}_I = -\mathbf{r}_{CG/P} \times m\mathbf{a}_{CG/A}$$

The inertia "force" for each component is given by the product of the component's mass and the acceleration of its centre of gravity:

$$\mathbf{F}_I = -m\mathbf{a}_{CG}$$

The inertia "moment" for each component, about a point, *P*, is given by the cross product of the position of the centre of gravity, relative to *P* and the inertia "force".

$$\mathbf{M}_I = \mathbf{r}_{P\_CG} \times \mathbf{F}_I$$

The angular inertia "moment" for each component is given by the negative rate of change of angular momentum:

$$
\begin{aligned}
\mathbf{M}_{ANG} &= -\frac{d\mathbf{H}_{CG}}{dt} \\
&= -\left[I_{xx}\ddot{\phi}_x + \left(I_{zz} - I_{yy}\right)\dot{\phi}_z\dot{\phi}_y - I_{xy}\left(\ddot{\phi}_y - \dot{\phi}_z\dot{\phi}_x\right) - I_{xz}\left(\ddot{\phi}_z + \dot{\phi}_y\dot{\phi}_x\right) - I_{yz}\left(\dot{\phi}_y{}^2 - \dot{\phi}_z{}^2\right)\right]\mathbf{i}_C \\
&\quad + \left[I_{yy}\ddot{\phi}_y + \left(I_{xx} - I_{zz}\right)\dot{\phi}_x\dot{\phi}_z - I_{yz}\left(\ddot{\phi}_z - \dot{\phi}_x\dot{\phi}_y\right) - I_{xy}\left(\ddot{\phi}_x + \dot{\phi}_z\dot{\phi}_y\right) - I_{xz}\left(\dot{\phi}_z{}^2 + \dot{\phi}_x{}^2\right)\right]\mathbf{j}_C \\
&\quad + \left[I_{zz}\ddot{\phi}_z + \left(I_{yy} - I_{xx}\right)\dot{\phi}_y\dot{\phi}_x - I_{xz}\left(\ddot{\phi}_x - \dot{\phi}_y\dot{\phi}_z\right) - I_{yz}\left(\ddot{\phi}_y + \dot{\phi}_x\dot{\phi}_z\right) - I_{xy}\left(\dot{\phi}_x{}^2 + \dot{\phi}_y{}^2\right)\right]\mathbf{k}_C
\end{aligned}
$$

For two-dimensional planar motion the above equation reduces to:

$$\left\{\mathbf{M}_{ANG}\right\}_x = -I_{xx}\ddot{\phi}_x$$

2.5. Numerical Solution Method for Component Dynamics

2.5.1. Globally Convergent Newton's Method

In order to define the component dynamics, we have six unknowns:

- The lateral position and velocity of the point P (piston, wrist-pin and small end of the connecting-rod).
- The angular position and velocity of the piston.
- The angular position and velocity of the wrist-pin.

To solve for these unknowns, we require that force and moment balances, as derived in Section 2.2, are satisfied for each of the components. Section 2.5.2 describes in more detail the algorithm for calculating the forces and moments acting on each component, based on linear and angular momentum balances, and interface model equations.

A globally convergent Newton's method [35] was chosen to solve these six highly nonlinear equations. This method was chosen due to the fact that:

- This is a highly nonlinear system without a well defined analytical jacobian.
- There are only a small number of variables, so an iterative method, based on calculating a numerical jacobian is reasonable in terms of computational time.

The performance of this solution method appears to be adequate, typically requiring about 2 iterations to achieve convergence, with a maximum of around 30 iterations.

The general aim of this method is to find the vector of unknowns, **X**, such that the function vector **FVEC(X)** is equal to zero. Given a current guess for the vector of unknowns, **X**, and the corresponding function vector, **FVEC(X)**, we can use a Taylor series expansion to define the variation in **FVEC** for small variations in **X**, **δX**:

$$\mathbf{FVEC}(\mathbf{X}+\boldsymbol{\delta}\mathbf{X})=\mathbf{FVEC}(\mathbf{X})+\sum_{j}\frac{\partial FVEC_i}{\partial X_j}\boldsymbol{\delta}\mathbf{X}_j+O\left(\boldsymbol{\delta}\mathbf{X}^2\right)$$

The numerical jacobian, **J**, of the function vector can be defined as:

$$J_{ij}(\mathbf{X},\varepsilon)=\frac{FVEC_i\left(\mathbf{X}+\varepsilon\left|X_j\right|\right)-FVEC_i(\mathbf{X})}{\varepsilon\left|X_j\right|}\cong\frac{\partial FVEC_i}{\partial X_j}$$

The accuracy of the numerical jacobian, compared to the analytical jacobian, is a trade off between taking a very small step size, ε, when calculating the jacobian, and the numerical errors introduced by dividing by a small number.

The variation in the vector unknowns, **δX**, such that the resulting function vector, **FVEC(X+δX)**, is approximately equal to zero, can therefore be estimated:

$$\mathbf{FVEC}(\mathbf{X}+\boldsymbol{\delta}\mathbf{X})\cong\mathbf{FVEC}(\mathbf{X})+\mathbf{J}\,\boldsymbol{\delta}\mathbf{X}=0$$

$$\boldsymbol{\delta}\mathbf{X}=-\mathbf{J}^{-1}\mathbf{FVEC}(\mathbf{X})$$

The closer the initial guess, **X**, is to the correct solution, that is, the smaller the size of **δX**, the more accurate this estimate will be. Taking the entire Newton step, **δX**, may lead to divergence, particularly for highly nonlinear systems such as this one. In order to improve the convergence behavior of this algorithm, an additional criteria is specified. The Newton step is scaled by a relaxation parameter, λ, such that the size of the function vector, as measured by the function FMIN, decreases:

$$\mathrm{FMIN}=\frac{1}{2}\mathbf{FVEC}(\mathbf{X}+\lambda\boldsymbol{\delta}\mathbf{X})\cdot\mathbf{FVEC}(\mathbf{X}+\lambda\boldsymbol{\delta}\mathbf{X})$$

$$\mathbf{X}_{new}=\mathbf{X}_{old}+\lambda\boldsymbol{\delta}\mathbf{X}$$

For this project, the vector of unknowns, **X**, is defined as:

X = Lateral position of point P, x_{P_y}
Lateral velocity of point P, $\dot{x}_{P_y}$
Angular position of piston, ϕ_{PS}
Angular velocity of piston, $\dot{\phi}_{PS}$
Angular position of wrist-pin, ϕ_{WP}
Angular velocity of wrist-pin, $\dot{\phi}_{WP}$

The function vector, **FVEC**, is defined as:

- Linear momentum balance in the lateral direction, for the piston.

$$\mathrm{FVEC}(1)=F_{WP/PSY}+F_{CB/PSY}+F_{P/PSY}+m_{PS}g_{Y}-m_{PS}a_{PS\_CG/AY}$$

- Piston lateral velocity equation

$$\mathrm{FVEC}(2)=\dot{x}_{P/AY}{}^{k}-\frac{x_{P/OY}{}^{k}-x_{P/OY}{}^{k-1}}{t^{k}-t^{k-1}}$$

- Angular momentum balance about the point *P*, for the piston.

$$\mathrm{FVEC}(3)=\tau_{WP/PSX}+\left\{\begin{matrix}\mathbf{r}_{CB/PS\_P}\times\mathbf{F}_{CB/PS}+\mathbf{r}_{P/PS\_P}\times\mathbf{F}_{P/PS}\\+\mathbf{r}_{PS\_CG/PS\_P}\times m_{PS}\mathbf{g}-\mathbf{r}_{PS\_CG/PS\_P}\times m_{PS}\mathbf{a}_{PS\_CG/A}\end{matrix}\right\}_{X}-I_{PS\_XX}\ddot{\phi}_{PS}$$

- Piston angular velocity equation

$$FVEC(4)=\dot{\phi}_{PS}{}^{i}-\frac{\phi_{PS}{}^{i}-\phi_{PS}{}^{i-1}}{t^{i}-t^{i-1}}$$

- Angular momentum balance about the point *P*, for the wrist-pin.

$$\mathrm{FVEC}(5)=\tau_{PS/WPX}+\tau_{CR/WPX}+\left\{\begin{matrix}\mathbf{r}_{WP\_CG/WP\_P}\times m_{WP}\mathbf{g}\\-\mathbf{r}_{WP\_CG/WP\_P}\times m_{WP}\mathbf{a}_{WP\_CG/A}\end{matrix}\right\}_{X}-I_{WP\_XX}\ddot{\phi}_{WP}$$

- Wrist-pin angular velocity equation

$$\mathrm{FVEC}(6)=\dot{\phi}_{WP}{}^{i}-\frac{\phi_{WP}{}^{i}-\phi_{WP}{}^{i-1}}{t^{i}-t^{i-1}}$$

Although explicit analytical functions for each of the individual terms of these equations are not available, we can consider the terms to be general functions of the vector of unknowns, **X**. Sections 2.3 and Section 2.4 describe in more detail the calculation of these terms. Each term of both the vector of unknowns, **X**, and the function vector, **FVEC**, must be normalized to bring their values to order(1), so that the numerical methods can be applied successfully.

The normalization is currently defined by user supplied parameters, FSCALE ~ 100 N, LSCALE ~ 100 μm, TSCALE ~ 1 revolution and DEGSCALE ~ 0.1 degrees, and the cylinder bore and wrist-pin radii:

$$\mathrm{FVEC}*(1)=\mathrm{FVEC}(1)/\,\mathrm{FSCALE}$$
$$\mathrm{FVEC}*(2)=\mathrm{FVEC}(2)/\,(\mathrm{LSCALE/TSCALE})$$
$$\mathrm{FVEC}*(3)=\mathrm{FVEC}(3)/\,(\mathrm{FSCALE}\times\mathrm{RBORE})$$
$$\mathrm{FVEC}*(4)=\mathrm{FVEC}(4)/\,(\mathrm{DEGSCALE/TSCALE})$$
$$\mathrm{FVEC}*(5)=\mathrm{FVEC}(5)/\,(\mathrm{FSCALE}\times\mathrm{RPIN})$$
$$\mathrm{FVEC}*(6)=\mathrm{FVEC}(6)/\,(\mathrm{DEGSCALE/TSCALE})$$

Given that we have chosen a globally convergent solution method, ideally our algorithm should be able to find the solution from almost any initial guess, but calculation of the piston – cylinder-bore interface forces can be computationally expensive, so it is worth spending a little computational effort on making a good initial guess, and thereby reducing the number of iterations required. The initial guess is calculated from the previous two time steps, using a user-defined weighting:

$$\mathbf{X}^{k+1} = \mathbf{X}^k + \text{Weight}\frac{\mathbf{X}^k - \mathbf{X}^{k-1}}{t^k - t^{k-1}}\left(t^{k+1} - t^k\right)$$

Based on this initial guess, the function vector is calculated using the algorithm described in Section 2.5.2, and then normalized as described above. If the function vector, **FVEC**, is already sufficiently close to zero, as specified by the stopping criterion given below, the algorithm exits at this point.

$$\text{Stopping criterion: } \max\left(\left|FVEC_i\right|\right) < 0.1\,\text{TOLF}$$

Otherwise, the numerical jacobian, $J_{ij}(\mathbf{X}, \varepsilon)$, is calculated, requiring repeated calls to the subroutine for calculating the function vector, **FVEC**. This is computationally very expensive due to the solution of the non-linear equations governing the piston – cylinder bore interface force, which is required for each calculation of **FVEC**.

$$J_{ij}(\mathbf{X}, \varepsilon) = \frac{FVEC_i\left(\mathbf{X} + \varepsilon\left|X_j\right|\right) - FVEC_i(\mathbf{X})}{\varepsilon\left|X_j\right|}$$

The following equation is then solved via Crout's Method (LU decomposition) [9], in order to calculate for the Newton step, **δX**.

$$\mathbf{J}\,\boldsymbol{\delta}\mathbf{X} = \mathbf{FVEC}(\mathbf{X})$$

The optimum step size, λ, such that f decreases is calculated and the resulting vector of unknowns, $\mathbf{X}_{\text{new}}$, is given by the following equation:

$$\mathbf{X}_{\text{new}} = \mathbf{X} + \lambda\boldsymbol{\delta}\mathbf{X}$$

The function vector, $\mathbf{FVEC}(\mathbf{X}_{\text{new}})$, is then calculated, and using the following stopping criterion we check whether the function vector is sufficiently close to zero, exiting the iteration loop if this criterion is satisfied.

$$\text{Stopping criterion: } \max\left(\left|FVEC_i\right|\right) < \text{TOLF}$$

Otherwise, we check whether the algorithm has converged to a local minimum of FMIN, by checking whether the gradient of FMIN is sufficiently close to zero. If this criterion is satisfied, the time step calculation is restarted from a new initial guess. The new guess is achieved by halving the time step size, D_CA, and restarting the calculation from the previous time step data.

$$\text{Stopping criterion: } \max(\nabla f) < \text{TOLMIN}$$

If neither the function vector, nor the gradient of FMIN, are sufficiently small, the change in the vector of unknowns is tested to see if it has converged. If this change is sufficiently small, the program exits the iteration loop, despite not satisfying convergence of the function vector.

$$\text{Stopping criterion: } \max(|\mathbf{X}_{\text{new}} - \mathbf{X}|) < \text{TOLMIN}$$

If all three stopping criterion are not met, then the iteration loop continues, and the numerical jacobian at the new vector of unknowns is calculated to begin the search for the next vector of unknowns. This algorithm is summarized in Figure 2.11.

2.5.2. Calculation of the Function Vector, FVEC

For an estimated lateral position and velocity of point *P* (the ideal centre of the pin bore, wrist-pin and small end of the connecting-rod), the lateral acceleration is calculated using a simple first order difference method.

$$\text{Guess: } x_{P/OY}, \dot{x}_{P/AY}$$

$$\ddot{x}_{P/AY_i} = \frac{\dot{x}_{P/AY_i} - \dot{x}_{P/AY_{i-1}}}{t_i - t_{i-1}}$$

For an estimated piston angular position (tilt) and angular velocity, the angular acceleration is calculated using a simple first order difference method.

$$\text{Guess: } \phi_{PS}, \dot{\phi}_{PS}$$

$$\ddot{\phi}_{PS_i} = \frac{\dot{\phi}_{PS_i} - \dot{\phi}_{PS_{i-1}}}{t_i - t_{i-1}}$$

For an estimated wrist-pin angular position and angular velocity, the angular acceleration is calculated using a simple first order difference method.

$$\text{Guess: } \phi_{WP}, \dot{\phi}_{WP}$$

$$\ddot{\phi}_{WP_i} = \frac{\dot{\phi}_{WP_i} - \dot{\phi}_{WP_{i-1}}}{t_i - t_{i-1}}$$

The connecting-rod angle and its time derivatives are then defined by:

$$\phi_{CR} = -\sin^{-1}\left[\frac{r_{CS}}{l_{CR}}\sin(\theta_{CA}) - \frac{y_{CS0}}{l_{CR}} + \frac{x_{P/AY}}{l_{CR}}\right]$$

$$\dot{\phi}_{CR} = -\frac{\dot{u}}{\sqrt{1-u^2}}$$

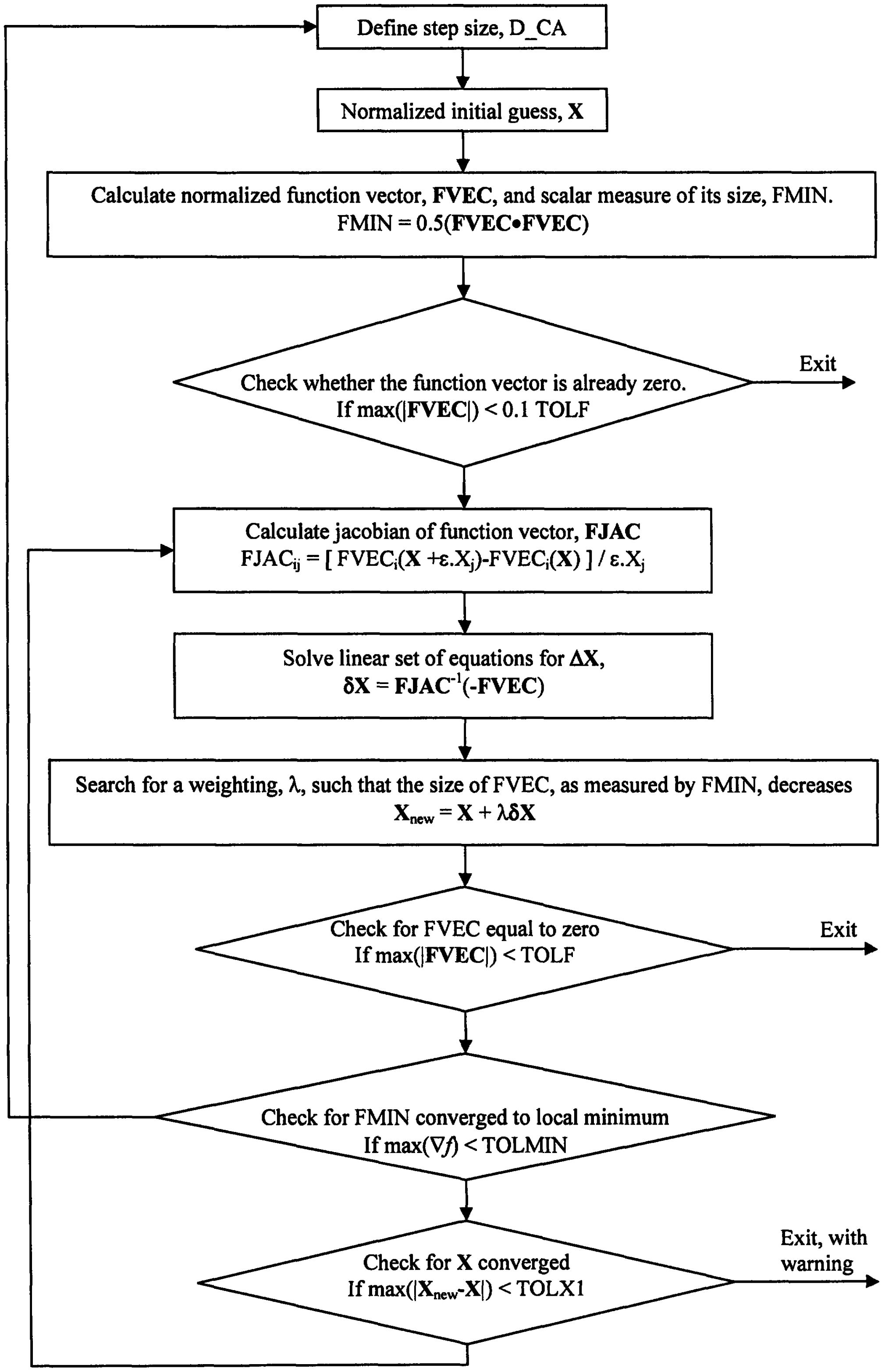

Figure 2.11: Globally Convergent Newton's Method

$$\ddot{\phi}_{CR} = -\frac{\ddot{u}}{\sqrt{1-u^2}} + \frac{u\dot{u}^2}{\left(1-u^2\right)^{3/2}}$$

where:

$$u \equiv \frac{r_{CS}}{l_{CR}}\sin\left(\theta_{CA}\right) - \frac{y_{CS0}}{l_{CR}} + \frac{x_{P/AY}}{l_{CR}}$$

$$\dot{u} = \frac{r_{CS}}{l_{CR}}\dot{\theta}_{CA}\cos\left(\theta_{CA}\right) + \frac{\dot{x}_{P/AY}}{l_{CR}}$$

$$\ddot{u} = \frac{r_{CS}}{l_{CR}}\ddot{\theta}_{CA}\cos\left(\theta_{CA}\right) - \frac{r_{CS}}{l_{CR}}\dot{\theta}_{CA}{}^2\sin\left(\theta_{CA}\right) + \frac{\ddot{x}_{P/AY}}{l_{CR}}$$

The axial position of point P, and its time derivatives, are then defined by:

$$x_{P/AZ} = r_{CS}\cos\left(\theta_{CA}\right) + l_{CR}\cos\left(\phi_{CR}\right)$$

$$\dot{x}_{P/AZ} = -r_{CS}\dot{\theta}_{CA}\sin\left(\theta_{CA}\right) - l_{CR}\dot{\phi}_{CR}\sin\left(\phi_{CR}\right)$$

$$\ddot{x}_{P/AZ} = -r_{CS}\ddot{\theta}_{CA}\sin\left(\theta_{CA}\right) - r_{CS}\dot{\theta}_{CA}{}^2\cos\left(\theta_{CA}\right) - l_{CR}\ddot{\phi}_{CR}\sin\left(\phi_{CR}\right) - l_{CR}\dot{\phi}_{CR}{}^2\cos\left(\phi_{CR}\right)$$

The motion of the piston, wrist-pin and connecting-rod centers of gravity are then calculated:

$$\mathbf{a}_{PS\_CG/A} = \mathbf{a}_{PS\_P/A} + \left[\left(\ddot{\phi}_{PS}\mathbf{i}\right)\times\mathbf{r}_{PS\_CG/PS\_P}\right] + \left(\dot{\phi}_{PS}\mathbf{i}\right)\times\left[\left(\dot{\phi}_{PS}\mathbf{i}\right)\times\mathbf{r}_{PS\_CG/PS\_P}\right]$$

$$\mathbf{a}_{WP\_CG/A} = \mathbf{a}_{WP\_P/A} + \left[\left(\ddot{\phi}_{WP}\mathbf{i}\right)\times\mathbf{r}_{WP\_CG/WP\_P}\right] + \left(\dot{\phi}_{WP}\mathbf{i}\right)\times\left[\left(\dot{\phi}_{WP}\mathbf{i}\right)\times\mathbf{r}_{WP\_CG/WP\_P}\right]$$

$$\mathbf{a}_{CR\_CG/A} = \mathbf{a}_{Q/A} + \left[\left(\ddot{\phi}_{CR}\mathbf{i}\right)\times\mathbf{r}_{CR\_CG/Q}\right] + \left(\dot{\phi}_{CR}\mathbf{i}\right)\times\left[\left(\dot{\phi}_{CR}\mathbf{i}\right)\times\mathbf{r}_{CR\_CG/Q}\right]$$

$$\mathbf{a}_{Q/A} = \left[-\alpha_{CA}r_{CS}\cos\left(\theta_{CA}\right) + \omega_{CA}{}^2 r_{CS}\sin\left(\theta_{CA}\right)\right]\mathbf{j} - \left[\alpha_{CA}r_{CS}\sin\left(\theta_{CA}\right) + \omega_{CA}{}^2 r_{CS}\cos\left(\theta_{CA}\right)\right]\mathbf{k}$$

The external forces and moments due to combustion pressure and gravity, and the inertia terms can then be calculated, as described in Section 2.4. Calculation of the piston – cylinder-bore interface force and moment is a significant proportion of this project, and is described in detail in Section 2.3.3 for the dry piston model, and in Section 5.5 for the lubricated model. Linear and angular momentum balances for each of the components, and wrist-pin bearing model equations, are then applied to calculate the remaining interface forces, and define the function vector, FVEC.

Solve conservation of linear momentum for the piston, in the axial direction, in order to obtain $F_{WP/PS\,Z}$:

$$F_{WP/PSZ} = -F_{CB/PSZ} - F_{P/PSZ} - m_{PS}g_Z + m_{PS}a_{PS\_CG/A_Z}$$

Using the fact that $\mathbf{F}_{WP/PS} = -\mathbf{F}_{PS/WP}$, solve conservation of linear momentum for the wrist-pin, in the axial direction, in order to obtain $F_{CR/WP\,Z}$:

$$F_{CR/WPZ} = -F_{PS/WPZ} - m_{WP}g_Z + m_{WP}a_{WP\_CG/A_Z}$$

Using the fact that $\mathbf{F}_{CR/WP} = -\mathbf{F}_{WP/CR}$, we then have the equation describing conservation of angular momentum for the connecting-rod, about point *Q*, in terms of two unknowns $F_{WP/CR\,Y}$ and $\tau_{WP/CR\,X}$:

$$F_{WP/CRY} = \frac{\tau_{WP/CRX}}{r_{CR\_P/Q_Z}} + \frac{1}{r_{CR\_P/Q_Z}}\begin{bmatrix} r_{CR\_P/Q_Y}F_{WP/CRZ} + r_{CR\_CG/Q_Y}m_{CR}g_Z - r_{CR\_CG/Q_Z}m_{CR}g_Y \\ -r_{CR\_CG/Q_Y}m_{CR}a_{CR\_CG/A_Z} + r_{CR\_CG/Q_Z}m_{CR}a_{CR\_CG/A_Y} - I_{CR\_XX}\ddot{\phi}_{CR} \end{bmatrix}$$

This equation can be simplified to:

$$F_{WP/CRY} = A_1\tau_{WP/CRX} + A_2$$

$$A_1 = \frac{1}{r_{CR\_P/Q_Z}}$$

$$A_2 = \frac{1}{r_{CR\_P/Q_Z}}\begin{bmatrix} r_{CR\_P/Q_Y}F_{WP/CRZ} + r_{CR\_CG/Q_Y}m_{CR}g_Z - r_{CR\_CG/Q_Z}m_{CR}g_Y \\ -r_{CR\_CG/Q_Y}m_{CR}a_{CR\_CG/A_Z} + r_{CR\_CG/Q_Z}m_{CR}a_{CR\_CG/A_Y} - I_{CR\_XX}\ddot{\phi}_{CR} \end{bmatrix}$$

where A_1 and A_2 are fully defined at this stage of the calculation.

The Connecting-Rod – Wrist-Pin interface equations given in Section 2.3.2 also describe the relationship between the forces and moments generated at this interface. For the purposes of calculating the friction coefficient only, we will assume that the force acts along the main axis of the connecting rod:

$$\mathbf{F}_{CR/WP} = -\left|\mathbf{F}_{CR/WP}\right|\sin(\phi_{CR})\mathbf{j} + \left|\mathbf{F}_{CR/WP}\right|\cos(\phi_{CR})\mathbf{k}$$

$$\left|\mathbf{F}_{CR/WP}\right| = \left|\frac{F_{CR/WPZ}}{\cos(\phi_{CR})}\right|$$

The friction coefficient can then be calculated:

$$f_{CR/WP} = -sign(\dot{\phi}_{WP} - \dot{\phi}_{CR})\left[1 - \exp\left(-\left|\frac{\dot{\phi}_{WP} - \dot{\phi}_{CR}}{0.1 \times a}\right|\right)\right]a_1\left(\frac{\mu r_{WP}l_{CR\_WP}\left|\dot{\phi}_{WP} - \dot{\phi}_{CR}\right|}{\left|\mathbf{F}_{CR/WP}\right|}\right)^{a_2}\left(\frac{r_{WP}}{c_{CR\_WP}}\right)^{a_3}$$

The equations governing the bearing interface are then:

$$F_{WP/CRY} = \left|F_{NWP/CR}\right|\{\cos(\theta_{BCR/WP}) + f_{CR/WP}\sin(\theta_{BCR/WP})\}$$

$$F_{WP/CRZ} = \left|F_{NWP/CR}\right|\{\sin(\theta_{BCR/WP}) - f_{CR/WP}\cos(\theta_{BCR/WP})\}$$

$$\tau_{WP/CRX} = -f_{CR/WP}\left|F_{NWP/CR}\right|r_{WP}$$

Substituting these into the angular momentum balance for the connecting-rod, about Q, and rearranging, we have:

$$\left(f_{CR/WP}F_{WP/CRZ} - A_2\right)\sin\left(\theta_{BCR/WP}\right) + \left(F_{WP/CRZ} + f_{CR/WP}A_2\right)\cos\left(\theta_{BCR/WP}\right) = -f_{CR/WP}F_{WP/CRZ}r_{WP}A_1$$

Using the following trigonometric identity we can solve for $\theta_{B\,WP/CR}$;

$$c_1 \sin x + c_2 \cos x = \sqrt{{c_1}^2 + {c_2}^2}\,\sin(x + \varphi)$$

$$\varphi = \begin{cases} \tan^{-1}\left(\dfrac{c_2}{c_1}\right), & \text{if } c_1 \geq 0; \\ \tan^{-1}\left(\dfrac{c_2}{c_1}\right) + \pi, & \text{if } c_1 < 0. \end{cases}$$

$$\theta_{BCR/WP} = \begin{cases} \sin^{-1}\left[\dfrac{-f_{CR/WP}F_{WP/CRZ}r_{WP}A_1}{\sqrt{\left(f_{CR/WP}F_{WP/CRZ} - A_2\right)^2 + \left(F_{WP/CRZ} + f_{CR/WP}A_2\right)^2}}\right] - \tan^{-1}\left[\dfrac{\left(F_{WP/CRZ} + f_{CR/WP}A_2\right)}{\left(f_{CR/WP}F_{WP/CRZ} - A_2\right)}\right], \\ \qquad \text{if } \left(f_{CR/WP}F_{WP/CRZ} - A_2\right) \geq 0; \\ \sin^{-1}\left[\dfrac{-f_{CR/WP}F_{WP/CRZ}r_{WP}A_1}{\sqrt{\left(f_{CR/WP}F_{WP/CRZ} - A_2\right)^2 + \left(F_{WP/CRZ} + f_{CR/WP}A_2\right)^2}}\right] - \tan^{-1}\left[\dfrac{\left(F_{WP/CRZ} + f_{CR/WP}A_2\right)}{\left(f_{CR/WP}F_{WP/CRZ} - A_2\right)}\right] - \pi, \\ \qquad \text{if } \left(f_{WP/CR}F_{WP/CRZ} - A_2\right) < 0. \end{cases}$$

We then have:

$$\left|F_{NWP/CR}\right| = \frac{F_{WP/CRZ}}{\left\{\sin\left(\theta_{BCR/WP}\right) - f_{CR/WP}\cos\left(\theta_{BCR/WP}\right)\right\}}$$

$$F_{WP/CRY} = \left|F_{NWP/CR}\right|\left\{\cos\left(\theta_{BCR/WP}\right) + f_{CR/WP}\sin\left(\theta_{BCR/WP}\right)\right\}$$

$$\tau_{WP/CRX} = -f_{CR/WP}\left|F_{NWP/CR}\right|r_{WP}$$

Using the fact that $\mathbf{F}_{CR/WP} = -\,\mathbf{F}_{WP/CR}$, solve conservation of linear momentum for the wrist-pin, in the lateral direction, in order to obtain $F_{PS/WP\,Y}$:

$$F_{PS/WPY} = -F_{CR/WPY} + m_{WP}a_{WP\_CG/A_Y}$$

Considering the Wrist-Pin – Piston interface equations described in Section 2.3.2 we then have:

$$f_{PS/WP} = -sign\left(\dot{\phi}_{WP} - \dot{\phi}_{PS}\right)\left[1 - \exp\left(-\left|\frac{\dot{\phi}_{WP} - \dot{\phi}_{PS}}{0.1 \times a}\right|\right)\right]a_1\left(\frac{\mu r_{WP}l_{PS\_WP}\left|\dot{\phi}_{WP} - \dot{\phi}_{PS}\right|}{\left|\mathbf{F}_{PS/WP}\right|}\right)^{a_2}\left(\frac{r_{WP}}{c_{PS\_WP}}\right)^{a_3}$$

$$\left|\mathbf{F}_{PS/WP}\right| = \sqrt{{F_{PS/WPY}}^2 + {F_{PS/WPZ}}^2}$$

$$\frac{F_{PS/WPZ}}{F_{PS/WPY}} = \frac{\left\{-\sin\left(\theta_{BPS/WP}\right) + f_{PS/WP}\cos\left(\theta_{BPS/WP}\right)\right\}}{\left\{-\cos\left(\theta_{BPS/WP}\right) - f_{PS/WP}\sin\left(\theta_{BPS/WP}\right)\right\}}$$

Rearranging, we obtain an equation for $\theta_{B\ WP/PS}$.

$$\left(-F_{PS/WPZ} - f_{PS/WP}F_{PS/WPY}\right)\cos\left(\theta_{BPS/WP}\right) + \left(-f_{PS/WP}F_{PS/WPZ} + F_{PS/WPY}\right)\sin\left(\theta_{BPS/WP}\right) = 0$$

$$\theta_{BPS/WP} = -\tan^{-1}\frac{\left(-F_{PS/WPZ} - f_{PS/WP}F_{PS/WPY}\right)}{\left(-f_{PS/WP}F_{PS/WPZ} + F_{PS/WPY}\right)}$$

$$\left|F_{NPS/WP}\right| = \frac{F_{PS/WPZ}}{\left\{-\sin\left(\theta_{BPS/WP}\right) + f_{PS/WP}\cos\left(\theta_{BPS/WP}\right)\right\}}$$

$$\tau_{PS/WPX} = f_{PS/WP}\left|F_{NPS/WP}\right| r_{WP}$$

All the terms required to fully define the function vector, **FVEC**, have now been calculated.

2.6. Numerical Solution Method for Dry Piston – Cylinder Bore Interface

The piston node locations are defined by the position of point *P*, and the reference location of the node, rotated by the piston tilt, ϕ_{PS}.

$$\mathbf{x}_{PS} = \mathbf{x}_P + [\text{Rotation}(\phi_{PS})]\mathbf{x}_{ref}$$

The bore radius is interpolated, for each piston node, from the bore data supplied by the user, as a function of circumferential and axial position. The rigid (undeformed) radial gap between the cylinder bore and the piston, at each of the piston nodes, is then calculated.

The calculate domain is reduced to those nodes at which the rigid radial gap is less than zero, as it is assumed that any resulting radial deformation will increase the radial gap at most nodes, and therefore that contact will not occur outside this reduced domain. A check is also added to the end of this calculation to ensure this assumption is valid, requiring the calculation to be repeated over the full domain otherwise.

For the reduced domain, the overlap is estimated using a simple time difference and user supplied weighting, WRDEF:

$$w = \text{WRDEF} * \frac{\Delta t^k}{\Delta t^{k-1}}$$
$$\{\text{overlap}\} = (1 + w)\{\text{overlap}\}^{k-1} - w\{\text{overlap}\}^{k-2}$$

The overlap is then scaled by the user supplied variable, OSCALE ~ 0.1 μm. The vector of scaled overlaps is supplied to the IMSL library function DNEQNJ [36] as the initial guess for the variable vector, **X**, along with the names of subroutines for calculating a function vector, **F(X)**, and its analytical jacobian, **J**. DNEQNJ uses a modified Powell hybrid algorithm to solve a system of nonlinear equations, defined by the used supplied function vector, using a user supplied jacobian, and returns the resulting variable vector, and the length of the function vector ($\Sigma F_i(X)^2$).

The function vector, **F(X)**, in this case is the difference between the radial deformation that would result from the asperity contact force, $\mathbf{F}_{asp}$, generated by the vector of overlaps, **X**, and the radial deformation calculated directly from the sum of the overlap and the rigid radial gap. The equations governing asperity contact pressure generation are discussed in more detail in Section 2.3.3.1.

$$F_{asp_i} = \begin{cases} -C_1\{X_i\}^{C_2}, & X_i > 0 \\ 0, & X_i \le 0 \end{cases}$$
$$\{\mathbf{F}\} = [\text{CMAT}]\{\mathbf{F}_{asp}\} - \{\mathbf{X}\} - \{\text{Rigid radial gap}\}$$
where
$$\{\mathbf{X}\} = \{\text{Overlap}\} = \{\text{Radial deformation}\} - \{\text{Rigid radial gap}\}$$
$$[\text{CMAT}] = \text{Compliance Matrix}$$
$$\{\text{Radial deformation}\} = [\text{CMAT}]\{\mathbf{F}_{asp}\}$$

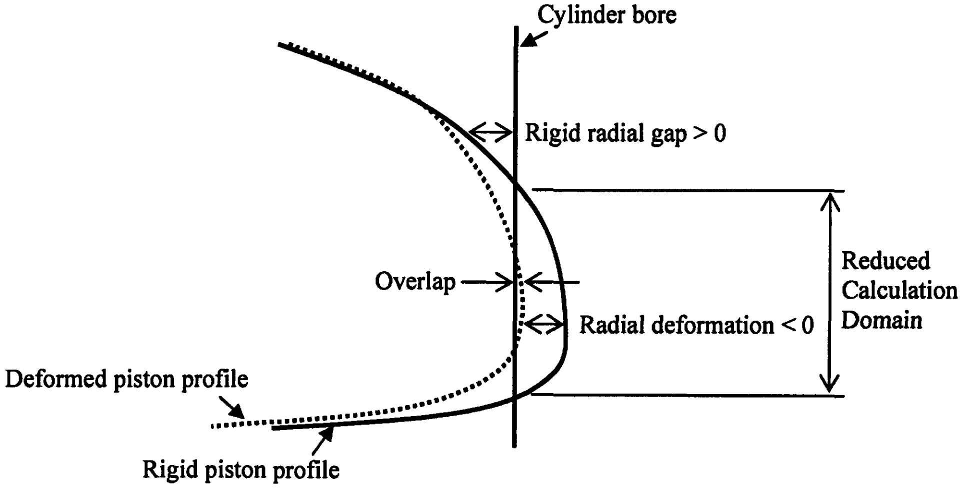

Figure 2.12: Definition of Overlap, Radial Deformation and Rigid Radial Gap

The analytical jacobian, **J**, is defined as:

$$
\begin{aligned}
J_{ij} &= \frac{\partial F_i}{\partial X_j} \\
&= \frac{\partial\{[\mathrm{CMAT}]\{\mathbf{F}_{asp}\}\}_i}{\partial X_j} - \frac{\partial X_i}{\partial X_j} - \frac{\partial\{\text{Rigid radial gap}\}_i}{\partial X_j} \\
&= \frac{\partial\left(\sum_j \mathrm{CMAT}_{ij} F_{asp_j}\right)}{\partial X_j} - \delta_{ij} \\
&= -C_1 C_2 \sum_j \begin{cases} \mathrm{CMAT}_{ij} X_j^{C_2 - 1}, & X_j > 0 \\ 0 \quad , & X_j \le 0 \end{cases} - \delta_{ij}
\end{aligned}
$$

Once the library function DNEQNJ returns the resulting vector of overlaps we map it back to the full domain, and the asperity contact force is calculated directly from the overlap at each node. The radial deformations at all piston nodes (full domain) are then calculated as a function of the asperity contact force vector and the compliance matrix, using the equations described above.

In order to check that our results are consistent within the reduced domain, we require that:

$$\{\text{Overlap}\} - \{\text{Radial deformation}\} + \{\text{Rigid radial gap}\} < \text{TOLOVERLAP}$$

If this condition is not satisfied, a warning is returned to the user, but the calculation continues.

In order to confirm that our reduced domain assumption was appropriate, that is, outside the reduced domain there is no overlap, and therefore no asperity contact force, we require that, outside of the reduced domain:

$$\{\text{Overlap}\} = \{\text{Radial deformation}\} - \{\text{Rigid radial gap}\} < \text{TOLOVERLAP}$$

If this condition is not satisfied, a warning is supplied to the user, and the calculation is repeated over the full domain.

It is currently estimated that this reduced domain calculation can reduce calculation time by a factor of around 18, but that this time saving is dependent on the geometry and load, as a full domain calculation is more often required in situations where there are large deformations and a wide contact area, such as interference fits and high loads.

3. User Specification of System

This chapter aims to provide a summary of the user supplied data which defines the power cylinder system for the purposes of our model, including:

- Pressure curve
- Piston geometry
- Piston structural deformations in response to combustion chamber, axial inertia and piston – cylinder bore pressure.
- Cylinder Bore geometry

The program user specifies the system geometry, material properties, running conditions and numerical parameters via several input files, as described in detail in the User Manual [37]. Essentially the input pressure curve and crankshaft speed drive the system's motion, while the piston and cylinder bore geometries constrain it. The piston's geometry is specified not only by its cold shape and range of thermal deformations, but also by the deformations induced by combustion chamber pressure, axial inertia and piston-cylinder bore interactions. The piston's structural behavior (compliance matrix, pressure and inertia deformation vectors) is specified via FEA data, which is converted by the pre-processor program to a uniform grid, ready for use in the main program. The cylinder bore is specified, for the purposes of this program by its cold shape (bore distortion) and range of thermal deformations. For a single engine design, a range of pressure traces and piston and cylinder-bore thermal deformations, corresponding to the range of operating speeds and loads should be provided.

3.1. General Specifications

General system and simulation parameters, including those listed below, are provided by the user via the file '*in_specs.txt*' as described in detail in the User Manual [37]:

- Number of cycles to be simulated and time step size,
- Crankshaft speed,
- Grid specification for skirt and lands,
- Initial Conditions,
- Input options, controlling expected format of inputs,
- Output options, controlling type and frequency of output,
- Bore sensor locations,
- Crankcase pressure,
- Component masses, inertias and macro-geometry,
- Piston – cylinder bore interface options and surface properties,

- Wrist-pin interface properties, and
- Gravity vector.

Numerical parameters for the various solutions algorithms are provided by the user via the file '*num_params.txt*', as described in detail in the User Manual [37].

3.2. Pressure Curve

The pressure force and crankshaft speed drive the system's motion. Combustion chamber and crankcase pressures, as functions of crank angle, are required for calculating the pressure force acting on the piston as described in Section 2.4.1. A vector of crank angle values and corresponding combustion chamber pressures is supplied by the user via the file '*in_press.txt*', as described in more detail in the User Manual [37]. The crankcase pressure can either be supplied as a single value, via the file '*in_specs.txt*', or as an additional column in '*in_press.txt*', depending on the value of the variable OPPRESS.

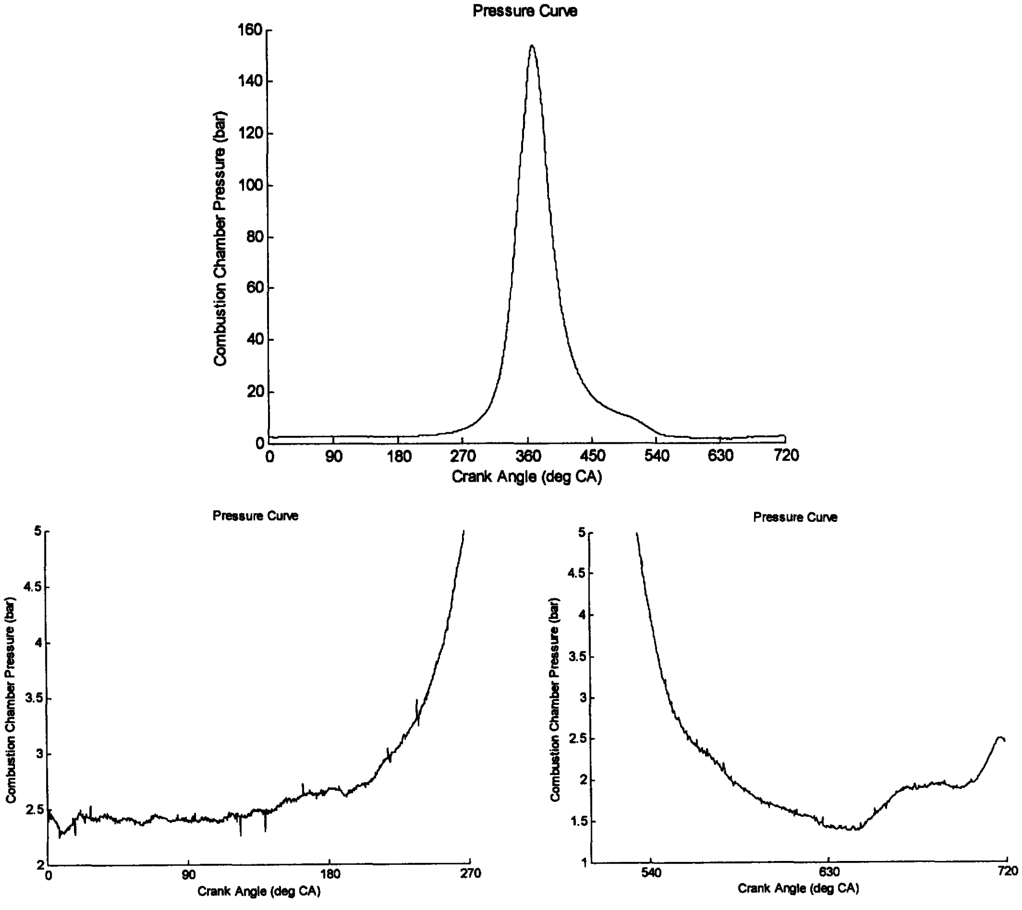

Figure 3.1: Combustion chamber pressure

3.3. Piston Geometry Specification

As discussed in more detail in the following sections, typically the program user specifies piston geometry via:

- Cold Shape
    - Nominal radius,
    - Cold shape profile,
    - Ovality
- Thermal deformation

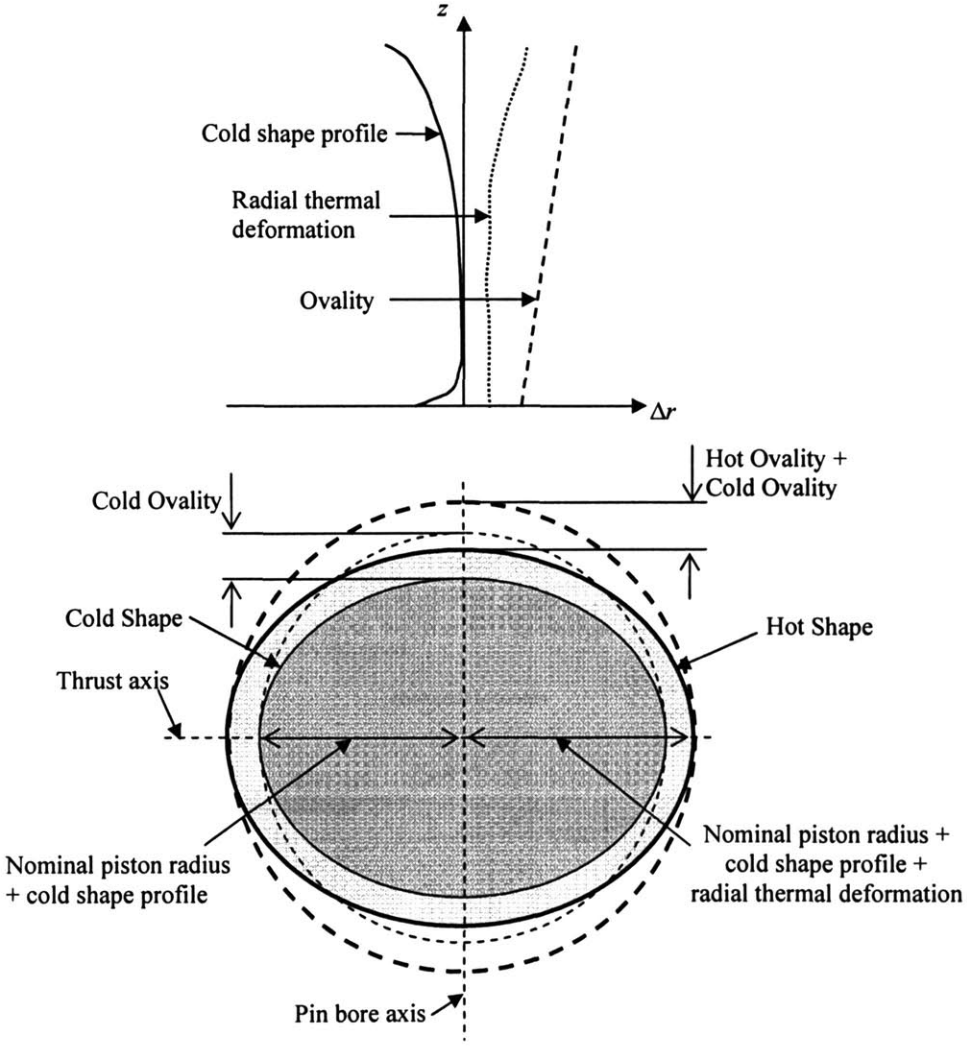

Cold Radius (z,θ) = Nominal piston radius + Cold shape profile (z) – Cold Ovality$(z)[1-\cos(2\theta-\pi)]/2$
Hot Radius (z,θ) = Cold Radius (z,θ) + Radial thermal deformation(z) – Hot Ovality$(z)[1-\cos(2\theta-\pi)]/2$

Figure 3.2: Cold shape skirt profile, ovality and thermal deformation

Alternatively, the combined piston shape (hot radii), can be specified by the FEA data provided by the user. This is discussed in more detail in Section 3.4. The control variable OP_PISR, provided in '*in_specs.txt*', indicates how the uniform piston grids are generated, as described in the User Manual [37].

3.3.1. Cold Shape Specification

The cold shape of the piston is typically specified for manufacturing purposes by a nominal radius and a set of data points describing radial profile at the thrust axis, and ovality (see Section 3.3.1.3), as a function of height from the base of the piston skirt. The finer details of the piston surface are then specified by the size and shape of the tooling marks, and the surface roughness. Coatings are often applied to the piston surface, significantly altering the surface geometry, roughness and friction coefficient.

3.3.1.1 Nominal Radius

The nominal radius of a piston is typically specified as the radius at the widest point on the piston skirt, which tends to be on the thrust axis. The nominal radius of a piston usually falls with the range 40-500 mm, with passenger car engine pistons having radii of about 50-60 mm.

3.3.1.2 Cold Shape Profile

The cold shape profile describes the radial variation from the nominal radius, at the thrust axis, as a function of axial position. These values tend to be negative, as the nominal radius of the piston is usually the radius at the widest point on the thrust axis.

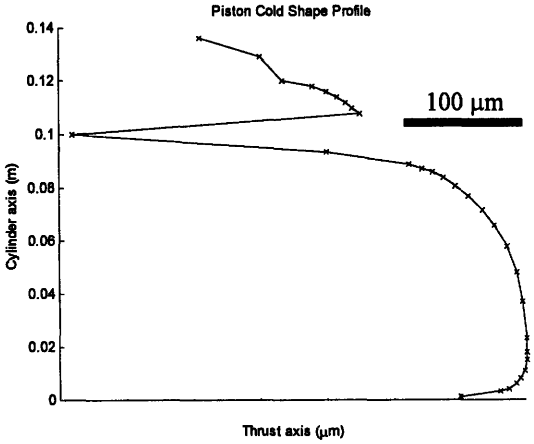

Figure 3.3: Cold Shape Profile

Typically the piston skirt has a convex initial shape which generates a converging/ diverging gap, thereby enabling the oil film to build pressure as the piston slides along the cylinder bore. The oil film pressure helps to support the side load on the piston and minimizes solid-solid contact and friction. The larger reductions in radius on the upper half of the skirt are compensated for by the higher thermal expansion at these points, leading to a relative flat central profile of the skirt. The chamfers at the top and base of the piston skirt are believed to act as oil reservoirs, collecting excess oil as the piston travels along the cylinder bore which may be partially retained for use as a supply when drier conditions are reached.

The lands tend to be recessed, compared to the piston skirt, so that the skirt supports the bulk of the side force, but in some cases the lands can make contact with the cylinder bore. Note that in Figure 3.3, the third land geometry is specified by only one data point. Since the third land in this case is significantly recessed, this may not effect the simulation results, but in general, care should be taken to specify each component of the piston (the skirt and each of the lands) by at least two data points in the axial direction, and to confine the program grid to within the data points.

3.3.1.3 Ovality

The piston ovality describes the radial variation in the circumferential direction. The ovality is defined as the difference between the piston radius at thrust axis and the piston radius at the pin bore axis. The radial variations at intermediate points are then defined by:

$$\Delta r(z,\theta) = \text{Ovality}(z)\frac{[1-\cos(2\theta-\pi)]}{2}$$

For this project, a positive value of ovality indicates a reduction in piston radius going from the thrust axis, to the pin bore axis.

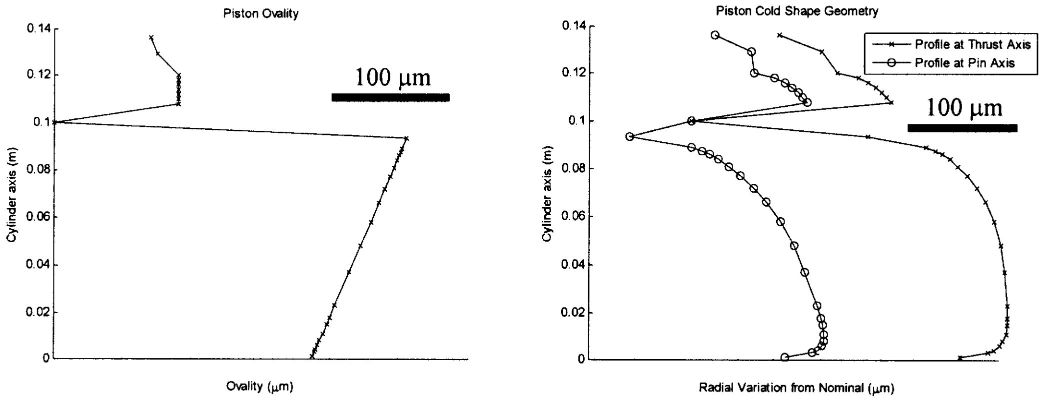

Figure 3.4: Ovality Profile

The main role of the piston is to support the side force transmitted by the connecting-rod, not to seal the combustion chamber (the top ring(s) seal the combustion chamber). This side force is most efficiently supported along the thrust axis of the piston, as away from this axis, additional force components are generated along the pin axis, resulting in increased friction. The piston's ovality allows the side force to be concentrated along the central portion of the skirt (along the thrust axis), reducing unnecessary interference and friction generation at the sides of the skirt.

3.3.2. Radial Thermal Deformation

During combustion, the piston crown and lands are exposed to combustion gases, resulting in heat transfer to the piston, and crown temperatures of about 200°C. The top ring(s) seal the combustion chamber, and there is significant clearance between the piston and the cylinder bore at the pin axis, so in general the piston skirt is not exposed to a significant amount of the combustion gases. The piston skirt temperature is therefore predominantly determined by conduction of heat from the crown, and typically varies axially through 60-100°C. Depending on the material and structure of the piston, and whether any cooling oil is supplied to the underneath of the piston, temperatures within the piston can vary significantly. These temperatures and the corresponding thermal expansion, which is of the same order as the piston-cylinder bore clearance, vary over time with running conditions from cold shape at start-up, to a significantly larger shape at steady-state, high load and speed. It is assumed for the purposes of this project that we have steady state thermal behavior, for a given running condition.

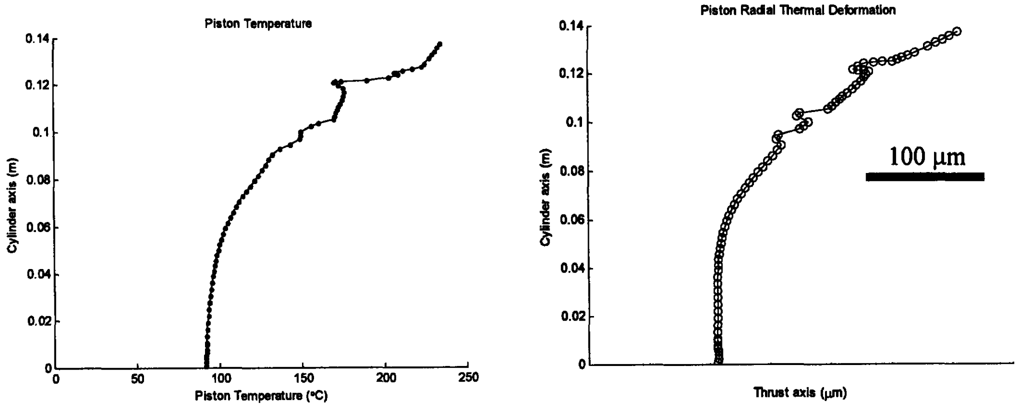

Figure 3.5: Piston temperature and thermal deformation profiles

The detailed geometry of the piston is used in determining the gap height between the piston and the cylinder bore. At this interface, variations of the order of a micron can, in some cases, significantly effect the pressure generated at the interface, lead to solid-solid contact, and result in a corresponding shift in lateral motion. Given the large variations in thermal expansion for various running conditions, and the fact that an engine can be expected to transition between these conditions during normal, unsteady, operation, it is not realistic to expect micron level accuracy of hot shape geometry, but it is important to recognize the effect of uncertainty in this data.

In determining thermal deformation, it is expected that the user will build a thermal finite element model of the piston, with appropriate boundary conditions, to predict the temperature distribution and corresponding thermal deformation for each running condition. For the purposes of this project the user may specify the thermal deformation in the same way as the cold shape, that is, via an axial profile and ovality.

3.3.3. Resulting Hot Shape Profile

The rigid radius of the piston at each grid point is defined by:

- nominal radius, plus
- linear interpolation of the cold shape profile and ovality, plus
- linear interpolation of the hot shape profile and ovality.

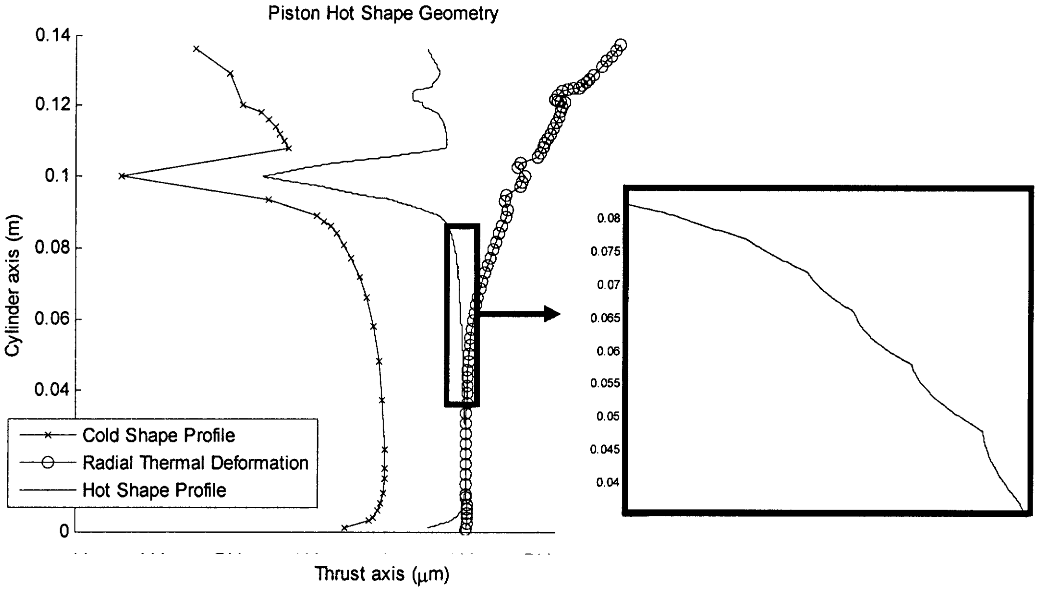

Figure 3.6: Piston Hot Shape Geometry

Depending on the relative grid densities of the user provided data sets and the program grid, the resulting piston hot shape can contain concave sections and other undesirable surface features which may be physically unrealistic and/or lead to a decrease in numerical stability. The enlarged section of Figure 3.6 shows such a case. The finer grid of the thermal deformation data, when added to the coarse grid cold shape results in undesirable concave sections connected by cusps. If the thermal deformation raw data is first interpolated at the same axial locations as the cold shape data, and then used to general the hot shape profile this problem is avoided as shown in Figure 3.7. In general this will add no more error to the profile than the existing uncertainty in the thermal deformation data. These changes may seem small, and given that they are within the uncertainty in the data it is concerning that they may result in significant different program behavior. This is due to the extremely nonlinear dependence of fluid pressure on gap height at small clearances.

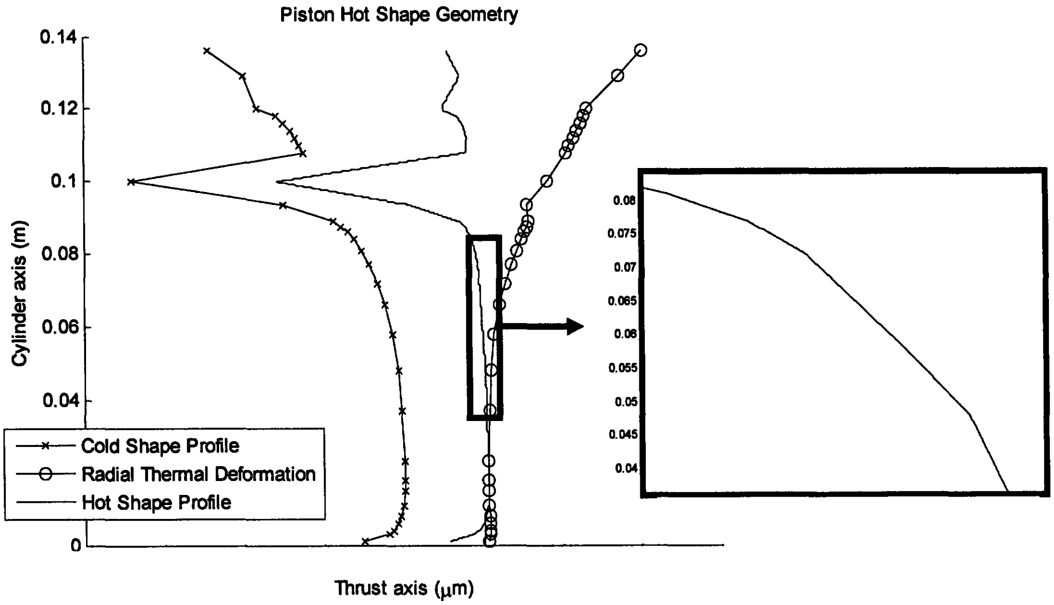

Figure 3.7: Piston Hot Shape Geometry - Adjusted

The hot shape profile at the pin axis should also be checked to confirm that a physically realistic and numerically desirable shape is obtained.

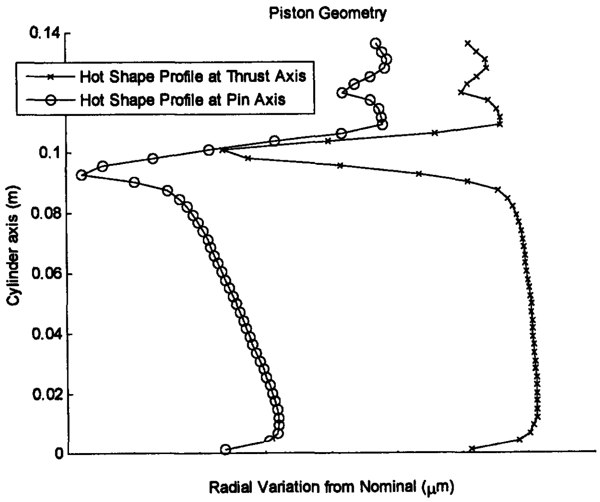

Figure 3.8: Piston Hot Shape Profiles

3.4. Piston Structural Specifications

A piston design is not only defined by the outer surface of the piston, but also by its internal structure and material(s) which determine its structural stiffness and weight. The piston surface is significantly deformed in the radial direction (significant relative to the piston – cylinder bore clearances) by:

- Combustion chamber pressure,
- Axial inertia, and
- Piston – Cylinder bore contact/hydrodynamic pressure.

Deformations in the axial and circumferential directions are negligible compared to the grid size and accuracy of node positions.

3.4.1. Piston Finite Element Model

It is expected that a finite element model of the piston will be generated by the user in order to determine the surface deformations caused by pressure, axial inertia, and piston – cylinder bore interface forces. This finite element model may also be used to specify the surface geometry of the piston. A preprocessing program is then used to convert this data to a uniform grid.

The correct development of such a model, with appropriate grid/elements and boundary conditions is outside the scope of this project, but some tentative guidelines are provided in the following sections. From the perspective of this project, it is simply required that the user provides the following:

- A list of nodes, which cover the piston skirt and lands (see Figure 3.9). In the case of a symmetric piston model, two separate lists are required: a list of the nodes along the symmetry line, and a list of the remaining (non-symmetry line) nodes.
- Positions of the nodes. For the case where these positions are used to specify the piston hot shape profile, the radial component of the position must be of sufficient accuracy.
- Deformation of those nodes, in Cartesian Coordinates, due to a unit pressure load applied to the piston crown.
- Deformation of those nodes, in Cartesian Coordinates, due to a unit inertia load applied throughout the piston.
- A Compliance matrix, C_{ij}, containing the deformation at node i, due to a unit radial load applied at node j.

The finite element model may either be a symmetric model, with the thrust and cylinder axes forming the symmetry plane, or an asymmetric model where the entire piston is simulated. Slightly different inputs are required for these two cases, as described in the User Manual, and there is a separate pre-processing program for each case.

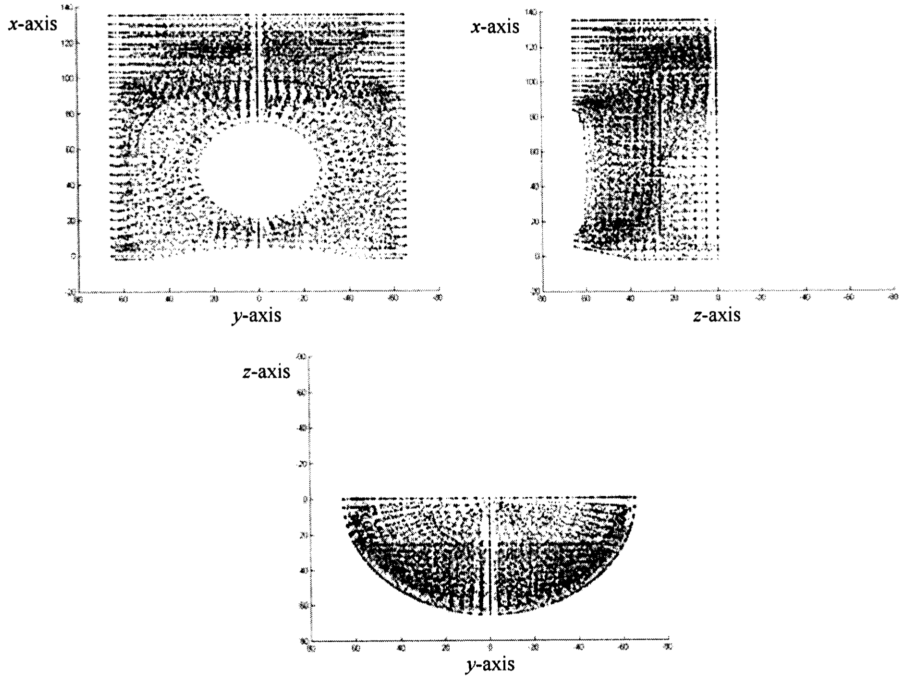

Figure 3.9: FEA Piston Nodes

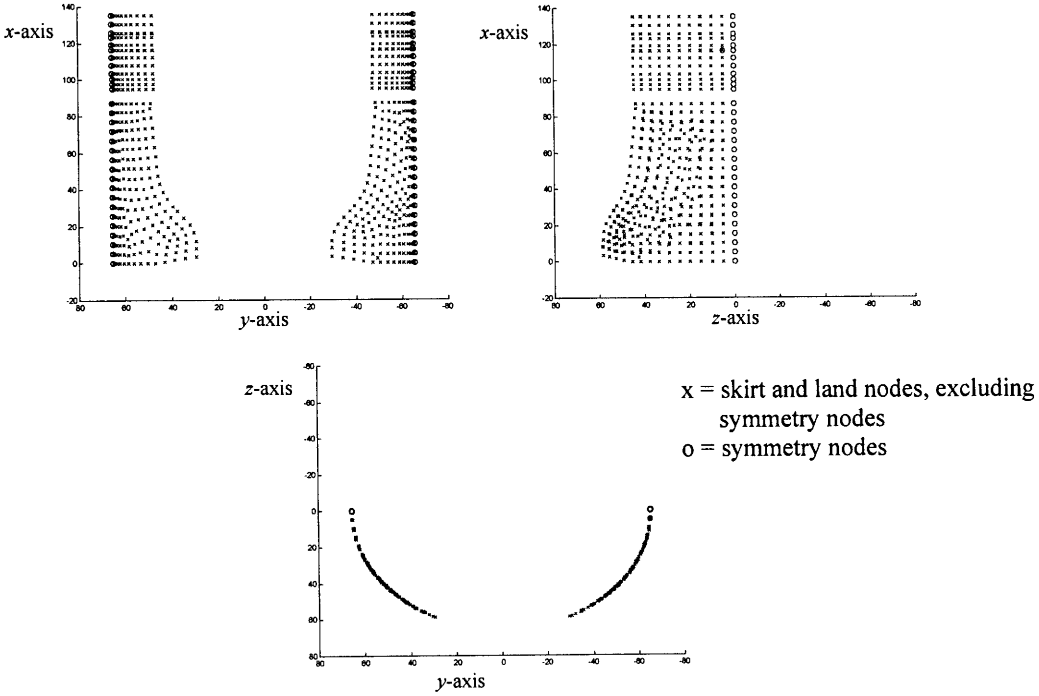

Figure 3.10: Subset of Piston Nodes Covering the Skirt and Lands

In most engines, the piston itself is symmetric, and asymmetry is introduced into the system by the Cylinder bore distortion, resulting in asymmetric loading of the piston -

cylinder bore interface, and perhaps requiring an asymmetrically generated compliance matrix.

For cases where both the piston and cylinder bore are symmetric, or where the system's asymmetry is negligible, a symmetric piston model is appropriate, and saves storage space and time for the pre-processing program only. The main program does not take symmetry into account, running a full piston model only.

3.4.2. Pressure Deformation

Combustion chamber pressure can result in significant radial deformation of the piston, relative to the piston – cylinder bore clearance, particularly close to combustion TDC. It is expected that a finite element model of the piston will be generated by the user in order to determine these deformations. A constant unit pressure of 1 bar should be applied to the crown of the piston, with the resulting load being supported by the wrist-pin.

A vector plot of the pressure deformation predicted for a heavy duty diesel engine, after conversion to a uniform grid, is shown in Figure 3.11.

The radial component of this pressure induced deformation is shown in Figure 3.12. The upper portion of the piston is deformed outwards, while the lower portion bends in and the soft, central portion of the skirt bends further inwards that the more rigid outer edges.

Pressure deformation becomes significant over the compression and expansion strokes, with typical peak pressures of around 100 bar resulting in deformations of 5-10 μm.

3.4.3. Inertia Deformation

Axial inertia can result in significant radial deformation of the piston, relative to the piston – cylinder bore clearance, particularly at TDC and BDC. It is expected that a finite element model of the piston will be generated by the user in order to determine these deformations. At each element of the model, a body force of 1 m/s^2 multiplied by the element mass should be applied, with the resulting load being supported by the wrist-pin.

A vector plot of the inertia deformation predicted for a heavy duty diesel engine, after conversion to a uniform grid, is shown in Figure 3.13.

Negative axial acceleration results in a positive axial inertia force, deforming the piston upwards. The lower portion of the skirt is deformed outwards while the crown bends inwards, and the soft, central portion of the skirt bends further outwards that the more rigid outer edges. The radial component of deformation due to axial inertia is shown in Figure 3.14.

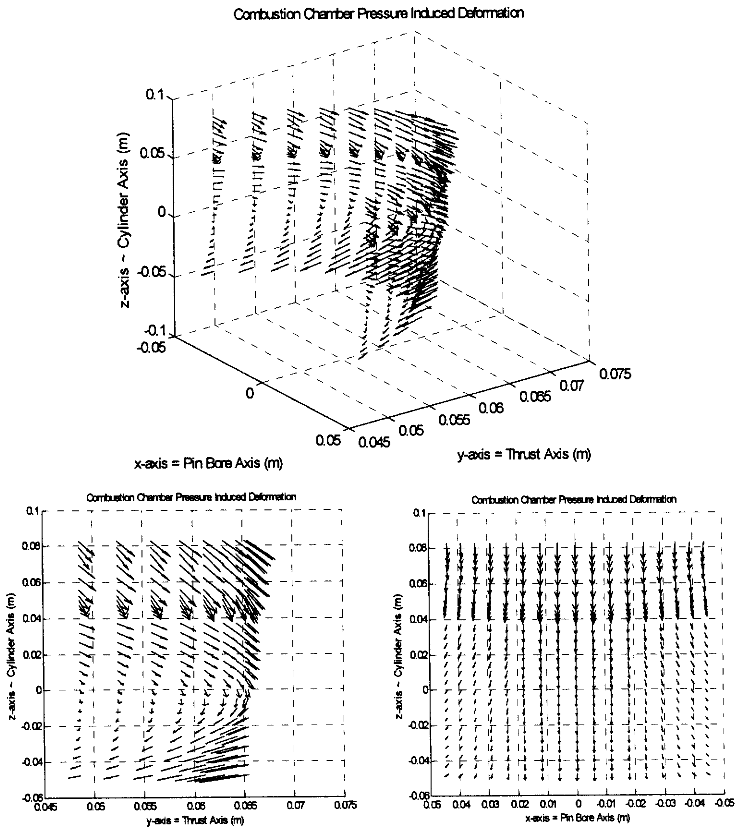

Figure 3.11: Pressure Deformation Vector Plot

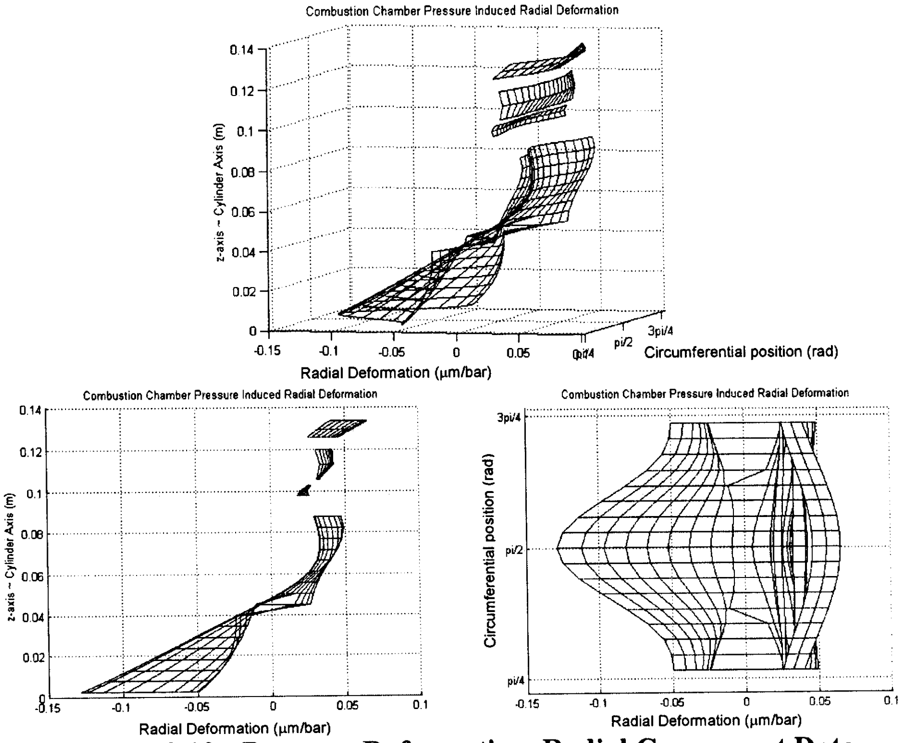

Figure 3.12: Pressure Deformation, Radial Component Data

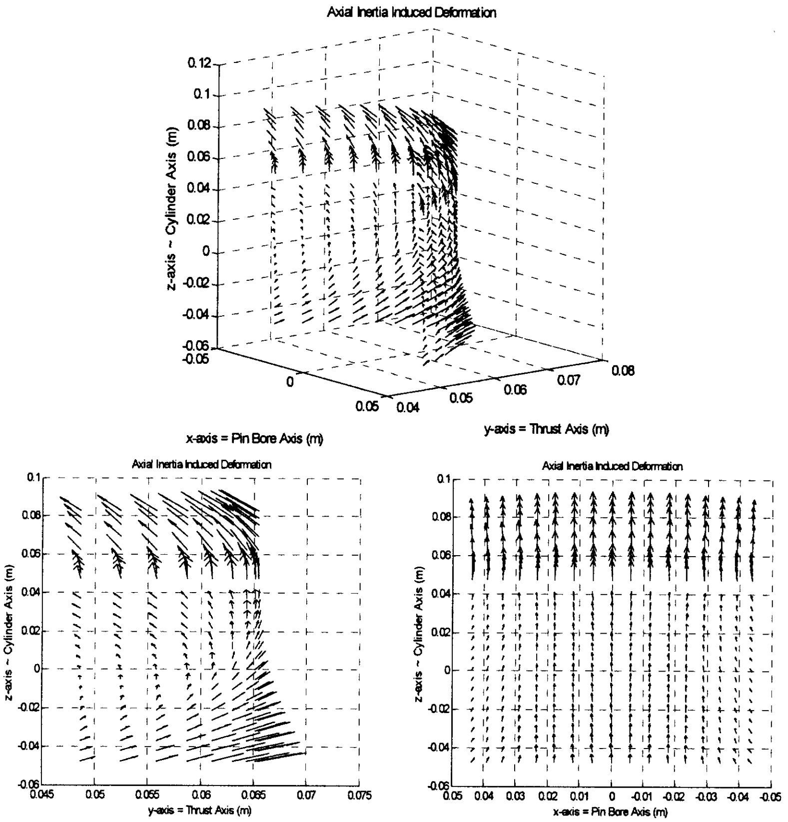

Figure 3.13: Axial Inertia Deformation Vector Plot

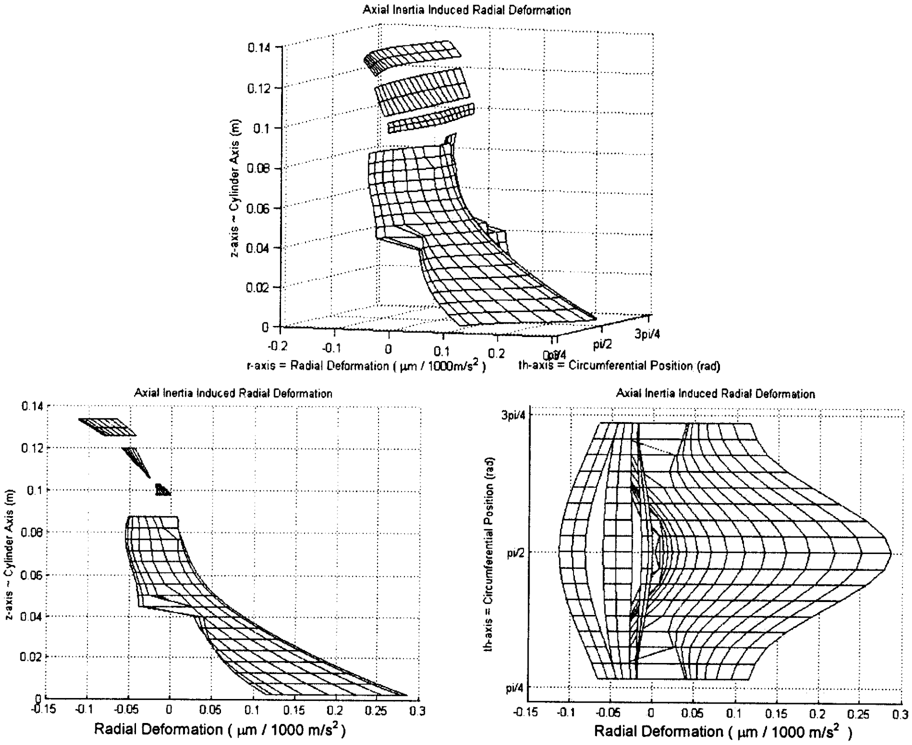

Figure 3.14: Axial Inertia Deformation, Radial Component Data

3.4.4. Compliance Matrix

3.4.4.1 Generation of symmetric compliance matrix.

When generating a compliance matrix, the way in which the physical component will be loaded must first be considered. In the case of a general piston, loads are applied to the skirt and lands in an almost symmetrical manner, with the load being mainly supported by the wrist-pin. Non-symmetric geometry and dynamics may lead to non-symmetric loading, but these effects are often small, depending on the degree of bore distortion. At times, the load applied to the skirt is partially supported by the opposite side of the skirt, but we will also choose to neglect this effect for the moment. Since the loading is assumed to be symmetrical, the net load to be supported is perpendicular to the wrist-pin axis.

The compliance matrix can be generated using a symmetric finite-element model in the following manner:

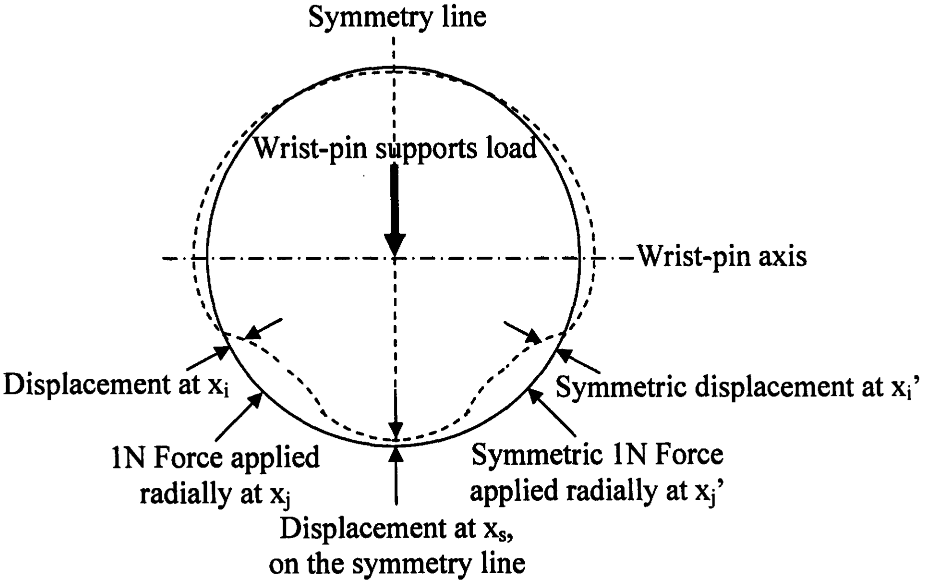

Figure 3.15: Generation of Symmetric Compliance Matrix

- For nodes not on the symmetry line, two unit forces were applied symmetrically at x_j and x_j', and the net displacement at each node, x_i, was measured.
- For nodes along the symmetry line, a single unit force (or equivalently, two forces of 0.5N) was applied at x_s, and the displacement at each node, x_i, was measured.
- These results are symmetric, and therefore data for only one half of the piston was recorded.

For each node j which is not on the symmetry line, the element of the compliance matrix, C_{ij} represents the deformation at node i due to two unit forces applied symmetrically at node j and the mirror node j. For a node s which is on the symmetry line, C_{sj} is equal to twice the displacement at x_s due to a unit load at either x_j or x_j'. As we move away from the symmetry line, the effect of the symmetric force decreases, and C_{ij} approaches the displacement at x_i due to a unit load at x_j. The variation is not monotonic, due to the fact that at intermediate distances, the symmetric load leads to a decrease in the magnitude of the displacement. For a node s which is on the symmetry line, C_{is} represents the deformation at node i due to a single unit force applied on the symmetry line at node s.

If we now consider the diagonal values of the compliance matrix, for a node s on the symmetry line, C_{ss} is the displacement at the node, due to a unit force applied at the same node. For node i a long way from the symmetry line, the effect of the force applied at the symmetric node is relatively small, so C_{ii} is very close to the displacement at node x_i due to a single unit force applied at x_i. For a node j close to the symmetry line, however, the symmetric force applied at x_j' has a significant effect on the displacement at x_j, and thereby significantly changes the value of C_{jj}, which approaches twice the displacement at node x_j due to a unit force at the same node.

The compliance matrix generated in this manner was then mapped to a simple, full piston compliance matrix for a uniform grid.

3.4.4.1 Generation of asymmetric compliance matrix.

For cases where the bore distortion, or other asymmetries, are sufficiently large, the loading on the piston can no longer be consider symmetric. It is still assumed that loads are applied to the skirt and lands are supported by the wrist-pin only, but the net load is no longer perpendicular to the wrist-pin axis, and requires a supporting force along the axis. At times, the load applied to the skirt is partially supported by the opposite side of the skirt, but we will also choose to neglect this effect for the moment. The piston itself is still symmetric, and therefore only requiring data to be collected for loading over half the piston, but the deformation data for each load must recorded for the full piston

The compliance matrix for this program was generated using a full piston finite-element model in the following manner:

- For nodes not on the symmetry line, a unit forces was applied at x_j, and the net displacement at each node, x_i, was measured, over the full piston.
- For nodes along the symmetry line, a unit force was applied at x_s, and the displacement at each node, x_i, was measured, over the full piston.
- The piston is symmetric, and therefore only one half of the piston was loaded.

The compliance matrix generated in this manner was then mapped to a simple, full piston compliance matrix for a uniform grid.

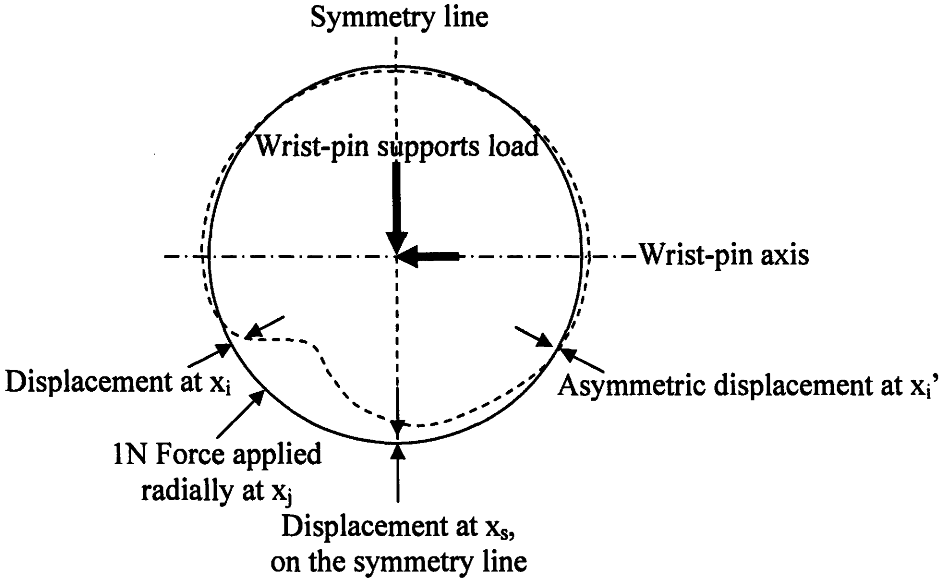

Figure 3.16: Generation of Asymmetric Compliance Matrix

3.4.4.2 Typical compliance matrix features.

The resulting full piston compliance matrix, for a uniform grid, is a very dense matrix, as shown in Figure 3.17. Values are in the range of 3×10^{-5} mm/N for the current uniform grid, with 17 x 17 nodes on the piston skirt, which corresponds to an element area of 3.17×10^{-5} m^2, and deformations of 0.1 µm/bar. It is difficult to determine the structural behavior of the piston from the full compliance matrix as represented in Figure 3.17, but we can note that:

- Compliance values along, and generally close to, the diagonal of the matrix are larger, as points loads will generally cause the most deformation at the point of application of the load, and in the surrounding area.
- There are periodic fluctuations in the matrix values due to the way in which the nodes were numbered (by circumferential position, then axial).
- There are also small but significant negative values in the compliance matrix, as structural effects cause the piston to be deformed outwards away from the load point.

If instead we consider the diagonal of the compliance matrix, C_{ii}, which represents the deformation at node *i*, due to a unit load at node *i*, and map it to the position of node *i*, as shown in Figure 3.18, we can see that:

- The central and lower portion of the skirt is significantly softer than the rest of the piston, resulting in larger radial deformations.

- The hardest part of the piston is not at the very side, or the very top of the skirt, but forms a horseshoe shaped perimeter around the soft portion of the skirt, similar to typically observed wear patterns.
- The compliance matrix values on the lands should not be compared directly with each other, or to the skirt, due to the different element areas. In general, pistons are often designed to avoid land contact, but this is not always the case, with the second land in particular sometimes providing support.
- As expected, none of the deformations are positive, that is, pressure applied to the piston surface cannot increase the radius of the piston.

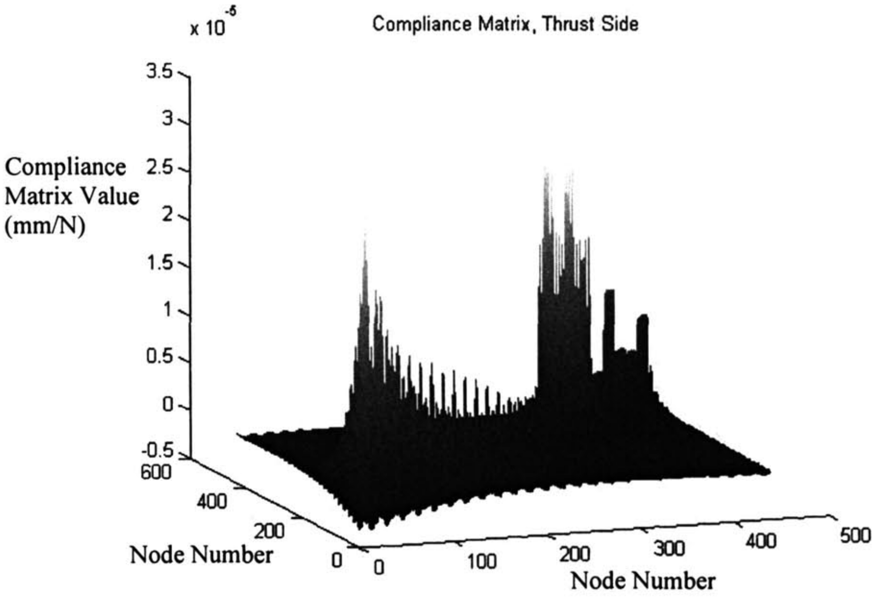

Figure 3.17: Compliance Matrix

It is expected that the softer portion of skirt will initially impact the bore, deforming under contact pressure and resulting in a larger contact area, thereby decreasing the contact pressure as the side load remains constant. The more rigid edges will limit the spread of this contact area though, and correspondingly limit friction generation. These two features therefore help maintain a balance between increasing contact area to limit contact pressure, and keeping the load centrally supported to avoid excess friction.

The deformation resulting from a single unit load is demonstrated in Figures 3.19 and 3.20. Note that there are significant deformations throughout the piston due to its structure.

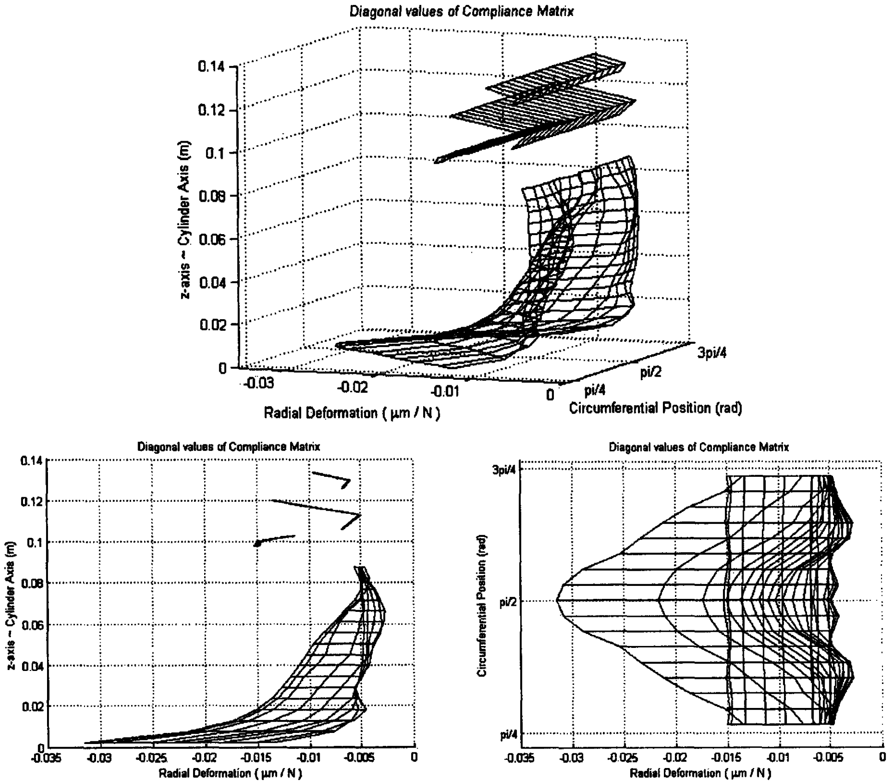

Figure 3.18: Diagonal of Compliance Matrix

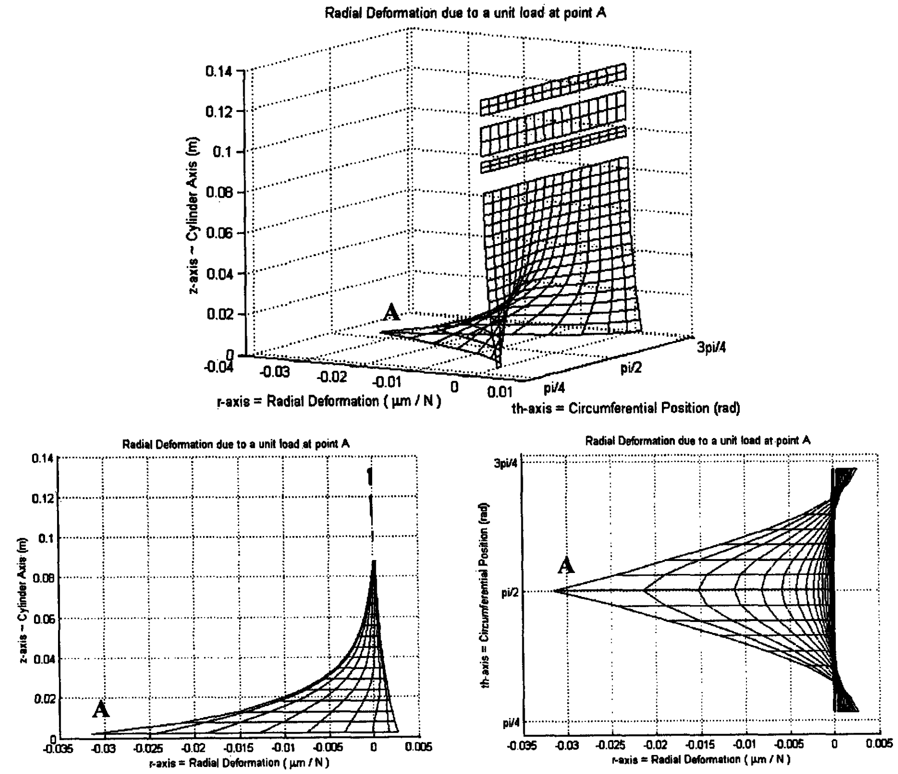

Figure 3.19: Row/Column Due to Load at Soft Centre of Skirt

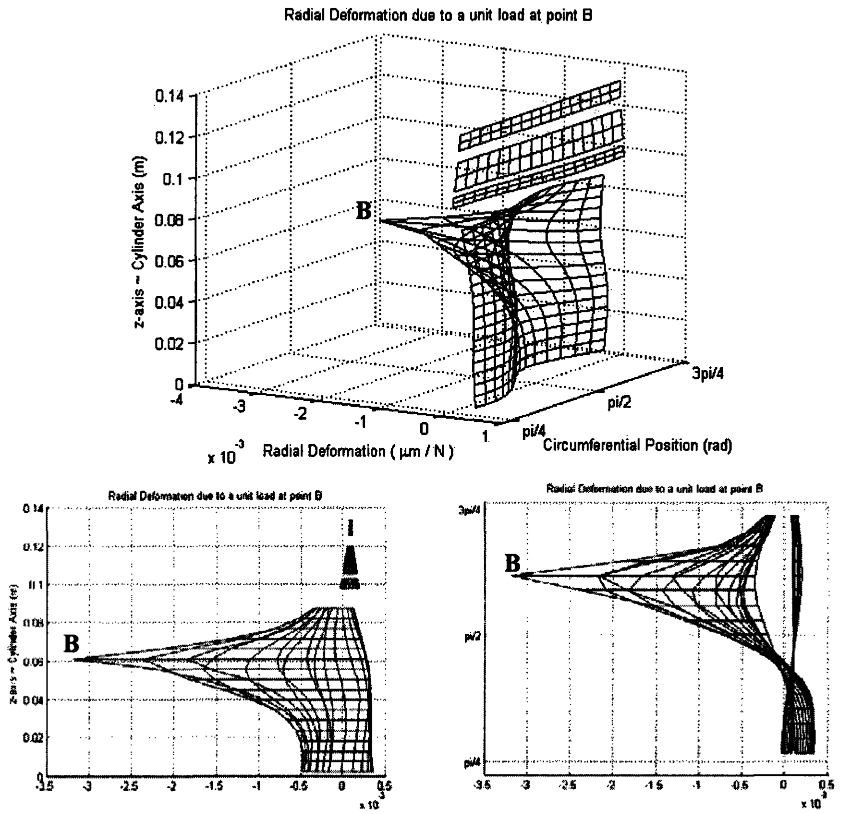

Figure 3.20: Row/Column Due to Load at Hard Top of Skirt

3.5. Cylinder Bore Specification

The cylinder bore is typically manufactured to a nominal radius, and then plateau honed to achieve the desired surface characteristics [31]. Typical values of roughness are $\sigma = 0.5\ \mu m$. Manufacturing processes and tolerances can result in significant variations in bore radius, as can the mechanical deformations due to engine assembly. The combined effect of these is specified by the user via the bore cold shape. During combustion significant energy is transferred to the cylinder bore, both directly by the combustion gas, and via the piston, ring pack and oil, resulting in temperatures ranging from atmospheric to around 300°C. These changes in temperature cause thermal deformations of the order of 100 µm, significantly changing the piston – cylinder bore clearance.

3.5.1. Cold Shape Specification

The cold bore shape can be specified in four ways:

- Nominal radius
- Nominal radius + data vector specifying radial variation as a function of axial position
- Nominal radius + data grid specifying radial variation as a function of axial and circumferential position
- Nominal radius + twelfth order ovality scheme specifying radial variation as a function of axial and circumferential position

The first three options are straightforward, and described in detail in the User Manual [37].

For the fourth option, a twelfth order ovality scheme, the user provides a set of data containing, for a set of axial positions, bore distortions up to twelfth order at each axial position. The variation in radius defined by a bore distortion of order *i* is given by the following equation:

$$\Delta r_i = \delta_i \cos[i \times (\theta + \alpha_i)]$$

where Δr_i = radial variation
δ_i = magnitude of bore distortion
i = order of bore distortion
θ = circumferential location
α_i = phase angle of bore distortion

The phase angle of bore distortion, α_i, defines the location of a peak of the cosine curve. For a phase angle of α_i, a peak of the cosine curve is located at $\theta = -\alpha_i$. The magnitude of bore distortion, δ_i, defines the height of the peak. The order of the bore distortion, *i*, defines the number of peaks per full circle (range of 2π radians, or 360 °).

The total bore distortion for a given axial position is therefore defined by the following formula:

$$\Delta r(z,\theta) = \delta_0(z) + \delta_1(z)\cos(\theta + \alpha_1(z)) + \delta_2(z)\cos[2(\theta + \alpha_2(z))] + \cdots + \delta_{12}(z)\cos[12(\theta + \alpha_{12}(z))]$$

where Δr = radial variation,
z = axial position, in Cylinder bore coordinate system,
θ = circumferential position, in Cylinder bore coordinate system,
δ_i = magnitude of *i*th order bore distortion,
α_i = phase angle of *i*th order bore distortion.

An example of the bore distortion for an instrumented heavy duty diesel engine is shown in Figure 3.22.

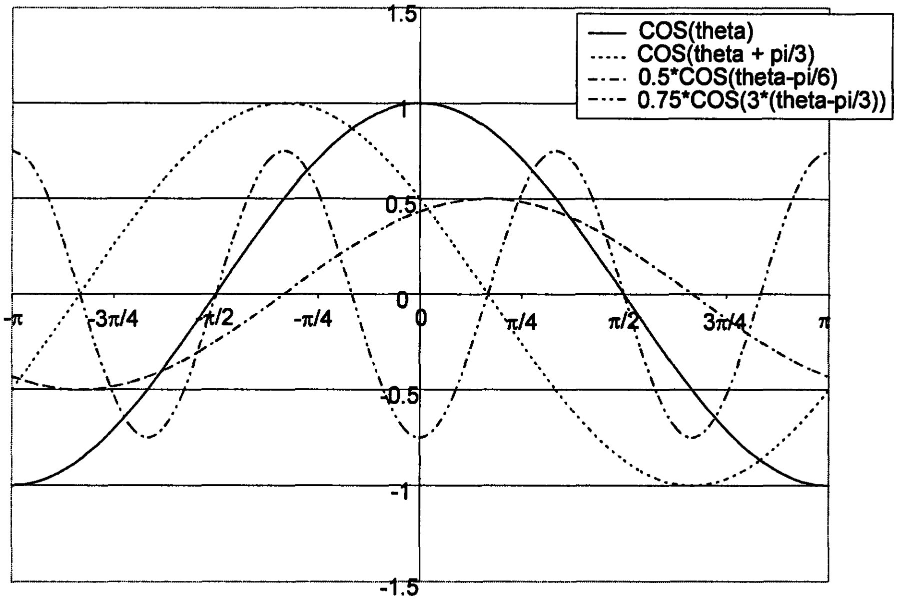

Figure 3.21: Bore Distortion Curves

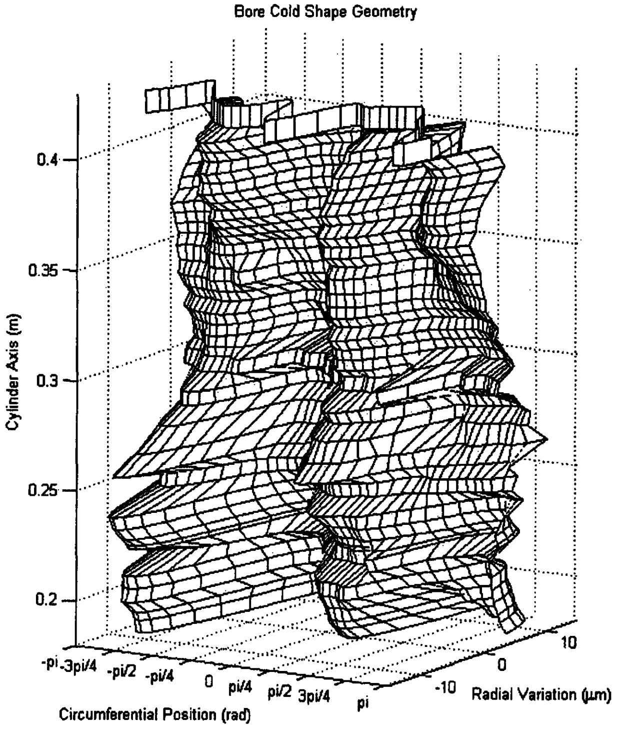

Figure 3.22: Bore Distortion Data

3.5.2. Radial Thermal Deformation

During combustion, a large portion of the cylinder bore is exposed to the combustion gases, resulting in heat transfer to the cylinder bore. Depending on engine design, cooling fluid may be supplied to the exterior of the cylinder in order to remove heat, and control temperature. Depending on the material and structure of the cylinder bore and surrounding engine block, and whether any coolant is supplied, temperatures within the cylinder bore can vary significantly. These temperatures and the corresponding thermal expansion, which is of the same order as the piston-cylinder bore clearance, vary over time with running conditions from cold shape at start-up, to a significantly larger shape at steady-state, high load and speed. It is assumed for the purposes of this project that we have steady state thermal behavior, for a given running condition.

The detailed geometry of the cylinder bore is used in determining the gap height between the piston and the cylinder bore. At this interface, variations of the order of a micron can, in some cases, significantly effect the pressure generated at the interface, lead to solid-solid contact, and result in a corresponding shift in lateral motion. Given the large variations in thermal expansion for various running conditions, and the fact that an engine can be expected to transition between these conditions during normal, unsteady, operation, it is not realistic to expect micron level accuracy of hot shape geometry, but it is important to recognize the effect of uncertainty in this data.

In determining thermal deformation, it is expected that the user will build a thermal finite element model of the cylinder bore, with appropriate boundary conditions, to predict the temperature distribution and corresponding thermal deformation for each running condition. For the purposes of this project the user may specify the thermal deformation in the same way as the cold shape, that is, via data points as a function of axial and/or circumferential position, or via a twelfth order ovality scheme.

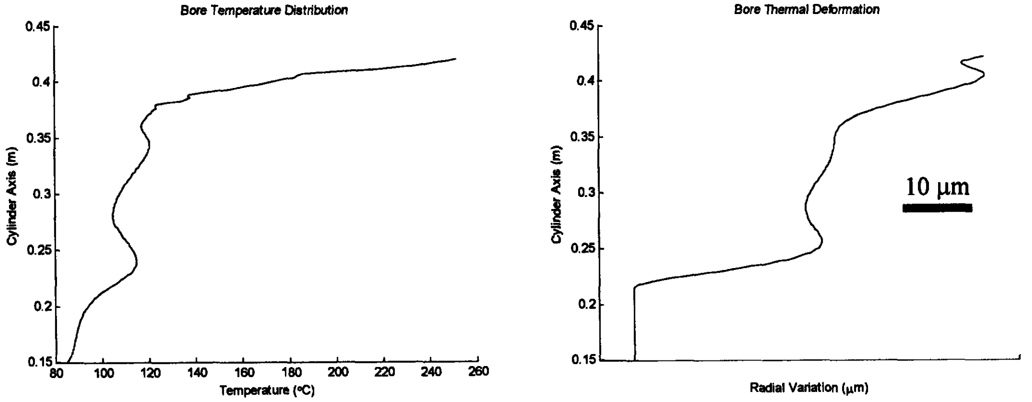

Figure 3.23: Cylinder Bore Temperature Distribution and Thermal Deformation

4. Dry Model Results

This chapter aims to:

- Demonstrate that the equations of motion governing the power cylinder dynamics, as derived in Section 2.2, are satisfied by the dry model.
- Provide a systematic explanation of the driving mechanisms for lateral motion and tilt, in the context of the dry model.
- Provide a simplified functional form for the forces and moments driving piston motion, where appropriate.
- Highlight the main parameters affecting piston secondary motion.
- Identify uncertainties or sources of error in the current model, and estimate their significance in accurate prediction of piston secondary motion.
- Demonstrate the model's ability to investigate the effect of key parameters on piston secondary motion.

Unless otherwise specified, the results included in this chapter are for a heavy-duty diesel engine at 1200rpm, full load (2200 Nm), with the key parameters as specified in Table 4.1. Figure 4.1 contains the hot piston profile, cold bore distortion and bore thermal deformation.

Parameter	**Value**	**Units**
Cylinder Bore radius	~ 65	mm
Piston – cylinder bore friction coefficient	0.05	-
Asperity contact model constant – multiplier	2.040×10^{13}	Pa $m^{-1.069}$
Asperity contact model constant – exponent	1.0689	-
Nominal piston – cylinder bore cold clearance	~ 60	μm
Piston mass	~ 3	kg
Piston moment of inertia	~ 0.01	kgm^2
Wrist-pin – piston friction coefficient	0.02	-
Wrist-pin radius	~ 0.03	m
Wrist-pin mass	~ 2	kg
Wrist-pin moment of inertia	~ 0.001	kgm^2
Connecting-rod – wrist-pin friction coefficient	0.02	-
Connecting-rod mass	~ 6	kg
Connecting-rod moment of inertia	~ 0.1	kgm^2
Connecting-rod length	~ 0.3	m
Crankshaft radius	~ 0.1	m
Crankshaft offset	0	m

Table 4.1: Baseline Model Parameters

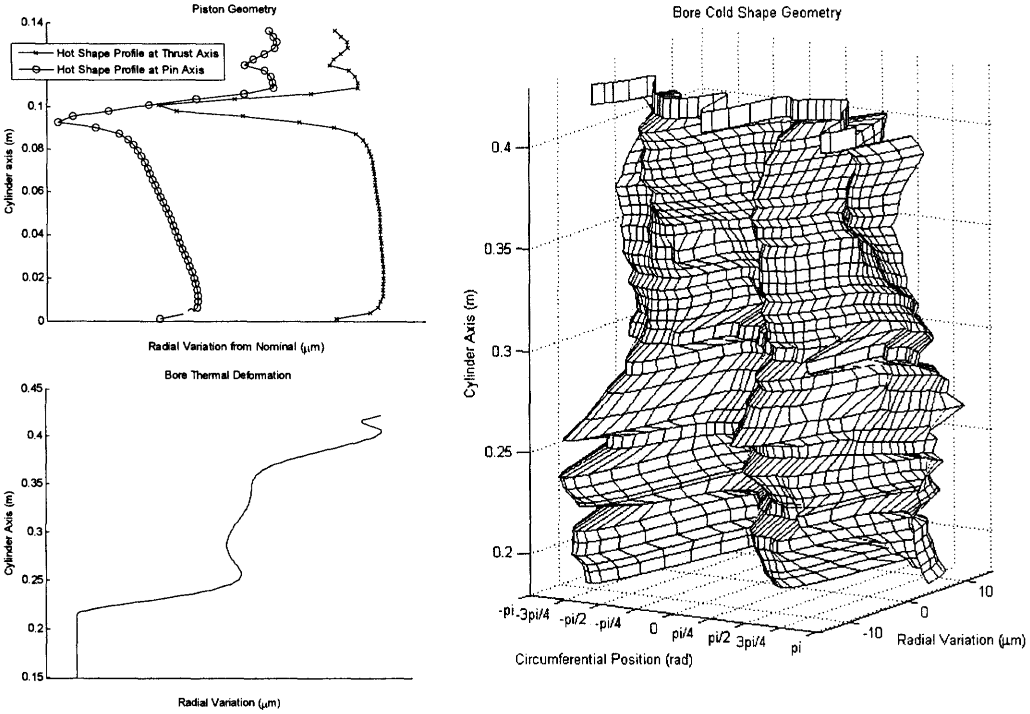

Figure 4.1: Baseline Piston and Bore Profiles

4.1. Equations of Motion

4.1.1. Axial Force Balance on Piston

The engine's motion is driven, in concept, by the combustion chamber pressure. For the purposes of this steady state model though, the piston's motion along the cylinder axis is prescribed by the crankshaft speed, and the force transmitted from the wrist-pin to the piston must balance the loads on the piston from combustion chamber pressure, inertia, friction, and gravity:

$$F_{WP/PSZ} = m_{PS} a_{PS\_CG/A_Z} - F_{CB/PSZ} - F_{P/PSZ} - m_{PS} g_Z$$

Results for a heavy duty diesel engine, at 1200 rpm, full load, are shown in Figure 4.2. Typically, for passenger car and truck engines, the pressure load dominates through the second half of the compression stroke and most of the expansion stroke. Outside of this range inertia becomes more significant, while the friction and gravity forces are generally small throughout the cycle. The lower left-hand plot in Figure 4.2 demonstrates that the force balance is met to within 0.1N.

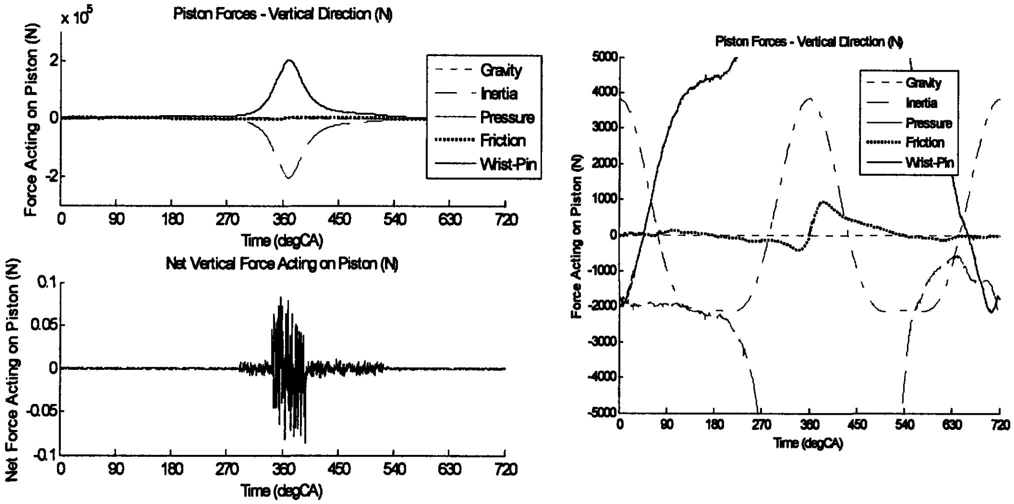

Figure 4.2: Axial Force Balance on Piston

In Figure 4.2, we can see that the force exerted on the piston, by the wrist-pin, changes sign during the intake and exhaust strokes, resulting in piston slap, as discussed in Section 4.2.1. The timing of this change is determined largely by the balance of inertia and pressure forces, and hence can shift significantly depending on load, speed, piston mass and engine geometry (crankshaft offset, crankshaft radius, connecting-rod length). Mid-stroke piston slaps are also possible during the compression and expansion strokes, though less common due to the increased pressure force.

A rough estimate of the magnitude of axial forces, for this heavy duty diesel engine demonstrates that the pressure and inertia forces are dominant in determining the load to be supported by the wrist-pin, while the friction and gravity forces are smaller. The simplified equations used in these estimates also help demonstrate which model parameters can significantly affect this force balance.

Force	Simplified Equation	Estimated Value
Pressure	~ Combustion pressure × Bore area ~ 150 bar × π (65 mm)^2	~ 200 kN
Inertia	~ Piston mass × (Crankshaft speed)^2 × Crankshaft radius ~ 2.5 kg × (1200 rpm)^2 × 0.08m	~ 3 kN
Friction	~ Friction coefficient × (Crankshaft radius /Con-rod length) × Pressure force ~ 0.05 × 1/3.5 × Pressure force	~ 1.1 kN
Gravity	= Piston mass × g ~ 2.5 kg × 9.81 m/s^2	~ 25 N
Wrist-Pin	~ Pressure + Inertia Forces	~ 200 kN

Table 4.2: Axial Piston Forces

Note that the friction is estimated to be about 1.5% of the pressure force, and hence when the pressure is small during the intake and exhaust strokes the friction is negligible compared to both pressure and inertia. The friction coefficient at the piston – cylinder bore interface is the greatest source of uncertainty in this force balance, but in general the friction force is very small, and hence this uncertainty does not significantly effect the piston dynamics at this point.

The friction-pressure relationship does not hold when an interference fit occurs between the piston and cylinder bore, resulting in significantly higher side forces and friction at the piston – cylinder-bore interface, as discussed in Section 4.4.1. For the running conditions investigated, however, the friction force did not significantly affect the axial force balance on the piston. It is possible that extreme cases of interference fit may result in sufficient friction to affect this force balance, but such severe running conditions would indicate an undesirable engine design, and most likely result in engine damage.

For engines with significantly higher rotational speeds, such as small two-stroke engines in chainsaws, and formula 1 racing car engines, or at low load running conditions, the inertia forces may be comparable to pressure forces during portions of all four strokes, significantly altering the power cylinder dynamics. A comparison of the effects of speed on piston dynamics is included in Section 4.5.1.

4.1.2. Axial Force Balance on Wrist-Pin

An axial force balance on the wrist-pin then determines the force that is transmitted through to the connecting-rod. In most cases, the connecting-rod force is dominated by the pressure force on the piston around combustion TDC, and the combined pressure and inertia loads throughout the rest of the cycle, as shown in Figure 4.3. The lower left-hand plot in this Figure demonstrates that the force balance is met to within 0.1N.

$$F_{CR/WPZ} = m_{WP}a_{WP\_CG/A_Z} - m_{WP}g_Z - F_{PS/WPZ}$$

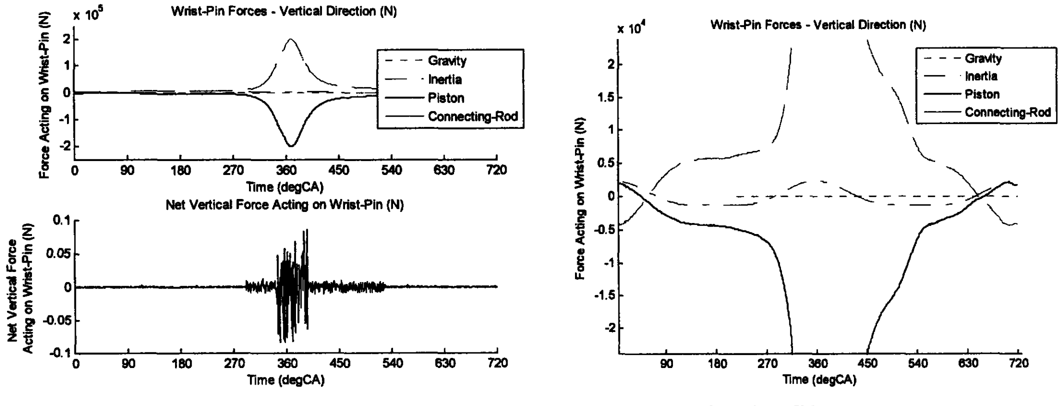

Figure 4.3: Axial Force Balance on Wrist-Pin

The wrist-pin inertia affects the timing of the mid-stroke piston slaps, significantly shifting the crank angle position at which the connecting rod changes from tension to compression, and vice versa. In general, the timing of mid-stroke piston slaps are determined by the balance of pressure load and component axial inertias. At high speeds, or lower loads, the effect of inertia becomes much more significant, as discussed in Section 4.5.1, significantly altering the wrist-pin – connecting rod axial force.

A summary of the wrist-pin forces, their estimated values for this engine and running condition, and the simplified equations these estimates are based on, are included in Table 4.3.

Force	Simplified Equation	Estimated Value
Piston	~ Pressure + Inertia Forces	~ 200 kN
Inertia	~ Wrist-Pin mass × (Crankshaft speed)^2 × Crankshaft radius ~ 1.5 kg × (1200 rpm)^2 × 0.08m	~ 1.9 kN
Gravity	= Wrist-Pin mass × g ~ 1.5 kg × 9.81 m/s^2	~ 14 N
Connecting- Rod	~ Pressure + Inertia Forces	~ 200 kN

Table 4.3: Axial Wrist-Pin Forces

4.1.3. Moment Balance on Connecting-Rod

Due to the fact that the connecting-rod acts at an angle to the cylinder axis, a lateral force will be generated as the connecting-rod supports its axial load. Assuming that the large end of the connecting-rod can be approximated as a frictionless pin joint, a moment balance about this point, combined with the wrist-pin – connecting-rod interface equations can be used to determine the lateral force and torque at the wrist-pin – connecting-rod interface.

The moment balance on the connecting-rod, about the centre of its large end, as derived in Section 2.2.2, is given by:

$$\begin{aligned}\tau_{WP/CRX} - r_{CR\_P/QZ} F_{WP/CRY} &= I_{CR\_XX}\ddot{\phi}_{CR} - r_{CR\_P/QY} F_{WP/CRZ} \\ &\quad - \left\{\mathbf{r}_{CR\_CG/Q} \times m_{CR}\mathbf{g} - \mathbf{r}_{CR\_CG/Q} \times m_{CR}\mathbf{a}_{CR\_CG/A}\right\}_X\end{aligned}$$

The terms on the right hand side of this equation are well defined at this point in the calculation, while the lateral force, $F_{WP/CR\,Y}$, and friction torque, $\tau_{WP/CR\,X}$, are unknown.

A detailed description of the wrist-pin – connecting-rod interface model is provided in Section 2.3.2. The resulting equations for the forces and moments generated at this interface are a function of two unknowns, the magnitude of the normal load on the bearing, $|F_N|$, and the angle at which this load acts, θ_B:

$$\mathbf{F}_B = |F_N|\left\{\cos(\theta_B) + \mathrm{sign}(\Delta\dot{\phi}) f_S \sin(\theta_B)\right\}\mathbf{j} + |F_N|\left\{\sin(\theta_B) - \mathrm{sign}(\Delta\dot{\phi}) f_S \cos(\theta_B)\right\}\mathbf{k}$$

$$\mathbf{M}_B = -\mathrm{sign}(\Delta\dot{\phi}) f_S |F_N| R\mathbf{i}$$

This set of equations must be solved simultaneously to define the lateral force and friction moment acting at the wrist-pin – connecting-rod interface.

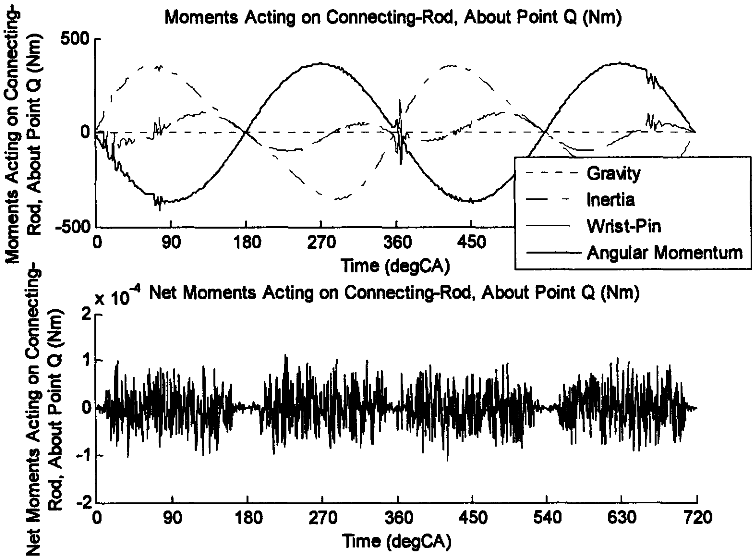

Figure 4.4: Moment Balance on Connecting-Rod

As shown in Figure 4.4, the rate of change of angular momentum of the connecting-rod, and the moment generated by its inertia, appear significantly larger than the total moment generated at the wrist-pin – connecting-rod interface, and are almost equal and opposite, with the wrist-pin moment making up the difference, as the connecting-rod carries out its pendulum-like motion. This impression however, is not entirely correct. If the wrist-pin – connecting-rod moment is separated into its three components (moment due to axial force, moment due to lateral force and friction moment), as shown in Figure 4.5, then it becomes apparent that the moments generated individually by the axial and lateral forces are significantly larger than their net effect.

The driving force in this balance is the axial load on the connecting-rod, combined with the significantly smaller moments due to the ideal motion of the connecting-rod, as shown in the upper plot in Figure 4.6. Fluctuations in the inertia terms due to lateral motion of the small end of the connecting-rod, particularly during piston slap, are also evident. The lateral force must then satisfy the moment balance, while simultaneously taking into account the friction moment that will be generated, and its contribution to this balance which is only significant around combustion TDC. The effect of gravity is negligible.

It is useful to estimate the magnitude of these moments in order to demonstrate their dependencies, and identify whether uncertainties, such as the friction coefficient at the wrist-pin – connecting-rod interface, have a significant effect on these results. Note that the wrist-pin moments are over-estimated due to the fact that the peak pressure force occurs at a smaller radius.

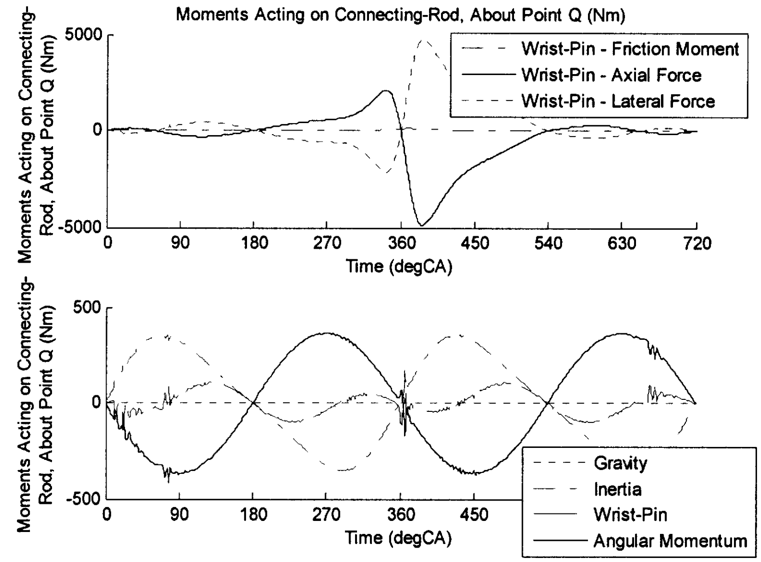

Figure 4.5: Moments Acting on Connecting-Rod

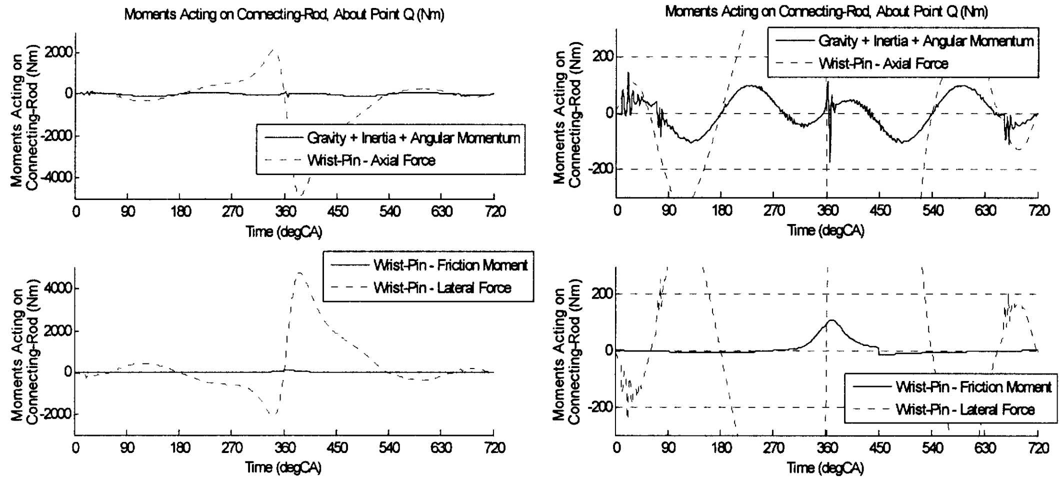

Figure 4.6: Driving and Reacting Connecting-Rod Moments

The wrist-pin – connecting-rod bearing friction is investigated in more detail in Section 4.4.2 and can be shown have a significant effect on piston tilt, particularly around combustion TDC, and results in small changes to the piston slap timing and lateral motion in this region.

Note that by using this bearing model of the wrist-pin – connecting-rod interface we allow the connecting-rod – wrist-pin force to have a component perpendicular to the main axis of the connecting-rod, contrary to the assumption made in some piston secondary motion models and friction measurement methods. If the connecting-rod force lies along the main axis of the connecting-rod, then it does not generate a moment about the point Q, and the lateral force at the wrist-pin – connecting-rod interface is completely defined by the corresponding axial force and the angle of the connecting-rod. This assumption decouples the connecting-rod inertia from the piston dynamics, and neglects the significant effect that connecting-rod mass, position of centre of gravity, and inertia can have on mid-stroke piston timing, as shown in Section 4.5.2.

Moment	Simplified Equation	Estimated Value
Wrist-Pin Axial	~ Pressure + Inertia Forces × Con-rod length × sin(ϕ_{CR}) ~ Pressure + Inertia Forces × Crankshaft radius ~ 200 kN × 0.08m	~ 16 kNm
Wrist-Pin Lateral	~ Pressure + Inertia Forces × tan(ϕ_{CR}) × Con-rod length × cos(ϕ_{CR}) ~ Pressure + Inertia Forces × Crankshaft radius ~ 200 kN × 0.08m	~ 16 kNm
Friction Moment	~ Friction Coefficient × Pressure + Inertia Forces / cos(ϕ_{CR}) × Pin radius ~ 0.02 × 200kN / 1 × 0.03m	~ 130 Nm
Inertia	~ Con-rod mass × Acceleration × Crankshaft radius ~ 5 kg × (1200 rpm)^2 × 0.08m × 0.08m	~ 500 Nm
Rate of Change of Angular Momentum	~ Con-rod moment of inertia × Con-rod angular acceleration ~ Con-rod moment of inertia × asin(Crankshaft radius / Con-rod length) / (90 °CA)^2 1200 rpm = 7200 °CA/s → 90 °CA = 0.0125 s ~ 0.07 kgm^2 × asin(1/3.5) rad / 0.0125^2 s^2	~ 130 Nm
Gravity	= Con-rod mass × g × Crankshaft radius ~ 5 kg × 9.81 m/s^2 × 0.08m	~ 4 Nm

* Wrist-pin moments are overestimated due to the fact that the peak pressure force and radius occur at different times.

Table 4.4: Connecting-Rod Moments

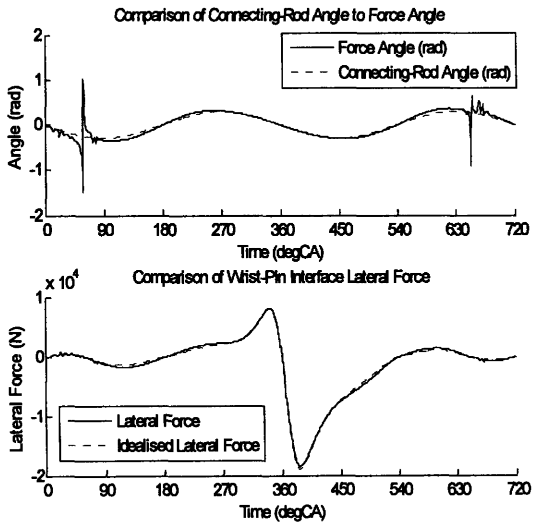

Figure 4.7: Wrist-Pin – Connecting-Rod Force, Angle of Action

Figure 4.7 shows a comparison between the connecting-rod angle, and the angle at which the wrist-pin – connecting-rod force acts. The second plot demonstrates the difference between the predicted lateral force, and the lateral force component that would be generated if the force acted along the main axis of the connecting-rod. These variations are generally small. However, if we consider the resulting force acting perpendicular to the connecting-rod axis, as shown in Figure 4.8, it is not negligible, particularly during the intake and exhaust strokes.

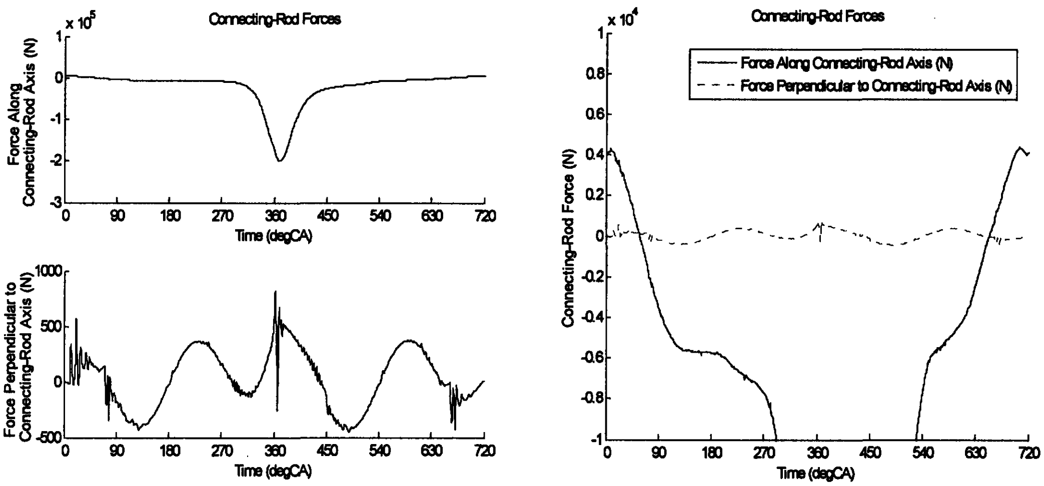

Figure 4.8: Forces Relative to Connecting-Rod Axis

Lateral and axial force balances on the connecting-rod can then be used to predict the forces that will be transmitted to the crankshaft, as shown in Figure 4.9.

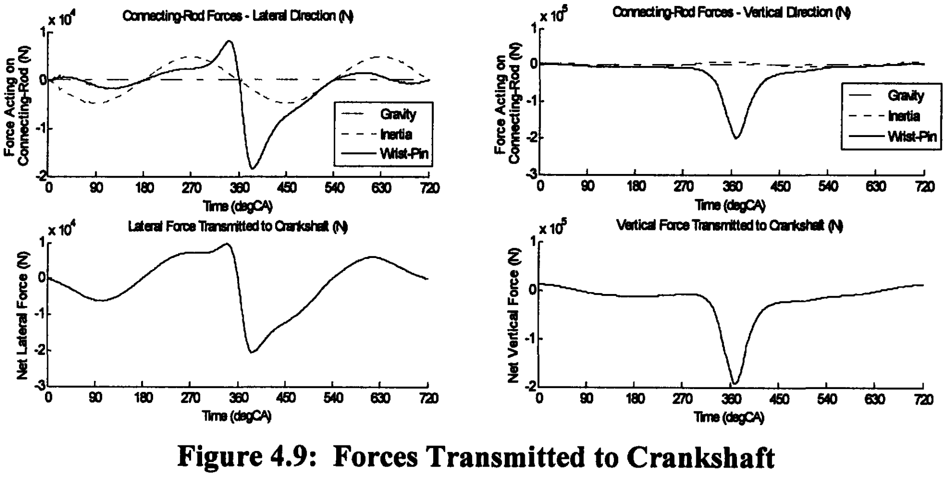

Figure 4.9: Forces Transmitted to Crankshaft

Force	Simplified Equation	Estimated Value
Wrist-Pin Axial	~ Pressure + Inertia Forces	~ 200 kN
Wrist-Pin Lateral	~ Pressure + Inertia Forces × tan(ϕ_{CR}) ~ Pressure Force × Crankshaft radius / Connecting-Rod length ~ 200 kN × 1/3.5	~ 57 kN
Inertia	~ Con-rod mass × Acceleration ~ 5 kg × (1200 rpm)^2 × 0.08m	~ 6 kN
Gravity	= Con-rod mass × g ~ 5 kg × 9.81 m/s^2	~ 49 N

* Wrist-pin lateral force is overestimated due to the fact that the peak pressure force and value of tan(ϕ_{CR}) occur at different times.

Table 4.5: Connecting-Rod Forces

4.1.4. Lateral Force Balance on Wrist-Pin

A lateral force balance on the wrist-pin is used to determine the lateral force transmitted to the piston, as shown in Figure 4.10.

$$F_{PS/WPY} = m_{WP}a_{WP\_CG/A_Y} - F_{CR/WPY} - m_{WP}g_Y$$

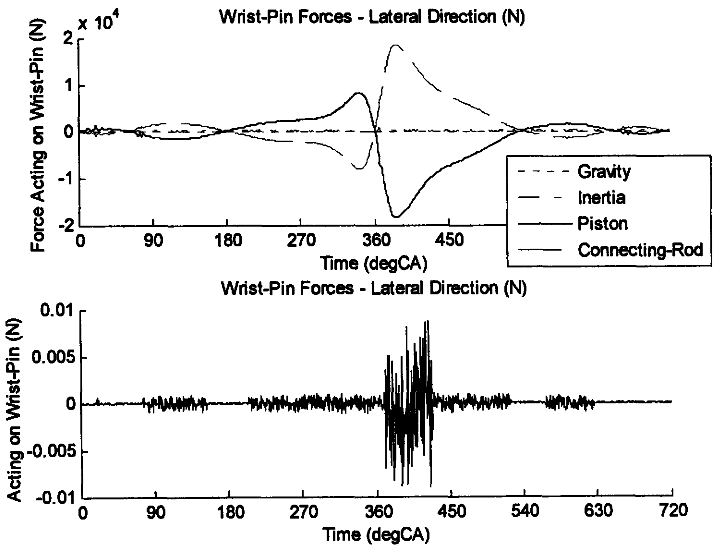

Figure 4.10: Lateral Force Balance on Wrist-Pin

The wrist-pin inertia is significantly smaller than the lateral force transmitted through the wrist-pin to the piston, except for during piston-slap events in the intake and exhaust strokes, where the combined effect of connecting-rod, wrist-pin and piston inertias can cause significant fluctuations in the lateral force, as shown in Figure 4.11. Gravity is negligible throughout the cycle.

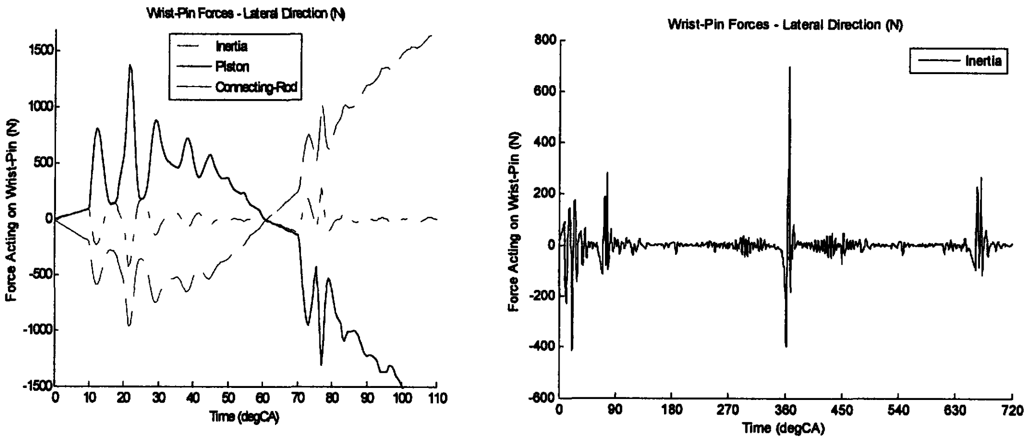

Figure 4.11: Effect of Component Inertias

Force	Simplified Equation	Estimated Value
Connecting-Rod	~ Pressure + Inertia Forces × tan(ϕ_{CR})	~ 57 kN
Inertia	~ Wrist-Pin mass × Lateral Acceleration ~ 1.5 kg × 100μm / (5 °CA)^2 1200 rpm = 7200 °CA/s → 5 °CA = 6.95 × 10^{-4} s ~ 310 kg m/s^2	~ 310 N
Gravity	= Wrist-Pin mass × g ~ 1.5 kg × 9.81 m/s^2	~ 15 N
Piston	~ Pressure + Inertia Forces × tan(ϕ_{CR})	~ 57 kN

* Connecting-rod and piston forces are overestimated due to the fact that the peak pressure force and value of tan(ϕ_{CR}) occur at different times.

Table 4.6: Lateral Wrist-Pin Forces

4.1.5. Moment Balance on Wrist-Pin

The torque at the wrist-pin - piston interface is defined by the bearing interface model as a function of the lateral and axial forces at this interface and a smoothed friction coefficient:

$$\mathbf{M}_B = -\mathrm{sign}(\Delta\dot{\phi}) f_S |F_N| R\mathbf{i}$$

The smoothed friction coefficient, f_S, is a function of the relative angular velocity of the wrist-pin and piston.

$$f_S = \left[1 - \exp\left(-\left|\frac{\Delta\dot{\phi}}{0.1 \times a}\right|\right)\right] a_1 \left(\frac{\mu R L \Delta\dot{\phi}}{|F|}\right)^{a_2} \left(\frac{R}{c}\right)^{a_3}$$

The angular position and velocity of the wrist-pin are initially unknown, and solved for iteratively based on satisfying a moment balance on the wrist-pin, about the pin axis. The angular acceleration of the wrist-pin is defined as:

$$\ddot{\phi}_{WP}^{\,k} = \frac{\dot{\phi}_{WP}^{\,k} - \dot{\phi}_{WP}^{\,k-1}}{t^{k} - t^{k-1}}$$

The moment balance is given by:

$$\begin{aligned} I_{WP\_XX}\ddot{\phi}_{WP} &= \tau_{PS/WPX} + \tau_{CR/WPX} + r_{WP\_CG/WP\_P_Y} \times m_{WP} g_Z - r_{WP\_CG/WP\_P_Z} \times m_{WP} g_Y \\ &\quad - r_{WP\_CG/WP\_P_Y} \times m_{WP} a_{WP\_CG/A_Z} + r_{WP\_CG/WP\_P_Z} \times m_{WP} a_{WP\_CG/A_Y} \end{aligned}$$

The friction moments generated at the wrist-pin's interfaces with the connecting-rod and piston drive the angular motion of the wrist-pin as shown in Figure 4.12. For this engine, the centre of gravity of the wrist-pin is on the pin axis, and therefore no inertia or gravity moments are generated.

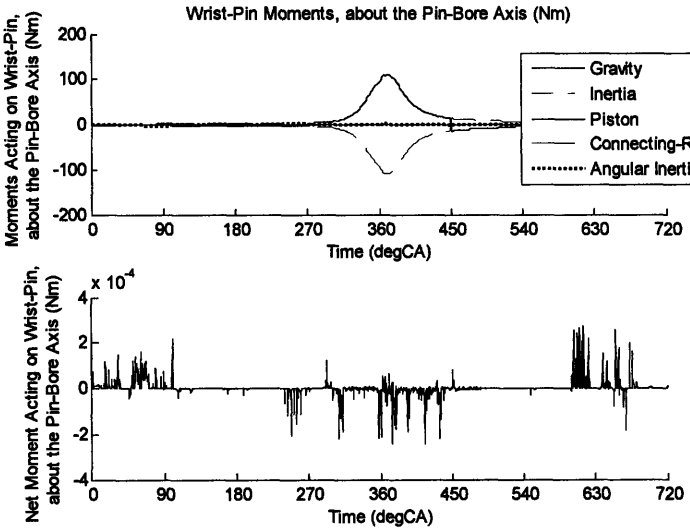

Figure 4.12: Moment Balance on Wrist-Pin

Differences in the friction moments are initially balanced by the rate of change of angular momentum of the wrist-pin, as the wrist-pin accelerates to follow the component with the highest friction moment. As the angular velocity of the wrist-pin approaches that of the driving component, though, the friction coefficient at this interface will decrease, thereby achieving the moment balance.

This process can be seen clearly in Figure 4.13:

- 0-60 °CA: Wrist-pin accelerated to follow the connecting-rod due to larger force at wrist-pin – connecting-rod interface (see Section 4.1.4).
- ~60 °CA Wrist-pin and connecting-rod angular velocities equal. Connecting-rod moment changes sign.

- 60-110 °CA: Wrist-pin rotation decelerated and reversed by both connecting-rod and piston rotation.
- ~110 °CA: Wrist-pin angular velocity equal to piston angular velocity. Piston moment changes sign.
- 110-240 °CA: Connecting-rod force continues to dominate, rotating wrist-pin to follow connecting-rod, but to a decreasing extent as connecting-rod angular velocity decreases after 180 °CA.
- ~240 °CA: Wrist-pin angular velocity close to connecting-rod velocity, resulting in decreased friction coefficient.
- 240-270 °CA: Wrist-pin driven by piston, due to decreased friction coefficient at wrist-pin – connecting-rod interface.
- ~270 °CA: All three angular velocities equal, direction of moments on wrist-pin change.
- 270-450 °CA: Wrist-pin driven by piston due to larger force at wrist-pin – piston interface.
- Similar analysis can be completed for the rest of the cycle.

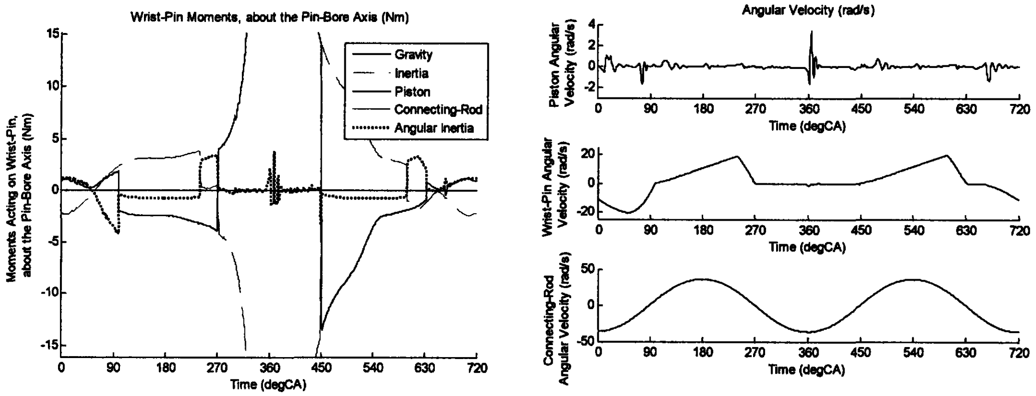

Figure 4.13: Wrist-Pin Angular Moments and Velocity

The resulting angular motion of the piston, along with the angular motions of the piston and connecting-rod are shown in Figure 4.14.

For cases where the friction coefficients of the two interfaces are significantly different, reduction of the friction coefficient is the only way to achieve a balance, and the wrist-pin will predominantly move with the component with the highest nominal friction coefficient. The lowest friction coefficient determines the friction moment that will be transmitted to the piston. The effect of wrist-pin friction coefficient on system dynamics is investigated further in Section 4.4.2.

The magnitudes and approximate functional dependence of the wrist-pin moments are summarized in Table 4.7.

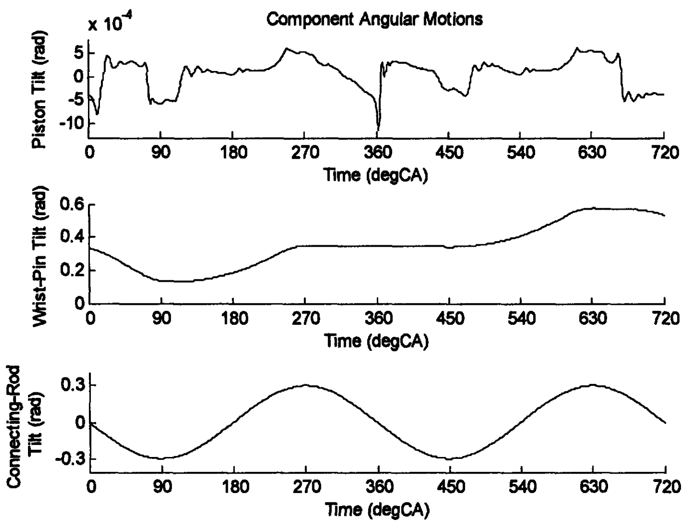

Figure 4.14: Component Angular Motions

Moment	Simplified Equation	Estimated Value
Connecting-Rod Moment	~ Friction Coefficient x Pressure + Inertia Forces / cos(ϕ_{CR}) x Pin radius ~ 0.02 x 200kN / 1 x 0.03m	~ 130 Nm
Inertia	~ Wrist-Pin mass x Acceleration x CG radius ~ 1.5 kg x (1200 rpm)^2 x 0.08m x 0	~ 0 Nm
Rate of Change of Angular Momentum	~ Wrist-pin moment of inertia x Wrist-pin angular acceleration ~ 0.0007 kgm^2 x 5000 rad/s^2	~ 3.5 Nm
Gravity	= Wrist-pin mass x g x CG radius ~ 1.5 kg x 9.81 m/s^2 x 0	~ 0 Nm
Piston Moment	~ Friction Coefficient x Pressure + Inertia Forces / cos(ϕ_{CR}) x Pin radius ~ 0.02 x 200kN / 1 x 0.03m	~ 130 Nm

Table 4.7: Wrist-Pin Moments

4.1.6. Lateral Force Balance on Piston

The lateral force transmitted from the wrist-pin to the piston is defined by the lateral force balance on the wrist-pin. This force, combined with the lateral pressure force around combustion TDC, drives the piston's lateral motion while interaction with the cylinder bore constrains it, and supports the driving force, as shown in Figure 4.15. The contribution of gravity is negligible.

The lateral position and velocity of the piston are initially unknown, and solved for iteratively based on satisfying a lateral force balance on the piston:

$$m_{PS}a_{PS\_CG/A_Y} = F_{WP/PSY} + F_{CB/PSY} + F_{P/PSY} + m_{PS}g_Y$$

The lateral acceleration of the piston is defined as:

$$\ddot{x}_{PSY}^{\,k} = \frac{\dot{x}_{PSY}^{\,k} - \dot{x}_{PSY}^{\,k-1}}{t^k - t^{k-1}}$$

The angular position and velocity of the piston are also initially unknown, and solved for iteratively based on satisfying a moment balance on the piston, about the pin axis, as discussed in Section 2.5. The piston tilt significantly impacts both the lateral pressure force generated around combustion TDC, and the piston – cylinder bore clearance distribution.

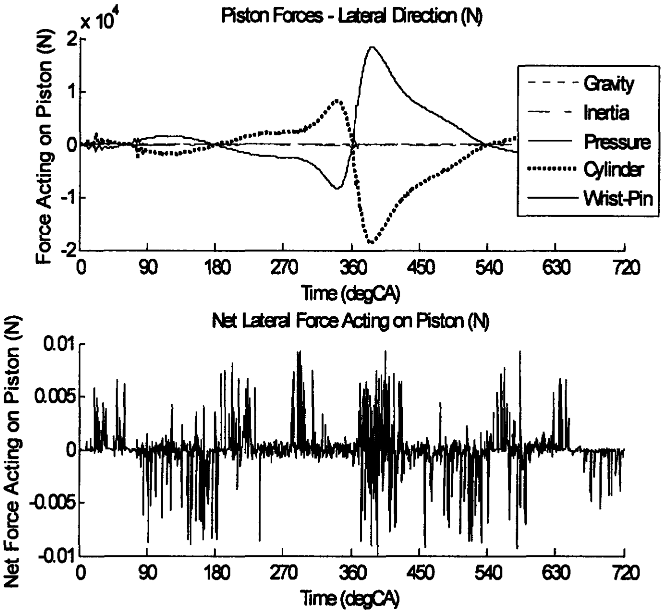

Figure 4.15: Lateral Force Balance on Piston

During the intake and exhaust strokes there are significant fluctuations in the wrist-pin force due to the wrist-pin and connecting-rod inertias, and corresponding fluctuations in the cylinder force due to these plus the added effect of piston inertia, as shown in Figure 4.16. These fluctuations are due to the fact that at light loads, the component's lateral inertias are significant and the elastic piston tends to bounce on the rigid cylinder bore during piston slap. It is expected that, in the physical system, oil would significant damp out this motion. At higher loads, the piston's tendency to bounce is significantly reduced as the piston's inertia becomes negligible compared to the large driving force.

As shown in Figure 4.17, the force supported at the piston – cylinder bore interface is essentially a function of the combustion chamber pressure and connecting-rod angle, both of which are well defined.

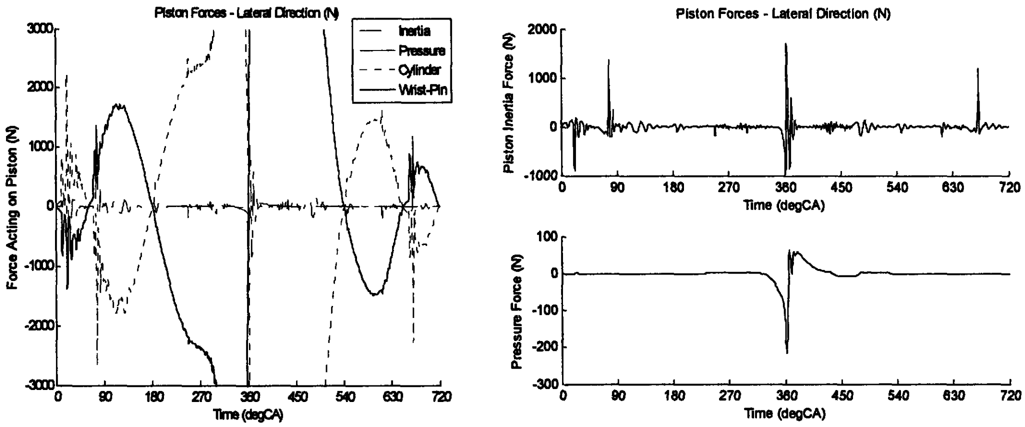

Figure 4.16: Piston Forces – Lateral Direction

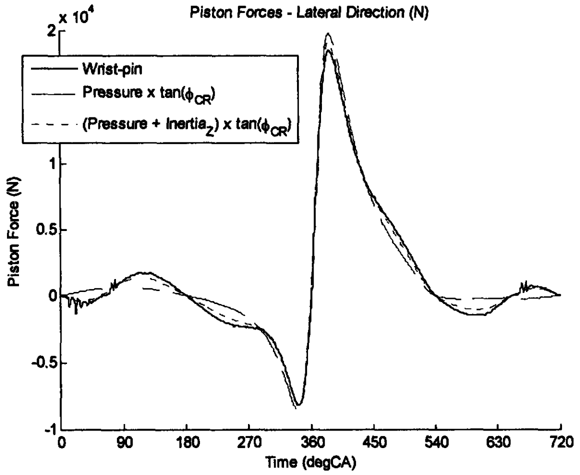

Figure 4.17: Piston Side Force

In the absence of a significant amount of interference, variations in the side force driving the piston's motion, from the ideal function of pressure force, are demonstrated in Figure 4.18:

- Piston and wrist-pin axial inertias lead to a difference between the pressure force on the piston, and the axial force on the connecting-rod. The balance of combustion chamber pressure and component inertias can significantly shift the timing of mid-stroke piston slaps during the intake and exhaust strokes, but all of these features are well defined and do not introduce significant uncertainty into our model.
- The angle at which the connecting-rod acts generates a lateral force from the axial load. Ideally this lateral force is given by:

$$\text{lateral force} = \text{axial force} \times \tan(\phi_{CR})$$

- Connecting-rod inertia and wrist-pin friction shift the moment balance on the connecting-rod, altering the angle of action of the connecting-rod force and the resulting lateral force on the connecting-rod. The wrist-pin friction is not well defined, but was investigated in more detail in Section 4.4.2, and found to not significantly impact the lateral force transmitted to the piston. Connecting-rod inertia is investigated in Section 4.5.2 and shown to significantly shift the timing of mid-stroke piston slaps, and in high speed, low load running conditions increasing component inertias significantly change the lateral force as they become more significant compared to the pressure load.

- The wrist-pin lateral inertia introduces further fluctuations in the lateral force. These fluctuations, and those due to lateral motion of the connecting-rod small end, are dependent on the detailed piston – cylinder bore interface interactions, and while they can be considered to represent a significant source of uncertainty in the exact motion of the system, the average behavior tends to be unchanged.
- The lateral component of the combustion chamber pressure force can become significant around combustion TDC, but is highly dependent on piston tilt.

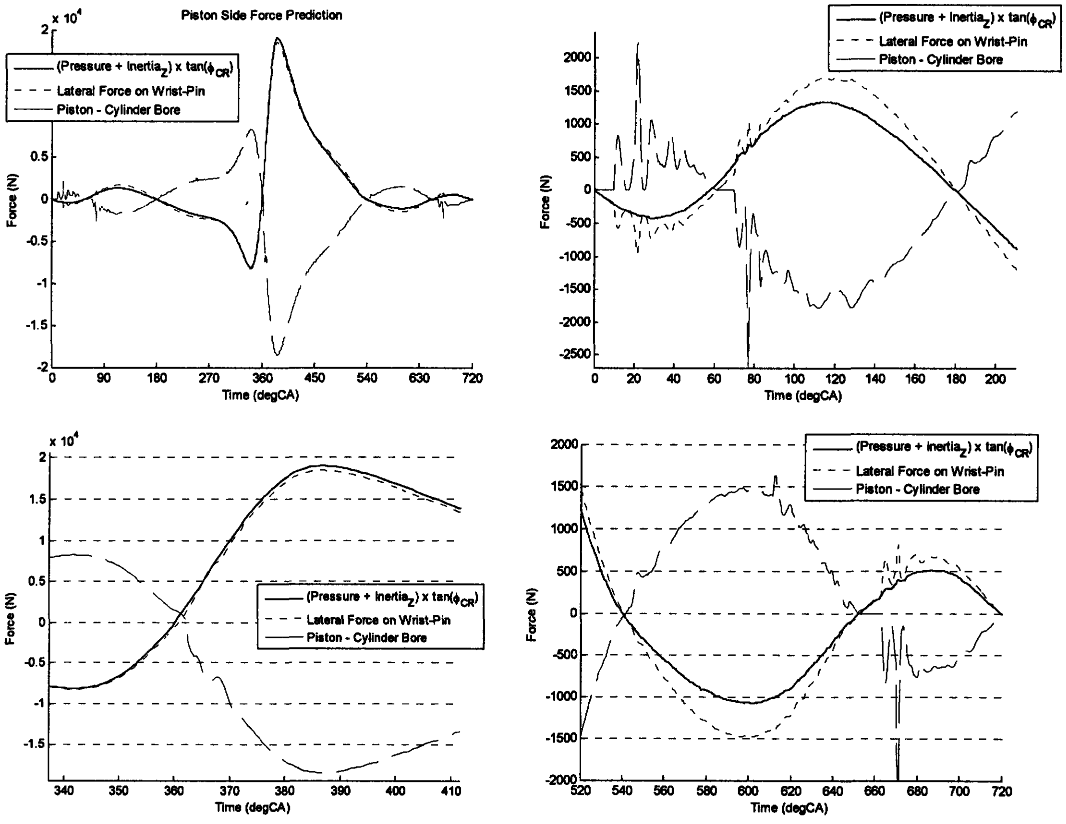

Figure 4.18: Piston Slap Timing

The side force driving the piston's motion is essentially well defined, and therefore the side force that must be generated at the piston – cylinder bore interface is well defined by the lateral force balance on the piston, as shown in Figure 4.18. The piston's inertia introduces additional fluctuations to the piston – cylinder bore interface force, and the translation of the piston across the cylinder during piston slap interrupts this force, particularly in the upper section of the cylinder bore where there are significant clearances.

A summary of the magnitude and approximate functional dependence of lateral forces acting on the piston is summarized in Table 4.8:

Force	Simplified Equation	Estimated Value
Pressure	~ Combustion pressure × Bore area × $\sin(\phi_{PS})$ ~ 150 bar × π (65 mm)^2 × sin(0.001)	~ 200 N
Inertia	~ Piston mass × Lateral Acceleration ~ 2.5 kg × 100μm / (5 °CA)^2 1200 rpm = 7200 °CA/s → 5 °CA = 6.95 × 10^{-4} s ~ 520 kg m/s^2	~ 520 N
Gravity	= Piston mass × g ~ 2.5 kg × 9.81 m/s^2	~ 25 N
Wrist-Pin	~ Pressure + Inertia Forces × $\tan(\phi_{CR})$	~ 57 kN
Cylinder Bore	~ Pressure + Inertia Forces × $\tan(\phi_{CR})$	~ 57 kN

* Wrist-pin and cylinder bore forces are overestimated due to the fact that the peak pressure force and value of $\tan(\phi_{CR})$ occur at different times.

Table 4.8: Lateral Piston Forces

Piston slap begins to occur when the side force driving the piston's motion changes sign. The timing of this sign change is well defined, as can be seen in Figure 4.18 and tends to occur for two reasons:

- The connecting-rod angle changes sign. The timing of this is a function of the engine's geometry, and for an engine with no crankshaft offset is 0, 180 , 360 and 540 °CA. There is a small shift in this timing due to the fact that the wrist-pin – connecting-rod force does not lie along the connecting-rod axis, as discussed in Section 4.1.3.
- The axial force transmitted through the components changes sign. This tends to occur mid-stroke during the intake and exhaust strokes as the inertia and pressure force terms balance, but may also occur in the compression or expansion strokes at high speed, low load running conditions. The exact timing is dependent on the pressure trace.

There is a small delay between the initiation of piston slap, and the piston actually leaving the cylinder bore surface. The piston may then translate freely across the cylinder, during which time there is no piston – cylinder bore interface force, before making contact with the other side of the cylinder bore. In cases where there is an interference fit, the piston will remain in contact with both side of the cylinder bore throughout this process. It is possible, even without an interference fit, for the piston to remain partly in contact with each side of the cylinder bore if there is sufficient tilt. Further discussion of the way in which the piston translates across the cylinder is provided in Section 4.2.3.

Although the required force at the piston – cylinder bore interface is well defined there are many uncertainties at this interface which affect the detailed distribution of the force, and therefore the piston lateral motion and tilt, as is discussed in more detail in Section 4.2. These uncertainties include:

- local surface geometry,
- asperity contact force,
- piston compliance matrix,
- friction coefficient, and
- in the case of the lubricated model, the oil film thickness.

4.1.7. Moment Balance on Piston

The friction moment transmitted to the piston, from the wrist-pin, is defined by the net force acting at the wrist-pin – piston interface, and the friction coefficient at this interface, as discussed in Section 2.3.2. This moment drives the rotational motion of the piston around combustion TDC, but throughout the rest of the cycle the moments generated at the piston – cylinder-bore interface dominate, and are balanced by the very oscillatory rotational motion of the piston as shown in Figure 4.19.

The angular position and velocity of the piston are initially unknown, and solved for iteratively based on satisfying a moment balance on the piston. The second plot in Figure 4.19 demonstrates that this balance is met to with 10^{-3} Nm.

$$I_{PS\_XX}\ddot{\phi}_{PS} = \tau_{WP/PS X} + \left\{ \begin{array}{l} \mathbf{r}_{CB/PS\_P} \times \mathbf{F}_{CB/PS} + \mathbf{r}_{P/PS\_P} \times \mathbf{F}_{P/PS} \\ + \mathbf{r}_{PS\_CG/PS\_P} \times m_{PS}\mathbf{g} - \mathbf{r}_{PS\_CG/PS\_P} \times m_{PS}\mathbf{a}_{PS\_CG/A} \end{array} \right\}_X$$

The angular acceleration of the piston is defined as:

$$\ddot{\phi}_{PS}{}^{k} = \frac{\dot{\phi}_{PS}{}^{k} - \dot{\phi}_{PS}{}^{k-1}}{t^{k} - t^{k-1}}$$

The magnitude and approximate function dependence of the moments acting on the piston are summarized in Table 4.9.

We can consider the moments acting on the piston to be of two types, as shown in Figure 4.20. Firstly, the external moments driving the piston motion, that is, the moments due to combustion chamber pressure, wrist-pin friction and gravity (negligible). In response to these moments, the piston moves and is constrained by the cylinder bore, thereby generating the moments due to inertia, interaction with the cylinder bore, and the rate of change of angular momentum of the piston.

As we approach combustion TDC, the moment due to wrist-pin friction increases significantly, and must be supported by the moments generated at the piston – cylinder bore interface, as shown in Figure 4.21. At this point, the connecting-rod is rotating clockwise, and will transmit a negative moment through the wrist-pin to the piston, rotating the piston away from the anti-thrust side of the cylinder, and shifting the normal force distribution to the lower portion of the skirt. The piston rotation continues as the piston crosses the cylinder. On making contact with the thrust side though, the moment generated by contact with the cylinder bore can become sufficiently large to dominate, controlling the piston's rotation which oscillates until the moments balance.

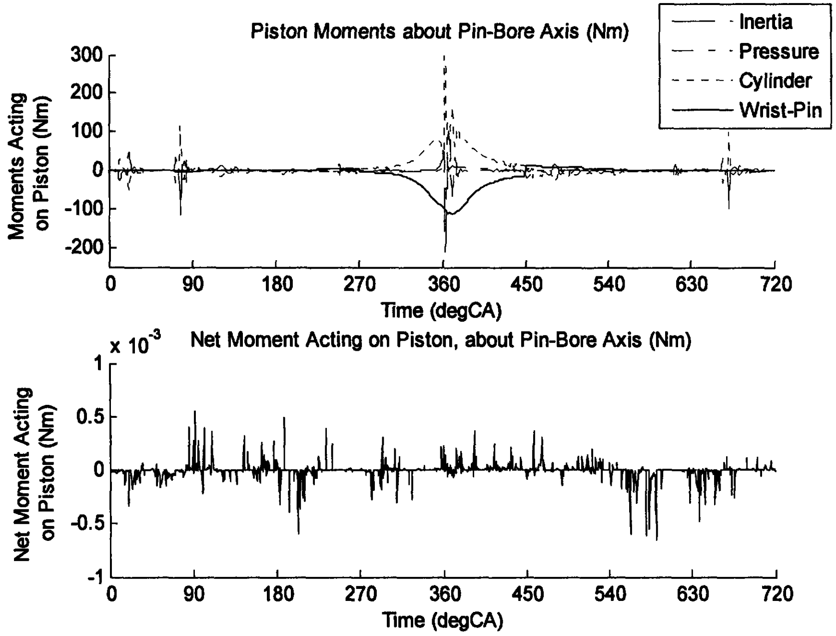

Figure 4.19: Moments Acting on Piston

Moment	Simplified Equation	Estimated Value
Wrist-Pin Moment	~ Friction Coefficient x Pressure + Inertia Forces / cos(ϕ_{CR}) x Pin radius ~ 0.02 x 200kN / 1 x 0.03m	~ 130 Nm
Inertia	~ Piston mass x Acceleration x CG radius Axial ~ 2.5 kg x (1200 rpm)^2 x 0.08m x 0.2mm Lateral ~ 2.5 kg x 100µm / (5 °CA)^2 x 36mm	~ 20 Nm
Rate of Change of Angular Momentum	~ Piston moment of inertia x Piston angular acceleration ~ 0.007 kgm^2 x 10,000 rad/s^2	~ 70 Nm
Gravity	= Piston mass x g x CG radius ~ 1.5 kg x 9.81 m/s^2 x 0.2mm	~ 0.003 Nm
Cylinder Bore Friction Moment	~ Friction Force x Piston radius ~ 0.01 x Pressure + Inertia Forces x tan(ϕ_{CR}) x 65 mm ~ 0.01 x 57kN x 65 mm	~ 40 Nm
Cylinder Bore Pressure Moment	~ Side Force x Force Radius ~ Pressure + Inertia Forces x tan(ϕ_{CR}) x 5mm ~ 57 kN x 5 mm	~ 300 Nm
Pressure Moment	~ Pressure Force x (Lateral Motion + Pin Offset) ~ 200 kN x 100 µm	~ 20 Nm

Table 4.9: Piston Moments

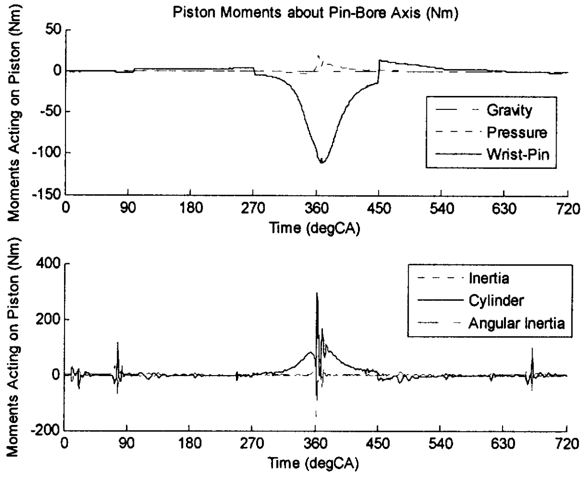

Figure 4.20: Moments Acting on Piston

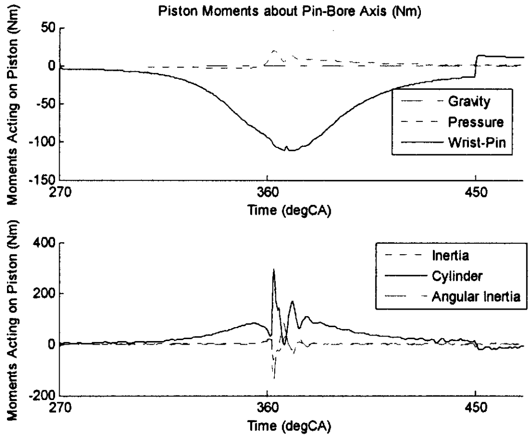

Figure 4.21: Piston Moments Close to Combustion TDC

For this particular engine, there is no wrist-pin offset, so the pressure moment is generated via two mechanisms, neither of which generate sufficient moment to significantly change the piston's motion:

- The lateral pressure force, generated due to piston tilt, acting at the distance between the wrist-pin and the piston crown.
- The axial pressure force, acting at a distance equal to the lateral motion of the piston.

When the wrist-pin is offset, the pressure moment is dominated by the component due to the axial pressure force, acting at a distance equal to the wrist-pin offset, and becomes significant around combustion TDC.

During the intake and exhaust stroke, the piston moments due to the wrist-pin, pressure force and gravity are small compared to the fluctuating moments generated at the piston –

cylinder bore interface, and the corresponding inertia moment and rate of change of angular momentum, as shown in Figure 4.22. The large fluctuations in piston – cylinder bore interface moment are generated after piston slap events as the piston impacts against the cylinder bore and tilts back and forth until a balance is found. The system's balance is also perturbed to a lesser degree by geometric features on the cylinder bore, leading to further fluctuations.

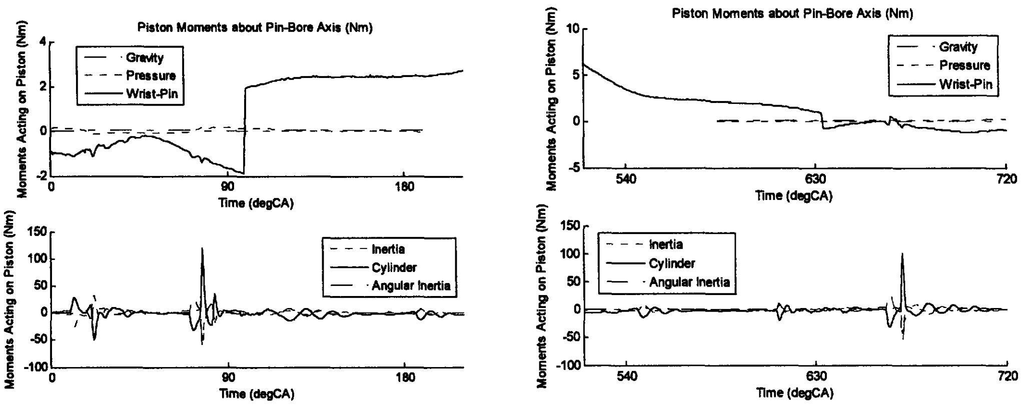

Figure 4.22: Moments Acting on Piston During Intake and Exhaust Strokes

Separating the moment generated at the piston – cylinder bore interface into the components due to the normal and friction forces at this interface it becomes apparent that the friction force, which acts at a distance equal to the piston radius, results in a moment which is relatively smooth and unaffected by piston tilt, as expected. In contrast, the point of action of the normal force is dependent on the detailed local geometry, which is in turn affected by piston tilt, and fluctuates significantly throughout the cycle. It can be seen, however, that the mean line of the moment generated by the normal force acts to balance the friction moment during the intake and exhaust strokes, and close to combustion TDC their combined effect will balance the wrist-pin moment.

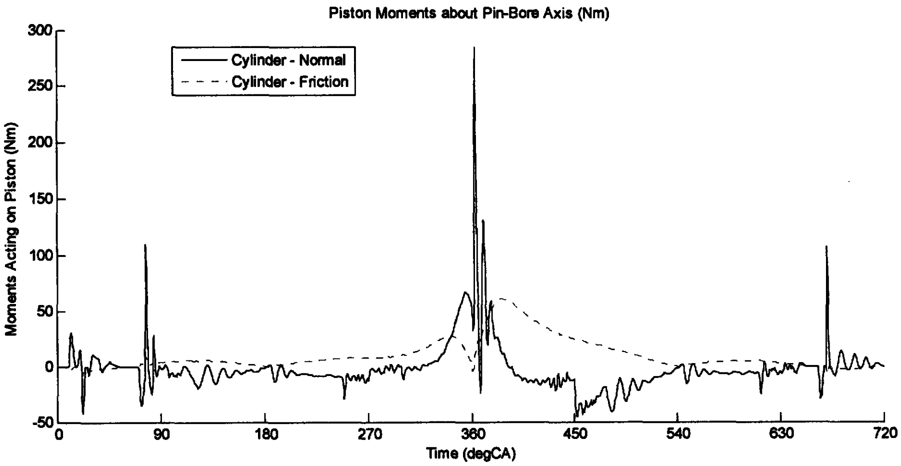

Figure 4.23: Piston – Cylinder Bore Moments

There are significant uncertainties in most of the moments acting on the piston:

- The wrist-pin friction coefficient is not well known, and its variation significantly impacts the wrist-pin moment which drives piston tilt around combustion TDC. This is discussed in more detail in Section 4.4.2.
- The pressure moment is a strong function of piston tilt, but does not become significant unless there is wrist-pin offset.
- The friction coefficient at the piston – cylinder bore interface is not well defined, and significantly impacts moment balance throughout the cycle, as discussed further in Section 4.4.1.
- The point of action of the normal force at the piston – cylinder bore interface is highly dependent on the detailed local geometry, interface model, and piston tilt. This point of action, combined with the piston's motion, is responsible for maintaining the moment balance, and therefore its equilibrium value is defined by the other moments.

4.2. Piston and Wrist-Pin Motion

4.2.1. Lateral Motion

The lateral motion of the piston is driven by the wrist-pin lateral force, and constrained by the piston – cylinder bore interface. As discussed in more detail in Section 4.1.6, the side force is essentially a function of the axial pressure load on the piston and the connecting-rod angle, with shifts due to component inertias. It is expected that the side force on the piston will change sign for two reasons:

- When the connecting-rod angle changes sign, which for an engine with no crankshaft offset is at 0, 180, 360 and 540 °CA, as shown in Figure 4.24.

$$\phi_{CR} = \arcsin\left[\frac{y_{CSO}}{l_{CR}} - \frac{r_{CS}}{l_{CR}}\sin(\theta_{CA}) - \frac{x_{Py}}{l_{CR}}\right]$$

- When the axial load on the connecting-rod changes from compression to tension, which is determined by the pressure trace and component inertias, as discussed in detail in Section 4.1.4, and typically occurs about mid-stroke during the intake and exhaust strokes. In Figure 4.24, we can see that for this running condition, mid-stroke piston slaps occur at 55°CA and 660°CA. For higher speed, or lower load, conditions mid-stroke piston slap can also occur during the compression and expansion strokes.

The timing of these changes in side force direction are well defined to sufficient degree of accuracy by the current dry model, and as shown in Figure 4.24, the piston translates across the cylinder bore at the expected crankshaft angles, and lies against the correct side of the cylinder bore.

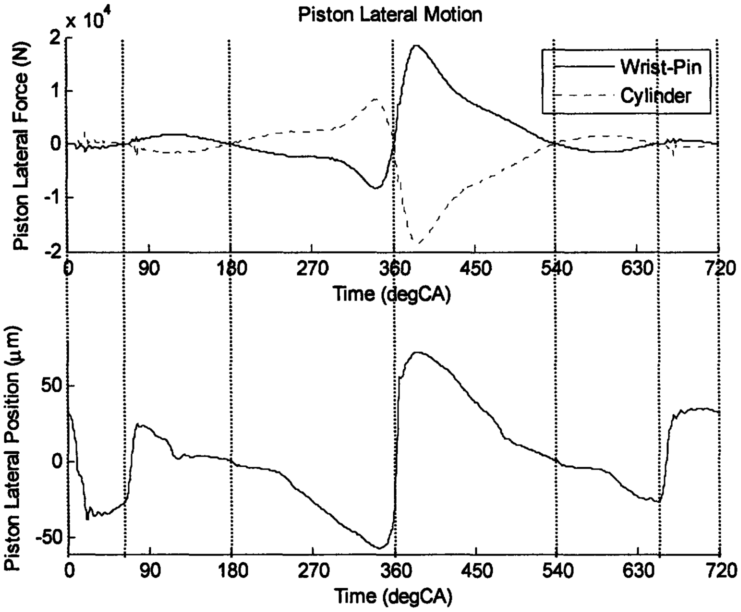

Figure 4.24: Timing of Piston Lateral Motion

While the timing of piston slaps, and the side of the cylinder against which the piston should rest, are well defined, the detailed lateral position is much more complicated. In a general sense, the lateral motion of the piston is a function of the local piston – cylinder bore clearance, and the side force acting on the piston.

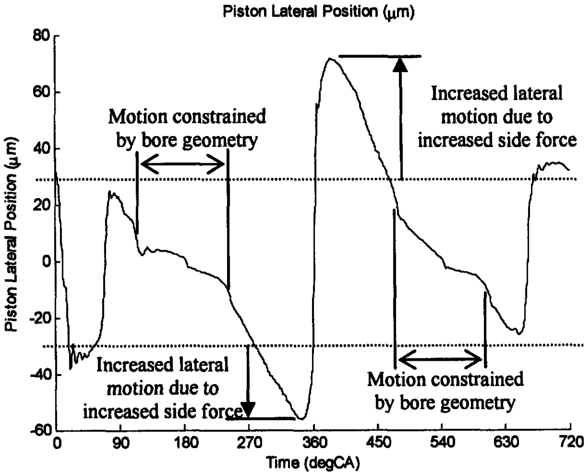

Figure 4.25: Piston Lateral Motion

We therefore expect that:

- In the upper portion of the bore (~ 270-450°CA and ~ 630-90°CA), where thermal expansion leads to significantly higher piston – cylinder bore clearances, lateral motion increases.
- In the lower portion of the bore (~ 90-270°CA and ~ 450-630°CA), where there is less thermal expansion, and smaller piston – cylinder bore clearances (for this running condition a slight interference fit), lateral motion is reduced, and in cases where there is significant interference, reduced to extent allowed by piston deformation due to the net side force.
- At lighter loads (during the intake and expansion strokes), there is very little piston deformation and the lateral motion is roughly determined by the piston – cylinder bore clearance, as shown in Figure 4.26.
- At higher loads (during the compression and expansion strokes), the piston skirt deforms significantly due to both the piston – cylinder bore interface normal force, and due to the combustion pressure load, and significantly higher lateral motions are obtained.

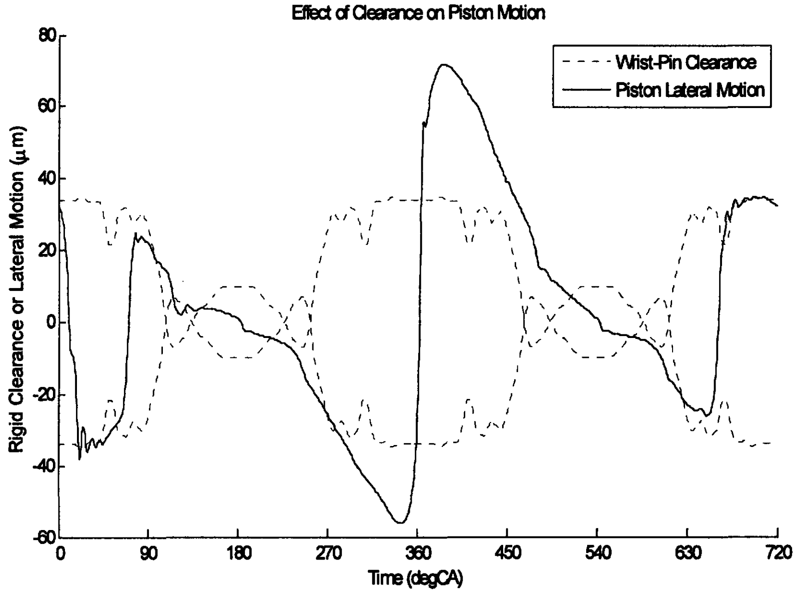

Figure 4.26: Piston Lateral Motion

Figure 4.26 compares the rigid clearance at a position on the piston skirt level with the wrist-pin to the piston lateral motion. The wrist-pin clearance appears to be the most appropriate point of comparison as the point of action of the normal contact force generally needs to be close to here in order to balance the friction moment. Obviously the length of the load bearing portion of the piston is significant, and therefore the clearance at a single point is not sufficient alone to predict lateral motion.

- At low loads during the intake and exhaust strokes, the piston lateral motion matches the wrist-pin clearance very closely in the upper portion of the bore.
- As the lower portion of the skirt reaches the interference region, the lateral motion is reduced, and the piston tilts.

- As the wrist-pin passes the interference region, piston tilt allows more lateral motion than the wrist-pin clearance predicts.
- At the piston's lowest positions, the upper portion of the piston is still in contact with the contact region, reducing lateral motion below the level predicted by the wrist-pin clearance.
- At high loads, significantly higher lateral motion occurs due to piston deformation.

More accurate prediction of piston lateral motion requires a detailed knowledge of:

- Local cylinder bore and piston geometries,
- Asperity contact and friction coefficient models,
- Piston deformation,
- Oil film thickness and pressure distribution,
- Piston tilt, which can significantly alter the gap height distribution.

Each of these parameters introduces significant uncertainty into the model. Variations in the piston and bore geometries are investigated in more detail in Sections 4.4.3 and 4.4.4, where it is shown that piston – cylinder bore clearance has a direct impact on lateral motion while the piston profile and cylinder bore gradient tend to affect lateral motion via changes in tilt.

The effect of variations in the friction coefficient at the piston-cylinder bore interface, on lateral motion, are found to be small, as discussed in more detail in Section 4.4.1.

The effect of an oil film is discussed in the lubricated system model sections of this report. It is expected that the presence of oil may reduce the effect that the detailed local geometries and friction have on piston motion, and that the dry model results represent, in most cases, the maximum possible lateral motion.

4.2.2. Tilt

Piston tilt is determined by the moment balance on the piston, about the wrist-pin axis. As discussed in Section 4.1.7, the wrist-pin friction moment tends to drive piston rotational motion approaching combustion TDC, while the friction and normal moments at the piston – cylinder bore interface, combined with the piston's rotational inertia, determine the tilt during intake and exhaust strokes, and all four are significant during combustion. In some cases, particularly when there is wrist-pin offset, the combustion chamber pressure moment also significantly affects piston tilt around combustion TDC, and can be used to counter-act the wrist-pin moment.

Approaching combustion TDC, the connecting-rod is rotating clockwise (negative), and drives both the wrist-pin and the piston to rotate clockwise, decreasing piston tilt. The large loads on the wrist-pin bearings at this point result in a large negative moment being applied to the piston. At TDC the side force on the piston goes to zero and piston slap is initiated. As the piston travels across the cylinder bore it rotates rapidly clockwise until contact is made on the upper portion of the skirt, generating a very large positive moment, which in turns results in rapid, anticlockwise rotation of the piston and brief oscillation until the tilt reaches a stable positive tilt.

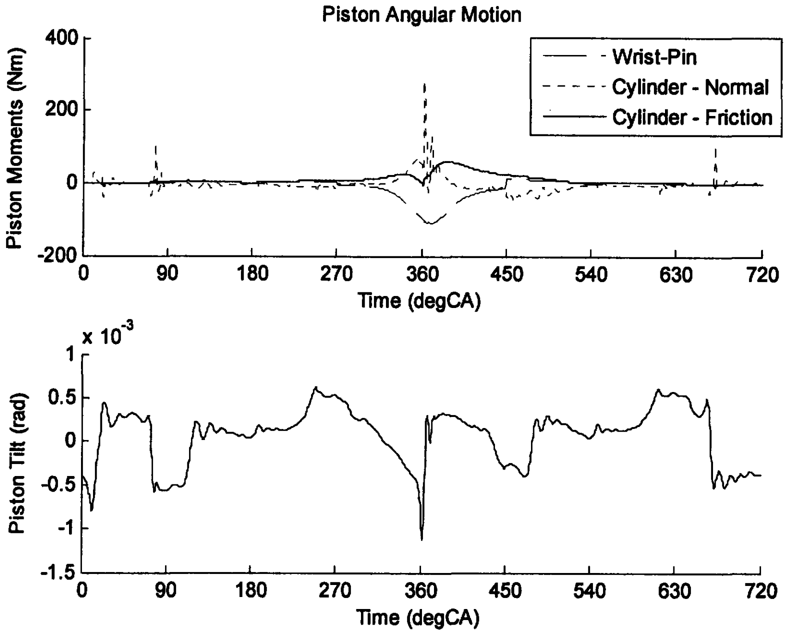

Figure 4.27: Piston Tilt

Piston tilt throughout the rest of the cycle is determined by the balance of normal and friction moments created at the piston – cylinder bore interface, and the piston's rotational inertia. This balance is very sensitive to the point of action of the normal force at the piston – cylinder bore interface, which in turn is dependent on the local geometry. Oscillations occur as the piston hits the cylinder bore at an angle, then rotates, over correcting, to find its balance point. To complicate matters further, the piston profile is significantly changed by radial deformation due to combustion chamber pressure, axial inertia, and contact with the cylinder-bore.

In the absence of significant wrist-pin and pressure moments, the "stable" piston tilt (neglecting oscillations) is therefore a function of:

- Deformed piston geometry: The location of the minimum clearance point and the slope of the profile determine the amount of tilt required to shift the point of action of the contact force, as described in more detail in Section 4.4.3.
- Cylinder bore geometry: Variations in bore geometry are investigated in more detail in Section 4.4.4, where it is shown that the average cylinder bore gradient, over the load bearing area of the piston, significantly contributes to piston tilt.
- Piston – cylinder bore friction coefficient: Around combustion TDC, the significant friction moments generated affect piston tilt, as discussed in more

detail in Section 4.4.1, while throughout the rest of the cycle it was found to have very little effect.

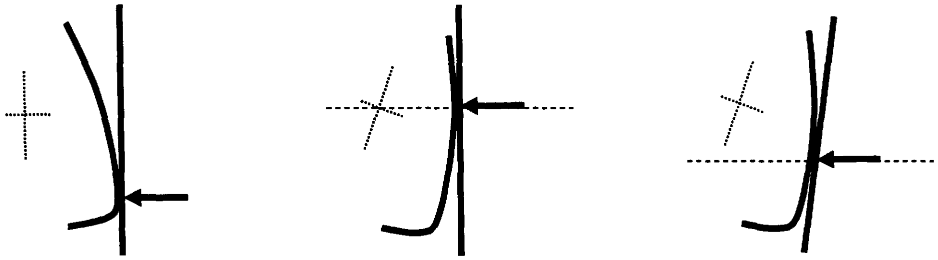

No friction, flat bore, no tilt: Negative moment generated due to piston profile. →

Negative tilt required to achieve zero moment →

Negative bore angle results in negative moment

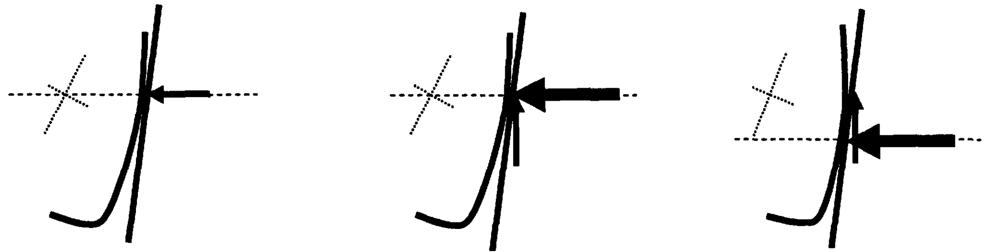

→ Larger negative tilt required to achieve zero moment →

Friction force creates positive moment →

Less negative tilt required to balance friction force and result in zero net moment

Figure 4.28: Stable Piston Tilt

4.2.3. Piston Secondary Motion

The piston secondary motion, combining lateral motion and piston tilt, and the effects of piston geometry and deformation, cylinder geometry, and side force, are best demonstrated pictorially.

At the beginning of the cycle the piston is resting against the thrust side of the bore, leaning toward the thrust side (negative tilt). The side force on the piston changes sign at TDC and the piston begins to move toward the anti-thrust side, with a slight rotation towards the thrust side as it translates across the cylinder bore, due to the wrist-pin moment, making contact on the lower portion of the skirt.

Significant piston tilt oscillation occurs as the piston rotates against the cylinder bore until a stable positive tilt is reached. The side load on the piston is small at this point, resulting in very little piston deformation, and the relatively constant bore gradient leads to a reasonably constant tilt value until around 67°CA, after the side force has changed sign, when the piston leaves the anti-thrust side.

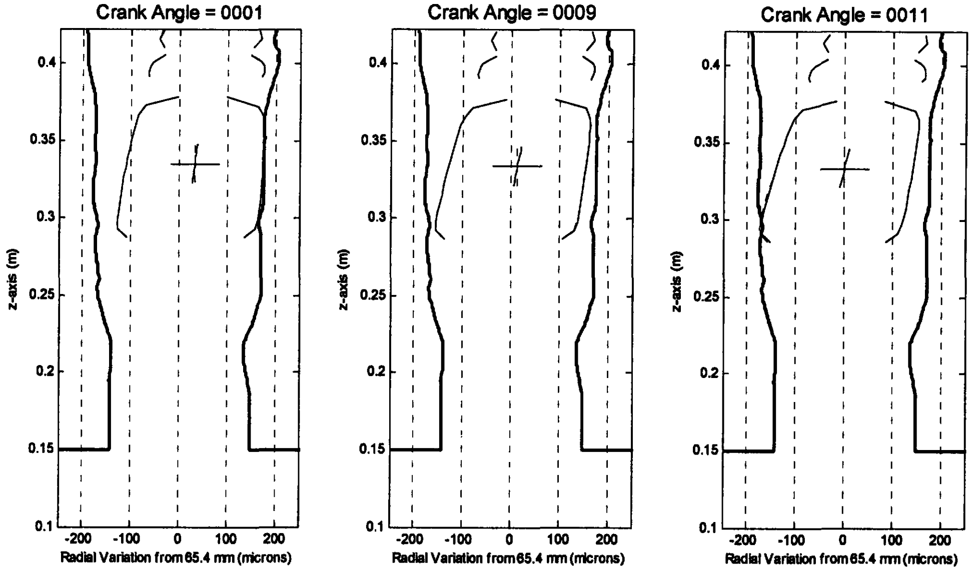

Figure 4.29: Piston Secondary Motion 0-11°CA

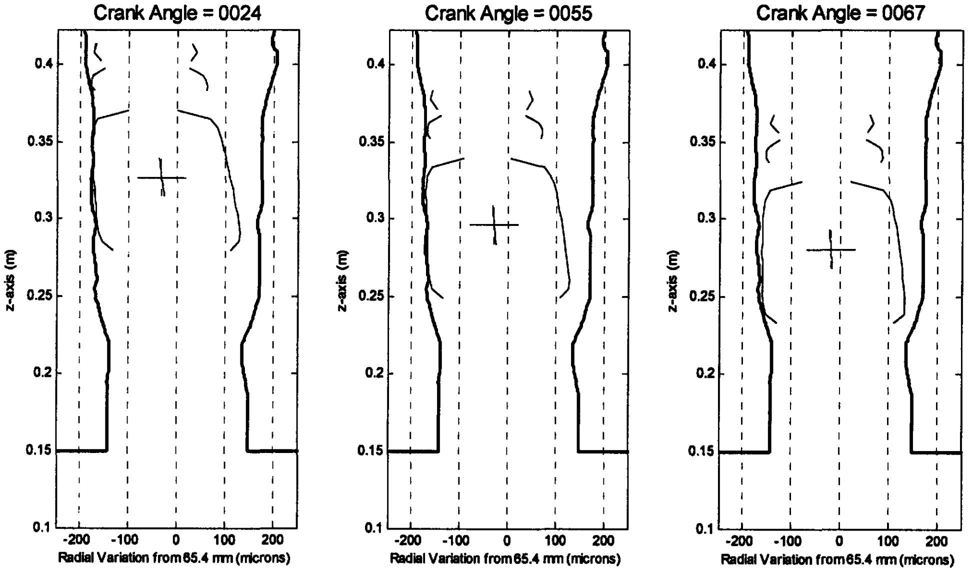

Figure 4.30: Piston Secondary Motion 24-67°CA

The piston translates across the cylinder with essentially no rotation, due to the fact that the axial force and therefore wrist-pin moment are both zero at this point, making contact on the thrust side with the lower portion of the skirt. The piston then rapidly tilts toward the thrust side, and settles after oscillation into a negative stable tilt. As the piston moves further down the bore, the bore narrows, resulting in contact on both sides of the piston, and deformation of the lower portion of the piston skirt.

As the piston moves into the lower portion of the bore, the interference fit results in significant deformation of the piston skirt and reduced lateral motion and tilt.

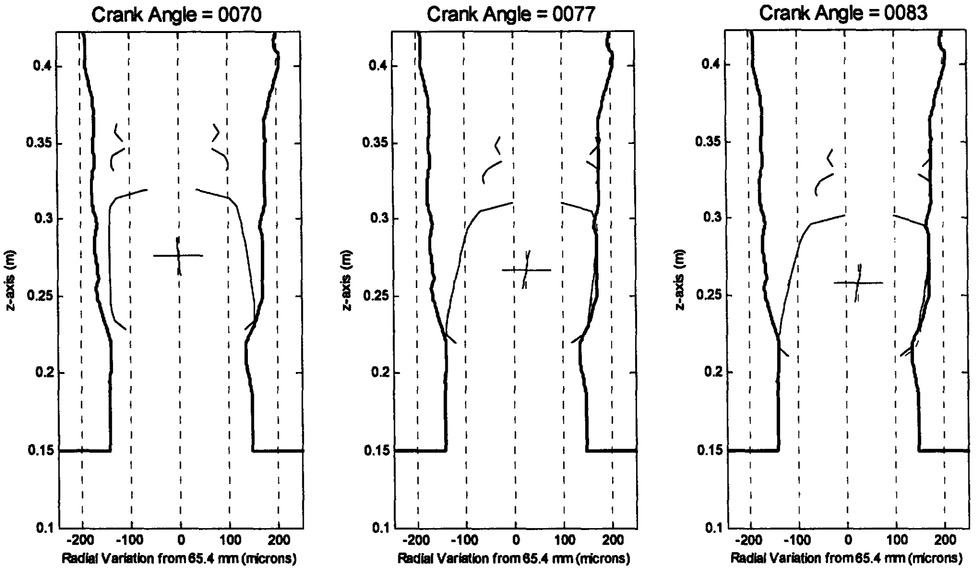

Figure 4.31: Piston Secondary Motion 70-83°CA

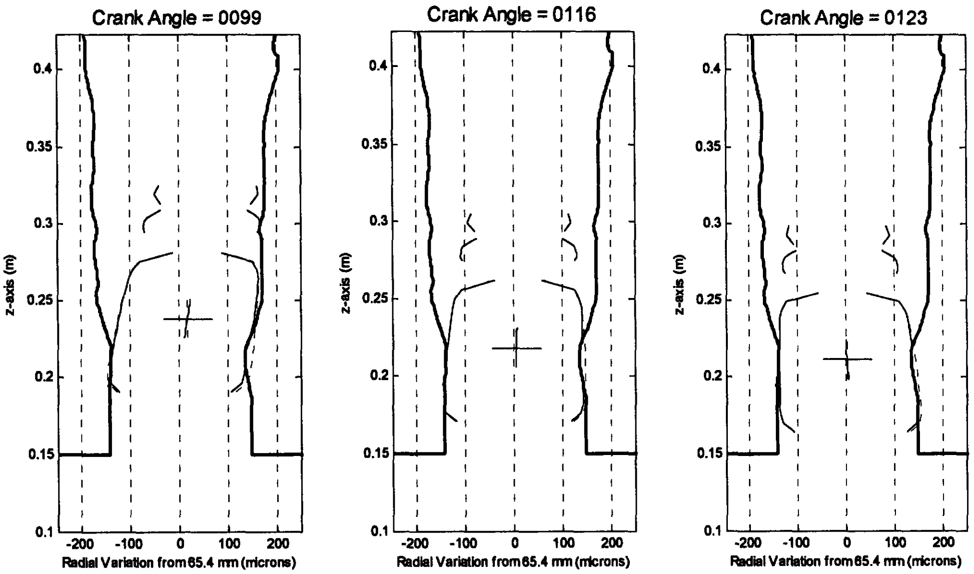

Figure 4.32: Piston Secondary Motion 99-123°CA

At 180°CA the side force changes direction, and the piston moves slightly to the anti-thrust side, where it remains for the compression stroke. Moving back up the bore, the lateral motion and tilt are initially constrained by the interference fit, with significant deformation of the anti-thrust side of the skirt.

With increasing side force, lateral motion increases, leading to larger deformations on the anti-thrust side and allowing more tilt. As the piston moves out of the interference region, lateral motion increases significantly, and the tilt initially decreases due to a decrease in bore gradient.

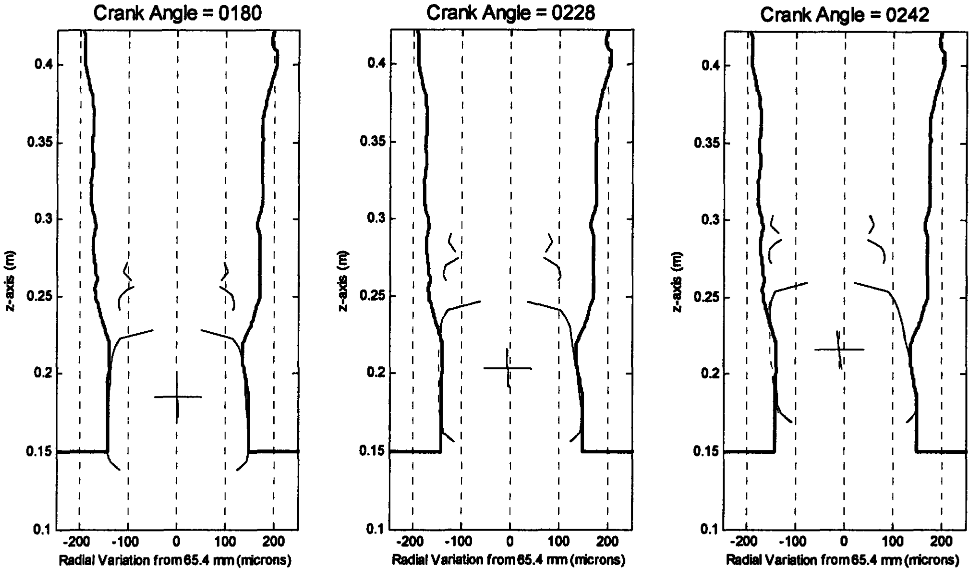

Figure 4.33: Piston Secondary Motion 180-242°CA

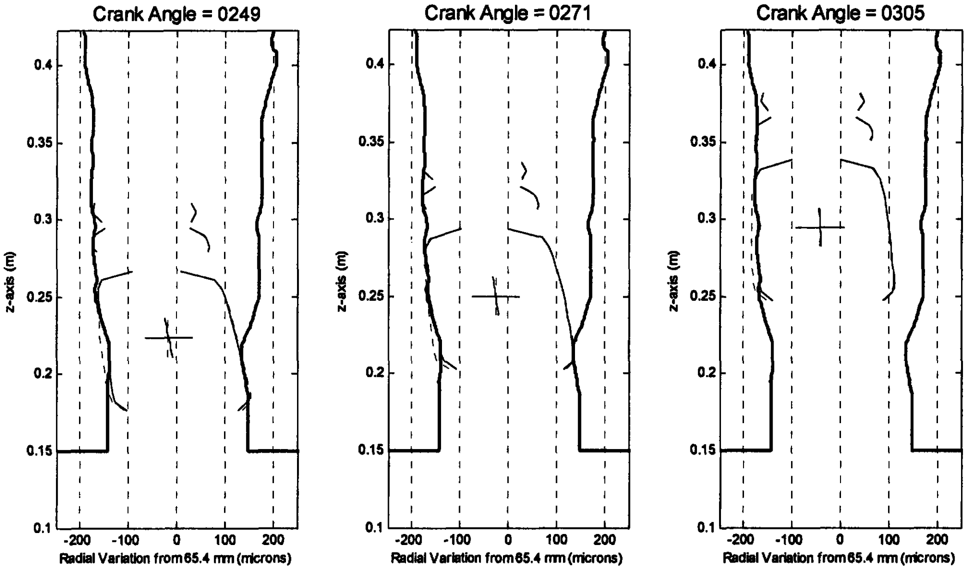

Figure 4.34: Piston Secondary Motion 249-305°CA

The piston tilt continues to decrease due to the combination of skirt deformation and the gradually increasing wrist-pin moment, resulting in a negative piston tilt (crown towards the thrust side) by combustion TDC.

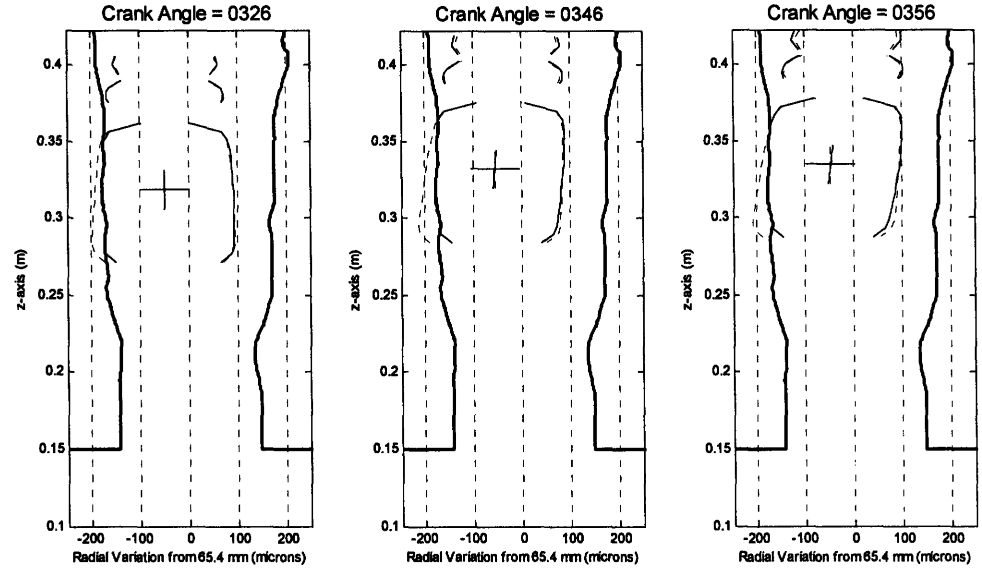

Figure 4.35: Piston Secondary Motion 326-356°CA

The piston moves rapidly across the cylinder at combustion TDC, rotating towards the thrust side, due to the wrist-pin moment, and contacting on the crown land before the lower portion of the skirt leaves the anti-thrust side. The piston then rotates rapidly towards the anti-thrust side, shifting the thrust side contact down the piston, and oscillates until a stable tilt is found. There is substantial piston deformation, not only on the thrust side skirt due to interaction with the cylinder bore, but also on the land and anti-thrust side due to the inertia and combustion pressure loads.

As the piston moves down the bore, the large side loads cause significant deformation of the piston skirt, resulting in an altered piston profile, and corresponding positive tilt which decreases along with lateral motion as the load is reduced. The combined effects of bore geometry and reduced load lead to a negative tilt around 445°CA.

Towards the end of the expansion stroke, as the side load and correspondingly lateral motion decreases, the piston behavior is similar to during the intake stroke, with the piston tilting around the large bore feature, and then settling into a neutral position at BDC.

The exhaust stroke can be analyzed in a similar manner.

Piston slap can be loosely separated into five stages:

1. Side force sign change: The onset of piston slap begins when the net external side force acting on the piston (typically wrist-pin force) changes sign.

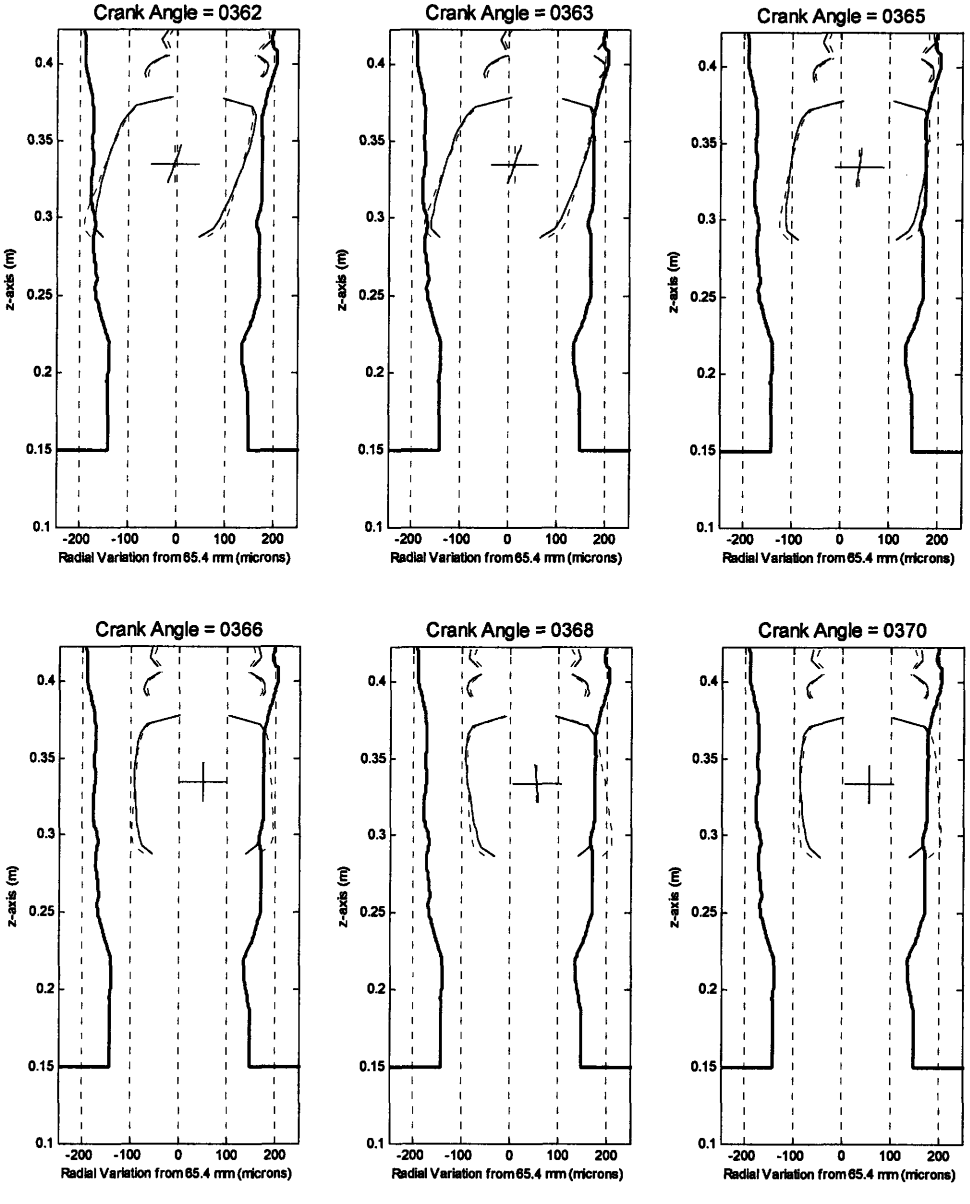

Figure 4.36: Piston Secondary Motion 362-370°CA

2. Piston leaves bore: A significant delay may occur between the force sign change and the piston leaving the surface of the cylinder bore due to:
   - Piston inertia
   - Piston rotation, which will continue to occur throughout piston slap in response to the moment balance, and may keep the piston in contact with the bore for longer than a simple translation.
3. Translation across the bore: During translation across the cylinder bore there is no force generated by the piston – cylinder bore interface. The piston is accelerated by the net external side force, and rotated by the net external moment, which is provided by the wrist-pin pressure moments at the end of each stroke,

but essentially zero during mid-stroke piston slaps. The time taken to translate is dependent on:

- Rate of acceleration, which is determined by the external side force
- Local piston – cylinder bore clearance.
- Piston tilt significantly alters the effective width of the piston and therefore the clearance.

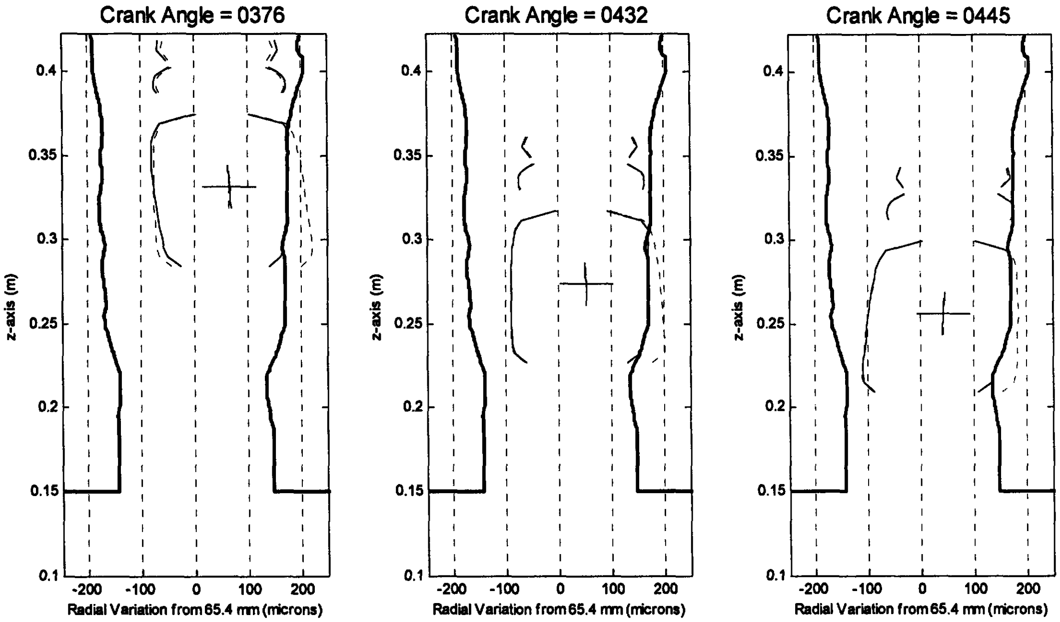

Figure 4.37: Piston Secondary Motion 376-445°CA

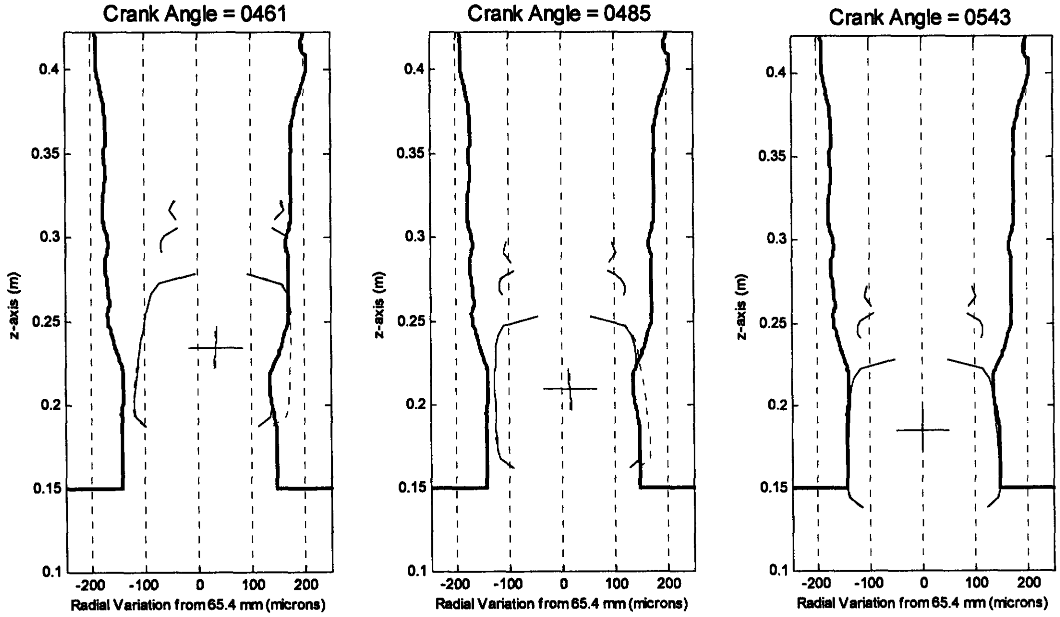

Figure 4.38: Piston Secondary Motion 461-543°CA

4. Initial contact: The location of initial contact is dependent on the piston and bore geometry, and the piston tilt at time of contact. Piston tilt at the time of contact is dependent on:
    - Piston tilt as piston leaves bore.
    - Rotation during piston slap, which is essentially zero for mid-stroke piston slaps, and driven by the wrist-pin and pressure moments at TDC and BDC.
5. Stable position reached: After making contact the piston lateral motion and tilt oscillate as the piston bounces and rotates until a relatively stable position is found.

For small clearances, though, the piston may not be able to freely translate across the bore, and with more extreme interferences fits it may remain in contact with both sides of the cylinder bore throughout piston slap.

As the piston moves along the bore in between piston slaps, the lateral motion is directly a function of the local clearances and piston deformation while the piston tilt tends to be governed by a combination of piston geometry, average bore gradient, piston-cylinder bore friction force and, close to combustion TDC, the wrist-pin moment.

4.3. Other Degrees of Freedom

The power cylinder system components are currently considered to carry out two-dimensional planar motion. In the physical system, however the piston is able to move a small amount along the pin axis and to rotate about the cylinder and thrust axes, as constrained by its connection to the wrist-pin. A rough estimate of the magnitude of the driving force and moments for these motions can be provided by the model.

4.3.1. Motion along pin axis

For a symmetric piston and bore, there should be no net force generated along the pin axis. Bore distortion, and possibly asymmetries of the piston, can lead to asymmetric contact pressure distributions at the piston – cylinder bore interface, resulting in an imbalance in the forces in this direction, as shown in Figure 4.39.

It is expected that, in the physical system, small motions in this direction would allow the balance to be restored, resulting in a much smaller net force being transmitted to the pin.

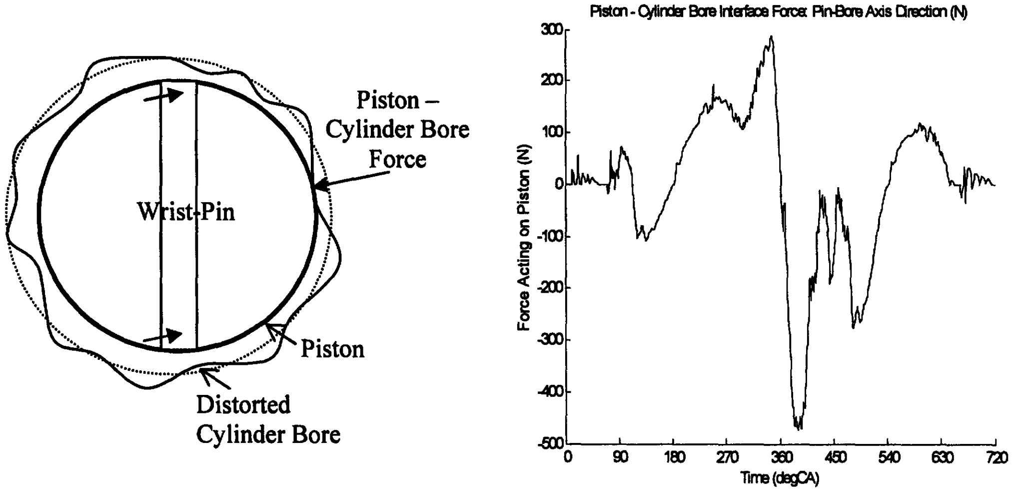

Figure 4.39: Net Force Along the Pin Axis

4.3.2. Rotation about cylinder axis

The same asymmetries and geometric variations that lead to a net force along the pin axis, as described above in Section 4.3.1, can result in a net moment about the cylinder axis, as shown in Figure 4.40, as does the location of the piston centre of gravity.

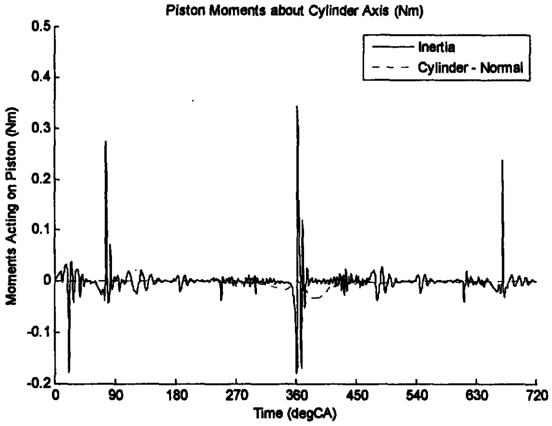

Figure 4.40: Net Moment About the Cylinder Axis

Once again, it is expected that small motions along the pin axis, combined with very small rotations about the cylinder axis would correct this imbalance, significantly reducing the forces transmitted to the wrist-pin.

4.3.3. Rotation about thrust axis

The same asymmetries and geometry variations that lead to a net force along the pin axis, as described above in Section 4.3.1, can also result in normal and friction forces which generate a net moment about the thrust axis, as shown in Figure 4.41, as well inertia moments due to the offset location of the piston centre of gravity.

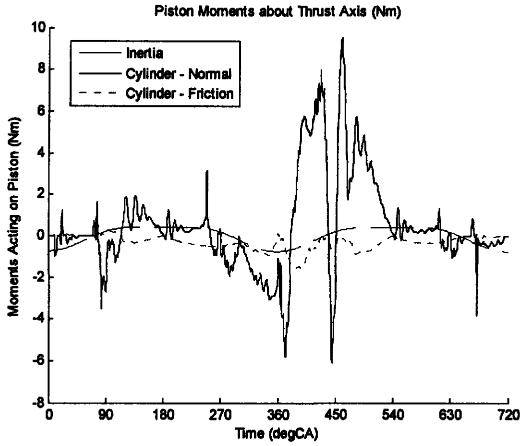

Figure 4.41: Net Moment About the Thrust Axis

Once again, it is expected that small motions along the pin axis, combined with very small rotations would correct this imbalance, significantly reducing the moments about the thrust axis.

4.4. Effect of Parameter Uncertainties on Piston Dynamics

Four main areas of uncertainty are investigated in this section in order to determine their importance in accurately predicting piston dynamics:

- Piston – Cylinder Bore Friction Coefficient, which for the dry model is not well defined as it is expected that in the physical system lubricating oil will support part of the load, and reduced asperity contact and friction generation.
- Wrist-Pin Friction Coefficient, which in the absence of a detailed bearing model, is not well defined.
- Piston Geometry, which varies in normal operation through a range of profiles due to temperature variations and the corresponding thermal deformations.
- Cylinder Bore Geometry, which also varies due to thermal deformation, and must take into account bore distortions due to manufacture and assembly.

4.4.1. Piston – Cylinder Bore Friction Coefficient

The piston-cylinder bore friction coefficient has two possible effects:

- Shifting the axial force balance on the piston, which is very unlikely in the absence of a large amount of piston – cylinder bore interference.
- Changing the friction moment generated at the piston – cylinder bore interface, and therefore the piston moment balance, piston tilt and lateral motion.

Results for a running condition with a small amount of interference (1200 rpm, 2200 Nm), and a range of piston – cylinder bore friction coefficients are shown in Figures 4.42 and 4.43. Figure 4.42 demonstrates that, despite significant changes in the axial friction force exerted on the piston, there is no significant change to the wrist-pin – piston axial force, nor to the wrist-pin – piston lateral force and piston lateral motion.

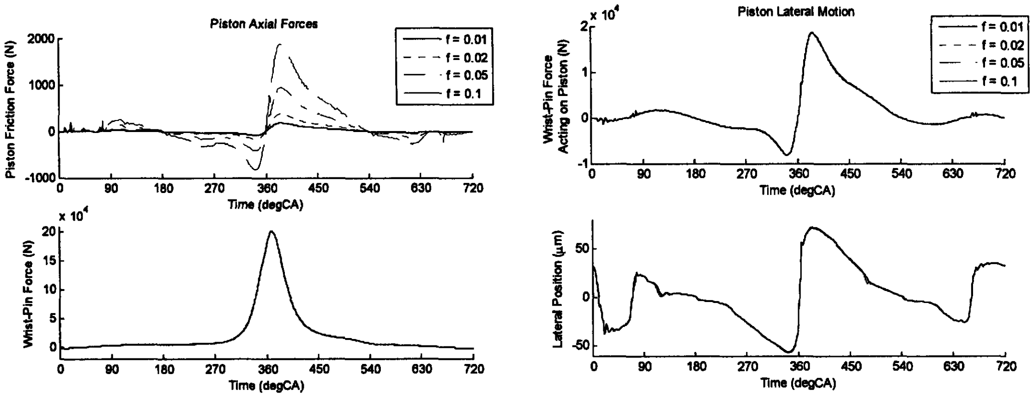

Figure 4.42: Effect of Piston Friction Coefficient on Lateral Motion

With no change to the wrist-pin – piston forces, there is correspondingly no change in the corresponding wrist-pin moment, as shown in Figure 4.43. There are, however, significant variations in the friction moment generated at the piston - cylinder bore interface, and these changes must be balanced by the moments generated by the normal force at this interface, and the piston's motion. The resulting changes in piston tilt are significant, but do not change the overall direction or character of the piston's rotational motion, and are not sufficient to impact the piston's lateral motion.

It was expected that the effect of the piston friction coefficient on piston dynamics may change when there is a large amount of interference, but this was found not to be the case. The following results are for a preheated, and therefore significantly larger piston, at 1200rpm, 1500Nm. There is a large amount of interference throughout the lower half of the stroke, resulting in a significant increase in the friction force on the piston, as shown in Figure 4.44. The variations in friction are not sufficient to significantly impact the lateral force transmitted from the wrist-pin to the piston though.

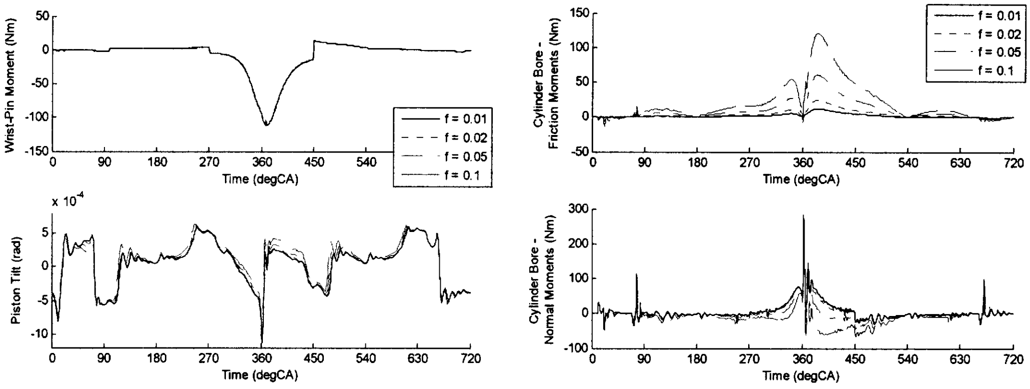

Figure 4.43: Effect of Piston Friction Coefficient on Piston Tilt

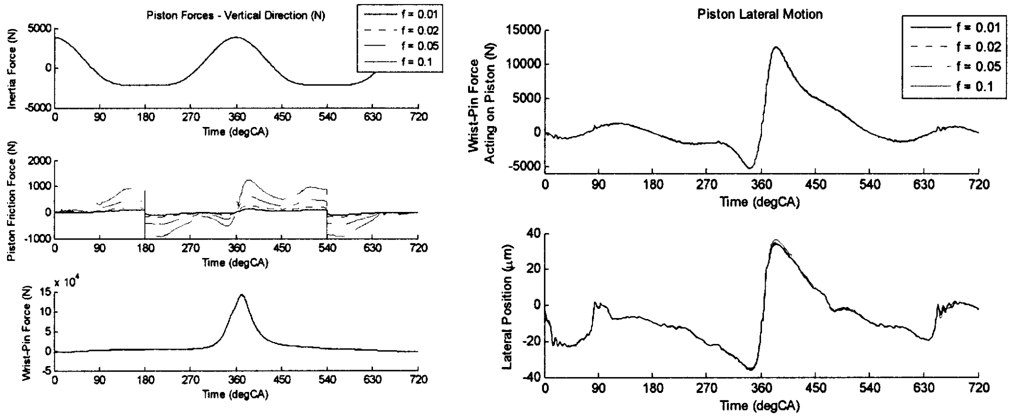

Figure 4.44: Effect of Piston Friction Coefficient with an Interference Fit

The corresponding wrist-pin moment is also unchanged over the range of friction coefficients, and the variations in piston tilt are limited to the region around combustion TDC, as shown in Figure 4.45. The changes in this region are similar to the case without significant interference, as the interference fit does not extend to this region.

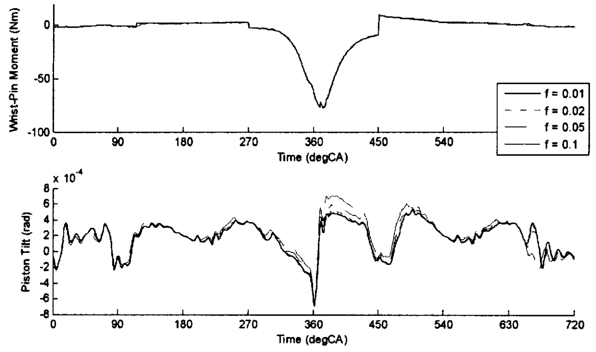

Figure 4.45: Effect of Piston Friction Coefficient on Piston Tilt

The reason for the lack of system dynamic response to friction coefficient through the interference fit region is due to the fact that when the piston is constrained tightly by the bore, normal and friction forces are generated on both sides of the piston. The moments tend to balance each other, so that the net result is relatively independent of friction coefficient throughout the interference region. The system dynamics therefore respond in a similar manner to the piston – cylinder bore friction coefficient with or without a significant interference fit.

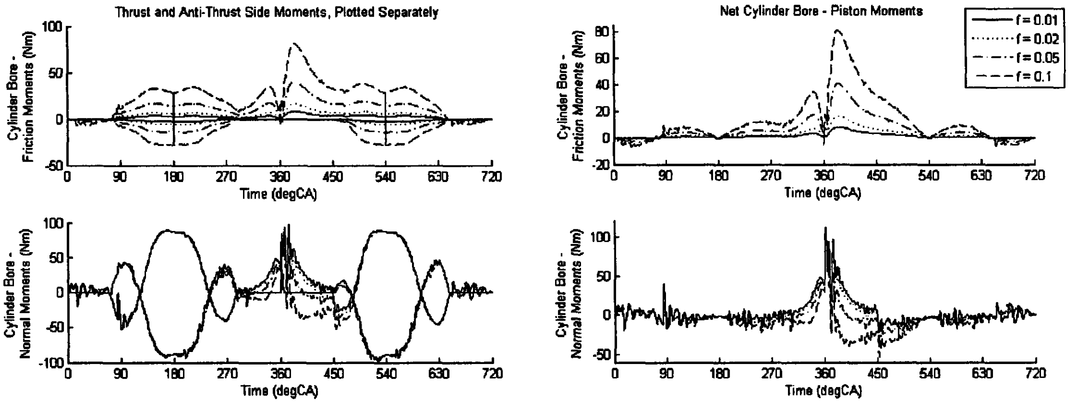

Figure 4.46: Effect of Friction Coefficient on Cylinder Bore – Piston Moments.

In the absence of severe interference between the piston and cylinder bore, the piston-cylinder bore friction coefficient does not significantly affect the axial force balance on the piston, and therefore does not affect the wrist-pin – piston force and moment. The piston – cylinder bore friction coefficient does, however, significantly affect the friction moment generated at the piston – cylinder bore interface, and therefore alters the moment balance on the piston, resulting in small changes to piston tilt, particularly around combustion TDC, and to a lesser degree, to lateral motion.

4.4.2. Wrist-Pin Bearing Friction Coefficient

The wrist-pin bearing friction coefficients determine the moments generated at the connecting-rod – wrist-pin and piston – wrist-pin interfaces. In the case where the two friction coefficients are similar, the friction moment generated at the connecting-rod – wrist-pin interface, due to the load on this interface, is transmitted to the piston – wrist-pin interface, with a small alteration due to the wrist-pin moment of inertia. The friction moment generated at the piston – wrist-pin interface becomes significant in determining piston tilt around combustion TDC. Increasing the friction coefficient increases the negative moment generated, and therefore decreases piston tilt in this region, as shown in Figure 4.47. For high levels of friction, the moment generated is sufficient to prevent the piston tilt from becoming positive during piston slap.

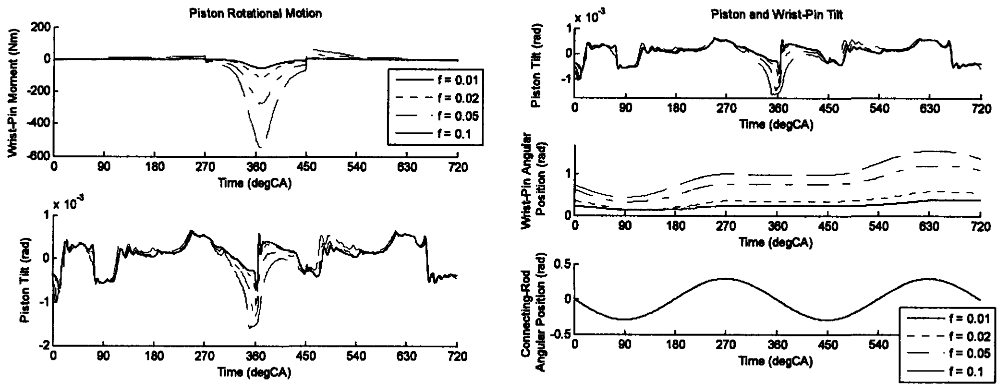

Figure 4.47: Effect of Wrist-Pin Friction on Component Angular Motion

Such large changes in tilt are very significant, affecting piston-cylinder bore clearances, particularly on the piston lands, and altering lateral motion, as shown in Figure 4.48. Piston tilt around combustion TDC is critical in determining the timing and point of impact for piston slap, thereby significantly effecting noise and oil transport.

The wrist-pin friction coefficient also impacts that connecting-rod moment balance, and therefore the lateral force transmitted to the piston, as shown in Figure 4.48. The piston lateral position is affected by both the side force, and the piston tilt, resulting in a significant reduction in peak lateral motion with increased friction coefficient.

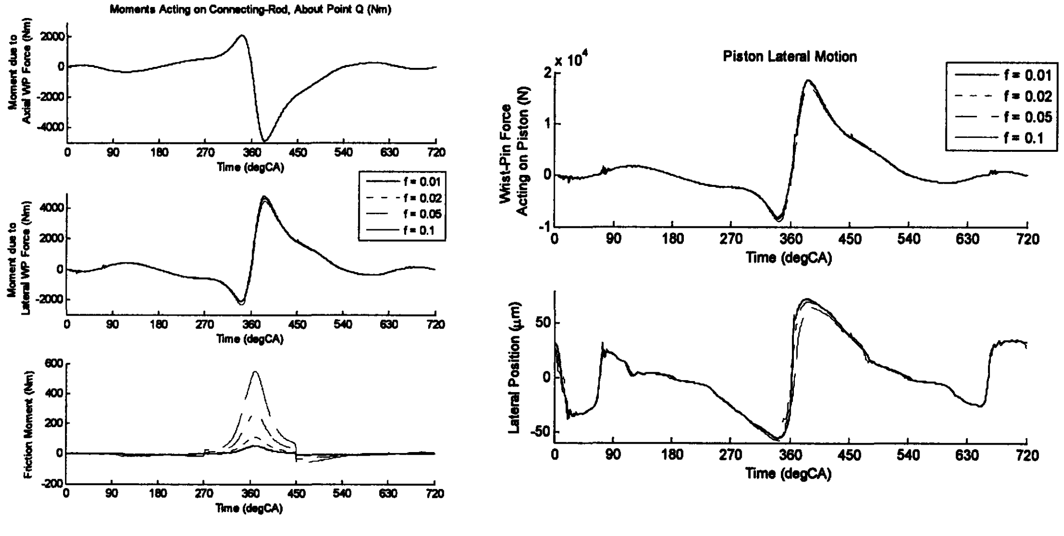

Figure 4.48: Effect of Wrist-Pin Friction on Force Generation and Lateral Motion

In the case where the friction coefficients are very different, it is not possible for the difference in moments to be balance by the wrist-pin's rotational inertia. Small differences in the friction moments are initially balanced by the rate of change of angular momentum of the wrist-pin, as the wrist-pin accelerates to follow the component with the highest friction moment. As the angular velocity of the wrist-pin approaches that of the driving component, though, the friction coefficient at this interface will decrease, thereby achieving the moment balance. The wrist-pin will therefore travel with the component with the highest friction coefficient, as shown in Figure 4.49, thereby reducing the friction coefficient at that interface so that the moment balance is achieved. The moment transmitted to the piston is therefore a function of the load on the wrist-pin, and the minimum of the two nominal friction coefficients, as shown in Figure 4.49.

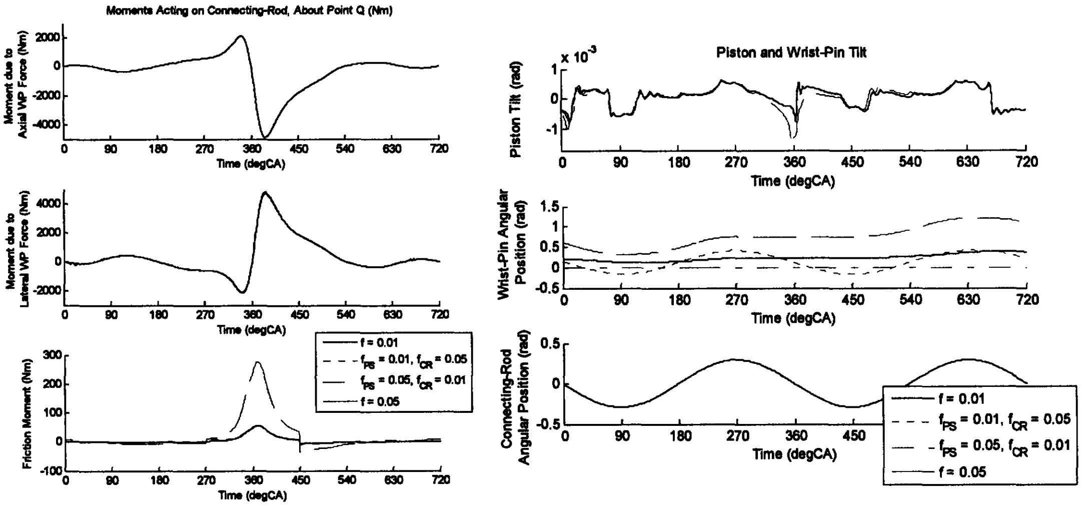

Figure 4.49: Effect of Difference Between Wrist-Pin Bearing Friction Coefficients

The friction moment generated at the piston – wrist-pin interface becomes significant in determining piston tilt around combustion TDC, where the moment generated can be sufficient to change the direction of piston tilt during piston slap, thereby affecting the timing and point of impact, and significantly changing piston land – cylinder bore clearances.

4.4.3. Piston Geometry

The piston's geometry has a significant impact on its motion. In order to investigate this further it is useful to first consider a simpler system, with a flat bore, larger clearances (165 μm nominal), and a simple quadratic piston skirt profile. Three different skirt profiles, with the minimum point located at the wrist-pin axis (Symm) and 10mm above or below this axis (Symm ± 10mm) are shown in Figure 4.50. The piston lands were significantly recessed to minimize their interaction.

With such a large nominal clearance, the lateral motion of the piston is relatively constant, but the following features can be noted in Figure 4.51:

- These piston profiles are relatively sharp, leading to large oscillations in piston tilt, which in turn cause general fluctuations in the lateral motion of around 20μm, and during the intake and exhaust strokes peak fluctuations of close to 100 μm. It is expected that these oscillations would be damped out in the physical system.

- At low loads the lateral position is roughly equal to the nominal clearance.
- At high loads, there is much less oscillation as the piston tilt stabilizes, and an increase in lateral motion due to piston deformation.

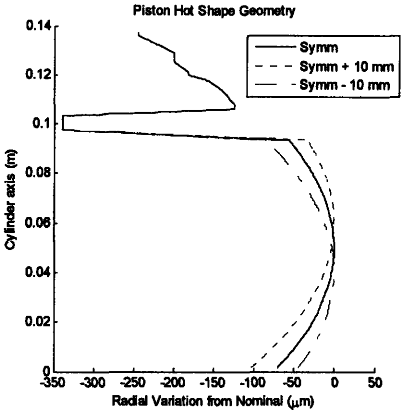

Figure 4.50: Simple Piston Profiles

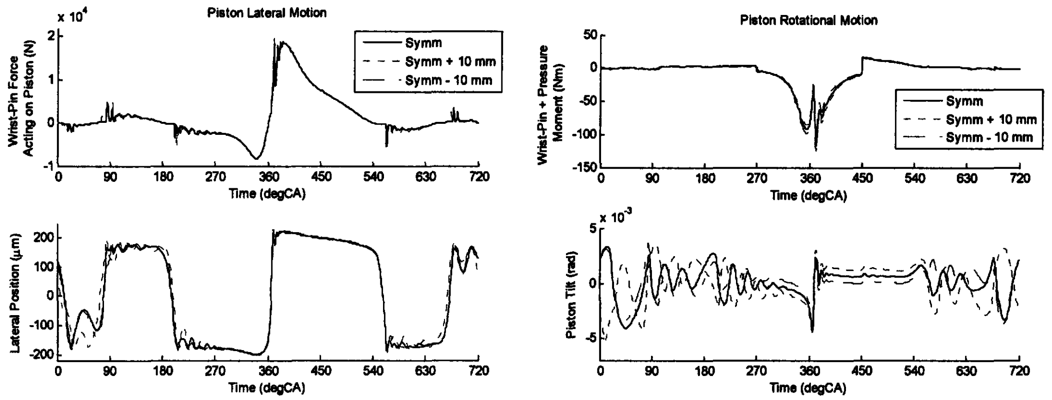

Figure 4.51: Effect of Piston Profile on Piston Secondary Motion

These relatively sharp piston profiles result in a significant amount of oscillation about the wrist-pin. This oscillation occurs as the moments generated at the piston-cylinder bore interface are balanced by the piston's motion, and it is expected that they would be damped out in the physical system by the lubricating oil. During the intake and exhaust strokes, the oscillations are so large for these examples that it is difficult to draw any conclusions about the piston's motion, but focusing on the expansion stroke we can note that:

- During this stroke the piston is moving downwards, against the thrust side of the bore, and therefore the friction force acts upwards, and the friction moment is positive.
- In the initial part of this stroke, the moment due to the wrist-pin and pressure is large and negative, but decreases in significance throughout the stroke.
- Initially the piston will make contact on the upper part of the skirt due to the negative tilt at this point, thereby generating a significant positive moment due to

the contact force, and driving the piston to rotate toward the anti-thrust side, making the tilt more positive.

- The equilibrium position of the piston toward the end of this stroke must result in the contact moment balancing the friction moment, therefore the net contact force must act at a point below the wrist-pin axis.
- Given that we have a flat bore, and therefore no bore inclination effect on piston tilt, for the piston with its minimum point at the wrist-pin axis, the piston must be tilted slightly to the anti-thrust side (positive tilt).
- For the piston with its minimum point below the wrist-pin axis (Symm – 10 mm), less tilt is required to achieve the same point of action for the contact force.
- Similarly, for the piston with its minimum point above the wrist-pin axis (Symm + 10 mm), more tilt is required, clearly showing the effect of piston profile on "stable" piston tilt.

When the bore geometry is more complicated, prediction of the required tilt is more difficult, but the same principles apply. In the absence of significant wrist-pin and pressure moments, the piston will tilt so that the balance between the friction and contact moments is achieved, and as discussed in Section 4.2.2, the piston tilt will essentially made up of three contributions: piston profile, bore inclination and friction coefficient. Wrist-pin and pressure moments only contribute significantly around combustion TDC, in which region the wrist-pin moment drives the piston to rotate towards the thrust side. The effect of bore geometry is discussed in more detail in Section 4.4.4.

There is considerable uncertainty in the thermal deformation of the piston during engine operation. While estimates can be made of the piston's temperature distribution and corresponding thermal deformation at a given steady state speed and load, under normal operation, the piston would transition from its cold shape through a variety of hot shapes depending on driving conditions. The predicted piston hot shapes, at 1200 rpm, for a range of loads are provided in Figure 4.52. Note that with increasing load, and therefore increasing temperature, not only does the average radius of the piston increase, but the profile becomes flatter, and the minimum clearance point moves slightly lower.

Simulations were run using the profiles shown in Figure 4.52, with a flat bore (~60 μm nominal clearance from the 2200Nm piston), and pressure traces corresponding to 1200 rpm, 2200Nm. From the piston lateral position plots shown in Figure 4.53 we can note that:

- In general, reduced piston – bore clearance due to increased average piston radius results in a corresponding reduction in lateral motion.
- During piston slaps, oscillations in side force due to inertia and tilt can result in larger peak lateral motions than would be predicted by the nominal clearance alone. For example at both the combustion TDC piston slap, and the mid-stroke, intake piston slap the peak lateral motion is achieved by the 300 Nm piston.
- At higher loads, flatter piston profiles, combined with smaller clearances, reduce oscillations.

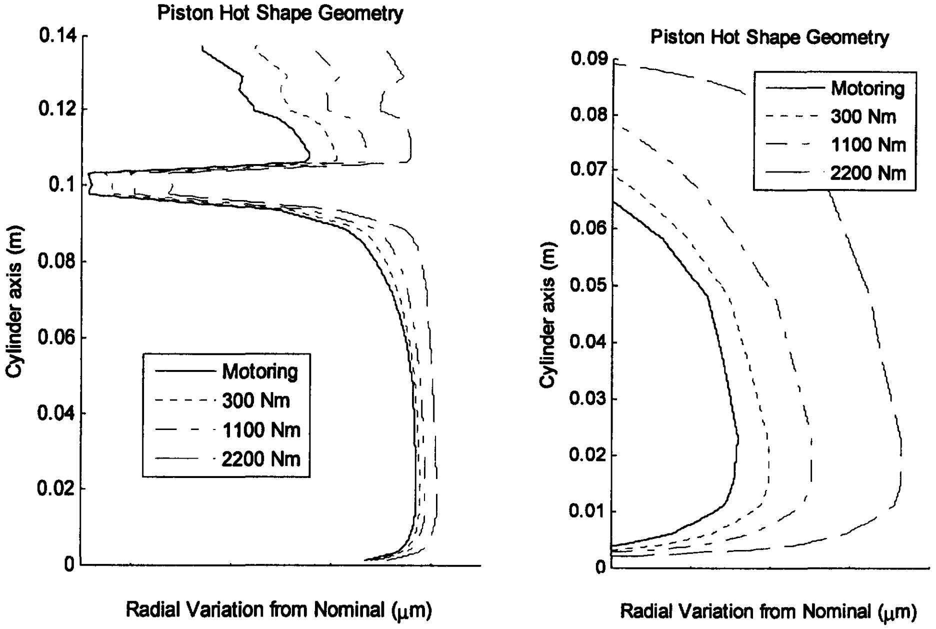

Figure 4.52: Piston Hot Shape Profiles

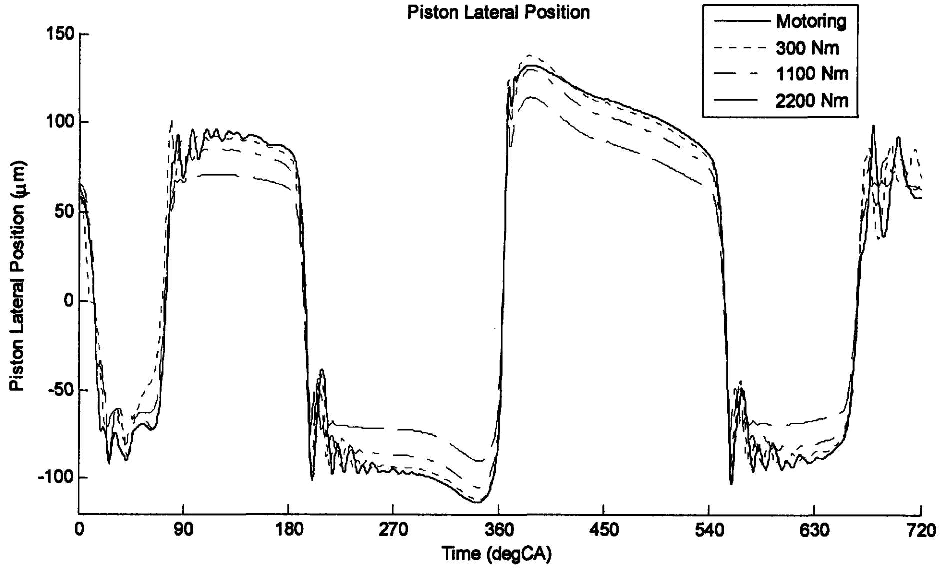

Figure 4.53: Effect of Piston Profile on Lateral Motion

Once again, the large oscillations predicted by the dry model, which are partially due to the increased bore radius, make it difficult to draw many conclusions, but we can note that:

- With increased load, and correspondingly flatter profiles, piston tilt oscillation is generally reduced (not clear that this is the case for the 300 Nm profile).
- Correspondingly, the flatter profiles that are achieved with increasing load require less tilt to achieve the same balance point, resulting in more positive tilts

approaching combustion TDC, and more negative tilts immediately after combustion TDC and throughout most of the expansion stroke.

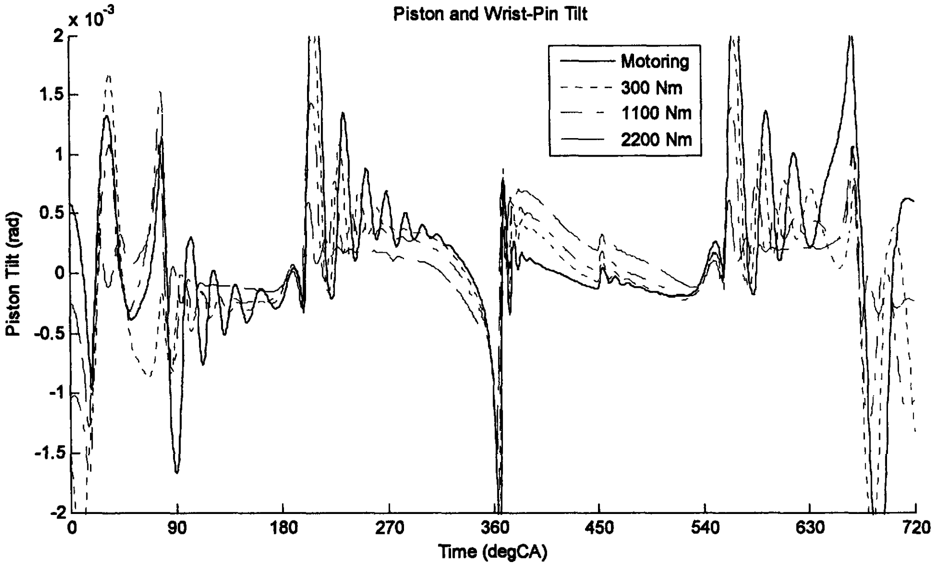

Figure 4.54: Effect of Piston Hot Shape on Piston tilt

For the dry model, the major affects of piston geometry on piston dynamics are:

- Piston – Cylinder Bore clearance directly affects lateral motion.
- The location of the minimum clearance point can significantly affect the "stable" tilt.
- Piston profile gradient, particularly about the minimum clearance point, significantly affects the amount of tilt required to achieve a "stable" tilt, and the amount of piston tilt oscillation, although much of this oscillation is expected to be damped out by the lubrication oil.

4.4.4. Bore Geometry

The bore geometry significantly impacts the piston's motion throughout the cycle. In order to investigate this further, simplified bore profiles, with larger clearances (nominal clearance for flat bore ~60μm), were initially simulated, as shown in Figure 4.55.

In Figure 4.56, while the net lateral force and moment acting on the piston are relatively constant, there are significant variations in the lateral motion and tilt:

- In the lower portion of the bore, the ~25μm reduction in clearance for the curved bore is clearly demonstrated by the decrease in lateral motion.
- During the expansion stroke, the difference between the lateral motion due to geometry and the lateral motion due to piston deformation is demonstrated, particularly during the second half of the stroke where the tilts are the same.

- Approaching combustion TDC, the curved bore requires the piston to tilt significantly further toward the anti-thrust side (positive tilt) in order to maintain the moment balance, while after combustion TDC it must tilt toward the thrust side (more negative tilt), demonstrating clearly the component of piston tilt due to bore inclination.
- The effect of the curved bore, on the piston tilt, is also observable approaching gas exchange TDC, around 630 °CA, when the piston is still against the anti-thrust side, the piston tilts further toward the anti-thrust side, and then after piston slap occurs, it tilts further towards the thrust side, and then returns back again after the piston slap at TDC.

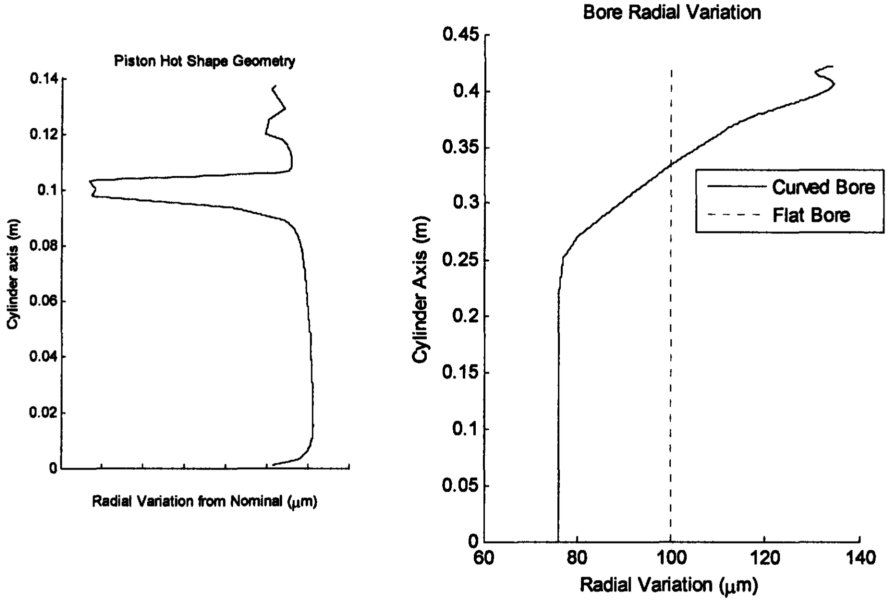

Figure 4.55: Simple Bore Geometries

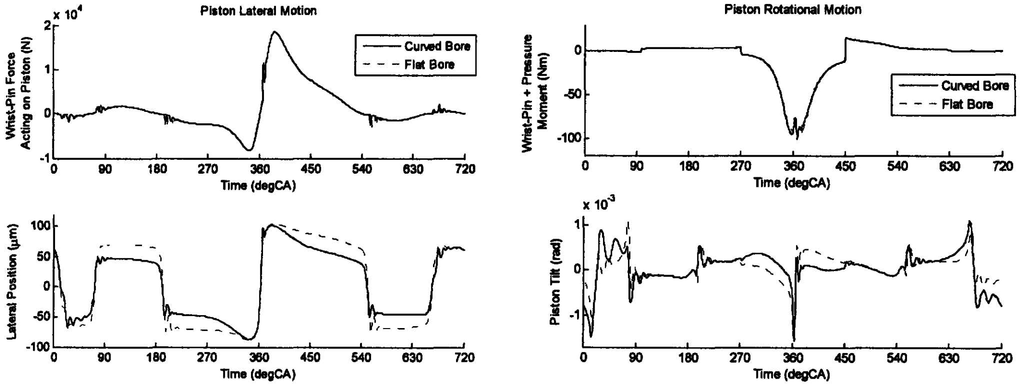

Figure 4.56: Effect of Simple Bore Geometry on Piston Motion

The flat and simple curved bore profiles were then compared to more realistic bore geometries, as shown in Figure 4.57. The baseline case has significant bore distortion, leading to large variations in bore radius in both the circumferential and axial directions. The other three profiles are axisymmetric.

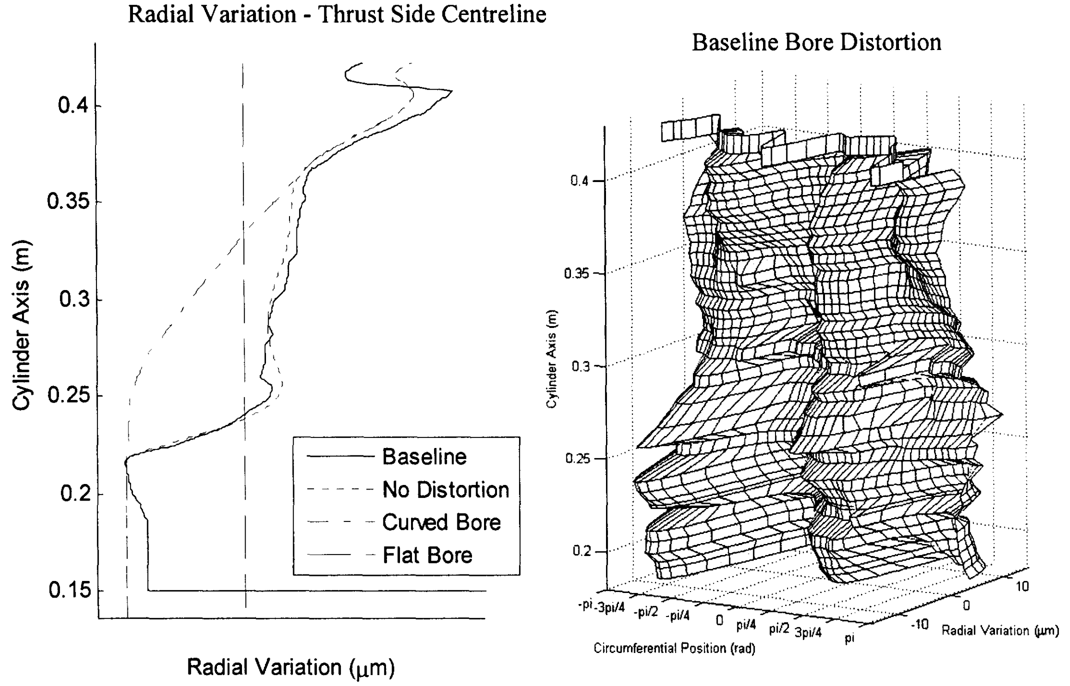
Radial Variation - Thrust Side Centreline

Baseline Bore Distortion

Figure 4.57: Realistic Bore Geometries

Figure 4.58 contains the lateral motion and tilt results for these bore geometries. It is useful to consider the bore in three sections:

1. The top portion, which does not significantly impact piston motion, as the majority of the skirt never enters this region.
2. The middle portion, where we have three different clearances, and three different slopes. This portion covers 0-120°CA, 240-480°CA and 600-720°CA. The lateral motion clearly shows the smaller clearance available for the curved profile, and the way in which the flat profile maintains a fairly constant clearance while the other three decrease toward BDC, causing the flat results to cross over the baseline and no distortion cases. The effect on piston tilt is clearest during the expansion stroke, where the flat, baseline and no distortion profile initially have similar tilts, while the curved profile results in the piston tilting significantly further toward the thrust side (negative). As the piston moves further down the bore, the baseline and no distortion results become significantly more negative as the lower portion of the skirt reaches the small clearance region, and the curved bore results increase as the bore gradient is reduced. Approaching combustion TDC the large wrist-pin moment dominates piston tilt for all bore geometries.
3. The lower portion of the bore where the flat bore represents a significant increase in clearance, but has the same slope as the curved and no distortion cases. This portion covers 120-240°CA, 480-600°CA. The lateral motion clearly demonstrates the significant increase in clearance for the flat profile. The effect on tilt, however, is less clear. On the downstrokes (120-180°CA and 480-540°CA), the piston is against the thrust side, and the baseline case tilts to the anti-thrust side due to the bore inclination, while the other profiles result in a tilt

to the thrust side. On the upstrokes (180-240°CA and 540-600°CA) all tilts are essentially the same, and toward the anti-thrust side (positive) apart from increased oscillation for the flat bore.

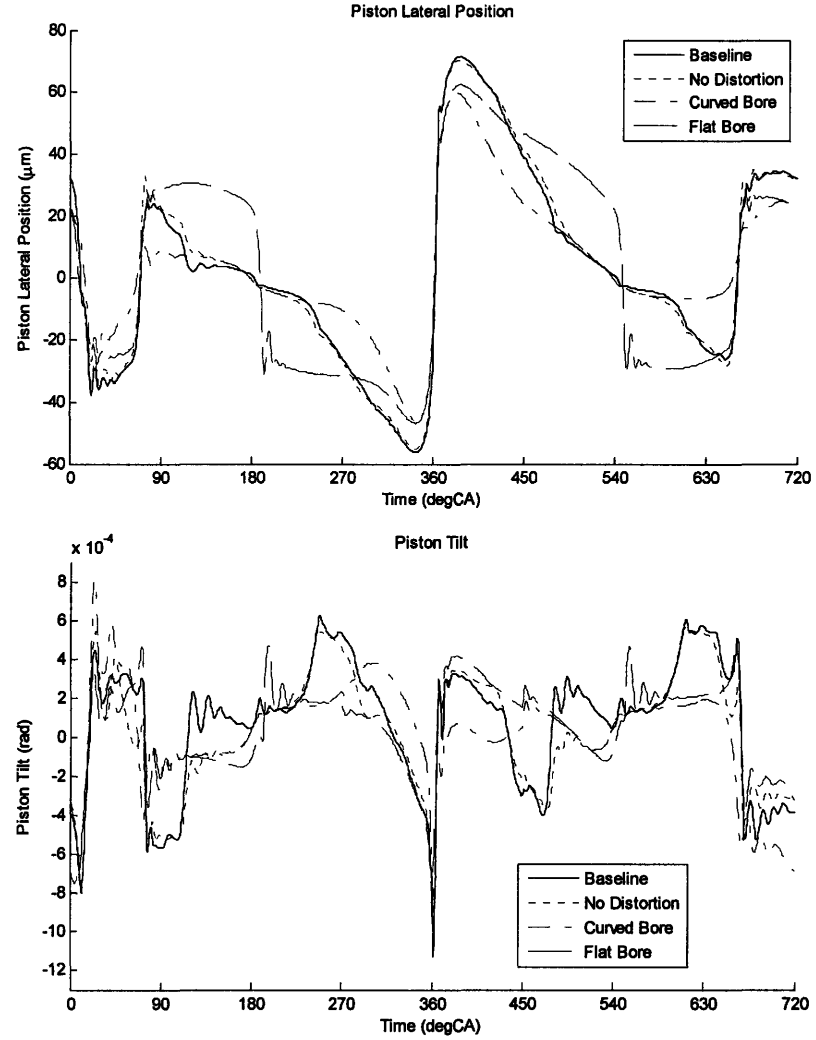

Figure 4.58: Effect of Simple and Realistic Bore Geometries on Piston Motion

For a given engine design, the range of operating conditions result in a range of geometry profiles as a function of load and speed, as shown in Figure 4.59. Correspondingly a range of piston dynamics are predicted. The results presented in Figure 4.60 are due to bore variation only, that is, the pressure trace, piston profile and engine speed were kept constant (1200 rpm, 2200 Nm). The increased clearances in the upper portion of the bore clearly correspond with the increase lateral motion in these regions. The variations in tilt at mid-stroke are due to the increased average bore gradient at these positions, with increasing load, while the more negative tilt with increased load after combustion TDC, and approaching gas exchange TDC, while the piston is against the thrust side, are due to the increased bore gradient in the top portion of the bore.

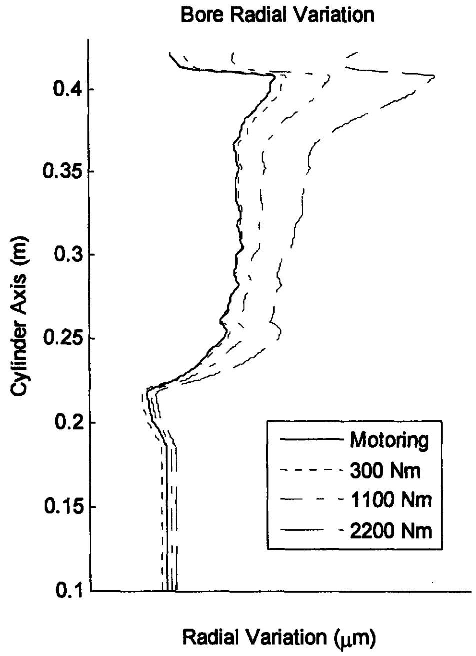

Figure 4.59: Bore Geometry as a Function of Load

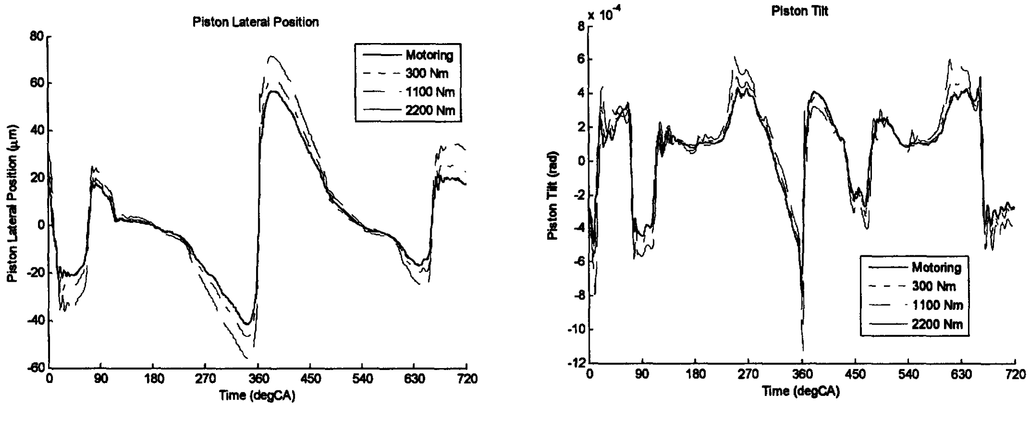

Figure 4.60: Effect of Load Related Bore Variation on Piston Dynamics

The cylinder bore profile essentially affects the piston dynamics in two ways:

- Piston – cylinder bore clearance directly affects lateral motion.
- The average cylinder bore gradient, over the load bearing portion of the piston skirt, significantly affects piston tilt.

The length of the load bearing portion of the piston determines how localized these affects are.

4.5. Interesting Parameters

4.5.1. Speed

In general, as the speed is increased, the combustion pressures and temperatures increase, resulting in larger thermal deformations of the piston and cylinder bore, and for an aluminum piston in a cast iron bore, smaller piston – cylinder clearances. Results for a range of speeds and loads, including all these effects are included in Section 4.6. In this section, by neglecting the changes in pressure trace, and piston and cylinder bore geometry, we can use the dry model to investigate the effect of engine speed alone.

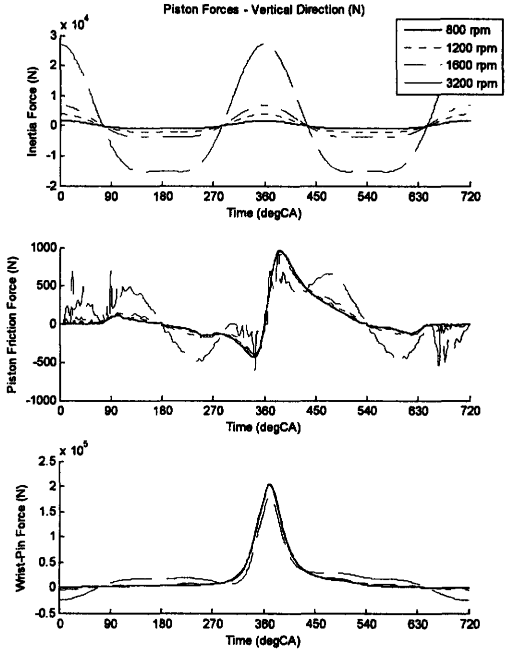

Figure 4.61: Effect of Speed on Axial Piston Forces

The only direct effect that speed has on the equations of motion is via the inertia terms, which increase with increasing speed, as shown in Figure 4.61. This significantly shifts the pressure – inertia balance used in determining the axial wrist-pin – piston force, and correspondingly results in significant changes to the lateral wrist- pin – piston force, as demonstrated in Figure 4.62.

The piston dynamics change significantly as inertia increases, initially resulting in significant shifts in the timing of mid-stroke piston slaps, as the pressure – inertia balance shifts. As the speed increases further, inertia terms becoming significant throughout the cycle and result in two mid-stroke piston slaps during the compression stroke as the inertia changes direction mid-stroke, and then the pressure increases sufficiently to force the piston back to the anti-thrust side close to 300 °CA. The lateral motion is changed throughout the cycle due to the significantly larger side loads at high speed. The changes in piston tilt are mainly due to the changes in piston slap timing, and the additional piston slap events.

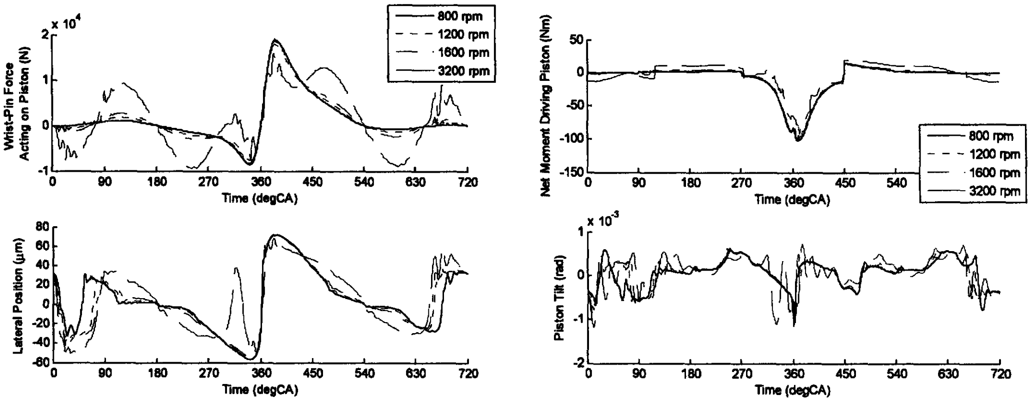

Figure 4.62: Effect of Speed on Piston Dynamics

4.5.2. Connecting-Rod Moment of Inertia, Mass and Centre of Gravity.

Variations in the connecting-rod moment of inertia and mass, and the position of its centre of gravity all affect the moment balance on the connecting-rod in a similar manner.

$$\tau_{WP/CRX} - r_{CR\_P/QZ}F_{WP/CRY} = I_{CR\_XX}\ddot{\phi}_{CR} - r_{CR\_P/QY}F_{WP/CRZ} - \left\{\mathbf{r}_{CR\_CG/Q} \times m_{CR}\mathbf{g} - \mathbf{r}_{CR\_CG/Q} \times m_{CR}\mathbf{a}_{CR\_CG/A}\right\}_X$$

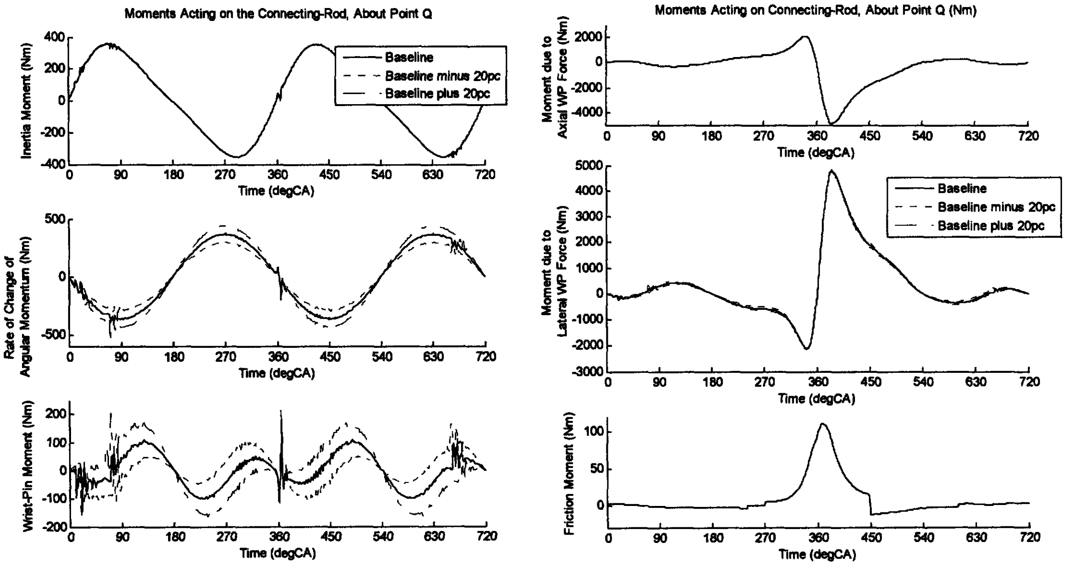

Figure 4.63: Effect of Connecting-Rod Moment of Inertia on CR Moments

Altering any one of these three variables will change the balance between the rate of change of angular momentum and the inertia moment, thereby changing the net moment that is applied to the connecting-rod, about point Q, by the wrist-pin forces. In order to investigate the effect that this will have on piston lateral motion and tilt, the moment of inertia of the connecting was varied by 20% of its baseline value. The resulting moments acting on the connect-rod are shown in Figure 4.63.

While there is a significant change in the net wrist-pin – connecting-rod moment, the corresponding change in the moment due to the lateral wrist-pin force appears quite small. It is not insignificant however, and results in a significant shift in mid-stroke piston slap timing, as shown in Figure 4.64.

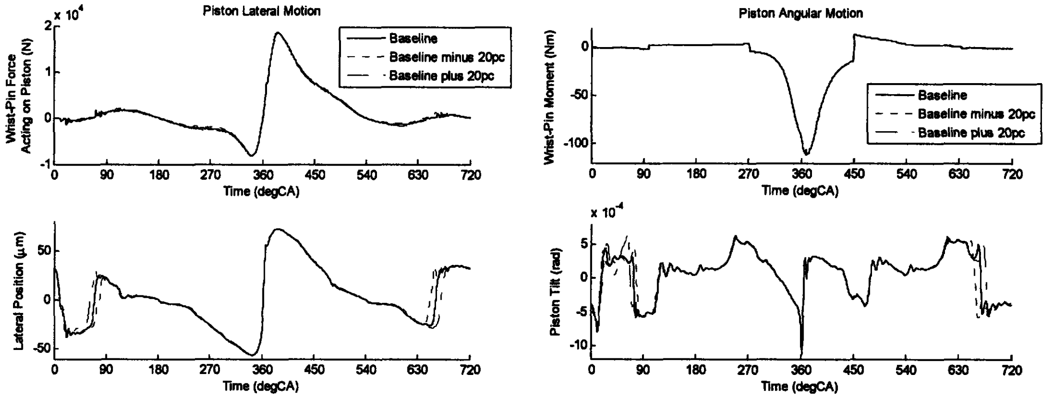

Figure 4.64: Effect of Connecting-Rod Moment of Inertia on Piston Motion

4.6. Effect of Operating Conditions on Piston Dynamics

For a given engine design, the range of operating conditions, in terms of temperature, speed and load leads to a corresponding range of piston and cylinder bore geometries, and combustion pressure traces. The pressure traces, piston cold profile and ovality, cylinder bore distortion, piston and cylinder bore thermal deformations, and piston compliance matrix were provided by the project sponsors, for a heavy duty diesel engine, over a range of operating speeds and load.

With increasing speed and load, combustion characteristics and the corresponding pressure trace are changed due to increased piston speed, altered fuel injection timing, and increased fuel mass. In general, with increasing load, combustion pressure is increased, and the peak pressure occurs later in the expansion stroke.

The engine temperature increases with speed and load, and correspondingly the thermal deformations of the piston and cylinder bore increase. In general both the piston and cylinder bore temperatures and thermal deformations increase with axial height, but the location of the coolant chamber affects the temperature distribution, and any reinforcements can restrict thermal deformation.

For this engine, with an aluminum piston and cast iron cylinder bore:
- the piston thermal deformations tend to exceed those of the cylinder bore, thereby decreasing piston – cylinder bore clearance with speed and load, particularly in the lower portion of the cylinder bore,
- thermal deformations flatten the piston profile, decreasing the piston surface gradient, particularly on the upper half of the piston skirt where the increasing thermal deformation counteracts the decreasing cold profile radii, and
- crown and second land clearances are significantly reduced due to the higher temperatures and thermal deformations toward the top of the piston.

For all of the speeds simulated, the motoring and idling piston profiles are the same, and for the 1000 rpm case, there was not any data for the 1100 Nm operation conditions, so the motoring/idling profile was used. Similarly, no data was provided for the 600 rpm conditions, so the 800 rpm motoring/idling profile was used.

Figures 4.65 and 4.66 show the lateral motion and piston tilt respectively over a range of operating conditions. In general, increasing load results in:
- Reduced lateral motion and tilt for 0-270 °CA and 450-720 °CA, due to the decreased piston – cylinder bore clearance, particularly in the lower portion of the cylinder bore (~90-270 °CA, ~450-630°CA).
- Increased lateral motion for 270-450 °CA despite the decreased clearances due to the increased pressure load, and resulting side force and piston deformation.
- Significant changes in piston tilt for 270-450 °CA, even leading to reversal of tilt direction due to the large deformations of the piston skirt and resulting changes to the piston profile.
- Reduced piston tilt oscillations due to the flatter piston profile.

The effect of increased pressure load is clearly demonstrated for the 1000 rpm case, where the same geometry was used for all three loads, and the changes in mid-stroke piston slap timing and increase in lateral motion during the expansion stroke are due to changes in the pressure trace alone.

4.7. Comparison with Experimental Results.

Experimental results were also provided by the sponsors, but are not included here for reasons of confidentiality. A heavy duty diesel engine was instrumented with gap sensors at five points along the cylinder bore, located at the thrust axis, on the thrust and anti-thrust sides. The experimentally obtained gap data was then post-processed by the sponsors to obtain calculated piston lateral motion and tilt. In comparing the experimental and simulated piston motion it is useful to note that each of them contain significant sources of uncertainty, and hence while general trends and behavior should match, there will also be many variations.

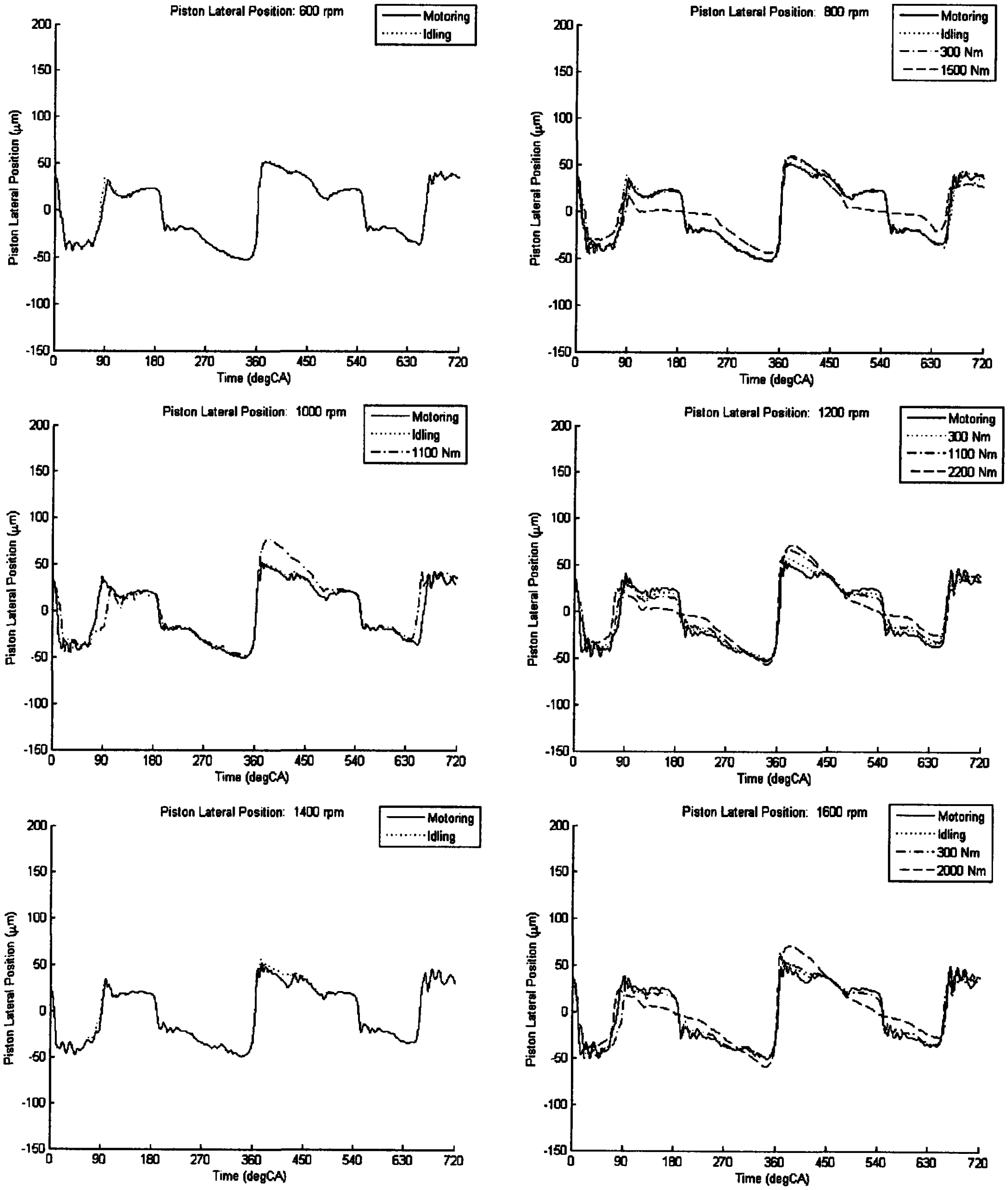

Figure 4.65: Effect of Speed and Load on Lateral Motion

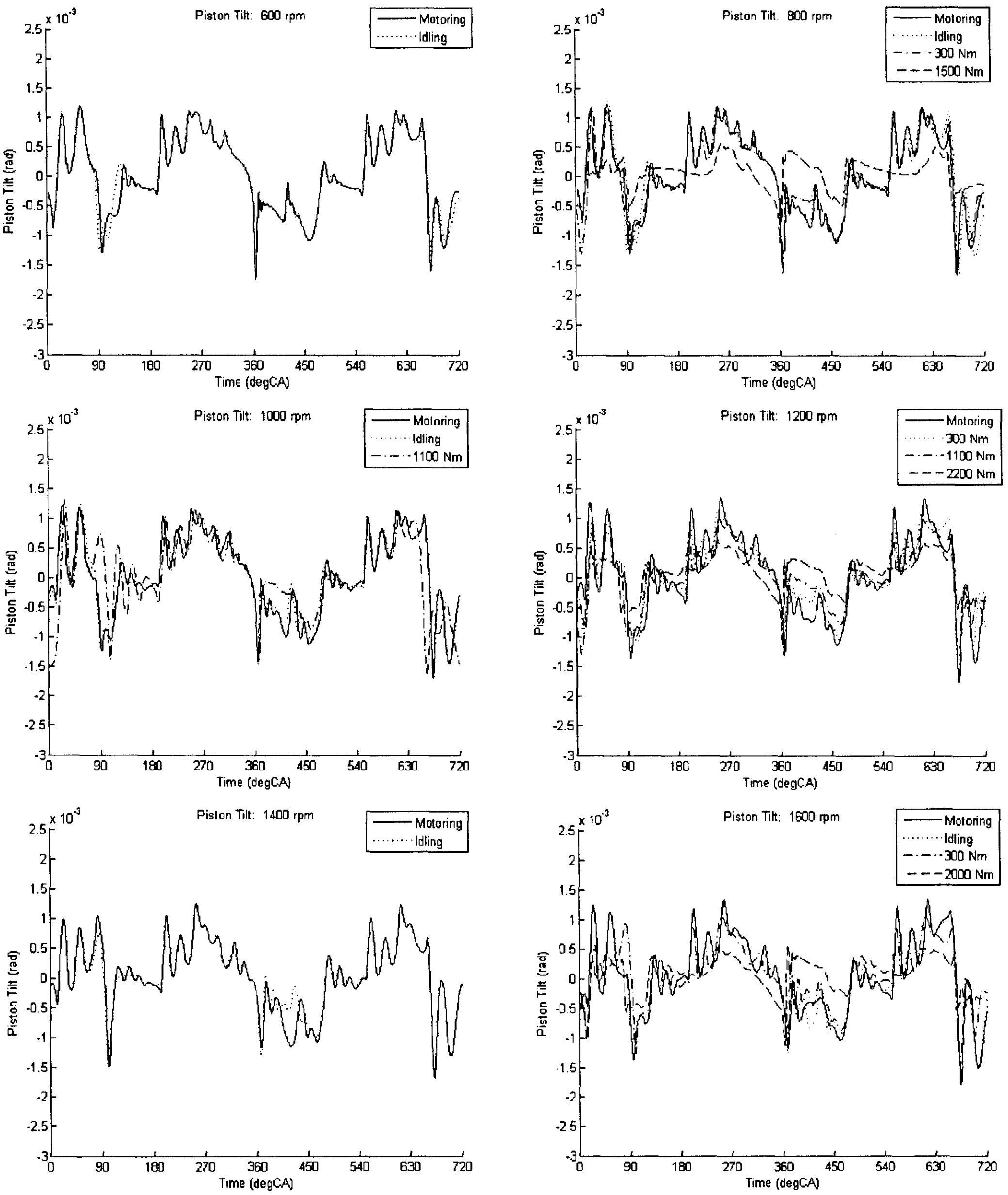

Figure 4.66: Effect of Speed and Load on Piston Tilt

For the experimental data:

- It is very challenging to obtain accurate gap measurement data under the high temperature and pressure conditions experienced in internal combustion engines.
- Any gap sensor measurement has a degree of accuracy which may vary over the range of gaps measured.
- The depth of the piston tooling marks is of the same order of magnitude as the gaps being measured.

- A calculation procedure is required to convert the gap sensor data into lateral motion and piston tilt, involving estimation of piston deformation, which introduces a degree of uncertainty.
- The running conditions must be specified carefully in order to allow for correct specification of inputs to the simulation model.

For the simulation data:

- The output can only be as accurate as the input data, which is dependent on accurate determination of the running conditions, and includes:
    - piston and cylinder bore geometry, and
    - piston compliance matrix.
- The following results are for the dry model, so there is no consideration of the effect of oil film thickness.
- The current model does not include cylinder bore deformation.

Comparing the experimental/calculated piston dynamics with those simulated using the dry model, we found that:

- General motion, magnitude and direction for both lateral motion and tilt are in good agreement, except for:
    - lateral motion during combustion, which is significantly larger for the experimental results, and
    - piston tilt, during combustion, at high loads, which is also significantly larger for the experimental results.
- At light loads, particularly during the upper half of the intake and exhaust strokes the lateral motions are in very good agreement.
- Simulated piston tilt is significantly more oscillatory due to the absence of oil in the dry model, but the mean line of these oscillations is in good agreement with the experimental results. It is expected that the lubricated model will significantly damp oscillations.
- There is significantly oscillation in the experimental lateral motion and tilt at combustion TDC, indicating a lack of damping and therefore perhaps oil, at this point.
- Toward the lower half of the bore, the simulated results consistently predict more lateral motion, implying larger piston – cylinder bore clearances, than the experimental results. It is quite possible that this variation is due to the presence of oil which is neglected in the dry model.
- The dry model results are limited by the accuracy of the input data. For example, for the 600 rpm cases, the same piston and cylinder bore geometry were provided for the two load conditions, and there is very little difference in the pressure traces. Correspondingly, there is very little difference in the simulated piston dynamics, but the experimental results showed significant variation in both the lateral motion and tilt.
- Both the simulated and experimental results demonstrate the same physical behaviour with increasing load:

- reduced lateral motion and tilt for 0-270 °CA and 450-720 °CA, due to the decreased piston – cylinder bore clearance, particularly in the lower portion of the cylinder bore (~90-270 °CA, ~450-630°CA), and
- increased lateral motion for 270-450 °CA despite the decreased clearances due to the increased pressure load, and resulting side force and piston deformation.

The experimental and simulated results were found to be in good agreement, demonstrating the same general motion, and similar responses to increasing load. There were significant differences around combustion TDC, where the experimental results displayed significantly larger lateral motions. In the lower portion of the bore, the simulation repeatedly predicted larger lateral motions, which may be due to a lack of oil film thickness, particularly given that the results are in very good agreement in the upper portion of the bore during the intake and exhaust strokes. Given the uncertainties present in both the experimental and simulated results, these results are very promising.

4.8. Conclusions Based on Dry Model Analysis

The engine's motion is driven by the combustion pressure, with the axial pressure and inertia loads on the piston and wrist-pin being supported by the connecting-rod. In the absence of extreme interference between the piston and cylinder bore, piston – cylinder bore friction is negligible for the purposes of determining axial connecting-rod force.

The lateral force on the connecting-rod must generate a moment which balances the moment generated by the axial force, with small shifts due to the net effect of connecting-rod angular inertia and rate of change of angular momentum, and takes into account the resulting wrist-pin – connecting-rod friction moment. The effects of connecting-rod inertia on lateral force tend to be small, but can result in a significant shift in mid-stroke piston slap timing, while the effect of wrist-pin friction, on this moment balance, appears to be negligible. The current wrist-pin bearing model allows the net connecting-rod force to act at an angle to the main axis of the connecting-rod generating a small but significant component perpendicular to this axis.

The resulting connecting-rod – wrist-pin lateral force is transmitted through the wrist-pin to the piston. Significant fluctuations in this force occur due to each of the component lateral inertias during piston slap events, particularly during the intake and exhaust strokes where the combustion pressure is low. A reasonable approximation for the lateral force applied to the piston is given by:

$$F_{PSY} = (\text{Pressure} + \text{Inertia})_Z \times \tan(\phi_{CR})$$

where the inertia term contains the piston and wrist-pin inertias.

This approximation can be improved further by adding an appropriate term to capture the effect of connecting-rod angular inertia and rate of change of angular momentum. The above equation captures both the driving force for piston motion, in terms of pressure, axial inertia, and connecting-rod angle, and the way in which the side force on the piston changes sign and therefore initiates piston slap, which occurs in two ways:

1. When the connecting-rod angle, ϕ_{CR}, changes sign, which is a function of engine geometry alone, and for an engine with no crankshaft offset occurs at 0, 180, 360, and 540 °CA.
2. When the balance of pressure and inertia forces changes sign, which is a function of load, speed, component mass and its distribution, and engine geometry, resulting in mid-stroke piston slaps. As speed is increased, the relative importance of inertia increases, and this can significantly change the character of the piston motion, as demonstrated in Section 4.5.1.

The piston lateral motion is driven by the wrist-pin - piston lateral force and constrained by its interactions with the cylinder bore. It is therefore essentially a function of piston – cylinder bore clearance, and piston deformation (and cylinder bore deformation) due to the applied side force. While the piston-cylinder bore lateral force must balance the driving side force and piston inertia, and is therefore reasonably well defined, the detailed piston – cylinder bore pressure distribution and the resulting friction generation, oil transport and point of action of the net normal force at this interface are dependent on many uncertainties including:

- detailed piston and cylinder bore surface geometries,
- asperity contact force,
- piston compliance matrix, and bore elasticity,
- piston – cylinder bore friction coefficient, and
- for the physical system and the lubricated model, the availability of oil.

Of these uncertainties, the effects of piston – cylinder bore friction coefficient, piston geometry and cylinder bore geometry on piston motion were investigated in Section 4.4. In the absence of a severe interference fit, the piston – cylinder bore friction coefficient was found to have essentially no effect on the wrist-pin – piston lateral force and therefore impacts piston lateral motion only via tilt. The piston and cylinder bore geometries directly impact the piston – cylinder bore clearance, resulting in corresponding changes in the lateral motion.

The timing of piston slap is well defined by the changes in sign in the wrist-pin – piston lateral force, and as demonstrated in Section 4.2.1, the current dry model results in the piston translating at the correcting times, and resting against the correct side of the cylinder bore. At light loads, during the intake and exhaust strokes, the lateral motion is in good agreement with the piston – cylinder bore clearance at the same height as the wrist-pin, while significantly larger lateral motions are achieved due to the increased side load and corresponding piston deformation during the compression and expansion strokes.

The wrist-pin tilt is driven by the friction moments applied at its bearing interfaces with the connecting-rod and piston. The coefficient of friction at these interfaces is a significant source of uncertainty. For cases where there is a large difference in the friction coefficients, the wrist-pin will travel with the component with the highest friction coefficient, thereby reducing the friction moment generated to that of the smaller coefficient of friction.

The piston tilt is influenced by many competing factors, with many uncertainties. Approaching combustion TDC, the wrist-pin friction moment and pressure moment drive the rotational motion of the piston until it impacts against the cylinder bore, at which point the cylinder bore normal and friction moments become significant. Away from combustion TDC, the piston's interactions with the cylinder bore dominate piston tilt, with the moment generated by the piston – cylinder bore normal force driving the very oscillatory motion predicted by the dry model. These oscillations occur as piston hits bore at an angle, then rotates, over correcting, to find balance point or "stable" tilt. It is expected that in the physical system and lubricated model these oscillations would be reduced significantly by the damping effect of the lubrication oil. Neglecting these oscillations, and in the absence of the wrist-pin and pressure moments, the "stable" piston tilt can be shown to be a function of:

- the location of the minimum clearance point and the gradient of the deformed piston profile,
- the average cylinder bore gradient, over the load bearing portion of the piston, and
- the piston – cylinder bore friction coefficient.

The piston – cylinder bore friction coefficient, wrist-pin friction coefficient and piston and bore geometries introduce significant uncertainty in determining piston tilt. The piston - cylinder bore friction coefficient significantly impacts the moment balance on the piston, and resulting piston tilt, around combustion TDC, but has a relatively small effect through rest of cycle, suggesting that tilt is mainly controlled by geometry in this region. The wrist-pin friction coefficient determines the moment generated at the piston – wrist-pin interface which becomes significant in determining piston tilt around combustion TDC. Variations in the wrist-pin moment can be sufficient to change the direction of piston tilt during piston slap, thereby affecting the timing and point of impact, and significantly changing piston land – cylinder bore clearances.

The current model restricts the piston motion to rotation about the wrist-pin axis, axial motion along the cylinder bore, and lateral motion across the cylinder bore, parallel to the thrust axis. Variations in bore geometry, and the location of the piston center of gravity lead to significant force generation along the pin-axis, and moments about the cylinder and thrust axes. In the physical system, small motions along the wrist-pin axis, and rotation about the cylinder and thrust axes would occur, alleviating the imbalance in piston – cylinder bore force along the wrist-pin axis, and reducing the force transmitted to the wrist-pin.

For a given engine design, the range of operating conditions, in terms of temperature, speed and load leads to a corresponding range of piston and cylinder bore geometries, and combustion pressure traces, which in turn alter the piston dynamics. It was found that, in general, increasing load results in:

- reduced lateral motion and tilt for 0-270 °CA and 450-720 °CA, due to the decreased piston – cylinder bore clearance, particularly in the lower portion of the cylinder bore (~90-270 °CA, ~450-630°CA), and
- increased lateral motion for 270-450 °CA despite the decreased clearances due to the increased pressure load, and resulting side force and piston deformation.

The simulated results were compared to experimentally obtained results over a range of operating conditions and found to be in good agreement, demonstrating the same general motion, and similar responses to increasing load. There were significant differences around combustion TDC, where the experimental results displayed significantly larger lateral motions. In the lower portion of the bore, the simulation repeatedly predicted larger lateral motions, which may be due to a lack of oil film thickness, particularly given that the results are in very good agreement in the upper portion of the bore during the intake and exhaust strokes. Given the uncertainties present in both the experimental and simulated results, these results are very promising.

5. Lubrication Flow and Oil Transport Models

This chapter aims to:

- Introduce the lubricated piston – cylinder bore interface
- Develop the governing equations for the lubricated piston – cylinder bore interface.
- Describe the quasi-steady and unsteady hydrodynamic lubrication models.
- Present results obtained using the hydrodynamic lubrication models, and discuss the factors affecting normal load, friction and oil transport, particularly for the power cylinder system.
- Investigate the effect of piston tooling marks, and compare the accuracy of different surface representations.
- Describe the unsteady elastohydrodynamic lubrication model, and its incorporation into the piston dynamics model.
- Introduce the piston oil transport model.

5.1. Introduction to Lubricated Piston – Cylinder Bore Interface

As discussed in Section 2.3.3, the piston – cylinder bore interface is essentially made up of three components:

1. The deformed piston surface geometry, taking into account piston motion.
2. The cylinder bore geometry, which is considered to be stationary and rigid for the purposes of this project.
3. The oil film thickness distribution.

Piston – cylinder bore clearances are typically in the range of 0-100 μm, with macro-scale surface gradients of around 1/100 on both the piston and bore, as shown in Figure 5.1. The variations in bore geometry are significant and lead to a height distribution which varies in time, relative to the piston, resulting in significant geometric squeezing of the oil film. The combined surface roughness is of the order of 0.5 μm. When piston tooling marks are present, they tend to have surface gradients of the order of 1/30, with a wave height of the order of 10μm, and are expected to dominate over any surface roughness effects.

The piston's axial sliding velocity is in the range 0-10 m/s, driving significant shear flow, particularly mid-stroke. There is significant squeezing due to the lateral motion of the piston both during piston slap events, and throughout the rest of the cycle due to the applied side load. The dry model predicts peak lateral velocities of around 0.01 m/s.

When there is sufficient oil present to fill the gap between the piston and cylinder, the profile of the piston in the axial direction leads to pressure generation during sliding, while the ovality of the piston allows significant circumferential flow, thereby decreasing hydrodynamic pressure, as shown in Figure 5.2. The effect of tooling mark geometry on pressure generation has been unclear, and is investigated in detail in Section 5.3.2.2.

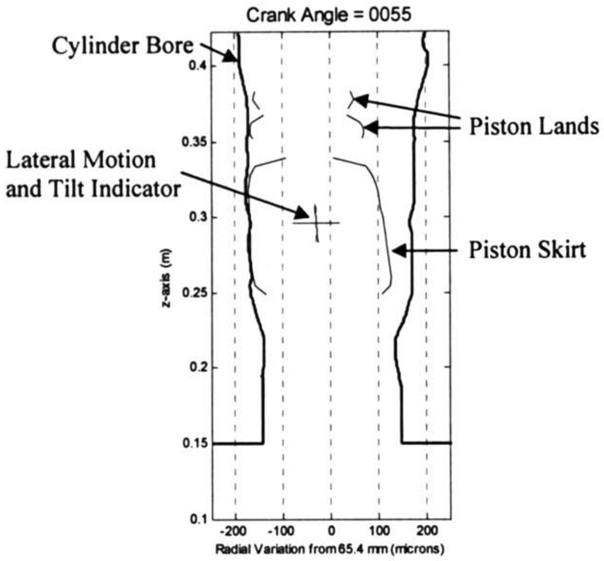

Figure 5.1: Diagram of Piston – Cylinder Bore Interface

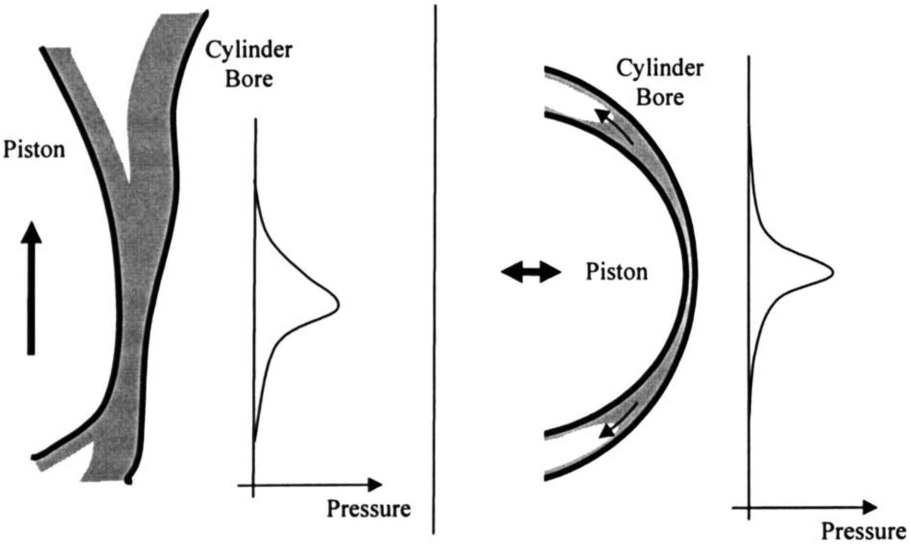

Figure 5.2: Diagram of Piston – Cylinder Bore Interface Lubrication Flow

The elasticity of the piston, as described by a compliance matrix, leads to structural deformations of the piston skirt and lands due to combustion chamber pressure, axial inertia, and pressure generated at the piston – cylinder bore interface. These deformations significantly alter profile of the piston, thereby changing both hydrodynamic pressure generation and the resulting asperity contact pressure.

The actual amount of oil present, at the piston-cylinder bore interface, is currently not well defined. Previous investigation results [2,8] suggest that the average oil film thickness, in the piston –cylinder bore interface, may be around 20 μm, which is insufficient to fully fill the gap between the piston and cylinder. A range of initial oil film thicknesses, and the resulting effect on piston motion, oil transport, and friction generation, are investigated in Section 6.2. Oil viscosities are expected to be around 0.01 Pas, and while it is expected that oil viscosity will vary with temperature along the axis of the cylinder, this variation is neglected in the current model.

When there is insufficient hydrodynamic pressure generated to support the side load on the piston, the two surfaces will become close enough for asperity contact to occur. A general asperity contact model is implemented, as described in Section 2.3.3.1. When piston tooling marks are present, it is expected that their geometry will dominate this interaction, and the model of a blunt wedge against a flat plane is used, as described in Section 2.3.3.1.

The governing equations describing the fluid flow, asperity contact, piston deformation and friction generation at the piston – cylinder bore interface are described in the following section. A detailed list of the nomenclature for this chapter is given below, in Table 5.1.

Symbol	Explanation of Variable
A	Control surface area
C_1, C_2	Asperity contact model parameters
f	Contact friction coefficient
F	Cavitation parameter: 1 = full film, 0 = partial film
$\mathbf{F}_F$	Friction force vector
F_N	Magnitude of normal force
h	Local gap height
h_{asp}	Asperity contact onset height
h_{lim}	Minimum height for hydrodynamic pressure calculation
h_{ref}	Reference height used for normalization
$\hat{h}$	Normalized gap height = h/h_{ref}
$\bar{h}$	Average height over a control volume
p	Local pressure, hydrodynamic pressure
p_{asp}	Asperity contact pressure
p_h	Hydrodynamic pressure
p_C	Cavitation pressure
p_{ref}	Reference pressure used for normalization
$\hat{p}$	Normalized pressure = $(p - p_c) / (p_{ref} - p_c) = F\Phi$
$\bar{p}$	Average pressure over a control volume
q_x, q_z	Mass flow rate across an x- or z- surface
$\bar{q}_x$, $\bar{q}_z$	Average mass flow rate across an x- or z- control surface
$\{rdef\}$	Radial deformation vector
$\{rrgap\}$	Rigid radial gap vector

t	Time
u	Scalar velocity component in the x-direction
U_1, U_2	Surface 1 or 2 velocity component in the x-direction
v	Scalar velocity component in the y-direction
$\mathbf{v}$	Velocity vector
V	Control volume
V_1, V_2	Surface 1 or 2 velocity component in the y-direction
w	Scalar velocity component in the w-direction
W_1, W_2	Surface 1 or 2 velocity component in the z-direction
$\boldsymbol{x}$	Vector position
x	Scalar position in x-direction (see Figure 5.3)
x_{ref}	Reference x-direction scale, used for normalization
$\hat{x}$	Normalized scalar position in x-direction = x / x_{ref}
y	Scalar position in y-direction (see Figure 5.3)
y_{ref}	Reference y-direction scale, used for normalization
$\hat{y}$	Normalized scalar position in y-direction = y / y_{ref}
z	Scalar position in z-direction (see Figure 5.3)
z_{ref}	Reference z-direction scale, used for normalization
$\hat{z}$	Normalized scalar position in z-direction = z / z_{ref}
ϕ_s	Shear flow factor for the Average Reynolds Equation
ϕ_x, ϕ_z	Pressure flow factors for the Average Reynolds Equation, in the x- and z-direction
ϕ_f, ϕ_{fs}, ϕ_{fp}	Shear stress factors
Φ	Global variable for Universal Reynolds Equation
γ	Scaling parameter = $6\mu U_1 z_{ref} / (p_{ref} - p_C) h_{ref}^2$
κ	Ratio of reference scales = x_{ref} / z_{ref}
μ	Dynamic viscosity
ρ	Density
ρ_{ref}	Reference density = density of liquid
$\hat{\rho}$	Normalized density = $\rho / \rho_{ref} = [1 + (1 - F)\Phi]$
σ	Surface roughness
τ_{xy}, τ_{zy}	Shear stress, on a y surface, in the x- or z- direction respectively
Ω	Triangular wave amplitude

Table 5.1: Nomenclature

5.2. Governing Equations for Piston – Cylinder Bore Interface

5.2.1. Lubrication Flow and Reynolds Equation

When there is sufficient oil present to fill the gap between the piston and the cylinder bore, the fluid flow at the piston – cylinder bore interface satisfies the requirements for a lubrication flow, as described in more detail in Appendix 2. For a lubrication flow, conservation of momentum in the y-direction requires that pressure does not vary across the gap, that is, that pressure is a function of x, z, and t only:

$$p = p(x,z,t)$$

Conservation of momentum in the *x*- and *z*- directions then provides the velocity profiles which are given by:

$$u(x,y,z,t) = -\frac{h^2}{2\mu}\left(-\frac{\partial p}{\partial x}\right)\left[\frac{y}{h}-1\right]\frac{y}{h} + (U_2 - U_1)\frac{y}{h} + U_1$$

$$w(x,y,z,t) = -\frac{h^2}{2\mu}\left(-\frac{\partial p}{\partial z}\right)\left[\frac{y}{h}-1\right]\frac{y}{h} + (W_2 - W_1)\frac{y}{h} + W_1$$

The shear stress at the piston surface ($y = 0$) is therefore given by:

$$\tau_{xy}\Big|_{y=0} = \mu\frac{\partial u}{\partial y}\Big|_{y=0} = \frac{h}{2}\left(-\frac{\partial p}{\partial x}\right) + \frac{\mu(U_2 - U_1)}{h}$$

$$\tau_{zy}\Big|_{y=0} = \mu\frac{\partial w}{\partial y}\Big|_{y=0} = \frac{h}{2}\left(-\frac{\partial p}{\partial z}\right) + \frac{\mu(W_2 - W_1)}{h}$$

The flow rate, across a control surface of unit width, is given by:

$$q_z = \int_0^h \rho w dy = \frac{\rho h^3}{12\mu}\left(-\frac{\partial p}{\partial z}\right) + \rho\frac{h}{2}(W_2 + W_1)$$

$$q_x = \int_0^h \rho u dy = \frac{\rho h^3}{12\mu}\left(-\frac{\partial p}{\partial x}\right) + \rho\frac{h}{2}(U_2 + U_1)$$

Consider conservation of mass across a fixed control volume as specified in Figure 5.3:

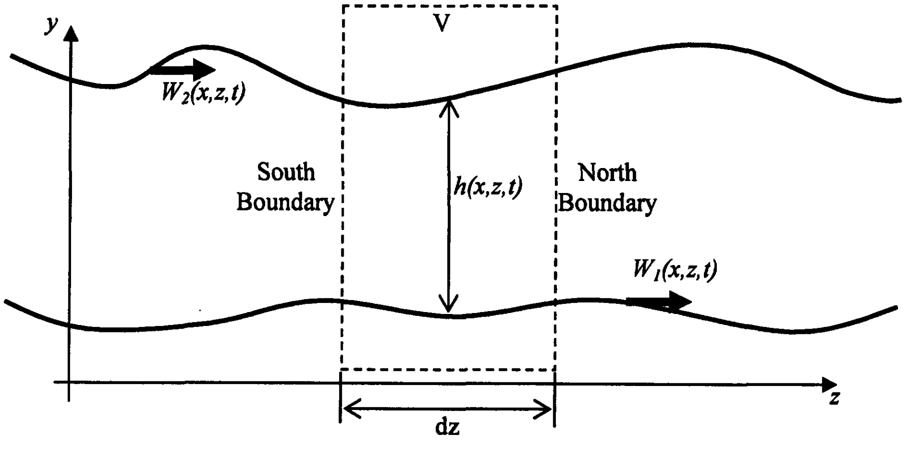

Figure 5.3: Fixed Control Volume

The rate of change of mass within the control volume is equal to the net inflow across the surface of the control volume.

$$\frac{d}{dt}\int_V \rho dV = -\int_A \rho \mathbf{v} \bullet \mathbf{dA}$$

$$dxdz\frac{\partial(\rho h)}{\partial t} = -dxq_z(z+dz) + dxq_z(z) - dzq_x(x+dx) + dzq_x(x)$$

In the limit as *dz* and *dx* go to zero, we obtain:

$$\frac{\partial(\rho h)}{\partial t} = -\frac{\partial q_z}{\partial z} - \frac{\partial q_x}{\partial x}$$

Substituting in the flow rate equations, we obtain the Reynolds equation, combining conservation of mass and momentum:

$$\frac{\partial}{\partial z}\left(\frac{\rho h^3}{12\mu}\frac{\partial p}{\partial z}\right) + \frac{\partial}{\partial x}\left(\frac{\rho h^3}{12\mu}\frac{\partial p}{\partial x}\right) = \frac{\partial}{\partial z}\left[\frac{\rho h(W_2+W_1)}{2}\right] + \frac{\partial}{\partial x}\left[\frac{\rho h(U_2+U_1)}{2}\right] + \frac{\partial(\rho h)}{\partial t}$$

Reynolds equation does not, however, take into account the fact that fluids cannot sustain significant tension, and that the fluid will cavitate at pressures below the cavitation pressure, forming vapor. Our fluid model must therefore be extended to include partial film phenomena, such as cavitation and separation.

5.2.2. Partial Film Phenomena

Fluids cannot sustain tension, and therefore cannot exist at pressures below their cavitation pressure. Once the pressure predicted by the Reynolds equation drops to a critical level (the cavitation pressure), as will occur for sufficiently divergent geometries, the fluid will cavitate, separating into liquid and vapor. In central regions of the flow, which are surrounded by fluid, cavitation will result in a region filled by a combination of oil vapor and liquid, at the cavitation pressure. Close to the fluid boundary, however, cavitation will result in the fluid separating, with part of the liquid oil remaining attached to each of the two surfaces, and air at the boundary pressure filling the gap in between, as shown in Figure 5.4.

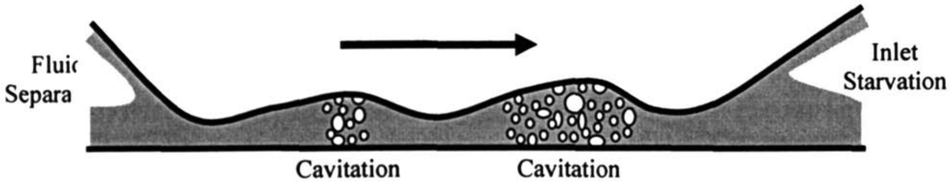

Figure 5.4: Cavitation, Fluid Separation and Inlet Oil Starvation

At the inlet to the fluid flow, if there is insufficient oil supplied to fill the gap between the piston and the cylinder bore, then we will also have a region filled by a combination of air and liquid oil due to inlet oil starvation, at the boundary pressure, as shown in Figure 5.4. For each of these three cases, where the liquid oil only occupies a fraction of the current control volume, we consider the flow to be *partial film*, and unable to generate hydrodynamic pressure. In contrast, when we have sufficient oil to fill the control volume, then the flow is *full film* and governed by Reynolds equation.

Jakobson-Floberg-Olsson (JFO) cavitation theory, as described by Elrod [38], proposes that the fluid domain can be divided into two distinct zones, a full film region where the Reynolds equation governs pressure generation, and a partial film region which is at a constant pressure, with only a fraction of the control volume being occupied by fluid. It is assumed that within the partial film region, the fluid distribution can be represented by multiple streamers of fluid, spanning the gap between the two surfaces, as shown in Figure 5.5. The oil transport rate is then determined using a linear velocity profile across the gap.

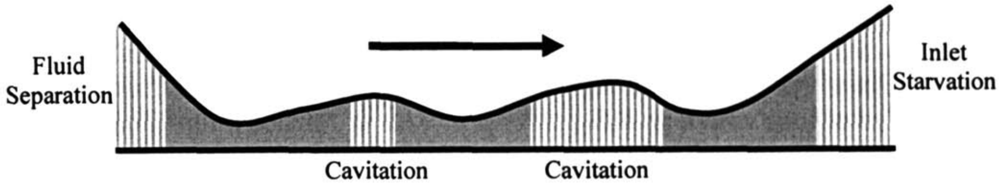

Figure 5.5: Partial Film Representation

5.2.3. Universal Reynolds Equation

Elrod [38] proposed a Universal Reynolds Equation, based on JFO cavitation theory, which combines the partial film and full film fluid regions into a single set of equations, based on the following assumptions:

- In the full film region:
    - The volume fraction of the liquid oil is 1.0, and therefore the density is that of the liquid oil.
    - Hydrodynamic pressure is generated, as governed by the Reynolds equation.
- In the partial film region:
    - The pressure is constant and equal to the cavitation pressure,
    - The fluid is in contact with both surfaces (see Figure 5.5), which is equivalent to assuming that half of the fluid is attached to each surface, and shear flow governs oil transport.
    - The volume fraction of the liquid is governed by conservation of mass.
    - The density of the combined vapour and fluid mixture is given by the volume fraction of the fluid multiplied by the fluid density, that is, the mass of vapour is neglected.

Further discussion of the method, and numerical algorithms for its solution were presented by Payvar and Salant [39], and a convenient formulation is provided by Harp and Salant [25].

A cavitation parameter, F, is introduced, which is 1 in the full film region, and 0 in a partial film region, and a global variable, Φ, which when combined with F allows both the pressure, p, and density, ρ, to be determined simultaneously throughout the calculation domain. The resulting Universal Reynolds Equation is given by:

$$\frac{\partial}{\partial \hat{z}}\left[\hat{h}^3 \frac{\partial (F\Phi)}{\partial \hat{z}}\right] + \kappa^2 \frac{\partial}{\partial \hat{x}}\left[\hat{h}^3 \frac{\partial (F\Phi)}{\partial \hat{x}}\right] = \gamma \frac{\partial}{\partial \hat{z}}\left\{\left[1+(1-F)\Phi\right]\hat{h}\right\} + 2\gamma \frac{\partial}{\partial \hat{t}}\left\{\left[1+(1-F)\Phi\right]\hat{h}\right\}$$

where

$$\hat{p} = F\Phi = \frac{p - p_C}{p_{ref} - p_C}$$

$$\hat{\rho} = \left[1+(1-F)\Phi\right] = \frac{\rho}{\rho_{ref}}$$

$$\gamma = \frac{6\mu U_1 z_{ref}}{(p_{ref} - p_c)h_{ref}^{\ 2}}$$

$$\kappa = x_{ref}/z_{ref}$$

For the full film region, where $F = 1$, and $p = \Phi$, these reduce to:

$$\frac{\partial}{\partial \hat{z}}\left[\hat{h}^3 \frac{\partial \hat{p}}{\partial \hat{z}}\right] + \kappa^2 \frac{\partial}{\partial \hat{x}}\left[\hat{h}^3 \frac{\partial \hat{p}}{\partial \hat{x}}\right] = \gamma \frac{\partial \hat{h}}{\partial \hat{z}} + 2\gamma \frac{\partial \hat{h}}{\partial \hat{t}}$$

For the partial film region, where $F = 0$, they reduce to:

$$0 = \gamma \frac{\partial}{\partial \hat{z}}\left\{\left[1+\Phi\right]\hat{h}\right\} + 2\gamma \frac{\partial}{\partial \hat{t}}\left\{\left[1+\Phi\right]\hat{h}\right\}$$

Coupling the equations in this manner allows for efficient solution throughout the calculation domain, but also introduces some limitations. There is no differentiation between the three different types of partial film, and in all three cases it is assumed that the fluid is in contact with both surfaces, and that shear flow governs oil transport. In the intake and outlet regions of the flow, this can lead to a significant redistribution of oil between the piston and bore surfaces, within the calculation domain, which is not physically correct. In the future, a detachment and reattachment model should be implemented to avoid the introduction of these errors.

There is also no differentiation between the pressure applied in each partial film region, with the cavitation pressure being applied even for regions that would clearly be at the boundary pressure. For situations where the boundary pressure is significantly larger that the cavitation pressure, relative to the pressure differences generated within the flow, this approximation may introduce a significant error. The current application of this work, however, has boundary pressures roughly equal to atmospheric pressure, and therefore the error introduced by this approximation will be small.

5.2.4. Flow Factor Methods

A very large number of nodes, and correspondingly large calculation time, are required to accurately capture the geometry of the piston tooling marks over the extent of the piston skirt using direct numerical simulation. It is currently unclear whether this calculation effort is justified, given that several average flow models have been developed for the purpose of estimating the effect of surface roughness on lubrication flows. Patir and Cheng [17] developed an average Reynolds equation, which was expanded by Tripp [24] to include general roughness distributions, and by Harp and Salant [25] to include inter-asperity cavitation.

In previous models of piston dynamics [18, 21], the average Reynolds equation developed by Patir and Cheng [17] has been applied in order to account for the effect of tooling marks. There has been very little justification, however, that this average equation is sufficiently accurate for the piston-cylinder system at very small clearances, and during solid-solid contact, or that the effect of tooling marks need to be included at all. Computer hardware and numerical methods have now developed to that stage where it is possible to use direct numerical simulation to investigate the effect of piston tooling marks on skirt lubrication, and compare these results to those obtained using flow factor methods in order to determine whether the additional computational expense results in a significant improvement in accuracy.

As a starting point, we have chosen to compare the direct numerical simulation results with the Patir and Cheng flow factor method [17]. Patir and Cheng proposed average flow rate equations for the full film region in terms of three flow factors, the average gap height and the average pressure. By equating the flow rates predicted by these equations with those generated by a rough surface, the flow factors for that particular surface can be calculated, as shown in Figure 5.6.

$$\bar{q}_z = -\phi_z \frac{\bar{h}^3}{12\mu}\frac{\partial \bar{p}}{\partial z} + \frac{W_1 + W_2}{2}\bar{h} + \frac{W_1 - W_2}{2}\sigma\phi_s$$

$$\bar{q}_x = -\phi_x \frac{\bar{h}^3}{12\mu}\frac{\partial \bar{p}}{\partial x}$$

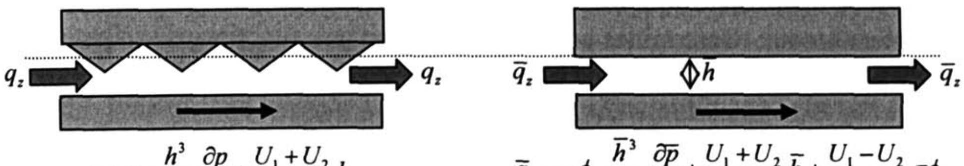

$$q_z = -\frac{h^3}{12\mu}\frac{\partial p}{\partial z} + \frac{U_1 + U_2}{2}h$$

$$\bar{q}_z = -\phi_z \frac{\bar{h}^3}{12\mu}\frac{\partial \bar{p}}{\partial z} + \frac{U_1 + U_2}{2}\bar{h} + \frac{U_1 - U_2}{2}\sigma\phi_s$$

Figure 5.6: Comparison of Rough and Smooth Surface Flow Rates.

The shear flow factor, ϕ_s, represents the changes in Poiseuille flow due to the pressure distribution that is generated by the sliding motion of the rough surface. The pressure flow factors, ϕ_x and ϕ_z, represent the changes in the Poiseuille flow due to roughness and average pressure difference alone. The Couette flow is unchanged by roughness, if we assume that there is no inter-asperity cavitation present.

A mass balance based on these average flow equations results in the average Reynolds equation, as proposed by Patir and Cheng [17]. When combined with the universal Reynolds equation, it results in a governing equation that allows macroscale cavitation, but does not account for inter-asperity cavitation [25].

$$\frac{\partial}{\partial \hat{z}}\left[\phi_z \hat{h}^3 \frac{\partial (F\Phi)}{\partial \hat{z}}\right] + \kappa^2 \frac{\partial}{\partial \hat{x}}\left[\phi_x \hat{h}^3 \frac{\partial (F\Phi)}{\partial \hat{x}}\right]$$
$$= \gamma \frac{\partial}{\partial \hat{z}}\left\{[1+(1-F)\Phi]\hat{h}\right\} + \gamma \frac{\sigma}{h_{ref}} \frac{\partial}{\partial \hat{z}}\{F\phi_s\} + 2\gamma \frac{\partial}{\partial \hat{t}}\left\{[1+(1-F)\Phi]\hat{h}\right\}$$

For striated, transverse roughness, as in the case of the piston tooling marks, analytical expressions for these flow factors have been derived [17, 40], and for the specific case of a triangular wave, of amplitude Ω, we can obtain the following equations [18].

$$\phi_z = \left[1 - \left(\frac{\Omega}{h}\right)^2\right]^2, \quad \phi_x = 1 + \left(\frac{\Omega}{h}\right)^2, \quad \phi_s = \frac{\Omega}{\sigma}\frac{\Omega}{h}$$

Similarly, shear stress factors were also developed by Patir and Cheng [41], and for striated, transverse roughness the analytical expressions were provided by Zhu et al [18]:

$$\tau_{zy} = -\frac{\mu W_1}{h}(\phi_f + \phi_{fs}) - \phi_{fp}\frac{h}{2}\frac{\partial p}{\partial z}$$
$$\phi_f = \frac{h}{2\Omega}\ln\left(\frac{h+\Omega}{h-\Omega}\right), \qquad \phi_{fs} = \frac{3}{2}\left[\frac{h}{\Omega}\ln\left(\frac{h+\Omega}{h-\Omega}\right) - 2\right], \qquad \phi_{fp} = 1 - \left(\frac{\Omega}{h}\right)^2$$

5.2.5. Combining the Piston – Cylinder Bore Interface Sub-Models

As discussed in Section 2.3.3, the piston - cylinder bore interface model can be considered to be made up of four sub-models:

- Contact model: Determines pressure generation as a function of surface overlap (see Section 2.3.3.1).

  $$p_{asp} = \begin{cases} C_1 (h_{asp} - h)^{C_2}, & h \le h_{asp} \\ 0, & h > h_{asp} \end{cases}$$

  where p_{asp} is the average asperity contact pressure, h is the local gap height between the mean surface lines, h_{asp} is a measure of asperity or tooling mark height, as appropriate, and C_1 and C_2 are the corresponding user supplied constants.

- Contact friction model: Determines friction force as a function of normal force and relative surface velocity (see Section 2.3.3.2).

$$\mathbf{F}_F = -sign(\Delta\dot{x}_z) f F_N \mathbf{k}$$

where f is the coefficient of friction, F_N is the contact force generated at the surface, and $\Delta\dot{x}_z$ is the axial velocity of the piston, relative to the cylinder bore.

- Fluid model: Determines hydrodynamic pressure generation, shear stress and oil flow as a function of surface motion and oil film thickness (see Section 5.2.3).

$$\frac{\partial}{\partial\hat{z}}\left[\hat{h}_T^{\,3}\frac{\partial(F\Phi)}{\partial\hat{z}}\right]+\kappa^2\frac{\partial}{\partial\hat{x}}\left[\hat{h}_T^{\,3}\frac{\partial(F\Phi)}{\partial\hat{x}}\right]=\gamma\frac{\partial}{\partial\hat{z}}\left\{[1+(1-F)\Phi]\hat{h}_T\right\}+2\gamma\frac{\partial}{\partial\hat{t}}\left\{[1+(1-F)\Phi]\hat{h}_T\right\}$$

- Compliance matrix: Determines piston surface deformation as a function of normal force (see Section 2.3.3.4).

$$\{\text{Radial Deformation}\} = [\text{Compliance Matrix}]\{\text{Normal Force}\}$$

Combining these equations we form a highly non-linear system, with a large number of variables. At each iteration of the solver for piston dynamics, that is, for a specified rigid position of the piston, at each node i of the piston-cylinder bore interface we have four unknowns:

1. The radial deformation of the piston, $rdef_i$,
2. The cavitation parameter, F_i,
3. The global variable (representing pressure or oil fraction), ϕ_i, and
4. The asperity contact pressure, p_{asp}.

For the purpose of calculating the hydrodynamic and asperity contact pressure distribution we require a very fine grid, particularly for direct numerical simulation of piston skirt tooling marks. The size of the compliance matrix is proportional to the square of the number of grid points, which very quickly becomes prohibitively large, both in terms of memory storage requirements, and calculation times. It is therefore more efficient to use two grids:

1. A coarse grid, over which the radial deformation of the piston is defined. Two-dimensional quadratic interpolation is then used to define the radial deformation over the fine grid.
2. A fine grid, over which the hydrodynamic and asperity contact pressures, and corresponding shear stress, contact friction and oil transport, are calculated. The normal and friction forces on the coarse grid are then obtained by integrating hydrodynamic and asperity contact pressures, shear stress, and contact friction over the coarse grid.

The solution procedure for combining these two grids is summarized in Figure 5.7. The solver for radial deformation is discussed in more detail in Section 5.5 and the hydrodynamic fluid solver is discussed in Section 5.3.1. The asperity contact pressure and contact friction are calculated directly at each grid point with a gap height less than the user specified limiting asperity contact height, h_{asp}, according to the above equations.

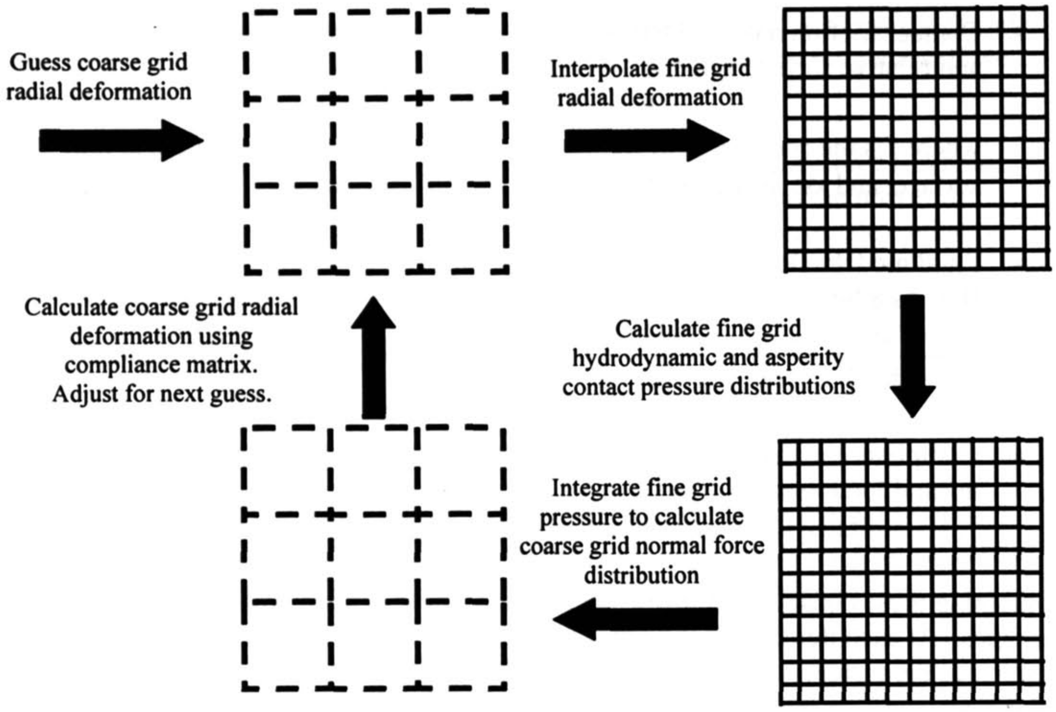

Figure 5.7: Solution Procedure for Piston – Cylinder Bore Interface

5.3. Quasi-Steady Hydrodynamic Lubrication Model

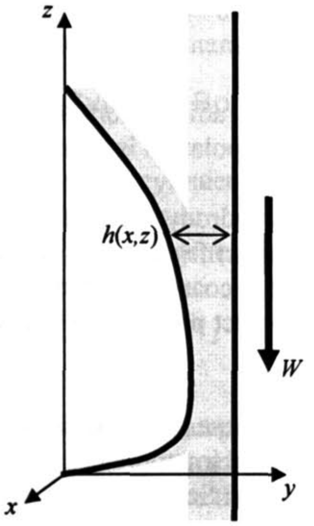

Figure 5.8: Quasi-Steady Hydrodynamic Lubrication

For situations where the two surfaces can be assumed to be rigid, and at least one surface is flat, the gap height distribution is steady with respect to the optionally contoured surface, as depicted in Figure 5.8, and the pressure distribution governed by the steady form of the Universal Reynolds equation:

$$\frac{\partial}{\partial \hat{z}}\left[\hat{h}^3 \frac{\partial(F\Phi)}{\partial \hat{z}}\right] + \kappa^2 \frac{\partial}{\partial \hat{x}}\left[\hat{h}^3 \frac{\partial(F\Phi)}{\partial \hat{x}}\right] = \gamma \frac{\partial}{\partial \hat{z}}\left\{\left[1+(1-F)\Phi\right]\hat{h}\right\}$$

A quasi-steady hydrodynamic lubrication model for the piston – cylinder bore interface was developed, based on an existing hydrodynamic model by Li [42].

5.3.1. Numerical Solution Scheme

The numerical algorithm used to solve the governing equations is described in detail by Li [42]. Similar to Payvar and Salant [39], the control volume method [43] was used to discretize the governing equation, but with some differences in the choices of interface values. The control volume method is based on the integration of the mass flux, over the boundaries of each control volume element, and therefore results in conservation of mass for each element. The mass flux across an interface is defined by:

- The conductivity of the interface, $\hat{h}^3$, defined by the harmonic mean of the conductivities at the two nodes related to that boundary.
- The pressure gradient on the interface, $\frac{\partial(F\Phi)}{\partial \hat{z}}$ or $\frac{\partial(F\Phi)}{\partial \hat{x}}$, defined as the difference in node pressures divided by the difference in node positions.
- The height of the interface, $\hat{h}$, defined by the harmonic mean of the heights at the two nodes.
- The upwind velocity, W_1, and relative density, $\left[1+(1-F)\Phi\right]$.

$$\dot{m}_z = \rho \frac{W_1 h_{ref}}{2\gamma}\left[-\hat{h}_T{}^3 \frac{\partial(F\Phi)}{\partial \hat{z}} + \gamma\left[1+(1-F)\Phi\right]\hat{h}_T\right]$$

$$\dot{m}_y = \rho \frac{W_1 h_{ref}}{2\gamma}\frac{z_{ref}}{x_{ref}}\left[-\hat{h}_T{}^3 \frac{\partial(F\Phi)}{\partial \hat{x}}\right]$$

A minimum allowable height for the fluid model, h_{lim}, is specified by the user. This limit should be used to prevent the hydrodynamic pressure from exceeding the Yield Stress of the surface, and the shear stress from exceeding a value which would cause the friction coefficient to exceed that of solid-solid contact. It should also be larger than the gap height at which the fluid can no longer be considered a continuous material, and smaller than the geometric resolution of the surface profiles. Typically a value of 0.1-0.5μm was set for the purposes of this project due to the fact that the surface profiles can not be considered to be accurate to this level. Any node below this limit is considered to be a contact node. To avoid discontinuity in the pressure, and more accurately represent to balance of hydrodynamic and asperity contact pressure, the fluid pressure at surrounding nodes is applied to the contact region.

Both the cavitation parameter, F, and global variable, Φ, were supplied along each boundary, as either full film at the crankcase pressure, or partial film with the global variable calculated from the ratio of oil film thickness, OFT, to gap height, h.

- Full film: $F = 1$, Φ = Crankcase pressure ~ 1 bar
- Partial film: $F = 0$, $\Phi = -(1 - \mathrm{OFT}/h)$

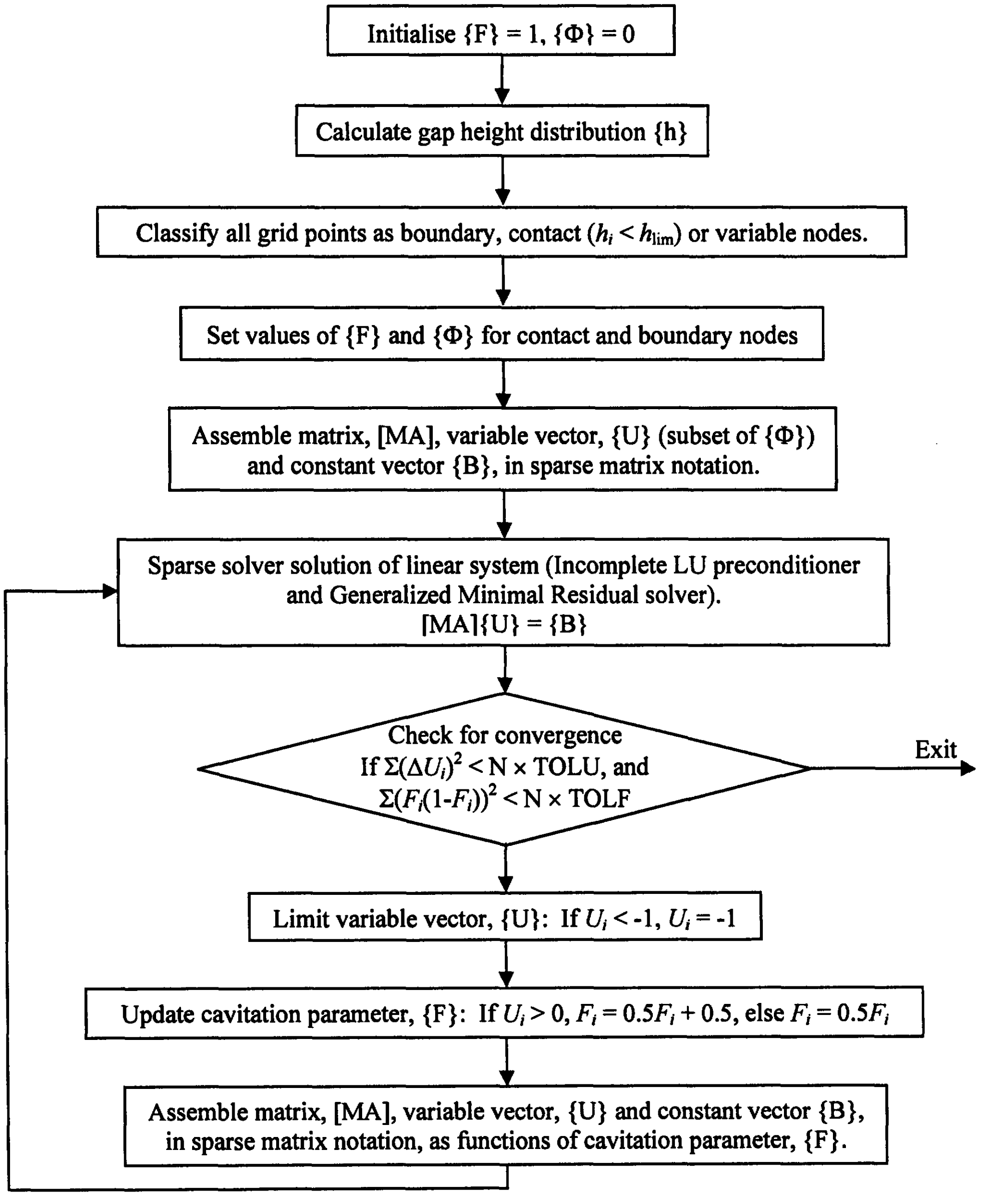

Figure 5.9: Quasi-Steady Hydrodynamic Lubrication Solution Algorithm

The resulting discretised equations form a very sparse system, so an iterative solution using a sparse solver for a linear system of equations from 'SPARSKIT, Version 2' [44], and a relaxation coefficient to adjust the cavitation parameter, was applied and found to be very efficient and stable. The sparse solver, *pgmres*, is a preconditioned generalized minimal residual solver [45], and makes use of an incomplete LU factorization preconditioner, *ilut*. The iterative solution algorithm is summarized in Figure 5.9.

5.3.2. Quasi-Steady Sliding Results

The quasi-steady hydrodynamic lubrication model provides a fast running and easy to use tool for investigating quasi-steady sliding behavior. In order to test the accuracy of the fluid model a set of simple 2D problems, for which analytical solutions are well defined, were simulated. For each test case it was confirmed that:

- the correct pressure distribution is generated,
- the calculated volume flow rates, shear stress, normal force and friction force are accurate, and
- mass is conserved for each control volume.

The results of these tests are included in Appendix 2.

5.3.2.1. Quasi-Steady Sliding of a Typical Piston Profile

A more realistic piston profile, shown in Figure 5.10, was then simulated. For the purpose of estimating piston dynamics, the net normal force generated at the piston – cylinder bore interface is our focus, while for investigating friction generation and oil transport, the friction force, friction coefficient and outflow rate are most important.

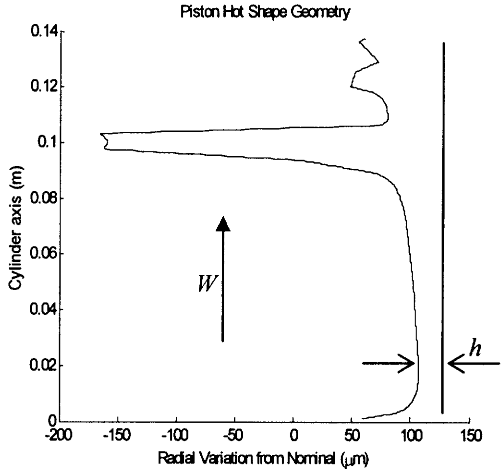

Figure 5.10: Quasi-Steady Sliding of a Typical Piston Profile

Grid convergence was tested, as demonstrated in Figure 5.11, and 51 x 51 grid was determined to be more than adequate to start our analysis. The oil flow rates in and out of the system were essentially independent of grid size, over the range tested, and are not presented here. To better decide where the trade off between calculation time and accuracy should be set, we must first develop a better understanding of the system's behavior, and what features are critical in accurately determining piston dynamics, friction generation and oil transport.

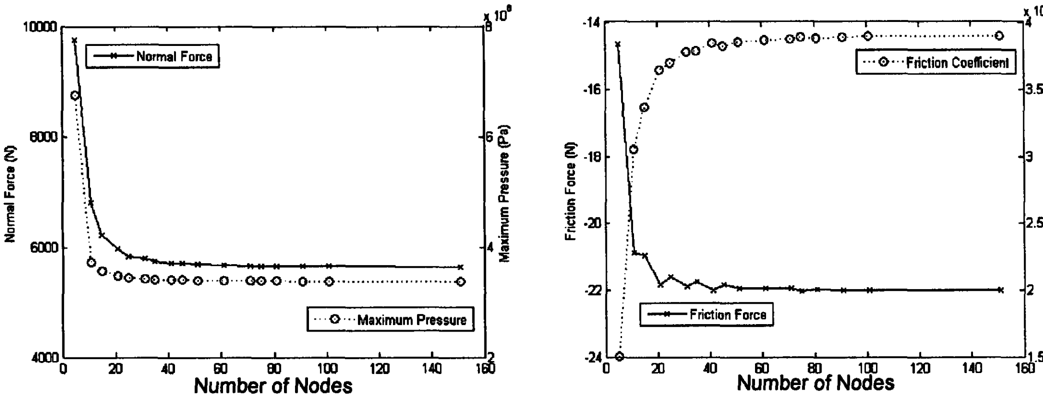

Figure 5.11: Effect of Grid Size on Normal and Friction Force Generation

The results presented in Figure 5.12 were obtained using a 51 x 51 grid, sliding speed, W, of 10m/s and fluid dynamic viscosity, μ, of 0.01 Pas, with no limit placed on the minimum allowable gap height for the fluid calculation, and no asperity contact. The log-log plot of normal force and maximum pressure against minimum gap height, h, demonstrates increasing pressure generation as the two surfaces approach each other, with a gradient of close to -3.2 for the pressure curve, and -2/3 for the normal force, implying that for this particular profile, at these conditions:

$$p_{\max} \sim \frac{1}{h^{3/2}}$$

$$F_N \sim \frac{1}{h^{2/3}}$$

No limit was set for the minimum fluid clearance in generating these results. Typically pistons are made of Aluminum or steel, and the minimum of their Yield stresses (0.3 GPa) was exceeded for clearances below 0.2 µm, providing a limiting lubrication flow clearance from a material point of view.

The log-log plot of friction force and friction coefficient versus minimum gap height demonstrates increasing friction force as the two surface approach each other, and generally a decreasing friction coefficient (although it does increase initially). The gradient of the friction force curve varies significantly from around -1 at large clearances where Couette flow dominates, becoming increasingly flat as the gap height decreases. With pure hydrodynamic lubrication, and a low dynamic viscosity, the friction coefficients are very small (0.0002 – 0.004), and decreases with decreasing gap height, with a gradient of about 1/3 indicating that for this profile, at this speed and viscosity:

$$f \sim h^{1/3}$$

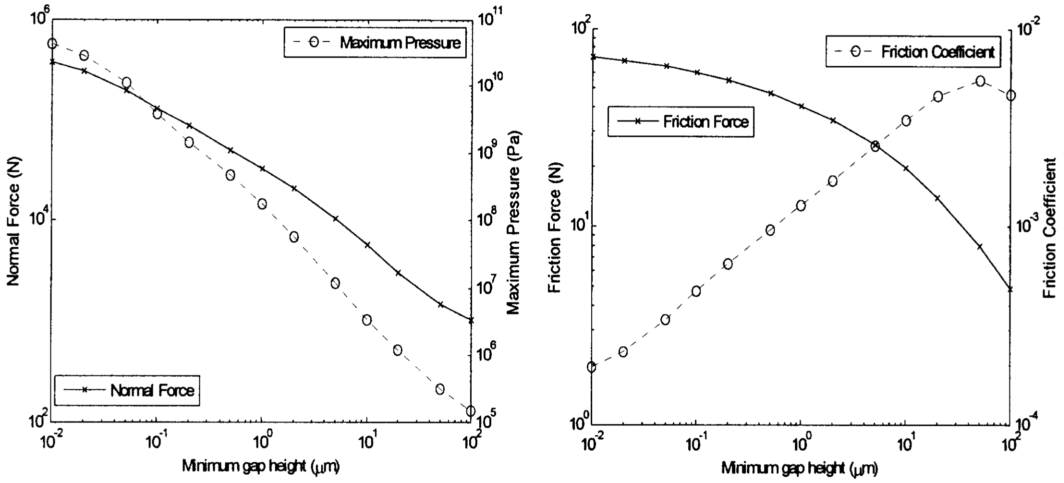

Figure 5.12: Effect of Gap Height on Pressure and Friction Generation.

The friction coefficient does not approach that of solid-solid contact friction and therefore does not require the clearance height to be limited. Given that the physically feasible clearances in terms of pressure generation and friction coefficient are smaller than the resolution of our surface geometry, we can limit the clearance height based on geometrical considerations alone.

The inlet and outlet flow rates are scaled by the sliding velocity and average over the width of the piston skirt to provide an oil film thickness, h_{oil}. The inlet is assumed to be fully flooded, so the inlet flow rate is given by:

$$q_{in} = \frac{h_{inlet}W}{2} = h_{oil}W$$

The inlet OFT therefore scales linearly with the minimum gap height. As shown in Figure 5.13, the outlet OFT also scales linearly with the minimum gap height over the range of conditions tested.

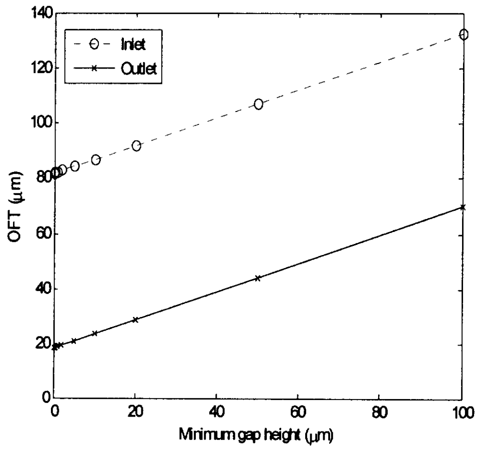

Figure 5.13: Effect of Gap Height on Oil Film Thickness

A limit of 0.5 μm was then placed on the fluid gap height, based on the geometry resolution. A range of sliding speeds, dynamic viscosities and minimum gap heights were simulated, and the results are presented in Figures 5.14 and 5.15.

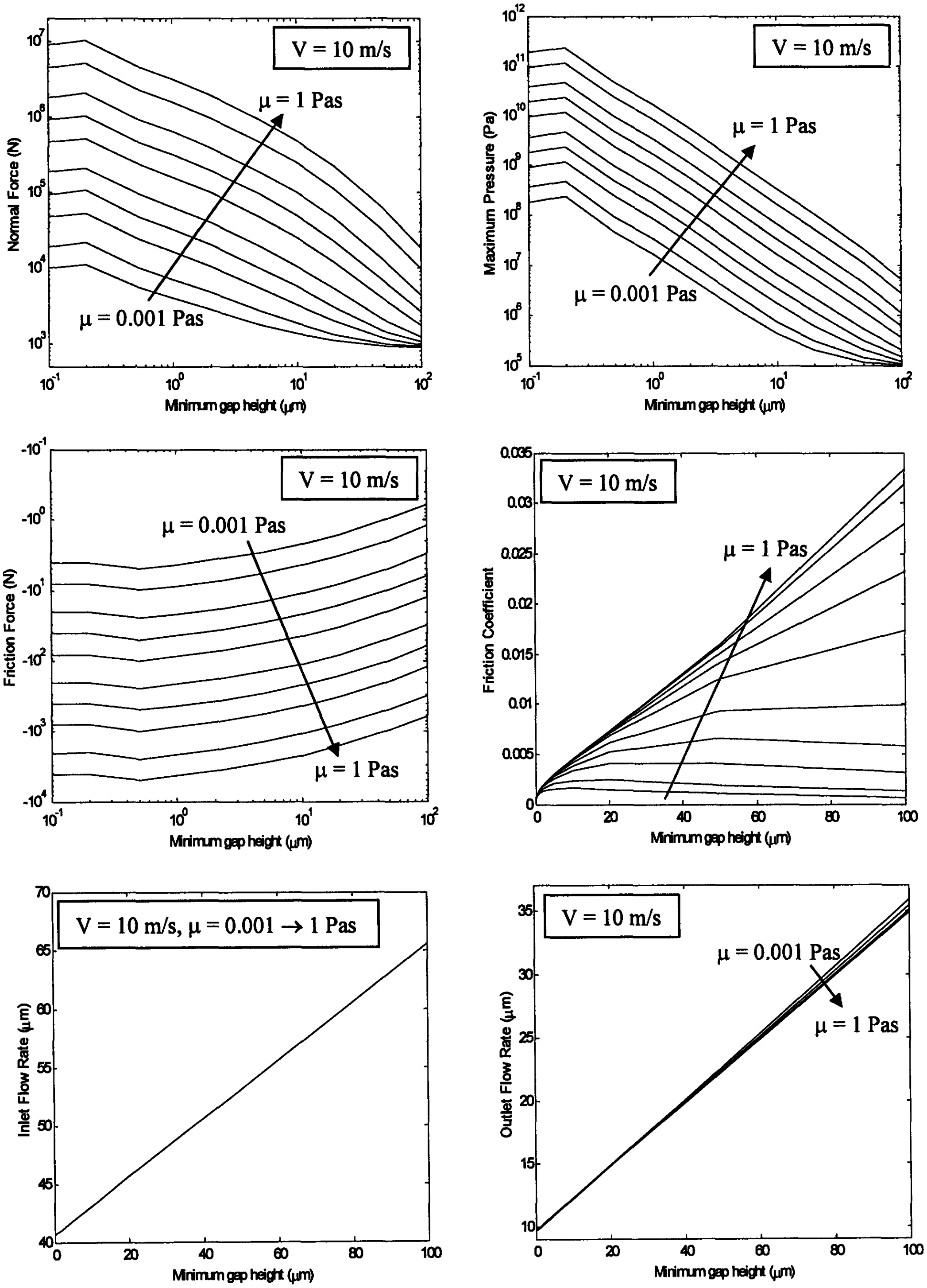

Figure 5.14: Effect of Dynamic Viscosity on Lubrication Flow

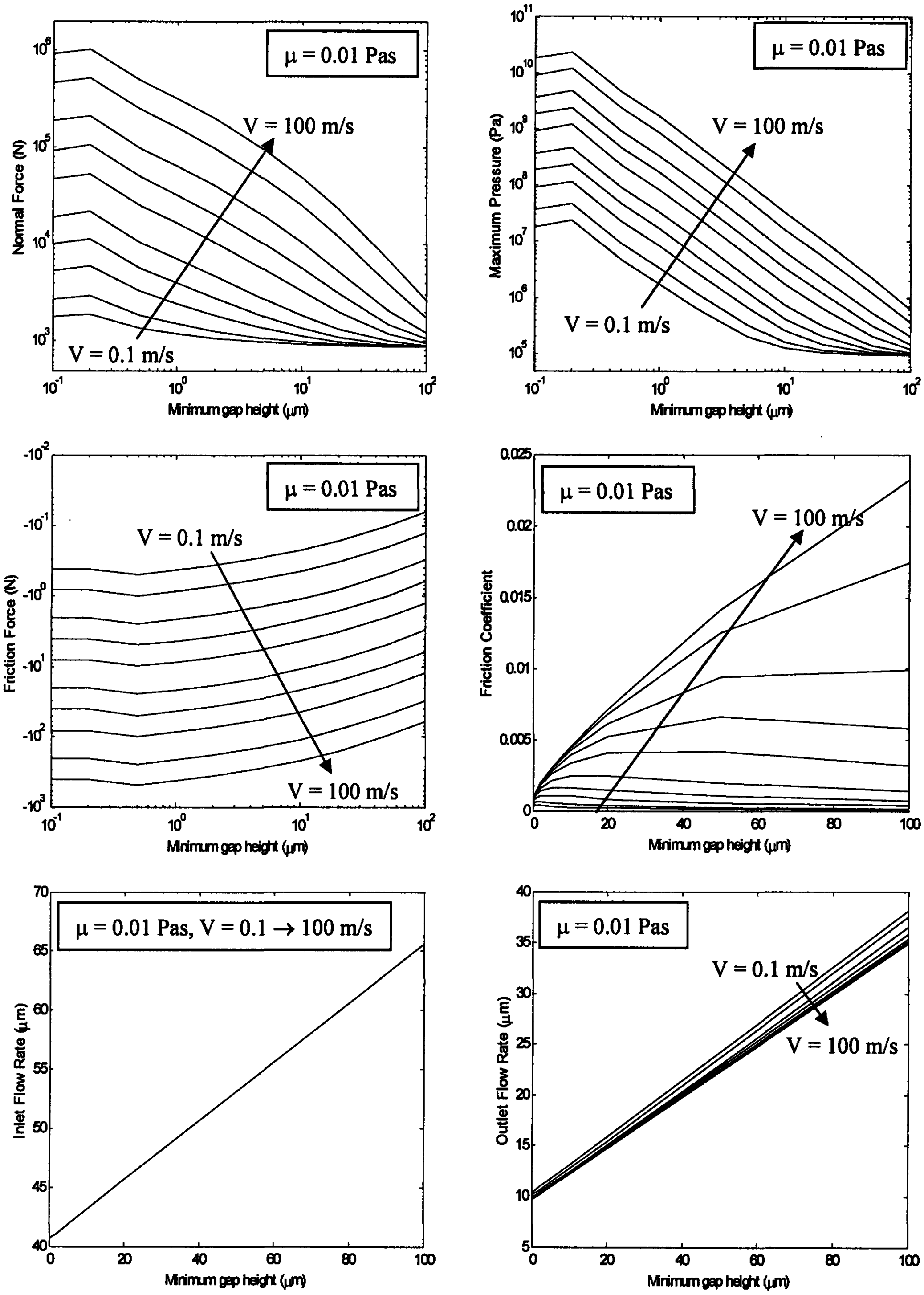

Figure 5.15: Effect of Speed on Lubrication Flow

These results demonstrate that the normal force and maximum pressure increase with increasing dynamic viscosity and speed, and that for the high viscosities simulated the maximum pressure exceeds the Yield Stress of Aluminum (typical piston material) indicating that the minimum allowable gap height should be increased if these running conditions are expected. The friction force and friction coefficient both increase significantly with increasing speed and dynamic viscosity, but the friction coefficient does not exceed that of solid-solid contact. The inlet flow rate, in microns of oil film thickness is unaffected by the speed or viscosity, but the outlet flow rate decreases slightly, particularly at larger clearances with increasing speed and viscosity.

In solving piston dynamics, it is essentially the side load that is specified, and gap height that is unknown. The side load on the piston is typically of the order of 10^4 N and the lateral force balance on the piston is solved to within about 0.1N. In this range, small changes in normal force correspond to extremely small changes in gap height. The hydrodynamic friction forces are very small, compared to those generated by asperity contact, and therefore our main priority is accurate determination of gap height. It would therefore appear that grid numbers as low as 21 are adequate for describing the piston – cylinder bore interface, in the absence of piston skirt tooling marks.

5.3.2.2. Investigation of the Effect of Tooling Marks During Sliding

A triangular wave was then added to the piston profile to represent the effect of tooling marks. Initially the ovality was removed and periodic boundary conditions applied, resulting in a two-dimensional flow.

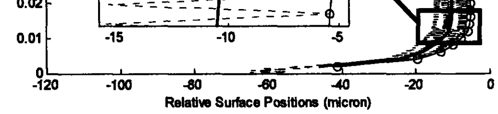

Figure 5.16: Tooling Marks - 2D Surface Position, Relative to Flat Sliding Surface.

Compared to the mean surface line, the wavy surface generated by the piston tooling marks significantly blocks flow in the axial direction, leading to an increase in pressure, as shown in Figure 5.17, which is significantly less than that which would be obtained by the outer surface profile. At this clearance, the general shape of the pressure distribution is determined by the piston profile, with increased pressure being generated on the intake side of the minimum height position, and cavitation occurring on the outlet side. The tooling marks have the effect of moving the two surfaces closer together, and add a small- scale wave, or perturbation, to the pressure distribution.

Commonly referred to as inter-asperity cavitation, the small-scale cavitation that occurs between wave peaks before the onset of large-scale cavitation, is clearly visible in Figure 5.18. Note that this model does not currently consider some of the detailed physics affecting cavitation, such as surface tension, and therefore without experimental results it is difficult to predict whether cavitation would physically occur.

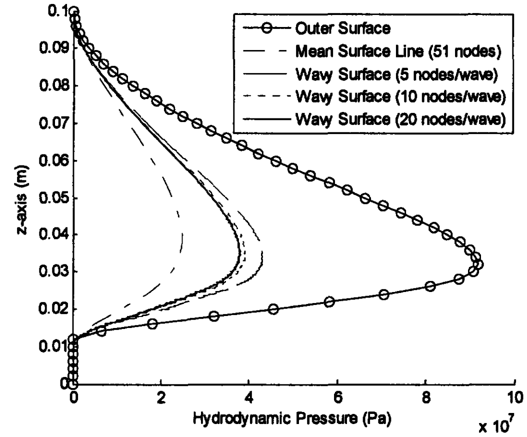

Figure 5.17: Pressure Distribution for 2D Sliding

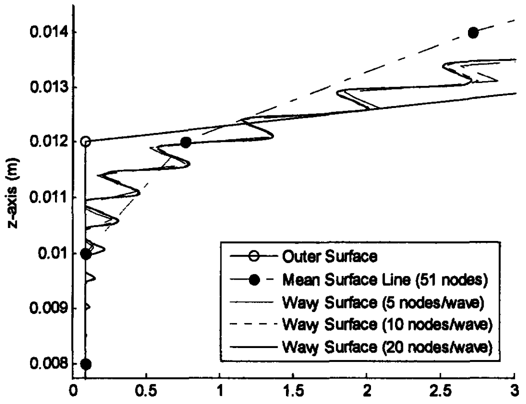

Figure 5.18: Cavitation Region for 2D Sliding

Three different grid densities were used to describe the wavy surface. The peak percentage pressure difference when comparing 10 and 20 nodes per wave is about 4% of the local value in the full film region, and 10% in the small-scale cavitation region.

The boundary conditions were then altered to allow circumferential flow out of the sides of the calculation domain. In Figure 5.19 we can see that by allowing circumferential flow, the pressures generated are significantly reduced, even with 2D geometry. Adding ovality, we then see a further reduction in pressure, and an alteration in the profile of the pressure distribution, due to the ovality profile. Figure 5.20 contains a contour plot of the pressure distribution for the mean surface line and wavy surface, with ovality. The wavy surface results in a significantly wider pressure distribution, particularly around the peak pressure. The tooling marks lead to significant small-scale cavitation in a very wide region, throughout which pressure varies significantly.

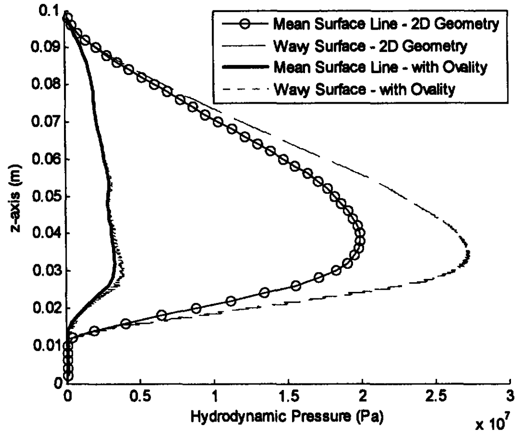

Figure 5.19: Centreline Pressure Distribution for 3D Sliding

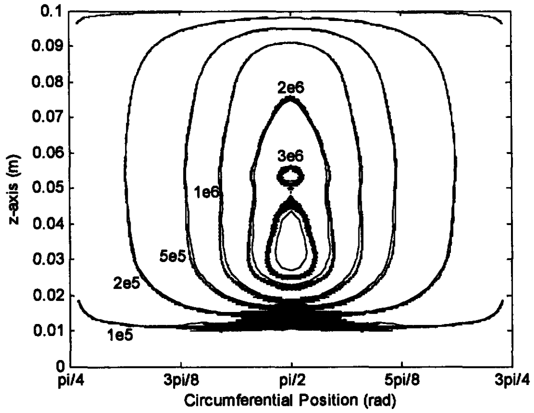

Figure 5.20: Pressure Distribution for 3D Sliding

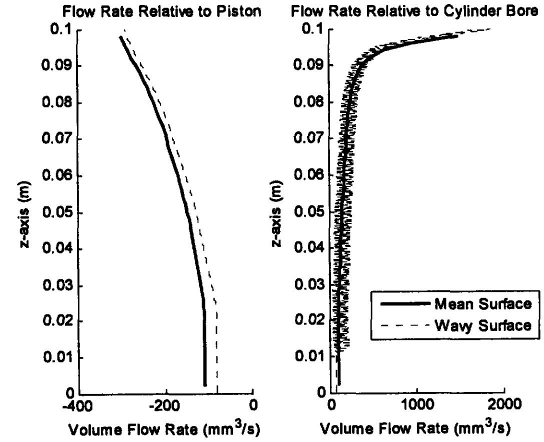

Figure 5.21: Centreline Axial Flow Rates

The axial flow rate relative to the piston is decreased due to the additional resistance created by the tooling marks, as shown in Figure 5.21. This results in more oil being scraped upwards by the piston, and a decrease in the oil film thickness left behind on the bore. The flow rate relative to the cylinder bore, which includes the additional transport term due to the moving control volumes, provides insight into the oil carrying capacity of the piston, and the way in which it is possible for oil to be transported along the cylinder bore.

As the clearance between the two surfaces decreases, the effect of the tooling marks increases. When the minimum clearance between the outer surfaces is zero, the pressure variation within the wave peaks increases to the same order of magnitude as the peak pressure, as shown in Figure 5.22. Pushing the surfaces even closer together, so that we obtain a nominal outer surface overlap of 1 micron, the pressure variation and width of the small-scale cavitation region increase further.

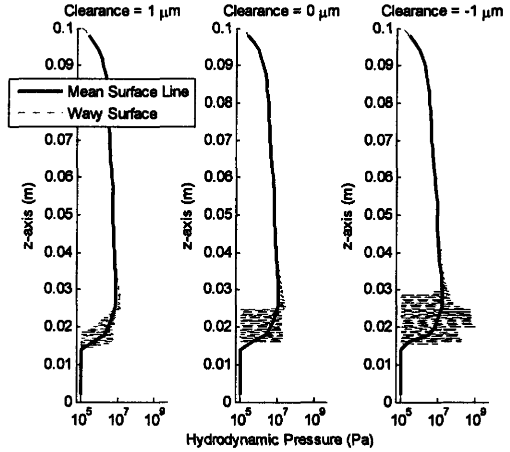

Figure 5.22: Onset of Contact

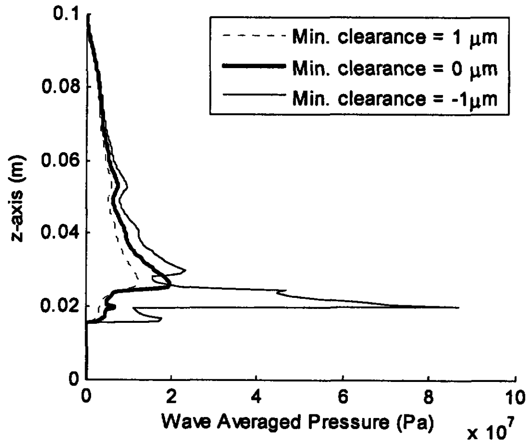

Figure 5.23: Wave-averaged pressure distribution

Averaging the hydrodynamic pressure over each wavelength, we obtain the plots shown in Figure 5.23. Significant variations in the wave-averaged pressure occur throughout the small-scale cavitation region. Outside of this region, the pressure distribution is relatively smooth.

Analytical expressions for Patir and Cheng flow factors were confirmed numerically, and then applied to the current situation. The wavy surface results obtained via direct numerical simulation were averaged over the same grid as the Patir and Cheng results, and the resulting pressure distributions are shown in Figures 5.24 and 5.25.

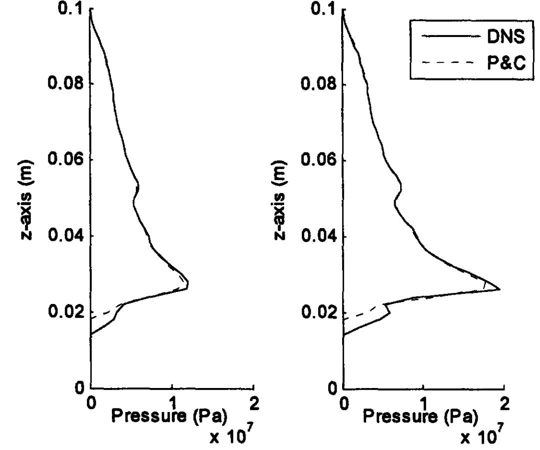

Figure 5.24: Centreline average pressure distributions

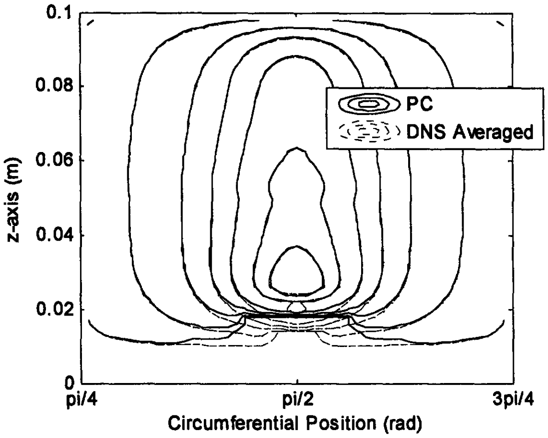

Figure 5.25: Average pressure distributions

Even at these very small clearances, the Patir and Cheng model performs very well over a large area of the skirt, but there is significant underestimation of the pressure in the region approaching the peak pressure, and extending throughout the small-scale cavitation region.

In modeling piston motion, friction and oil transport, we are more concerned with the net forces and moments acting on the piston, and the net oil flow rate, rather than the detailed pressure distribution. It is therefore on this basis that we should compare our results. Figures 5.26 and 5.27 show the total normal force and side flow rates, at a range of minimum separations. These results indicate that the Patir and Cheng model allows more flow out the sides of the calculation domain, resulting in a lower normal force. Table 5.2 shows the percentage variation, or error, in normal force and side flow, compared to the results obtained via direct numerical simulation with 20 nodes/wave.

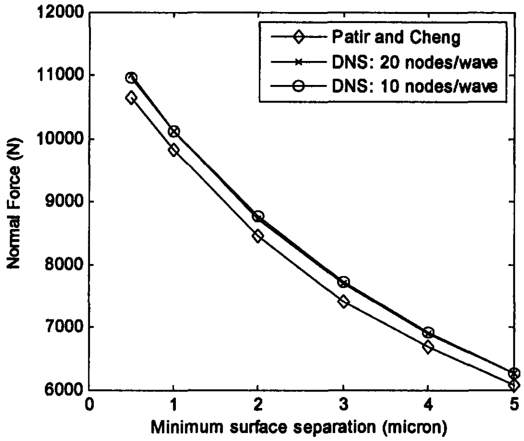

Figure 5.26: Normal Force

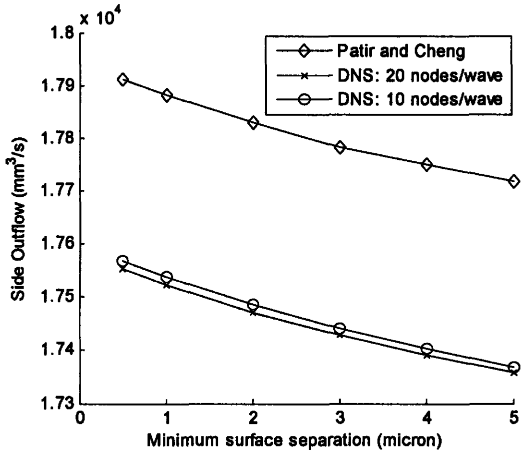

Figure 5.27: Side Flow Rate

Method	Calc. Time	Normal Force % Error	Side Flow % Error
Patir & Cheng	2s	3-4	2
DNS: 10 Nodes/wave	70-80s	0.1-0.4	0.06-0.08
DNS: 20 Nodes/wave	120-155s	0	0

Table 5.2: Comparison of Solution Methods

Comparing the calculation times and the typical percentage errors, we can see that there is a significant trade off. The decision of which method is most appropriate to use depends very much on the application. If our focus is accurate determination of the piston dynamics, then it may be acceptable to have an error of 3% in the normal force generated, but if our focus is accurate determination of friction or oil transport, these errors would appear to be unacceptable. It is in the very region where the variation between the two methods occur that asperity contact friction is generated, and a small difference in normal load (and therefore surface position) or oil availability, can lead to a significant change in friction.

Given that the variation in pressure appears to be limited to the region around peak pressure and the small-scale cavitation region, it may be possible to develop a hybrid method wherein the average Reynolds equation is used first to obtain the pressure over the entire domain, and then a very fine grid is used on a small portion of the domain, using the previously obtained results as boundary conditions.

5.3.2.3. Quasi-Steady Hydrodynamic Lubrication Flow Conclusions

The quasi-steady hydrodynamic lubrication model has been tested over a range of sliding flows, and proven to provide a fast running and easy to use tool for investigating quasi-steady sliding behavior. Depending on the specific surface geometry, grid sizes as low as 21 x 21 can be sufficient to accurately capture pressure generation.

Using a very fine grid, it has been demonstrated that piston tooling marks have a significant impact on pressure generation and oil transport. Compared to the mean surface line, the wavy surface generates:

- higher average pressures,
- lower axial flow rates, and increased side flow,
- pressure perturbations up to the same order as the peak pressure for very small clearances, and
- a significant small-scale cavitation region in which accurate tracking of oil availability will become critical for estimating asperity contact friction, particularly in the unsteady case.

These features are unable to be resolved accurately using a coarse grid, even when combined with the average Reynolds equation proposed by Patir and Cheng. The results obtained using Patir and Cheng's method, however, are very accurate outside of the critical region from just before the peak pressure until the end of the small-scale cavitation region. It may therefore be possible to develop a hybrid method combining the average flow model, with a correction applied on a smaller domain containing the critical region, thereby allowing accuracy to be achieved in a more efficient manner.

5.4. Unsteady Hydrodynamic Lubrication Model

An unsteady hydrodynamic lubrication model is required when the two surfaces can be assumed to be rigid, but:

- neither of the surfaces are flat,
- there is surface motion parallel to the gap height, or
- the oil supply boundary conditions vary in time.

The first two of these result in a gap height distribution which is a function of time, as depicted in Figure 5.28, while the last one results in variation in the cavitation parameter and oil fill ratio. The pressure distribution is then governed by the unsteady form of the Universal Reynolds equation:

$$\frac{\partial}{\partial \hat{z}}\left[\hat{h}_T{}^3 \frac{\partial (F\Phi)}{\partial \hat{z}}\right] + \kappa^2 \frac{\partial}{\partial \hat{x}}\left[\hat{h}_T{}^3 \frac{\partial (F\Phi)}{\partial \hat{x}}\right] = \gamma \frac{\partial}{\partial \hat{z}}\left\{[1+(1-F)\Phi]\hat{h}_T\right\} + 2\gamma \frac{\partial}{\partial \hat{t}}\left\{[1+(1-F)\Phi]\hat{h}_T\right\}$$

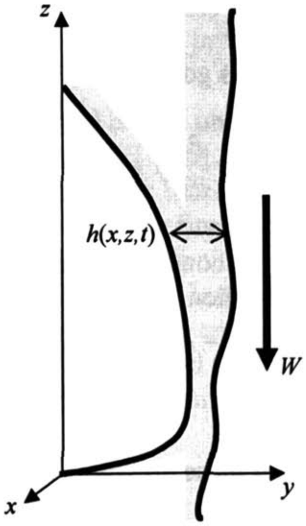

Figure 5.28: Unsteady Hydrodynamic Lubrication

The quasi-steady hydrodynamic lubrication model discussed in Section 5.3 was used as the basis for the unsteady model, with the additional of the unsteady term, which represents the time rate of change of mass contained in each control volume.

5.4.1. Numerical Solution Scheme

As described in Section 5.3.1, the control volume method [43] was used to discretize the governing equations in space. A fully implicit formulation of the time derivative was used, with the local node cavitation parameter, global variable and gap height (this is not an interface quantity). Initial conditions are required in addition to the boundary conditions described in Section 5.3, which must now also be provided as functions of time. The cavitation parameter, global variable and gap height distribution (and therefore radial surface deformation) must be provided in order to define the initial condition. For the purposes of this project, the solution to the quasi-steady Universal Reynolds equation was used to define the initial conditions, and then the unsteady Universal Reynolds equation was solved stepping forward in time, using a fully implicit formulation. The solution algorithm at each time step is essentially the same at that for the quasi-steady hydrodynamic lubrication.

5.5. Elastohydrodynamic Lubrication Model

An elastohydrodynamic lubrication model is required when at least one of the two surfaces can no longer be assumed to be rigid, and therefore the surface deformations caused by the hydrodynamic and asperity contact pressures must be taken into account.

The hydrodynamic pressure distribution is governed by the unsteady form of the Universal Reynolds equation:

$$\frac{\partial}{\partial \hat{z}}\left[\hat{h}_T^{\,3}\frac{\partial(F\Phi)}{\partial \hat{z}}\right]+\kappa^2\frac{\partial}{\partial \hat{x}}\left[\hat{h}_T^{\,3}\frac{\partial(F\Phi)}{\partial \hat{x}}\right]=\gamma\frac{\partial}{\partial \hat{z}}\left\{[1+(1-F)\Phi]\hat{h}_T\right\}+2\gamma\frac{\partial}{\partial \hat{t}}\left\{[1+(1-F)\Phi]\hat{h}_T\right\}$$

The solid-solid contact pressure (asperity contact pressure) is governed by a contact model, as described in more detail in Section 2.3.3.1.:

$$p_{asp}=\begin{cases}C_1\left(h_{asp}-h\right)^{C_2}, & h\le h_{asp}\\ 0, & h>h_{asp}\end{cases}$$

The surface deformation resulting from these pressures is described using a Compliance matrix, as described in Section 2.3.3.4.:

$$\{\text{Radial Deformation}\}=[\text{Compliance Matrix}]\{(p_h+p_{asp})dA\}$$

The compliance matrix is a full, dense matrix, and therefore very expensive in terms of computation time and memory storage. It is often sufficiently accurate to use quite a coarse grid for the compliance matrix, while a significantly finer grid may be required to accurately describe the surface geometry and pressure generation, particularly for direct numerical simulation of piston skirt tooling marks. A method based on two grids was therefore implemented, interpolating the radial deformation between coarse grid points to determine deformed surface geometry at the fine grid nodes, and integrating hydrodynamic and asperity contact pressures over the fine grid to evaluate the normal force acting at coarse grid nodes.

The elastohydrodynamic model was then incorporated into the piston dynamics model, replacing the numerical solution method for the dry piston – cylinder bore interface, which is described in Section 2.6.

5.5.1. Numerical Solution Scheme

For each time step, the radial deformation is first estimated over the coarse grid, based on the gap height distribution for the two previous time steps, and the current rigid radial gap height distribution.

$$\begin{aligned}\{rdef\}^k = \{rdef\}^{k-1} &+ \text{WEIGHTR}\left(\{rdef\}^{k-1} - \{rdef\}^{k-2}\right)\\ &+ \text{WEIGHTH}\left[\{rrgap\}^k - \{rrgap\}^{k-1} - \text{WRRGAP}\left(\{rrgap\}^{k-1} - \{rrgap\}^{k-2}\right)\right]\end{aligned}$$

For WEIGHTH = 1, WRRGAP = WEIGHTR:

$$\begin{aligned}\{rdef\}^k - \{rrgap\}^k &= \left(\{rdef\}^{k-1} - \{rrgap\}^{k-1}\right)\\ &\quad + \text{WEIGHTR}\left[\left(\{rdef\}^{k-1} - \{rrgap\}^{k-1}\right) - \left(\{rdef\}^{k-2} - \{rrgap\}^{k-2}\right)\right]\\ \{h\}^k &= \{rrgap\}^k - \{rdef\}^k = \{h\}^{k-1} + \text{WEIGHTR}\left(\{h\}^{k-1} - \{h\}^{k-2}\right)\end{aligned}$$

The radial deformation of the fine grid is then obtained using a two-dimensional quadratic interpolation function, DQD2VL [36]. The resulting gap height distribution is calculated, and the unsteady hydrodynamic lubrication model is solved for the hydrodynamic pressure distribution over the fine grid, as described in Section 5.4. For nodes where the local height is less than the limiting fluid height, *hlim*, the hydrodynamic pressure is not calculated by the fluid solver. Instead, the hydrodynamic pressure generated at neighboring nodes is interpolated and applied to these nodes. Asperity contact pressure is calculated for all nodes, and the total normal force on each coarse grid node is evaluated by integrating the hydrodynamic and asperity contact pressures over the fine grid.

The radial deformation that would result from the normal forces exerted on the coarse grid, as predicted by the compliance matrix, is then compared to the estimated radial deformation:

$$\{Error\} = [\text{Compliance}]\{(p_h + p_{asp})dA\} - \{rdef\}$$

The solution is considered to be converged if maximum absolute value of the error is less than the user specified TOLFREE, which is a relatively large value used to ensure a free surface is sufficiently converged, and either the maximum absolute value of the error is less than TOLX, or the maximum absolute variation in the pressure distribution is less than TOLP. If convergence is not satisfied, then a new estimate for the radial deformation is generated using a user supplied weighting, WRDEF, multiplied by the previous error vector:

$$\{rdef\}^j = \{rdef\}^{j-1} + \text{WRDEF}\{Error\}^{j-1}$$

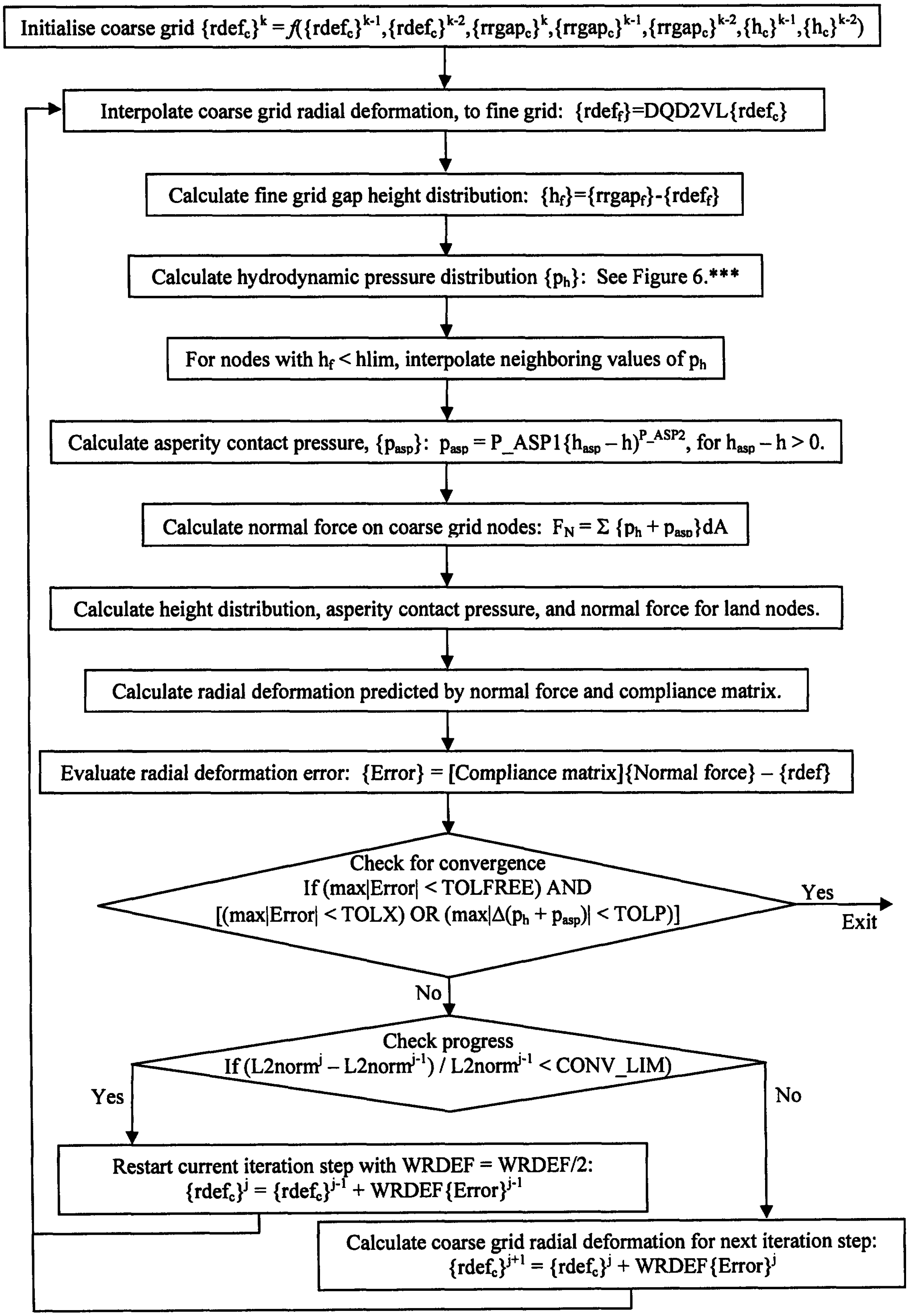

Figure 5.29: Numerical Algorithm for Elastohydrodynamic Lubrication

The convergence of this numerical method is very sensitive to the value of WRDEF. For large WRDEF the solution method will become unstable and diverge, while for very small values, progress will become too slow.

An aggressive scheme for optimizing WRDEF has therefore been employed. An initial value of WRDEF is supplied by the program user. At each new iteration step, the size of the error vector, *Error*, as defined by its l^2-norm is calculated:

$$L2norm = \sqrt{\sum_i Error_i^2}$$

The size of the error vector is then compared to that at the previous iteration step, and if there is not sufficient reduction, as specified by the user supplied, CONV_LIM, then the weighting, WRDEF is halved and the current iteration step is restarted using the new weighting:

```
If $\left( \frac{L2norm^j - L2norm^{j-1}}{L2norm^{j-1}} > \text{CONV\_LIM} \right)$ then
        $\text{WRDEF} = \text{WRDEF}/2$
        $\{rdef\}^j = \{rdef\}^{j-1} + \text{WRDEF}\{Error\}^{j-1}$
else
        $\{rdef\}^{j+1} = \{rdef\}^j + \text{WRDEF}\{Error\}^j$
end if
```

Additional adjustments to the weighting are made every NCHECK iteration steps depending on whether the convergence appears to be monotonic or oscillating, as predicted from the maximum value of the error vector. A minimum allowable value of this weighting, W_LIM, is supplied by the user.

Initially if the lower limit of the weighting, or the maximum number of iterations, are reached, the time step calculation is restarted with relaxed convergence criteria. The solution procedure for solving this set of equations is summarized in Figure 5.29.

5.6. Piston Oil Transport Model

In order to more accurately model the transport of oil, the following features were added to the piston dynamics model, as shown in Figure 5.30:

- Reservoirs were added to the top and base of the piston calculation domain to represent the ability of the piston chamfers to hold oil, and to allow additional oil to be added to the boundary of the calculation domain when the piston turns around, representing oil scraped by the oil control ring.

- Additional oil supply rates at the top and base of the piston can also be specified, corresponding to a pressurized oil supply or oil ring scraping throughout the stroke.
- The cylinder bore oil film thickness is specified at the start of the calculation, and can also be reset outside of the piston calculation domain each time the piston turns around to a new constant or distribution, or a linear combination of the old and new distributions. This resetting of the oil film thickness distribution can be used to represent the effect of oil supply to the cylinder bore from the crankshaft or pressurized oil supplies, and the effect oil being scraped from the cylinder bore by the ring pack.
- Cylinder bore oil reservoirs enable accurate mapping between the cylinder bore oil film thickness and the piston – cylinder bore interface calculation domain, both at the trailing edge of the calculation domain, and when the piston is scraping oil at the leading edge.
- Simple fractions are used to define the proportion of scraped oil that is placed in the piston and bore oil reservoirs, and the proportion of oil, in the reservoirs, which is available for release to the calculation domain or bore oil film thickness distribution.
- The reservoirs are specified as functions of circumferential position.

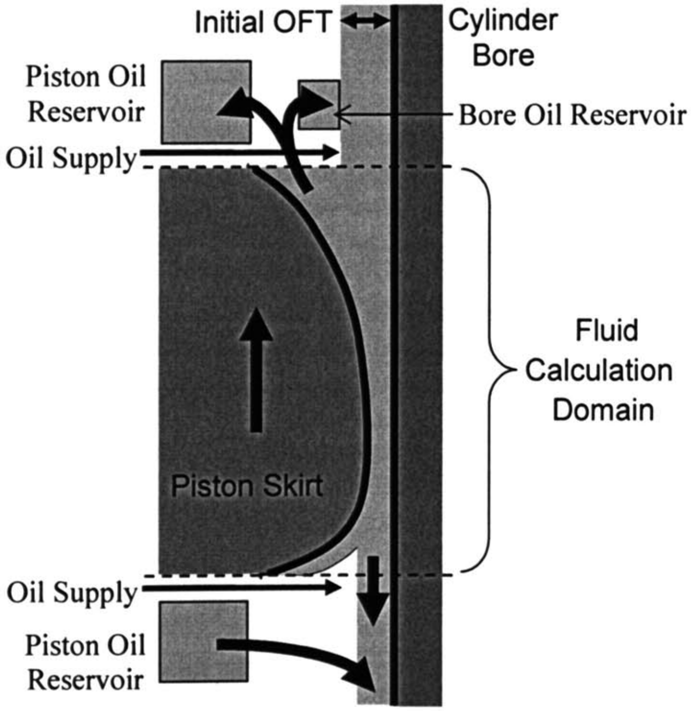

Figure 5.30: Oil Transport Model

6. Lubricated Piston Model Results

This chapter aims to:

- Provide a brief review of piston secondary motion, and discuss the expected effects of oil.
- Compare dry model and lubricated model results, and explain the dominant oil effects.
- Evaluate effective friction coefficient for lubricated model, as a function of crank angle position.
- Compare surface representations: outer surface, mean surface line, flow factor method, and direct numerical simulation of tooling marks.
- Examine oil transport on the piston skirt, and the effect of oil supply.

6.1. Expected Piston Secondary Motion

The dry model analysis carried out in Chapter 4 would lead us to the following expectations for the lubricated model results:

- Wrist-pin lateral force and moment are well defined, and relatively independent of the detailed piston – cylinder bore interface behavior, with the exception of lateral inertia driven fluctuations during the intake and exhaust stroke, which should be reduced by the cushioning effect of the oil.

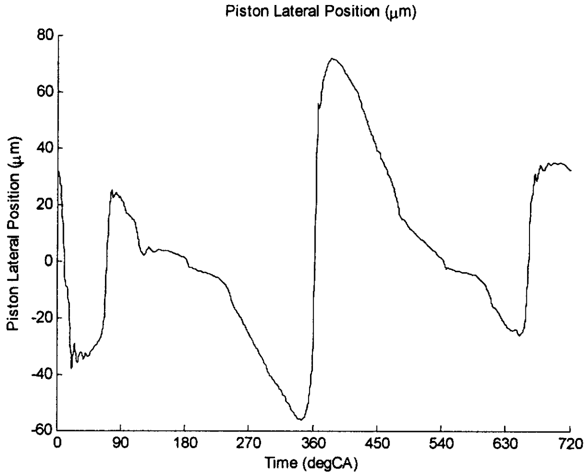

Figure 6.1: Dry Model – Piston Lateral Motion

- The piston – cylinder bore friction force should be significantly reduced by the presence of oil, as the side load is partially supported by hydrodynamic pressure, thereby reducing the extent of asperity contact. This may affect the piston tilt to a small degree, but is not expected to have a significant effect on lateral motion.
- As shown by the dry model results in Figure 6.1, for our sample heavy duty diesel engine, with the default running condition of 1200 rpm, full load, piston slap is expected to occur at:
  - 0, 180, 360 and 540 °CA due to the connecting-rod changing angle.
  - 55 and 650 °CA as the connecting-rod force changes from tension to compression and back again.
- It is expected that the presence of oil will not change the timing of the start of piston slaps, but will provide cushioning, slowing the piston's travel across the cylinder bore once contact with the oil is made, and reducing oscillations due to bouncing and tilt.
- Lateral motion in general will be reduced due to the fact that the incompressible oil physically reduces the available clearance, and can only be squeezed out in a finite amount of time.
- During piston slap, it is expected that squeeze flow will dominate, while around mid-stroke the peak velocities may result in shear flow dominating. Towards the end of each stroke, the low velocities will result in decreasing pressure generation, and the piston will move closer to the cylinder bore to compensate until the side load decreases sufficiently.
- In terms of piston tilt, we expect that:
  - The cushioning effect of the oil will reduce tilt oscillations, significantly changing the character of piston tilt during the intake and exhaust strokes.
  - Approaching combustion TDC, the wrist-pin moment will dominate, driving the piston to rotate negatively, toward the thrust side.

6.2. Comparison of lubricated and dry model behaviour

A simplified bore geometry was considered, consisting of a flat bore, with an increased nominal clearance (about 70μm), as shown in Figure 6.2. For the purposes of the fluid model, the piston was considered to be a smooth surface located at the mean surface line of the piston tooling marks, based on a 17 x 81 grid. An asperity contact model was then used to add contact forces beginning at a gap height of half the tooling mark wave height. Further discussion of different ways to model the piston – cylinder interface, and accurately capture the effect of piston tooling marks, is included in Section 6.3.

A range of oil film thicknesses were simulated, and the bore oil film thickness (OFT) outside of the piston skirt area, was replenished at each reversal of piston direction in order to achieve a constant inlet OFT, throughout the cycle. More realistic oil supply conditions are discussed in Section 6.4. Unfortunately, due to numerical instabilities discussed in Section 6.5, we were not able to obtain converged results for the 20 μm OFT case beyond 350 °CA.

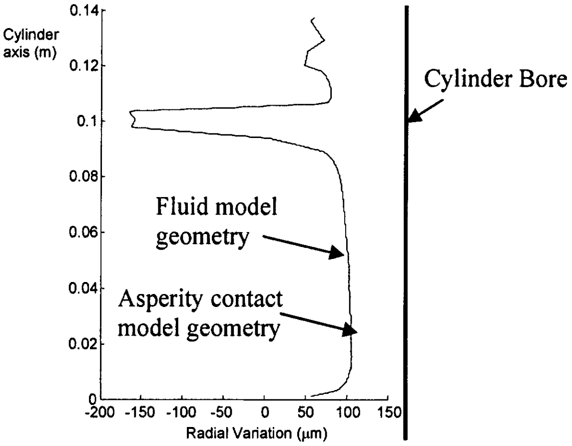

Figure 6.2: Bore and Piston Geometry

Figure 6.3 contains the piston lateral motion results for this set of simulations. From this figure we can note that:

- Piston slaps occur at the expected timings (0, 55, 180, 360, 540 and 660 °CA)
- The oil acts as a cushion during and immediately after piston slap:
  - slowing the piston's travel across the cylinder, and therefore decreasing the impact velocities,
  - reducing oscillations, and
  - reducing the lateral motion significantly.
- During the compression and expansion strokes:
  - The piston remains on one side of the cylinder throughout the stroke.
  - The side load is relatively large, resulting in thinner oil films and significant asperity contact.
  - Almost all the oil is squeezed out of the interface by the end of the stroke, and the lubricated lateral motion results approach those of the dry model. Oil transport is discussed in more detail in Section 6.4.
- In contrast, during the intake and exhaust strokes:
  - The side load is relatively small.
  - Mid-stroke piston slaps lead to less oil being squeezed out of the interface due to shorter sliding distances and provide the opportunity for oil to re-enter the piston domain.
  - Oil films are significantly thicker, particularly at the end of the stroke.
- Considering the various intake oil film thicknesses that were simulated, the results are consistent, up to a limiting value, with increasing oil resulting in:
  - slower travel across the cylinder,
  - less oscillation, and
  - reduced lateral motion.
- The oil flow rate past the piston is limited, however, as shown by the convergence of the 50 and 100 μm OFT results in all but the exhaust stroke, and any oil supplied in

excess of this rate will be scraped by the leading edge of the piston, as discussed in more detail in Section 6.4. This limiting rate is a function of:

- deformed geometry,
- amount of oil present in the calculation domain, and
- pressure difference across the calculation domain (which is zero).

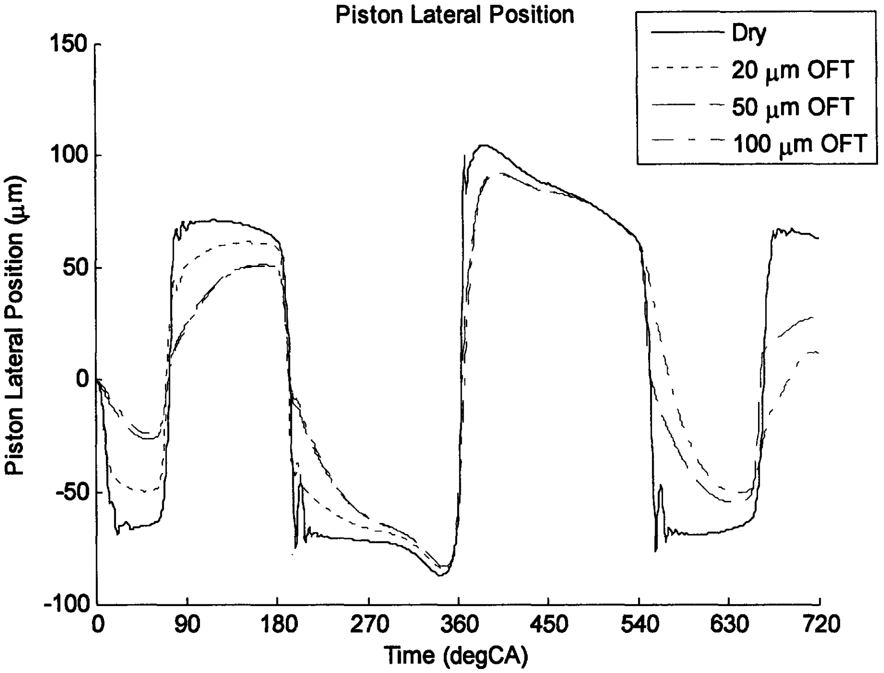

Figure 6.3: Effect of OFT on Lateral Position

Piston tilt is significantly affected by OFT, as shown in Figure 6.4:

- As expected, oil has a cushioning effect, reducing oscillations and thereby smoothing out the piston tilt.
- Approaching combustion TDC, the wrist-pin moment dominates, and the piston is rotated toward the thrust side (negative tilt).
- As mentioned in the above discussion of lateral motion, toward the end of the compression and expansion strokes, most of the oil is squeezed out of the load bearing side of the interface, and the lubricated model results approach those of the dry model.
- For the intake stroke, and the first half of the compression and exhaust strokes there is a significant increase in tilt, with increasing OFT, particularly after each piston slap. This is due to the way in which the piston scrapes oil at its leading edge, building pressure, and tends to have a significant region of separated oil film at its trailing edge.
- For the second half of the exhaust stroke, the combination of upwards piston motion, and the absence of a significant wrist-pin moment result in a positive tilt for larger oil film thicknesses, but a negative tilt for the dry model and 20 μm case.

- Piston tilt during the expansion stroke is more complicated due to significant deformation of the piston profile, combined with the effects of oil puddles, OFT and piston – cylinder bore friction.

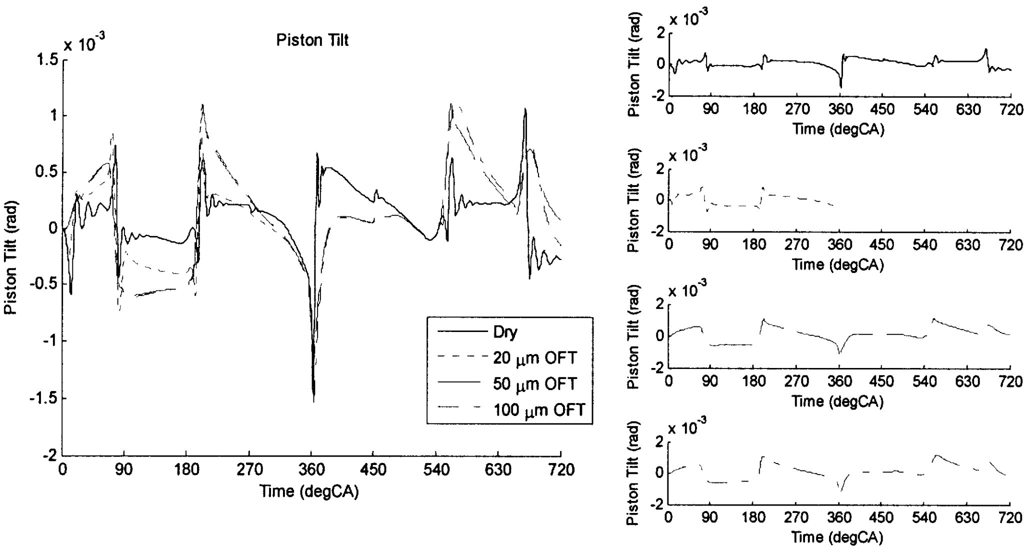

Figure 6.4: Effect of OFT on Piston Tilt

Figure 6.5 demonstrates that, as expected, the wrist-pin lateral force is not significantly effected by OFT, with the exception of the lateral inertia driven fluctuations away from combustion TDC which are reduced with increasing OFT. Similarly, the combined wrist-pin and combustion pressure moment is only effected is a very small region at combustion TDC due to variations in tilt. These results reinforce the conclusion from the dry model analysis that the other forces transmitted between the components of the power cylinder system are relatively independent of the behavior at the piston – cylinder bore interface, with the exception of fluctuations due to lateral inertia.

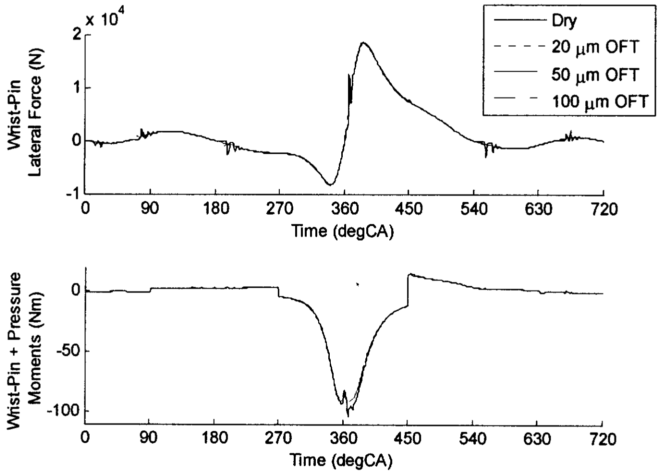

Figure 6.5: Effect of OFT on Driving Forces

Given that the moment transmitted to the wrist-pin from the piston is relatively independent of the piston – cylinder bore interface behavior, we expect that the wrist-pin tilt will not be significantly changed, as is confirmed by the plot in Figure 6.6. The lateral motion of pin and connecting-rod small end are fixed to piston in this model, but this motion does not significantly change the connecting-rod angle, or the position of its center of gravity.

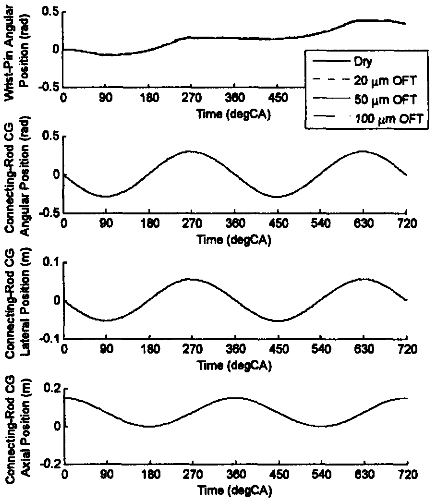

Figure 6.6: Effect of OFT on Component Positions.

The piston – cylinder bore lateral and friction forces can be separated into three components due to:

- hydrodynamic pressure and shear stress generated in the fluid,
- solid-solid contact of the piston and cylinder bore, as calculated using the asperity contact model and friction coefficient, and
- piston land – cylinder bore contact, which is calculated using an asperity contact model and friction coefficient.

From Figure 6.7, we can note the following effects of OFT on the piston – cylinder bore interface forces:

- The total side force supported by the piston – cylinder bore interface does not vary significantly with OFT, as it must balance the lateral force imposed by the wrist-pin.
- Away from combustion TDC, most of the side load is supported by hydrodynamic pressure, thereby significantly reducing the asperity contact force, and the total friction force, as expected.
- Approaching combustion TDC, and throughout the expansion stroke, a significant proportion of the side force is supported by asperity contact, even for the 100 μm OFT case, particularly towards the end of the expansion stroke as the oil is squeezed out of the piston-cylinder bore interface, and the lubricated results approach those of the dry model. Up until this point, however, the oil provides significant support via hydrodynamic pressure resulting in reduced friction.

- Hydrodynamic friction is extremely small compared to asperity contact friction. It is a very strong function of viscosity though, and therefore at cold start conditions could be a lot higher (these results are based on $\mu = 0.005$ Pas).
- Due to the increased piston tilt, there is significantly more land contact immediately after combustion TDC for the lubricated model.

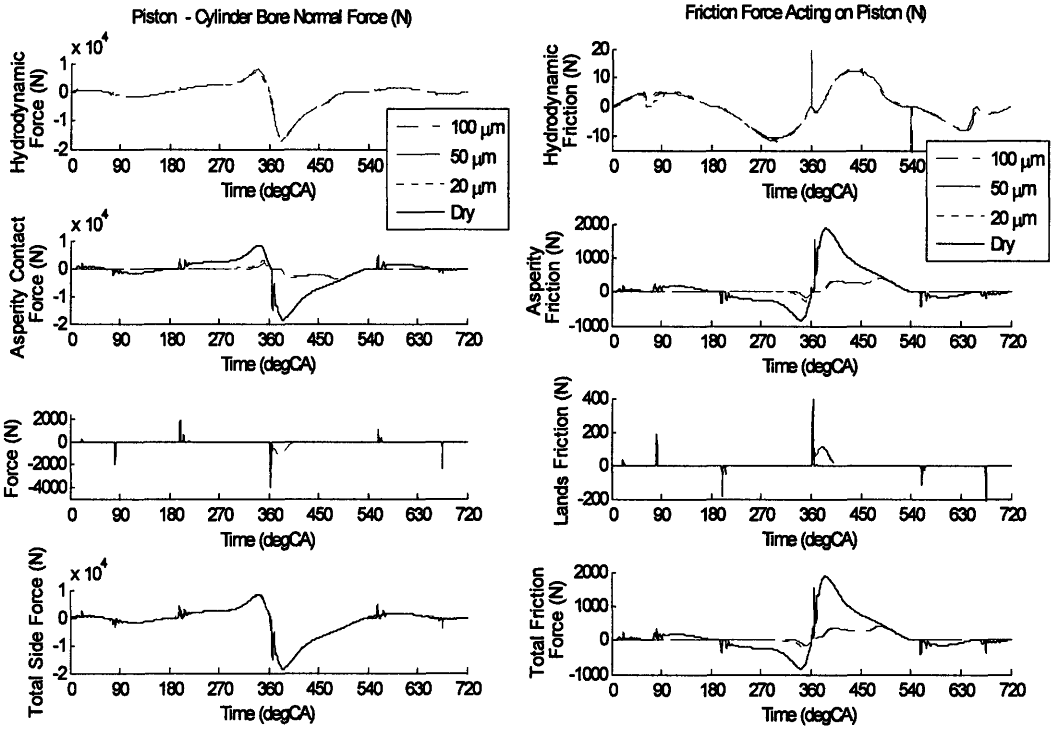

Figure 6.7: Effect of OFT on Piston – Cylinder Bore Interface Forces

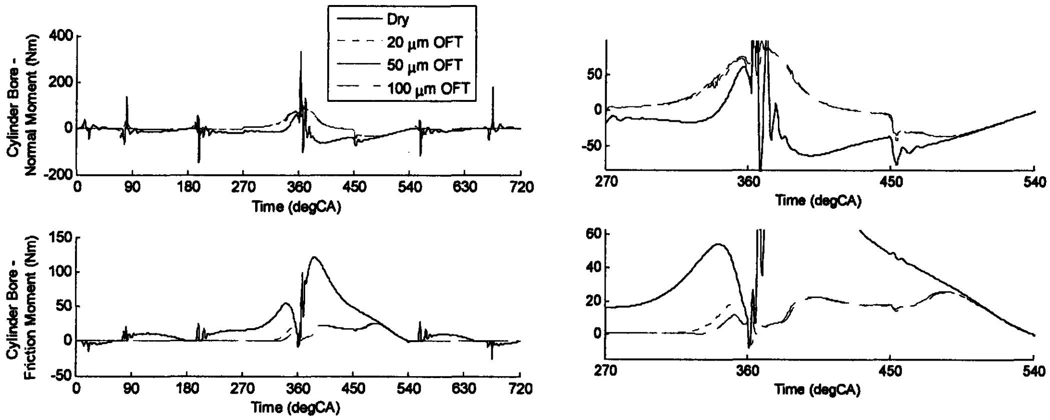

Figure 6.8: Effect of OFT on Piston – Cylinder Bore Interface Moments and Tilt

The effective friction coefficient can then be calculated as essentially the ratio of friction force to normal force, with a limiting value of 1N used to avoid dividing by very small numbers:

$$f = \begin{cases} \dfrac{\text{Friction Force}}{\max(\text{Normal Force},1)} & ,|\text{Friction Force}| > 1 \\ 0 & ,|\text{Friction Force}| \leq 1 \end{cases}$$

The thrust and anti-thrust side friction coefficients were evaluated separately. There are several spikes in friction coefficient, and increased friction coefficient during low load, due to the fact that even as the normal force essentially becomes zero (mid-stroke piston slaps in particular), there is still shear stress being generated in the fluid.

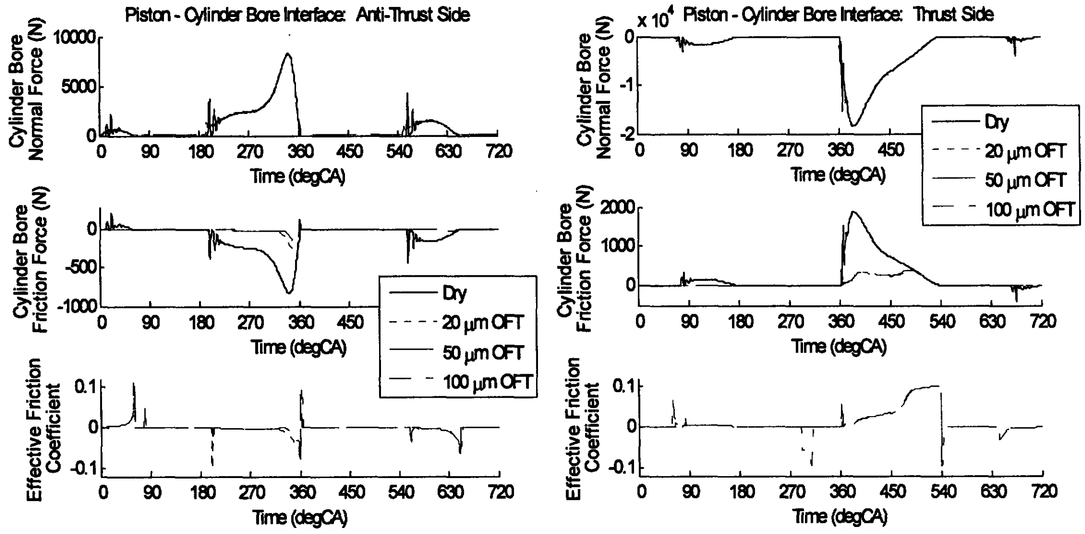

Figure 6.9: Effect of OFT on Piston – Cylinder Bore Interface Friction Coefficient

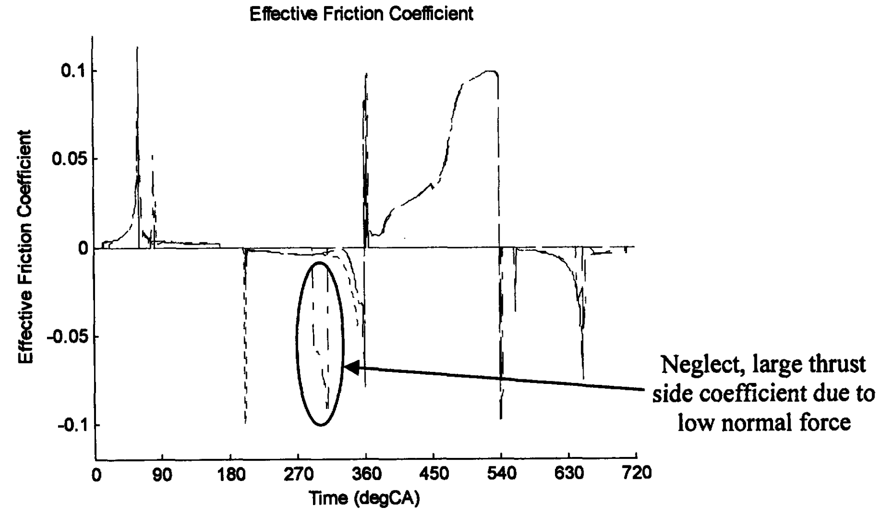

Neglect, large thrust side coefficient due to low normal force

Figure 6.10: Combined Piston – Cylinder Bore Interface Friction Coefficient

Combining these friction coefficients into one plot, as shown in Figure 6.10, the most important features to focus on are:

- During the intake and exhaust strokes, friction is very low, and the friction coefficients are generally small. There would be little error incurred by neglecting the spikes in friction coefficient in this region, typically caused by decreasing normal load, by limiting the value to 0.02 for example.
- Through the second half of the compression stroke, and throughout the expansion stroke, the friction coefficient increases significantly due to asperity contact, and it is in this region that accurate estimation of the friction coefficient can have a significant impact of the predicted friction generation and piston tilt.

6.3. Piston Surface Representations

When significant tooling marks are present on the piston's surface, accurate representation of the piston – cylinder interface geometry can be challenging. For the purposes of our fluid model the piston's surface can be represented in several ways, as shown in Figure 6.11:

- Using a relatively coarse grid:
  - by the mean surface line of the tooling marks,
  - by the outer surface line, or
  - using the average Reynolds equation with flow factors which take into account the effect of the tooling marks, or
- Using a very fine grid so that the geometry of the tooling marks is accurately captured, enabling direct numerical simulation of the effect of the tooling marks.

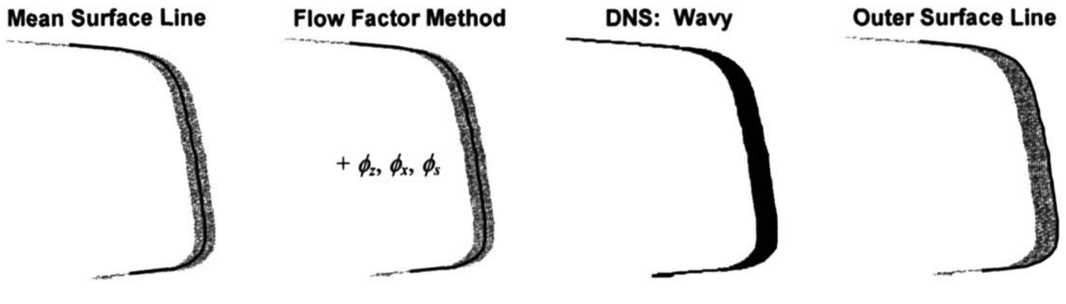

Figure 6.11: Piston Surface Representations

While finer grids may be required to accurately capture system geometry, even for the relatively coarse grid representations, there is a significant penalty in terms of calculation time and memory requirements. The optimum grid size may vary, depending on the primary aim of the study. For example, typically a finer grid is required to accurately predict piston – cylinder bore friction that to estimate piston dynamics, as demonstrated by the results in Figures 6.13-6.18.

Even for the very fine grid used for direct numerical simulation of piston tooling marks, there can be significant discretization error in the gap height for the fluid model, as shown in Figure 6.12. The number of nodes is limited by memory availability to 10 nodes per wavelength. The discretization method we have chosen uses the geometric average of $(1/h)$ for the Couette flow term at a control volume boundary and the geometric average of $(1/h^3)$ for the Poiseuille flow term. The limiting gap height for the fluid, *hlim*, was therefore set to 0.5 μm, which is less than the geometric resolution of our surface representation.

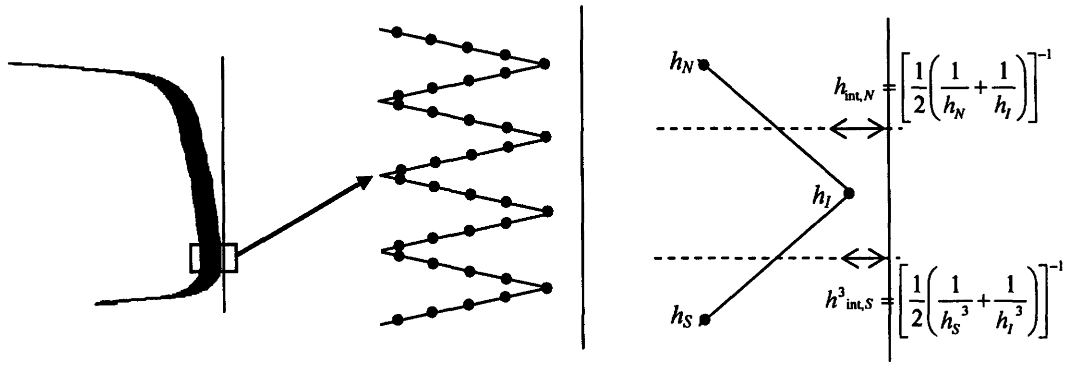

Figure 6.12: Discretization Error in Gap Height

The asperity contact model is affected by the surface representation in terms of:

- piston – cylinder bore gap height, or overlap, and
- grid spacing determines the area over which a point of asperity contact acts, significantly increasing the asperity contact force in some cases.

The user specifies the asperity contact model via three constants, as explained in Section 2.3.3.1. The constant, h_{asp}, specifies the clearance or gap height at which asperity contact is assumed to begin, and allows for adjustment between the mean surface line and outer surface representations, while the constant C_l can be used to scale the area over which asperity contact pressures are applied.

Table 6.1 summarizes the surface representations that are presented in the following sections, their calculation times and approximate errors. The approximate errors are a simple visual estimate of the maximum difference, over the calculation range, between the current set of results and either the finest grid for that surface representation (left hand column of errors) or the direct numerical simulation (DNS: Wavy) results (right hand column of errors). Calculation times for 0-340 °CA range from 3 to 140 hours, and full cycle results (0-720 °CA) were obtained after a minimum of 14 hours.

Representation	Grid Size	Inlet OFT (μm)	Calculation Time: 0-340 °CA (hr:min)	Calculation Range and Time (°CA, hr:min)	Lateral Motion Error (μm)		Tilt Error (10^{-4} rad)		Friction Force Error (N)	
Mean Surface Line	17 x 17	20	6:00	354, 7:35	2	-	0.4	-	70	-
Mean Surface Line	17 x 49	20	14:12	344, 15:40	0.5	-	0.1	-	10	-
Mean Surface Line	17 x 81	20	12:53	350, 16:41	0	2	0	0.4	0	10
Flow Factor Method	17 x 17	20	4:52	720, 17:05	3	-	3	-	75	-
Flow Factor Method	17 x 81	20	12:21	720, 40:00	0	2	0	0.4	0	30
Outer Surface Line	17 x 17	20	6:18	720, 18:46	2	12	1	0.7	20	8
Outer Surface Line	17 x 49	20	13:41	452, 38:05	0	-	0	-	0	-
DNS: Wavy	17 x 1585	20	103:47*	310, 103:47	-	0	-	0	-	0
Mean Surface Line	17 x 17	50	3:15	720, 14:40	8	-	1.6	-	100	-
Mean Surface Line	17 x 49	50	7:29	354, 11:36	0.2	-	0.2	-	6	-
Mean Surface Line	17 x 81	50	11:05	720, 40:48	0	1	0	0.2	0	30
Flow Factor Method	17 x 17	50	3:27	450, 8:10	2	-	0.8	-	100	-
Flow Factor Method	17 x 81	50	10:28	720, 38:13	0	1	0	0.2	0	50
Outer Surface Line	17 x 17	50	5:39	452, 14:37	2	-	0.5	1.5	30	-
Outer Surface Line	17 x 49	50	9:51	448, 23:08	0.1	10	0.05	-	0.1	4
Outer Surface Line	17 x 81	50	14:37	349, 19:07	0	-	0	-	0	-
DNS: Wavy	17 x 1585	50	139:01*	336, 139:01	-	0	-	0	-	0

* Simulation did not reach 340°CA, total calculation time is given.

Table 6.1: Piston Surface Representations

6.3.1 Effect of Grid Size on Piston Dynamics and Friction

It is useful to first compare the accuracy of each surface representation over a range of grid sizes. Using the mean surface line to represent the piston surface, with inlet OFTs of 20 μm and 50 μm, there is very little change in the predicted piston dynamics throughout most of the cycle, as demonstrated in Figure 6.13, with errors of 1-2 μm and 0.5×10^{-4} rad. The maximum errors for the 50 μm OFT case occur during the second half of the exhaust stroke and are around 8 μm and 1.6×10^{-4} rad. Note that the 50 μm, 17 x 49 case ends at 356 °CA, but that until that time it lies directly under the 17 x 81 results, with approximate errors of 0.5 μm and 0.1×10^{-4} rad.

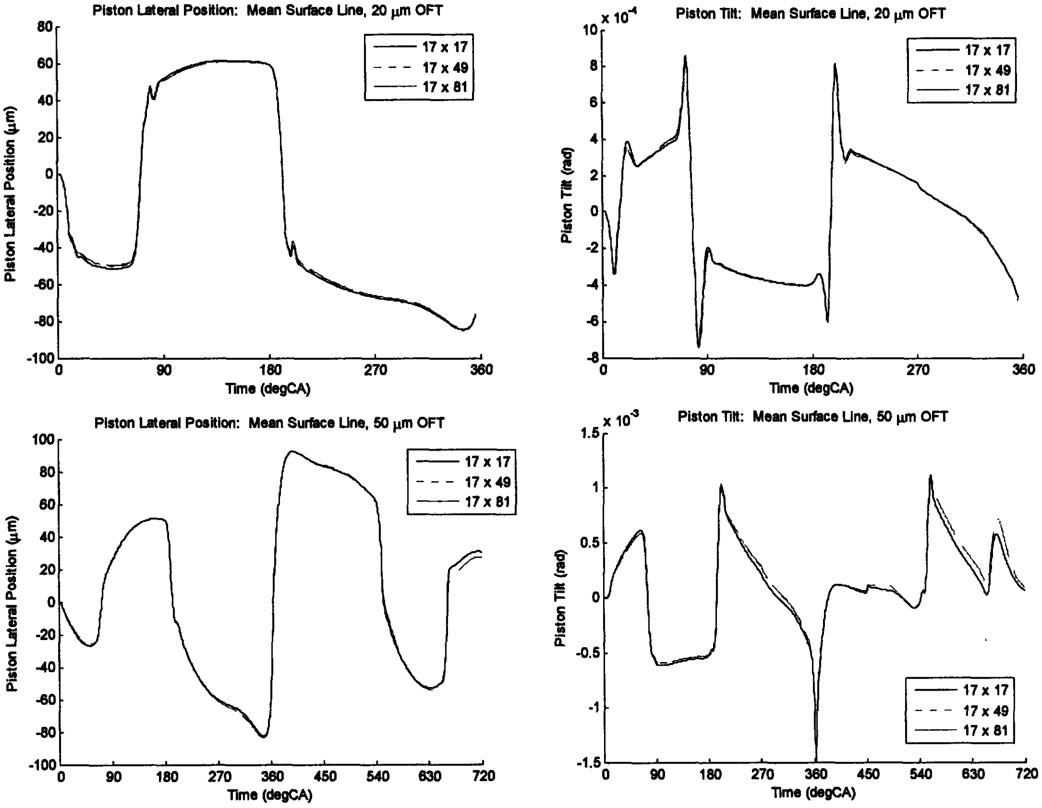

Figure 6.13: Effect of Grid Size on Piston Dynamics – Mean Surface Line

Similarly for the Outer Surface Line and Flow Factor representation results, provided in Figures 6.14 and 6.15, there is very little difference in the piston dynamics predicted with a maximum error of around 3 μm and 3×10^{-4} rad, over the ranges available for comparison. Unfortunately numerical stability continues to be a problem in obtaining a full set of results, and it was not possible to make a comparison over the full cycle for the outer surface line representation. The outer surface line, 20 μm OFT, 17 x 49 case ends at 450 °CA, and is hidden by the 17 × 81 case up until this point. The maximum errors in both lateral motion and tilt tend to occur during the second half of the exhaust stroke.

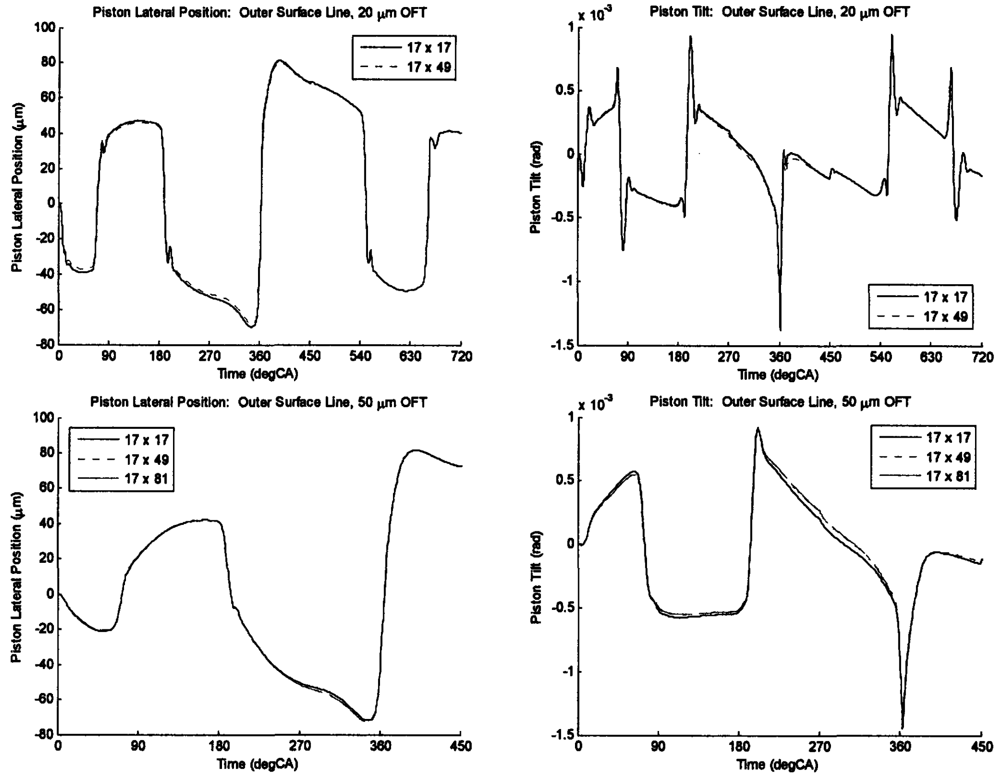

Figure 6.14: Effect of Grid Size on Piston Dynamics – Outer Surface Line

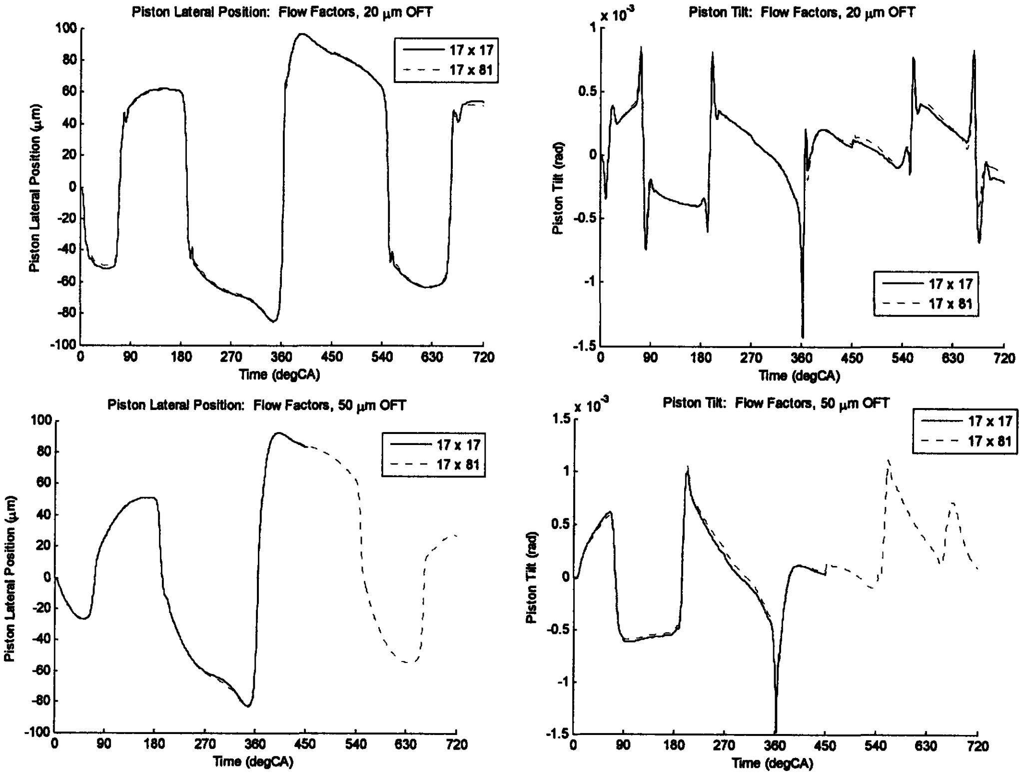

Figure 6.15: Effect of Grid Size on Piston Dynamics – Flow Factor Method

If we now consider the friction force predicted by these surface representations, there is significantly more variation, as shown in Figure 6.16, indicating that friction is more sensitive to surface representation. For the Mean Surface Line, 20 μm case, the coarse grid predicts significantly more friction (~ 70 N) approaching combustion TDC than the finer grids, while for the Mean Surface Line, 50 μm case, the finer grids predict more friction both approaching combustion TDC, and for the second half of the expansion stroke, where there is a maximum friction force error of about 100 N.

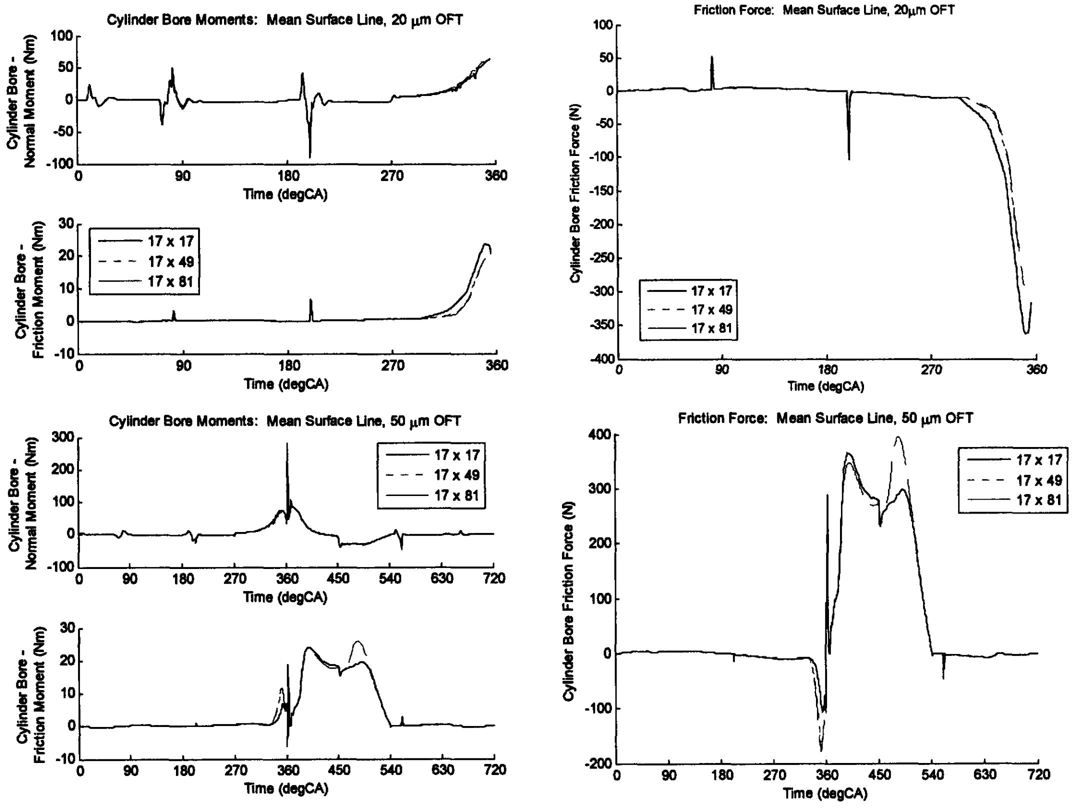

Figure 6.16: Effect of Grid Size on Friction Generation – Mean Surface Line

The Outer Surface Line predicts significantly lower friction approaching combustion TDC and throughout the expansion stroke, compared to the Mean Surface Line representation due to the fact that asperity contact is not predicted, as discussed in more detail in Section 6.3.2. The resulting variation in friction generation as a function of grid size, over the range available for comparison is reduced to about 30 N, and this peak error occurs during the friction force spikes at combustion TDC. The Flow Factor Method results, presented in Figure 6.18, predict similar levels of friction to the Mean Surface Line, with similar variations (~100 N maximum) due to grid size.

These results indicate that the grid size is not significantly affecting the hydrodynamic friction, or shear stress, during sliding, but can be more important during piston slap events, and is critical in determining onset and extent of asperity contact and the resulting contact friction.

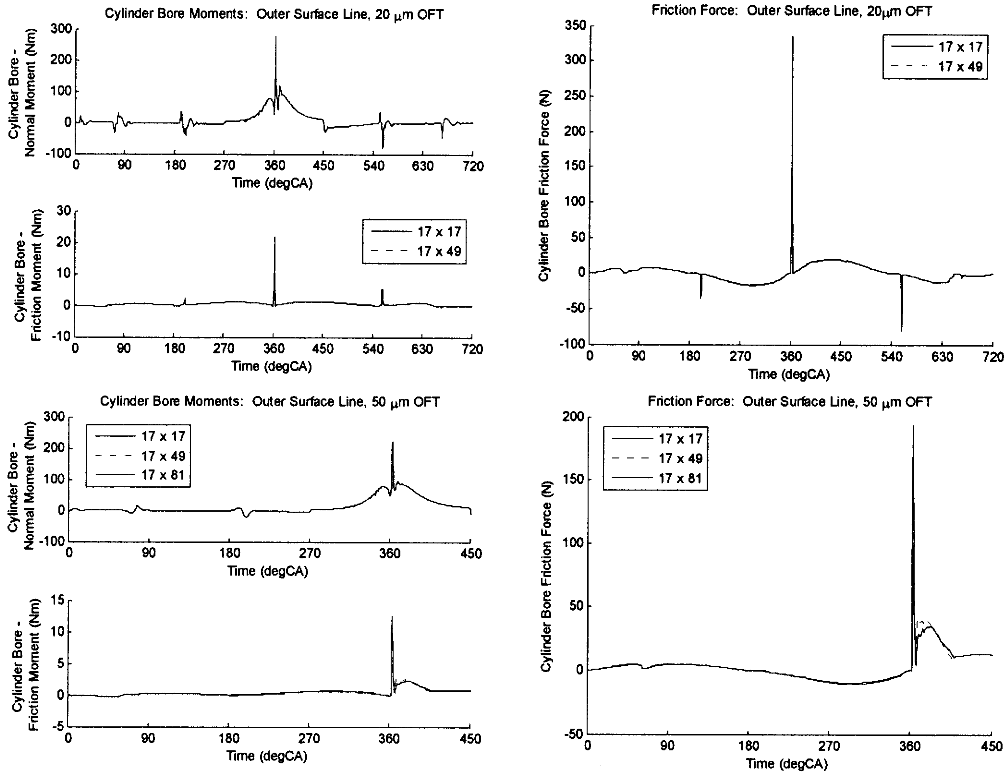

Figure 6.17: Effect of Grid Size on Friction Generation – Outer Surface Line

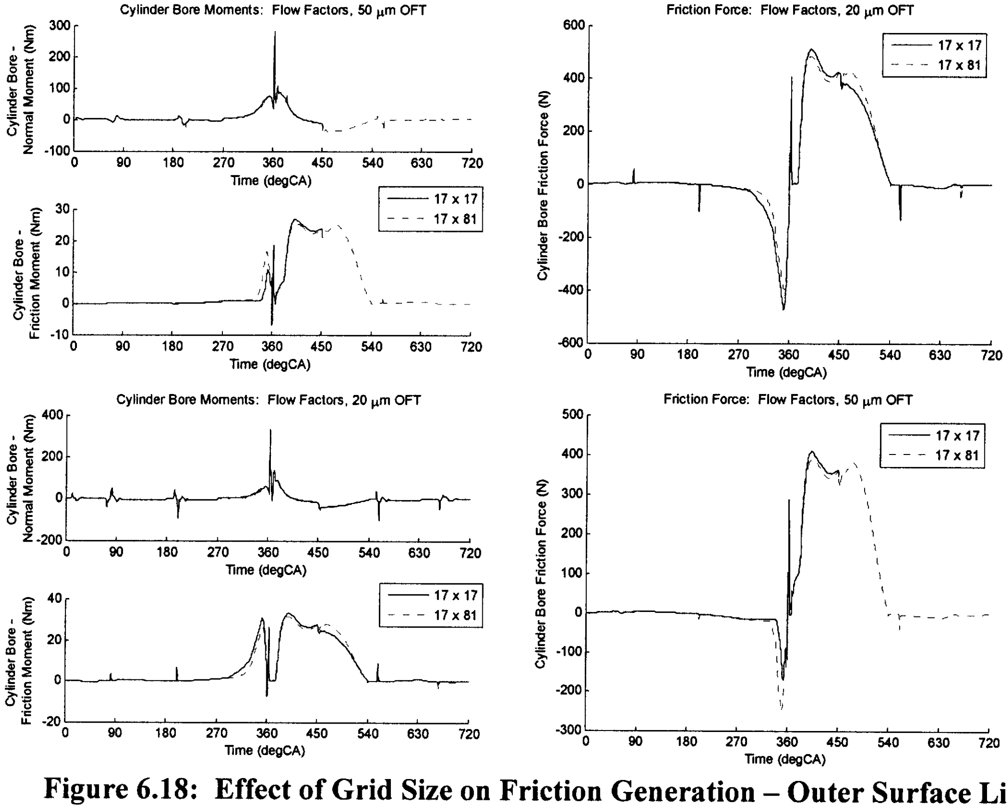

Figure 6.18: Effect of Grid Size on Friction Generation – Outer Surface Line

6.3.2 Effect of Surface Representation on Piston Dynamics and Friction

Figure 6.19 demonstrates the effect of the various surface representations on piston dynamics. As would be expected, in regions where hydrodynamic pressure supports the side load, the lateral motion of the Outer Surface and Mean Surface representations are separated by about half the wave height (10-12 μm). Piston tilt is relatively unaffected in these regions, as essentially the shift in lateral motion means that the piston – cylinder bore interface is unchanged. Approaching combustion TDC and throughout the expansion stroke, as the Mean Surface and Flow Factor representations begin to make asperity contact, the distance between the lateral motions decreases, and there is a significant shift (3×10^{-4} rad) in piston tilt due to the difference in friction moments.

There is less than 2μm difference in the lateral motion predicted via direct numerical simulation of the piston tooling marks, compared to the mean surface line and flow factor surface representations, and less than 0.5×10^{-4} rad of difference in the piston tilt.

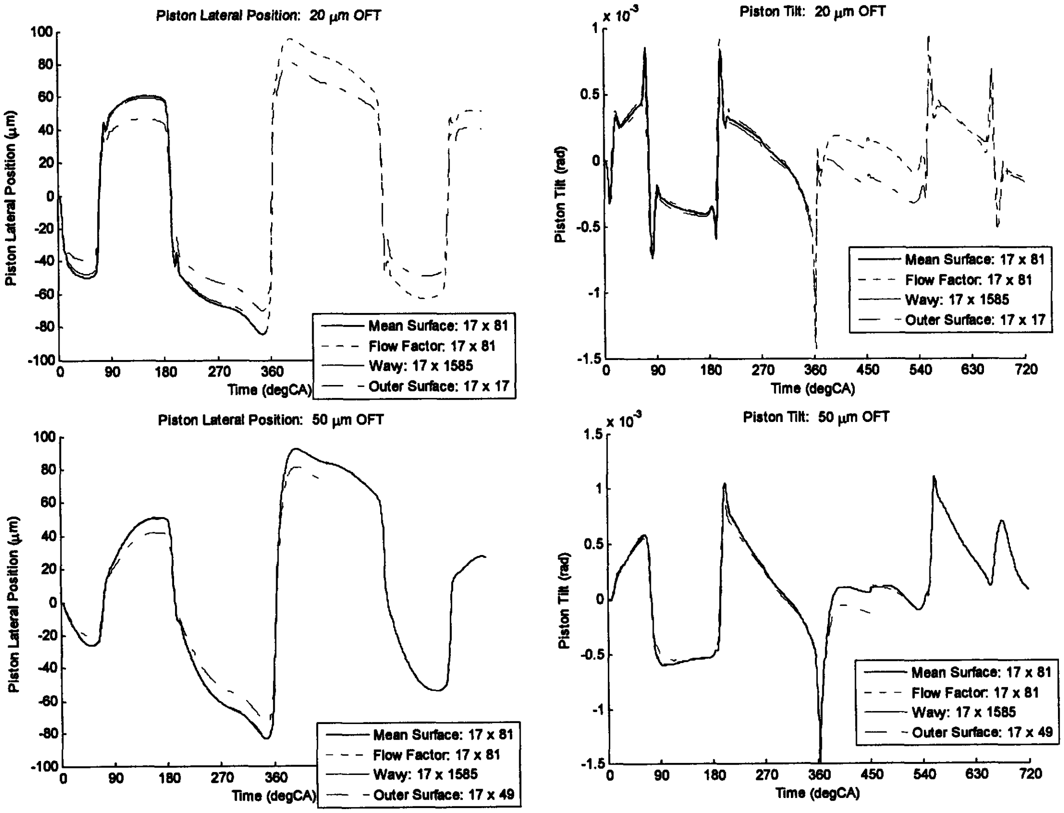

Figure 6.19: Effect of Surface Representations on Piston Dynamics

These differences are insufficient, particularly compared to the geometric resolution of our discretization, to justify the large increase in calculation time and memory requirements for direct numerical simulation, for the purposes of prediction piston dynamics. Unfortunately, due to continued problems with numerical stability of the EHL algorithm, direct numerical simulation results were not obtained for the second half of the exhaust stroke, which has previously been the area with the largest variations in lateral motion and tilt.

In terms of friction generation, there is initially very little difference between the four surface representations, but during the second half of the compression stroke, the flow factor method is the first to predict increasing friction, followed by the mean surface line. Throughout the rest of the compression stroke and most of the expansion stroke the flow factor method predicts the highest friction generation, followed by the mean surface line. The outer surface line representation does not predict any asperity contact with hydrodynamic pressure supporting the side load throughout the cycle. Interestingly the Mean Surface Line representation generally results in a better prediction of the friction obtained via direct numerical simulation that the Flow Factor Method. Unfortunately converged results were not able to be obtained for the direct numerical simulation beyond 356°CA due to numerical stability challenges, which are discussed in more detail in Section 6.5. Improvements to the EHL algorithm and further investigation of the friction generated by direct numerical simulation throughout the expansion stroke are required before conclusions can be drawn regarding the accuracy of the flow factor method and mean surface line representations in this region.

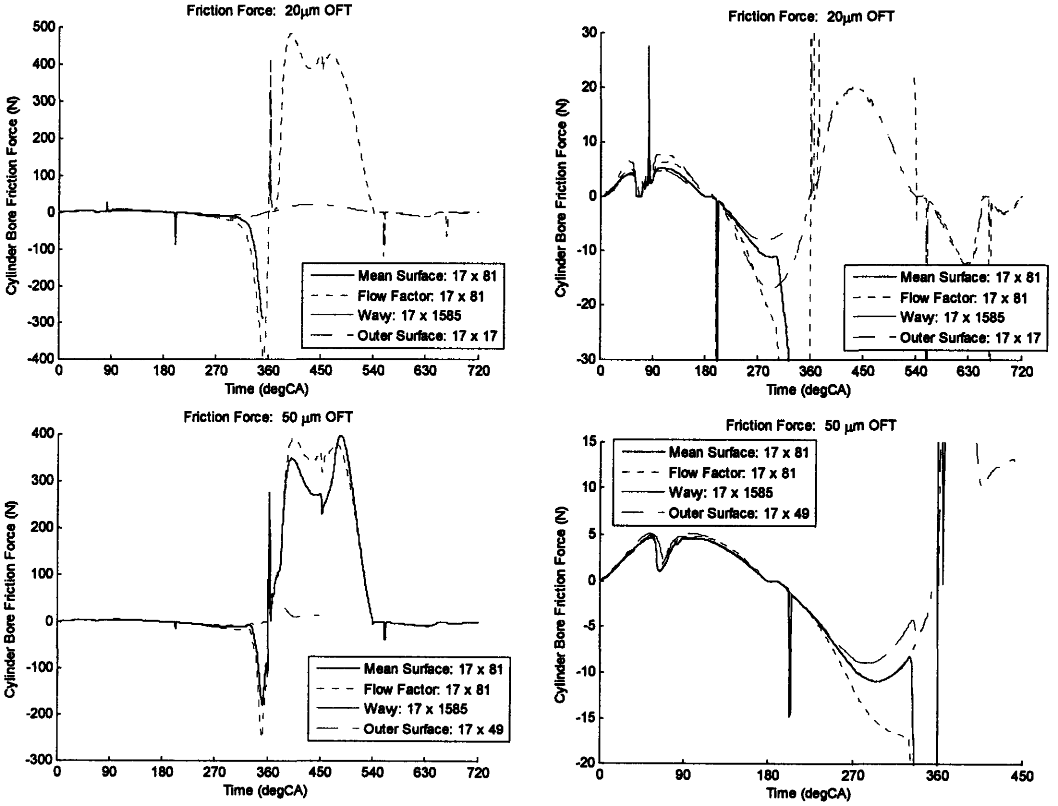

Figure 6.20: Effect of Surface Representation on Friction Generation

6.4. Piston Oil Transport Model Results

In order to more accurately model the transport of oil, reservoirs were added to the top and base of the piston along with additional user specified oil supply rates. The cylinder bore oil film thickness is specified at the start of the calculation, and can also be reset each time the piston turns around to a new constant or distribution, or a linear combination of the old and new distributions. Cylinder bore oil reservoirs enable accurate mapping between the cylinder bore oil film thickness and the piston – cylinder bore interface calculation domain. These features are discussed in more detail in Section 6.6, and summarized in Figure 6.21.

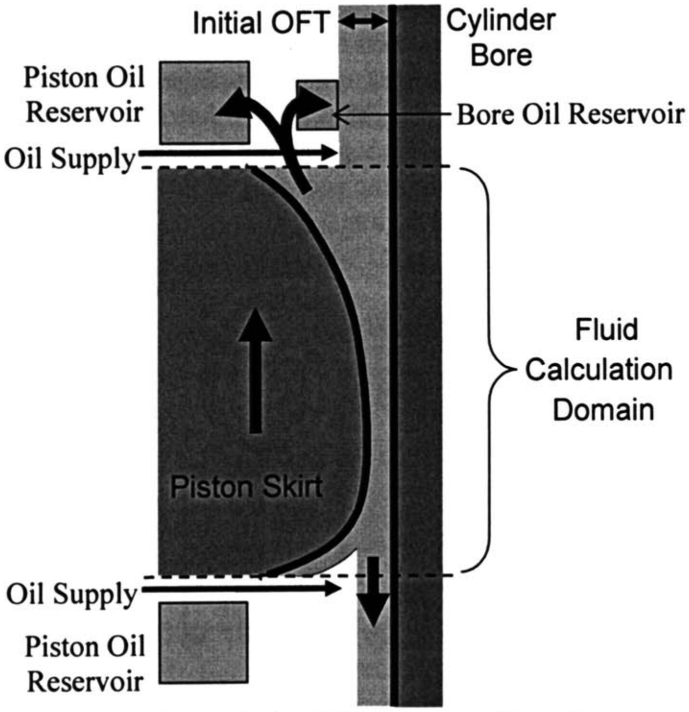

Figure 6.21: Oil Transport Model

The previous results presented in this chapter are based on a constant initial cylinder bore OFT, which is reset to its initial value (outside of the calculation domain only) each time the piston turns around, resulting in a constant inlet OFT. The piston reservoirs were allowed to collect half the scraped oil, with the remaining half being transferred to the bore, but not to release it back into the calculation domain. This is not a realistic picture of piston oil supply, but allowed the effects of different inlet OFTs to be investigated, demonstrating that:

- There is significant redistribution of the bore OFT due to the piston skirt's motion, which squeezes oil away from the centre of the calculation domain, and scrapes oil in front of the piston.

- In order for the piston to scrape oil along the bore in front of its motion there must be an excess of oil supply. This does not necessarily correlate with the leading edge gap height, or inlet OFT, but is rather a function of:
  - existing OFT in the piston domain,
  - minimum clearance gap height,
  - gap height distribution, and
  - leading edge gap height and inlet OFT.

More realistically it is expected that:

- Oil supplied to the cylinder bore by oil spray from the crankshaft will decrease with distance from the crankshaft due to both the distance itself and the exposure time, that is, the proportion of the cycle over which the section of bore is exposed to the oil spray (not blocked by the piston).
- The ring pack, and in particular the oil control ring, follow the piston down the cylinder bore, scraping the oil that passes the piston, and redistributing it. It is expected that some of this oil will remain in the chamfer at the top of the piston skirt and on the upper portion of the piston skirt, and act as oil supply during the upstroke.
- During the upstroke, the piston skirt follows the oil control ring. It is expected that the oil control ring will only leave 1-5 μm of oil behind it, significantly reducing inlet oil supply to the piston, although this supply maybe augmented by oil from the chamfer at the top of the piston skirt.
- In some engine designs, pressurized oil supply is provided to the piston skirt.

In order to begin to investigate more realistic oil transport, the following cases were simulated.

Case 1: 0-100 μm
  - Linear oil supply to the cylinder bore as a function of axial position, ranging from 0 μm to 100 μm, added at TDC.
  - Cylinder bore OFT above the piston is reset to 2 μm at BDC, and an equivalent amount of oil to that removed (approximately) is added to the piston oil reservoir at the top of the skirt.
  - 5% of piston oil reservoirs are released at inlet and outlet, at each time step.

Case 2: 0-100 μm + 2 × chamfer supply
  - As for Case 1, but with double the amount of oil added to the piston oil reservoir at the top of the skirt, at BDC.

Case 3: 10-100 μm
  - As for Case 1, but with the linear oil supply to the cylinder bore ranging from 10 μm to 100 μm.

The changes to the cylinder bore oil film thickness distribution are demonstrated in Figure 6.23.

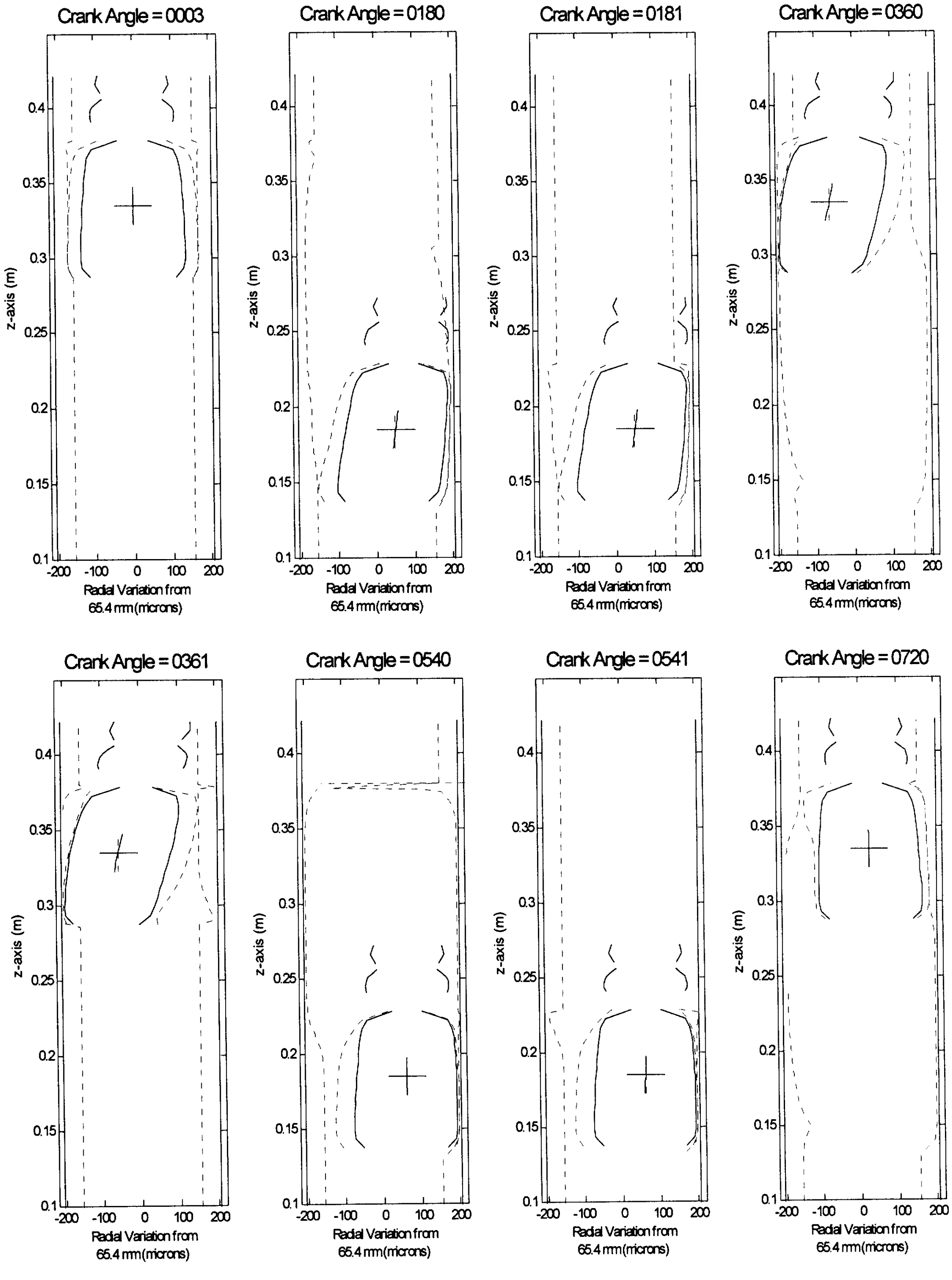

Figure 6.22: Oil Film Distribution – 50 μm Inlet OFT

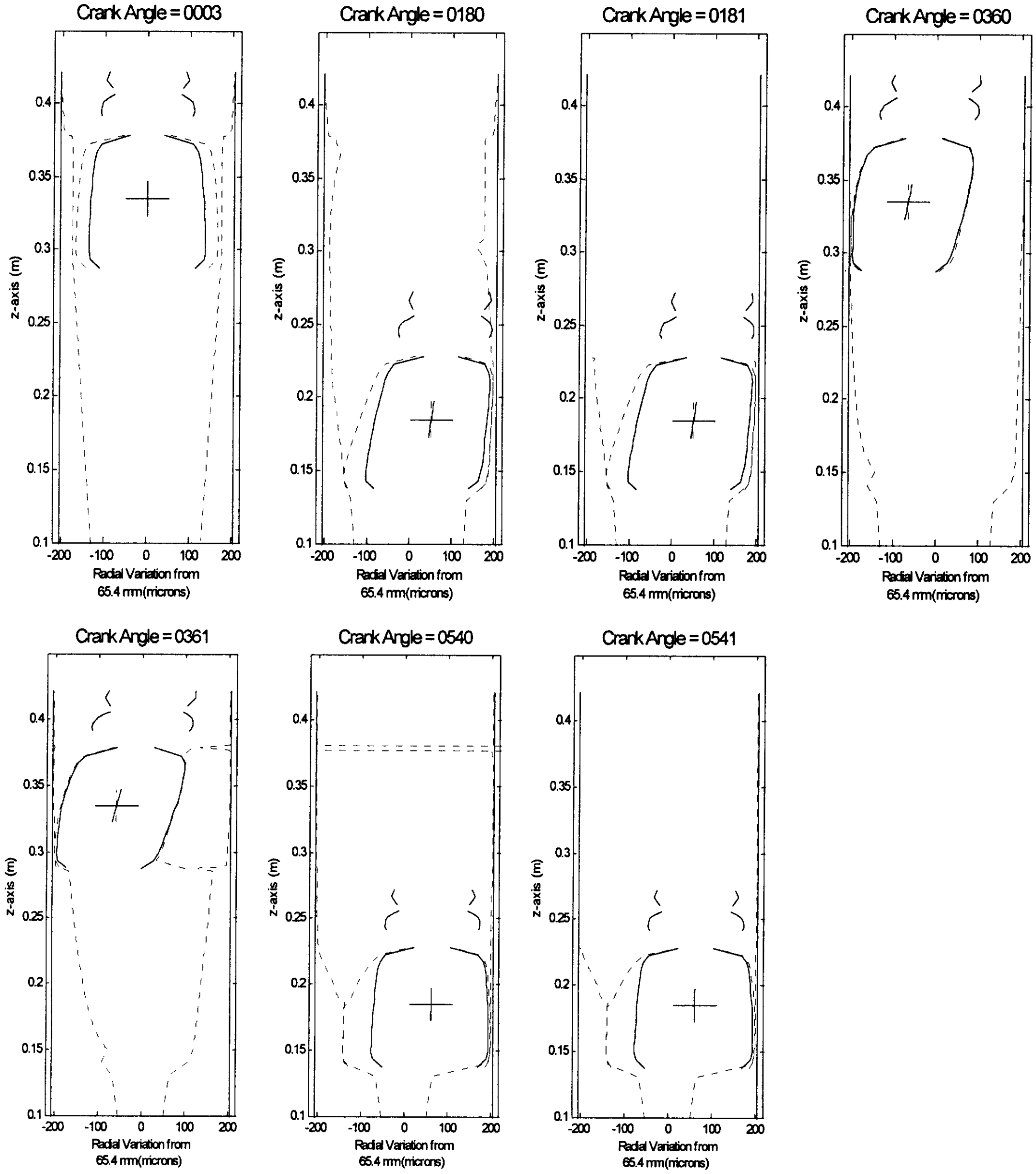

Figure 6.23: Changes to Oil Film Distribution

Comparing the results of these simulations with the constant 50 μm inlet OFT case, we can note from the piston motions presented in Figure 6.24:

- In the lower half of the cylinder bore, all four cases are very similar.
- In the upper half of the cylinder bore, the significant reduction in oil film thickness for the linear oil distribution cases results in larger lateral motions, and a significant shift in piston tilt after combustion TDC.
- Beyond 180 °CA, there is no significant difference between the three linear oil distribution cases.

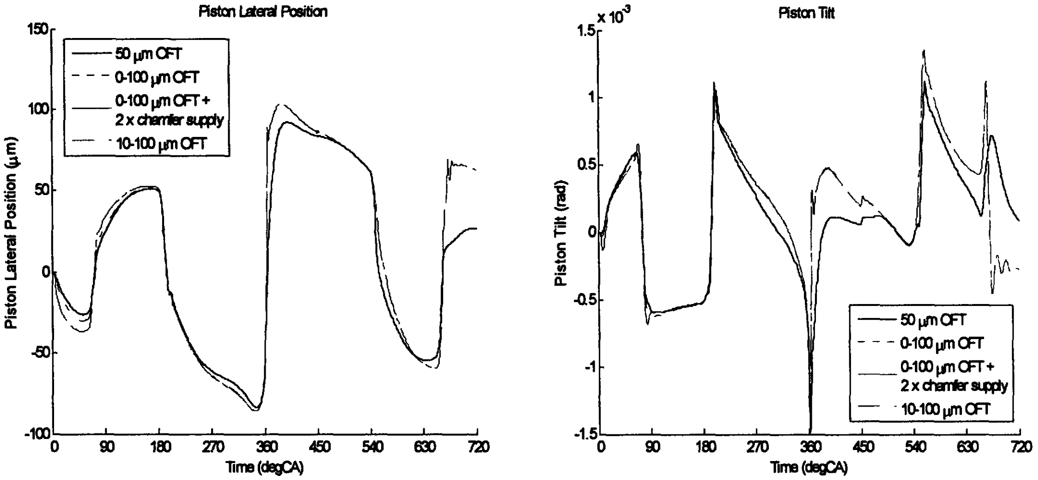

Figure 6.24: Effect of Oil Transport Model on Piston Dynamics

It is also useful to compare these results with those from the dry model. Figure 6.25 demonstrates that although the initial results vary, beyond 180 °CA the linear oil distribution results are essentially the same as the 50 μm OFT case in the lower half of the bore, and the same as the dry model results in the upper half of the bore. The initial variation in results is due to the quasi-steady solution that we use to provide the oil film initial conditions, and it is expected that, for cycle to cycle converged results, this variation will be removed.

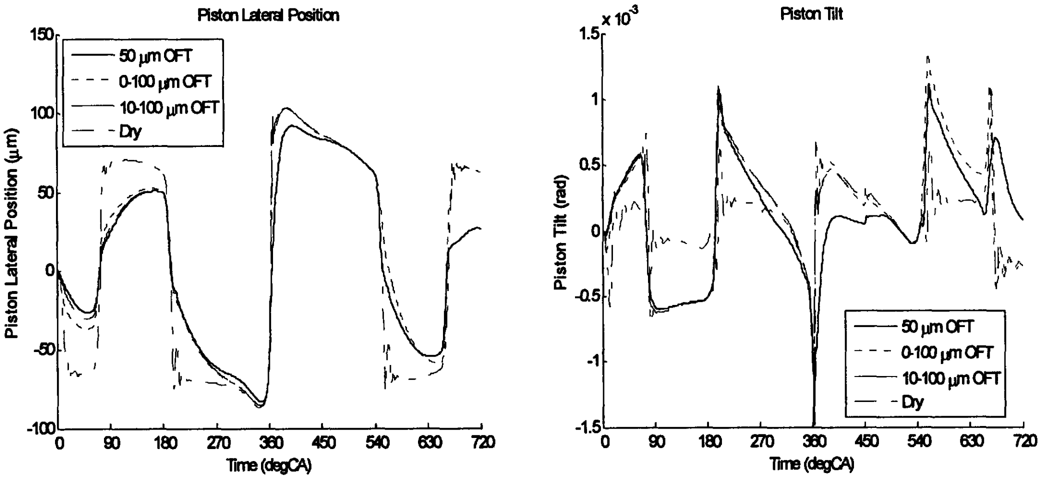

Figure 6.25: Comparison of Oil Transport Model Results with Dry Model

The friction force generated, and corresponding effective friction coefficient, are shown in Figures 6.26 and 6.27. As would be expected from the piston motions and oil film distributions there is a significant increase in friction, from the 50 μm OFT case, during the compression and expansion strokes. There is still a significant reduction though, compared to the dry model.

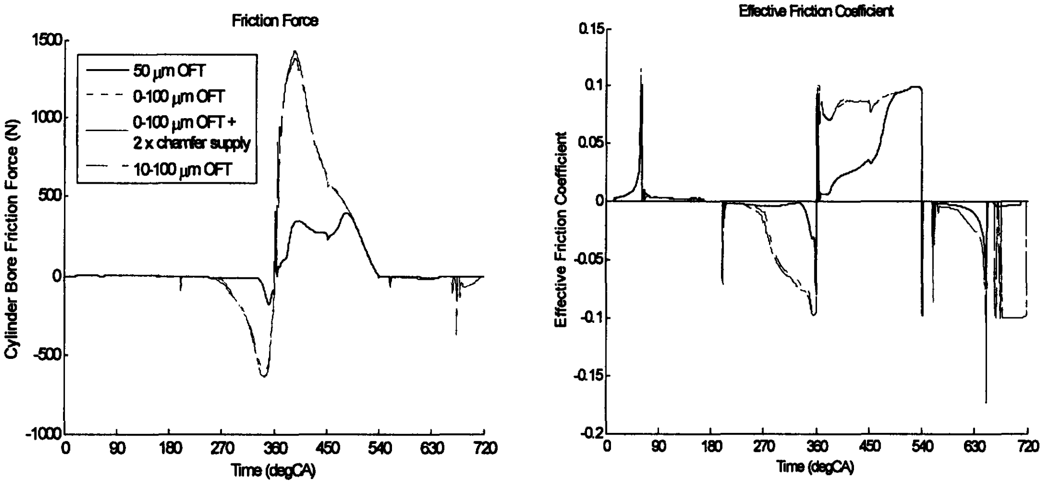

Figure 6.26: Effect of Oil Transport Model on Friction

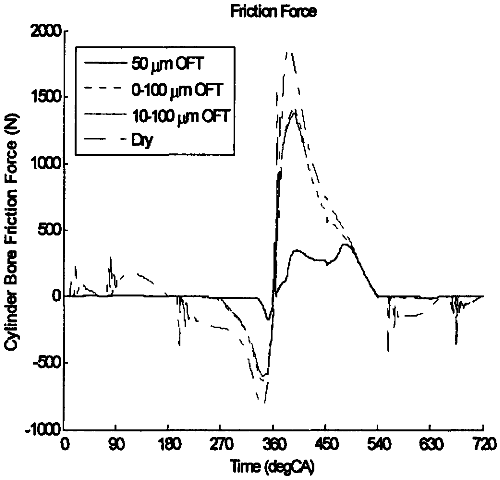

Figure 6.27: Comparison of Oil Transport Model and Dry Model Friction Forces

6.5. Conclusions Based on Lubricated Model Results

For a simplified bore geometry, a range of oil film thicknesses were simulated, demonstrating that:

- The timing of the onset of piston slap is unaffected by the presence of oil, with piston slaps occurring at the crank angles determined by the dry model.
- The oil acts as a cushion during and after piston slap:
  - slowing the piston's travel across the cylinder,
  - reducing impact velocity, bouncing and oscillations, and
  - reducing lateral motion.

- Piston tilt oscillations are reduced, but the presence of oil, particularly after it is scraped into puddles by the piston, can result in large changes to the piston tilt, even reversal of tilt direction. The wrist-pin moment still dominates piston tilt approaching combustion TDC, for this engine and running condition.
- Due to increased piston tilt, there is significantly more land contact immediately after combustion TDC for the lubricated model.
- The wrist-pin lateral force, wrist-pin and pressure moments, and the motion of the wrist-pin and connecting-rod are essentially unaffected by the behaviour of the piston – cylinder bore interface.
- The total side force supported by the piston – cylinder interface does not vary significantly with OFT, as it must balance the lateral force imposed by the wrist-pin. The balance between hydrodynamic support and asperity contact support shifts throughout the cycle though, with hydrodynamic pressure providing support for most of the cycle, and asperity contact becoming significant towards the end of the compression stroke, and throughout the expansion stroke.
- Squeezing is significant throughout the cycle, removing oil from the load bearing piston – cylinder bore interface, resulting initially in asperity contact during the compression and expansion strokes, and finally in complete support of the side load via asperity contact toward the end of the expansion stroke.
- During the intake and exhaust stokes, light loads and mid-stroke piston slaps provide an opportunity for oil film thickness to be replenished in the piston – cylinder bore interface.
- The piston – cylinder bore friction force is reduced significantly throughout most of the cycle by the presence of oil.
- The effective friction coefficient throughout the intake and exhaust strokes and first half of the compression stroke is typically very low (< 0.02). It increases with increasing asperity contact during the second half of the compression stroke and through the expansion stroke, resulting in a dry contact value of 0.1.

A range of surface representations were tested using the lubricated piston dynamics model. It was found that surprisingly coarse grid representations are sufficient to accurately describe the piston dynamics, with a 17 × 49 grid resulting in less than 0.5 μm variation in lateral motion and 0.2×10^{-4} rad variation in piston tilt compared to a 17 × 81 grid. A comparison between mean surface line, outer surface line, flow factor method and direct numerical simulation of the piston skirt tooling marks (17 × 1585 grid) demonstrated that, in terms of piston dynamics, there is a significant underestimate of lateral motion by the outer surface line results, but there is insufficient difference between the results of the other three methods to justify the large increase in computational time and memory required for direct numerical simulation.

An oil transport model was then implemented, and a range oil supply configurations were tested, demonstrating the usefulness of the oil transport model in investigating how oil is supplied and removed from the piston – cylinder bore interface, and the effect that this has on piston dynamics and friction generation.

7. Conclusions and Future Research

7.1. Model Development

A suite of numerical models have been developed, including:

- A fast, quasi-dry model of piston dynamics.
- Quasi-steady hydrodynamic lubrication, hydrodynamic lubrication and elastohydrodynamic lubrication models.
- A lubricated piston dynamics and oil transport model.

The quasi-dry piston dynamics model has been tested over a range of operating conditions for a single, heavy duty diesel engine. It was confirmed that the specified governing equations were satisfied to sufficient degree of accuracy, and that the numerical algorithm is stable and results in relatively fast running times of about 10 minutes per cycle for a 17 x 30 grid. The dry model's usefulness in investigating the effect of system parameters (not including oil effects) on component dynamics, force generation and transmission was demonstrated.

Experimental results obtained and processed by our sponsors, and corresponding input files for modeling the same engine, enabled comparisons to be made between the simulated and experimental piston dynamics, over a range of operating conditions. The results were found to be in surprisingly good agreement in terms of general behavior, magnitude and timing, apart from a significant increase in lateral motion during combustion in the experimental results, and increased piston tilt oscillations in the dry model results, due to the lack of oil damping.

Comparison with the lubricated model results indicate that, for the cases tested, the dry model provides a useful upper bound for lateral motion, but tends to underestimate piston tilt, particularly during piston slap, resulting in an underestimate of land contact at combustion TDC. The degree to which these variations affect the dry program's accuracy depends on the amount of oil present in the system. If we compare the effect of oil film thickness (OFT) on lateral motion with the differences between the experimental and dry model results, it would appear that there is very little oil present in the system (10-50μm), particularly towards the top of the cylinder bore.

The quasi-dry model has been shown to provide useful information as an engineering analysis tool and has been released, with documentation, to our sponsors.

The lubrication models were tested over a range of simple 2D flows for which analytical solutions are available and found to satisfy the governing equations to sufficient degree of accuracy. The effects of parameters such as grid size, gap height, surface velocity, oil viscosity and tooling marks were investigated for a single surface geometry, demonstrating that the quasi-steady hydrodynamic lubrication model is a fast running, numerically stable, and useful tool for investigating piston sliding behavior. The average Reynolds' equation, and corresponding flow factors were also incorporated into these models, allowing comparison between the results obtained via direct numerical simulation with those from flow factors.

The elastohydrodynamic lubrication model was then combined with the piston dynamics model and additional oil reservoirs and supply points to achieve a lubricated model of piston dynamics and oil transport. Preliminary results from this model demonstrate the effects of oil film thickness, surface representation and oil supply conditions on lateral motion, piston tilt and friction generation. Long calculation times and numerical instability hamper its usefulness as an engineering analysis tool though, and further work is required before this model will be released for practical design use.

7.2. Piston Dynamics

The results presented in this thesis are for a single, heavy duty diesel engine. The degree to which conclusions drawn from these results can be applied to other engines is sometimes limited, particularly when there are significant differences in the combustion pressure - inertia balance, piston - cylinder bore relative stiffness or oil supply conditions.

The quasi-dry model analysis demonstrated that the piston's lateral motion is essentially driven by the combustion pressure, component axial inertias and angular position of the connecting-rod. Piston – cylinder bore friction and wrist-pin friction, while not well defined, were found to not play a significant role in determining the side force acting on the piston. The connecting rod angular inertia and rate of change of momentum do not play a large role in determining the magnitude of the side force but can significantly affect the mid-stroke piston slap timing. Significant fluctuations in the side force occur due to the component lateral inertias, but these fluctuations were significantly damped out in the lubricated model results. The side force acting on the piston, and driving lateral motion, is therefore very well defined by both the quasi-dry and lubricated models, and relatively unaffected by oil film thickness.

The lateral motion of the piston is constrained by the cylinder bore and oil film, and is therefore essentially a function of the piston - cylinder bore clearance, oil film thickness, side force, and piston deformation (and cylinder deformation). The lubricated model results clearly demonstrate the large effect that oil film thickness can have on lateral motion if there is sufficient oil supply, significantly reducing lateral motion and impact velocities, and damping out oscillations.

Piston tilt is much more sensitive than lateral motion to the many uncertainties in the model. The angular motion of the piston is driven by the friction moments at the piston – wrist pin and piston – cylinder bore interfaces, and the moments generated by the pressure force and piston-cylinder bore side force. In the absence of wrist-pin offset, the wrist-pin friction moment dominates this moment balance approaching combustion TDC until piston slap occurs, at which point the piston's interactions with the cylinder bore also become significant. Away from combustion TDC, where the loads transmitted through the system are much smaller, the piston is essentially searching for a stable position on the cylinder bore where the side force and friction force moments will balance. For the quasi-dry model, this results in a lot of oscillation at light loads which is damped out by the presence of oil in the lubricated model. The quasi-dry model results demonstrated that this stable tilt is a function of the location of the minimum clearance point on the piston, the gradient of the deformed piston profile, the average cylinder bore gradient, over the load bearing portion of the bore, and the piston – cylinder bore friction coefficient. The lubricated results, however, demonstrated that oil film thickness also plays a significant role in piston tilt, effectively changing the geometry constraining piston motion, and resulting in larger tilts, particularly during piston slap and an increase in land contact at combustion TDC.

A range of surface representations were tested using the lubricated piston dynamics model. It was found that surprisingly coarse grid representations are sufficient to accurately describe the piston dynamics, with a 17 × 49 grid resulting in less than 0.5 μm variation in lateral motion and 0.2×10^{-4} rad variation in piston tilt compared to a 17 × 81 grid. A comparison between mean surface line, outer surface line, flow factor method and direct numerical simulation of the piston skirt tooling marks (17 × 1585 grid) demonstrated that, in terms of piston dynamics, there is a significant underestimate of lateral motion by the outer surface line results, but there is insufficient difference between the results of the other three methods to justify the large increase in computational time and memory required for direct numerical simulation.

7.3. Friction Generation

Accurate determination of the friction generated at the piston – cylinder bore interface continues to pose a significant challenge. The lubricated piston dynamics model results demonstrate the significant effect that oil film thickness can have on reducing friction generation at the piston – cylinder bore interface, but the accuracy of these results come into question when we compare the different surface representations, particularly approaching combustion TDC and throughout the expansion stroke, where there significant variations in the friction predicted.

The quasi-steady lubrication model results demonstrated the sensitivity of hydrodynamic pressure generation to detailed surface geometry and gap height. While the net normal force generated by the piston – cylinder bore interface is relatively well defined by the lateral wrist-pin force, the proportion of it that can be supported by hydrodynamic vs asperity contact pressure is not. At small clearances, small variations in surface geometry or piston deformation can result in significant variations in the hydrodynamic and asperity contact pressures, and corresponding changes in the resulting contact friction. Further investigation is required to determine the degree of accuracy that can be placed on friction predictions using these methods.

7.4. Possible Areas for Future Research

The current research provides us with a new suite of tools for investigating the behavior of the power cylinder system, and other tribological systems. Further investigation of the effect of tooling marks and other surface features on hydrodynamic and elastohydrodynamic lubrication may result in a better understanding of pressure and friction generation and oil transport, and corresponding recommendations for reducing friction and wear.

There are also several opportunities for improvements to these models. The current numerical algorithm used for solving the radial deformation of the piston at the piston – cylinder bore interface has proved to be costly in terms of calculation time, and numerically unstable. A replacement algorithm should be developed in order to improve the models robustness and allow a greater range of systems to be investigated.

The current fluid model, based on the Universal Reynolds Equation applied over the extent of the piston skirt does not accurately capture the phenomena of fluid film detachment and reattachment, and the corresponding oil transport on the piston. The development of a subroutine for more accurately tracking this oil transport, and accounting for the free surface flow of oil on the piston would be a very interesting and useful addition.

The addition of artificial damping and a more realistic estimate of the piston-cylinder bore friction coefficient as a function of axial position to the quasi-dry model, while requiring calibration, could result in a fast running and sufficiently accurate model of lubricated piston dynamics.

A1. Derivation of Governing Equations

A1.1. Review of Rigid Body Motion

For the purpose of deriving the governing dynamic equations of the power cylinder system we will assume that each of the system components can be considered to be a rigid body. It is therefore useful to review the general dynamic equations governing rigid body motion.

A1.1.1. Conservation of Linear Momentum:

Consider a particle, *i*, and two reference frames, A and B, where A is a stationary reference frame and B rotates relative to A with an angular velocity, $\omega_{B/A}$, as shown in Figure A1.1:

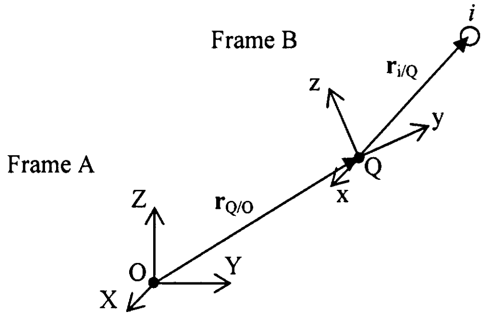

Figure A1.1: Particle Dynamics

The position, velocity and acceleration of the particle, *i*, are then given by the following set of equations [46]:

$$\mathbf{r}_{i/O} = \mathbf{r}_{Q/O} + \mathbf{r}_{i/Q}$$

$$\mathbf{v}_{i/A} = \mathbf{v}_{Q/A} + \mathbf{v}_{i/B} + \left(\boldsymbol{\omega}_{B/A} \times \mathbf{r}_{i/Q}\right)$$

$$\mathbf{a}_{i/A} = \mathbf{a}_{Q/A} + \mathbf{a}_{i/B} + \left(\boldsymbol{\alpha}_{B/A} \times \mathbf{r}_{i/Q}\right) + \boldsymbol{\omega}_{B/A} \times \left(\boldsymbol{\omega}_{B/A} \times \mathbf{r}_{i/Q}\right) + 2\left(\boldsymbol{\omega}_{B/A} \times \mathbf{v}_{i/B}\right)$$

Conservation of linear momentum, or Newton's Second Law, for a particle can be expressed as [46]:

$$\mathbf{F}_i = m_i \mathbf{a}_{i/A}$$

Consider a rigid body with centre of gravity, *CG*, and two reference frames, A and B, where A is a stationary reference frame and B rotates relative to A with an angular velocity, $\omega_{A/B}$:

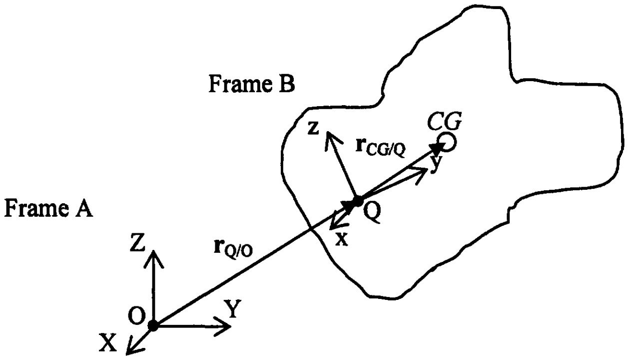

Figure A1.2: Rigid Body Dynamics

The rigid body can be considered to be a collection of infinitesimal particles which have fixed relative positions. The position of the centre of gravity of the body is defined as the mass averaged position of the body [46]:

$$\mathbf{r}_{CG} \equiv \frac{1}{m}\int \mathbf{r}\,dm$$

The position, velocity and acceleration of the centre of gravity of a rigid body can therefore be defined by the following set of equations:

$$\mathbf{r}_{CG/O} = \mathbf{r}_{CG/Q} + \mathbf{r}_{Q/O}$$

$$\mathbf{v}_{CG} \equiv \frac{1}{m}\int \mathbf{v}\,dm$$

$$\mathbf{v}_{CG/A} = \mathbf{v}_{Q/A} + \mathbf{v}_{CG/B} + \left(\boldsymbol{\omega}_{B/A} \times \mathbf{r}_{CG/Q}\right)$$

$$\mathbf{a}_{CG} \equiv \frac{1}{m}\int \mathbf{a}\,dm$$

$$\mathbf{a}_{CG/A} = \mathbf{a}_{Q/A} + \mathbf{a}_{CG/B} + \left(\boldsymbol{\alpha}_{B/A} \times \mathbf{r}_{CG/Q}\right) + \boldsymbol{\omega}_{B/A} \times \left(\boldsymbol{\omega}_{B/A} \times \mathbf{r}_{CG/Q}\right) + 2\left(\boldsymbol{\omega}_{B/A} \times \mathbf{v}_{CG/B}\right)$$

Conservation of linear momentum, or Newton's Second Law, for a rigid body can be expressed by:

$$\int d\mathbf{F} = \int \mathbf{a}_{/A}\,dm = m\mathbf{a}_{CG/A}$$

All internal forces will cancel each other out, and the above equation can be reduced to:

$$\sum \mathbf{F}_{ext} = m\mathbf{a}_{CG/A}$$

For the case where coordinate frame B is fixed to the rigid body (defined as a body coordinate system), each particle within the body does not move relative to coordinate frame B, resulting in the following expression of Newton's Law:

$$\mathbf{a}_{CG/B} = \mathbf{v}_{CG/B} = 0$$

$$\sum \mathbf{F}_{ext} = m\left[\mathbf{a}_{Q/A} + \left(\boldsymbol{\alpha}_{B/A} \times \mathbf{r}_{CG/Q}\right) + \boldsymbol{\omega}_{B/A} \times \left(\boldsymbol{\omega}_{B/A} \times \mathbf{r}_{CG/Q}\right)\right]$$

A1.1.2. Definition of Angular Momentum:

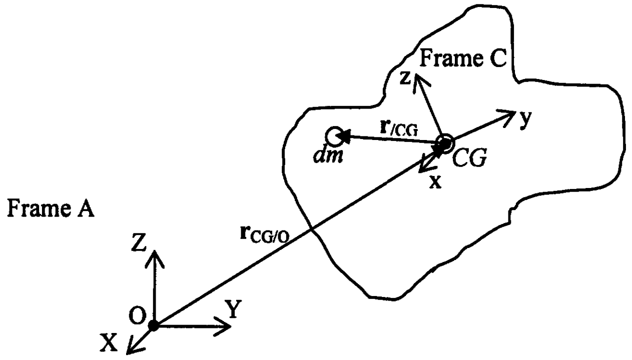

Figure A1.3: Angular Momentum about the Centre of Gravity

The angular momentum of a rigid body about its centre of gravity can be defined as follows [46]:

$$\mathbf{H}_{CG} = \int d\mathbf{H}_{/CG} = \int \mathbf{r}_{/CG} \times \mathbf{v}_{/A} dm$$

$$\mathbf{v}_{/A} = \mathbf{v}_{CG/A} + \mathbf{v}_{/C} + \left(\boldsymbol{\omega}_{C/A} \times \mathbf{r}_{/CG}\right)$$

If coordinate frame C is fixed to the rigid body, then we have $\mathbf{v}_{/C} = 0$ for all particles in the body, and the above equation can be reduced to:

$$\mathbf{H}_{CG} = \left(\int \mathbf{r}_{/CG} dm\right) \times \mathbf{v}_{CG/A} + \int \mathbf{r}_{/CG} \times \left(\boldsymbol{\omega}_{C/A} \times \mathbf{r}_{/CG}\right) dm$$

By definition, we have:

$$\int \mathbf{r}_{/CG} dm = 0$$

resulting in the following equation for the angular momentum of a rigid body about its centre of gravity:

$$\mathbf{H}_{CG} = \int \mathbf{r}_{/CG} \times \left(\boldsymbol{\omega}_{C/A} \times \mathbf{r}_{/CG}\right) dm$$

This equation can be further expanded in the following manner:

$$\mathbf{r}_{/CG} = x\mathbf{i}_C + y\mathbf{j}_C + z\mathbf{k}_C$$

$$\boldsymbol{\omega}_{C/A} = \omega_x\mathbf{i}_C + \omega_y\mathbf{j}_C + \omega_z\mathbf{k}_C$$

$$\mathbf{H}_{CG} = \int \mathbf{r}_{/CG} \times \left\{(\omega_y z - \omega_z y)\mathbf{i}_C + (\omega_z x - \omega_x z)\mathbf{j}_C + (\omega_x y - \omega_y x)\mathbf{k}_C\right\}dm$$

$$\begin{aligned}\mathbf{H}_{CG} = &\left[\omega_x \int (y^2 + z^2)dm - \omega_y \int yxdm - \omega_z \int zxdm\right]\mathbf{i}_C \\ &+ \left[\omega_y \int (z^2 + x^2)dm - \omega_z \int zydm - \omega_x \int xydm\right]\mathbf{j}_C \\ &+ \left[\omega_z \int (x^2 + y^2)dm - \omega_x \int xzdm - \omega_y \int yzdm\right]\mathbf{k}_C\end{aligned}$$

$$\mathbf{H}_{CG} = \left[I_{xx}\omega_x - I_{xy}\omega_y - I_{xz}\omega_z\right]\mathbf{i}_C + \left[I_{yy}\omega_y - I_{yz}\omega_z - I_{xy}\omega_x\right]\mathbf{j}_C + \left[I_{zz}\omega_z - I_{xz}\omega_x - I_{yz}\omega_y\right]\mathbf{k}_C$$

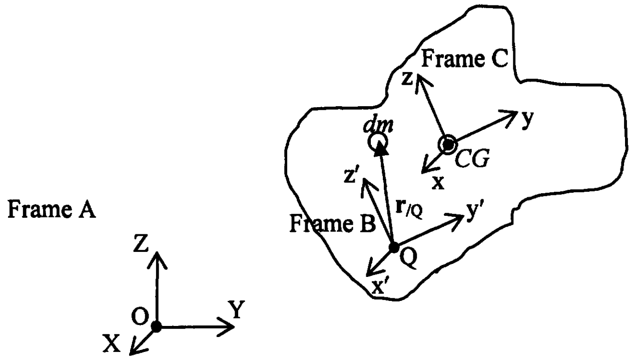

Figure A1.4: Angular Momentum about an Arbitrary Point, Q

The angular momentum of a rigid body about an arbitrary point, *Q*, can be defined as follows:

$$\mathbf{H}_Q = \int d\mathbf{H}_{/Q} = \int \mathbf{r}_{/Q} \times \mathbf{v}_{/A}dm$$

$$\mathbf{r}_{/Q} = \mathbf{r}_{/CG} + \mathbf{r}_{CG/Q}$$

$$\mathbf{H}_Q = \mathbf{H}_{CG} + \mathbf{r}_{CG/Q} \times m\mathbf{v}_{CG/A}$$

A1.1.3. Conservation of Angular Momentum:

Consider the time rate of change of angular momentum of a rigid body about an arbitrary point, Q:

$$\mathbf{H}_Q = \int \mathbf{r}_{/Q} \times \mathbf{v}_{/A}dm$$

$$\frac{d\mathbf{H}_Q}{dt} = \int \left[\mathbf{v}_{/B} + (\boldsymbol{\omega}_{B/A} \times \mathbf{r}_{/Q})\right] \times \mathbf{v}_{/A}dm + \int \mathbf{r}_{/Q} \times \mathbf{a}_{/A}dm$$

The moment, about an arbitrary point, Q, created by a force acting on a particle within the rigid body, can be defined by:

$$d\mathbf{M}_{/Q} = \mathbf{r}_{/Q} \times d\mathbf{F}$$

Applying Newton's Second Law for each infinitesimal particle of the body, and assuming that all internal moments cancel, we have:

$$\int d\mathbf{M}_{/Q} = \sum \mathbf{M}_{ext/Q} = \int \mathbf{r}_{/Q} \times \mathbf{a}_{/A} dm$$

The rate of change of angular momentum can then be expressed as:

$$\frac{d\mathbf{H}_Q}{dt} = \int \left[\mathbf{v}_{/B} + \left(\boldsymbol{\omega}_{B/A} \times \mathbf{r}_{/Q}\right)\right] \times \left[\mathbf{v}_{Q/A} + \mathbf{v}_{/B} + \left(\boldsymbol{\omega}_{B/A} \times \mathbf{r}_{/Q}\right)\right] dm + \sum \mathbf{M}_{ext/Q}$$

Recalling that $\mathbf{v}_{/B} = 0$ for a body coordinate frame, and rearranging, this can be further reduced to:

$$\frac{d\mathbf{H}_Q}{dt} = -\mathbf{v}_{Q/A} \times m\left(\boldsymbol{\omega}_{B/A} \times \mathbf{r}_{CG/Q}\right) + \sum \mathbf{M}_{ext/Q}$$

Note that since both body coordinate frames (B and C) are fixed to the same rigid body, the angular velocities, $\omega_{B/A}$ and $\omega_{C/A}$, are equal, and will be used interchangeably here.

As was shown in Section A1.1.2, we can also express the angular momentum about an arbitrary point in terms of the angular momentum about the centre of gravity and the motion of the centre of gravity:

$$\mathbf{H}_Q = \mathbf{H}_{CG} + \mathbf{r}_{CG/Q} \times m\mathbf{v}_{CG/A}$$

$$\frac{d\mathbf{H}_Q}{dt} = \frac{d\mathbf{H}_{CG}}{dt} + \left[\mathbf{v}_{CG/B} + \left(\boldsymbol{\omega}_{B/A} \times \mathbf{r}_{CG/Q}\right)\right] \times m\left[\mathbf{v}_{Q/A} + \mathbf{v}_{CG/B} + \left(\boldsymbol{\omega}_{B/A} \times \mathbf{r}_{CG/Q}\right)\right] + \mathbf{r}_{CG/Q} \times m\mathbf{a}_{CG/A}$$

Recalling that $\mathbf{v}_{/B} = 0$ for a body coordinate frame, and rearranging, this can be further reduced to:

$$\frac{d\mathbf{H}_Q}{dt} = \frac{d\mathbf{H}_{CG}}{dt} - \mathbf{v}_{Q/A} \times m\mathbf{v}_{CG/A} + \mathbf{r}_{CG/Q} \times m\mathbf{a}_{CG/A}$$

Combining these two expressions for the rate of change of angular momentum, and rearranging, the following general conservation of angular moment equation is obtained:

$$\frac{d\mathbf{H}_{CG}}{dt} + \mathbf{r}_{CG/Q} \times m\mathbf{a}_{CG/A} = \sum \mathbf{M}_{ext/Q}$$

The time rate of change of angular momentum of a rigid body about its centre of gravity can also be written in the following manner:

$$\frac{d\mathbf{H}_{CG}}{dt} = \frac{\partial \mathbf{H}_{CG}}{\partial t} + \boldsymbol{\omega} \times \mathbf{H}_{CG}$$

$$\begin{aligned}\frac{d\mathbf{H}_{CG}}{dt} &= \frac{\partial}{\partial t}\left\{\left[I_{xx}\omega_x - I_{xy}\omega_y - I_{xz}\omega_z\right]\mathbf{i}_C + \left[I_{yy}\omega_y - I_{yz}\omega_z - I_{xy}\omega_x\right]\mathbf{j}_C + \left[I_{zz}\omega_z - I_{xz}\omega_x - I_{yz}\omega_y\right]\mathbf{k}_C\right\} \\ &\quad + \boldsymbol{\omega} \times \left\{\left[I_{xx}\omega_x - I_{xy}\omega_y - I_{xz}\omega_z\right]\mathbf{i}_C + \left[I_{yy}\omega_y - I_{yz}\omega_z - I_{xy}\omega_x\right]\mathbf{j}_C + \left[I_{zz}\omega_z - I_{xz}\omega_x - I_{yz}\omega_y\right]\mathbf{k}_C\right\}\end{aligned}$$

$$\begin{aligned}\frac{d\mathbf{H}_{CG}}{dt} &= \left[I_{xx}\dot{\omega}_x + \left(I_{zz} - I_{yy}\right)\omega_z\omega_y - I_{xy}\left(\dot{\omega}_y - \omega_z\omega_x\right) - I_{xz}\left(\dot{\omega}_z + \omega_y\omega_x\right) - I_{yz}\left(\omega_y^{\,2} - \omega_z^{\,2}\right)\right]\mathbf{i}_C \\ &\quad + \left[I_{yy}\dot{\omega}_y + \left(I_{xx} - I_{zz}\right)\omega_x\omega_z - I_{yz}\left(\dot{\omega}_z - \omega_x\omega_y\right) - I_{xy}\left(\dot{\omega}_x + \omega_z\omega_y\right) - I_{xz}\left(\omega_z^{\,2} + \omega_x^{\,2}\right)\right]\mathbf{j}_C \\ &\quad + \left[I_{zz}\dot{\omega}_z + \left(I_{yy} - I_{xx}\right)\omega_y\omega_x - I_{xz}\left(\dot{\omega}_x - \omega_y\omega_z\right) - I_{yz}\left(\dot{\omega}_y + \omega_x\omega_z\right) - I_{xy}\left(\omega_x^{\,2} + \omega_y^{\,2}\right)\right]\mathbf{k}_C\end{aligned}$$

Combining this with the general conservation of angular moment equation from above, and reducing to two-dimensional planar motion we obtain:

$$I_{xx}\dot{\omega}_x = \left\{\sum \mathbf{M}_{ext/Q} - \mathbf{r}_{CG/Q} \times m\mathbf{a}_{CG/A}\right\}_x$$

A1.2. Component Dynamics and Equations of Motion

A1.2.1. Crankshaft Dynamics

It is assumed that the crankshaft has no linear motion, and rotates about its axis with a given angular speed, $\omega_{CA}(t)$. The crankshaft – connecting-rod bearing is assumed to be an ideal frictionless pin joint, allowing relative rotational motion of the two components without friction generation, and without relative displacement at point *Q*. Reference Frame A is defined as a non-inertial reference frame, the origin of which is located at the intersection of the cylinder bore axis and the horizontal centerline of the crankshaft, point *O*. The motion of the centre of the connecting-rod large end bearing, point *Q*, as a function of crankshaft angle, $\theta_{CA}(t)$, relative to reference frame A, is therefore given by:

$$\mathbf{r}_{Q/O} = \left[-r_{CS}\sin(\theta_{CA}) + y_{CSO}\right]\mathbf{j} + r_{CS}\cos(\theta_{CA})\mathbf{k}$$

$$\mathbf{v}_{Q/A} = -\dot{\theta}_{CA}r_{CS}\cos(\theta_{CA})\mathbf{j} - \dot{\theta}_{CA}r_{CS}\sin(\theta_{CA})\mathbf{k}$$

$$\mathbf{a}_{Q/A} = \left[-\ddot{\theta}_{CA}r_{CS}\cos(\theta_{CA}) + \dot{\theta}_{CA}^{\,2}r_{CS}\sin(\theta_{CA})\right]\mathbf{j} - \left[\ddot{\theta}_{CA}r_{CS}\sin(\theta_{CA}) + \dot{\theta}_{CA}^{\,2}r_{CS}\cos(\theta_{CA})\right]\mathbf{k}$$

A1.2.2. Connecting-Rod Dynamics and Equations of Motion

The connecting-rod connects the wrist-pin to the crankshaft, helping to convert the linear motion of the piston into the angular motion of the crankshaft. It is assumed that the angular motion of the crankshaft is prescribed, that it has no linear motion, and that there is no relative displacement between the centre of the large end of the connecting-rod and the corresponding point on the crankshaft, *Q*. The large end of the connecting-rod is attached to the crankshaft via bearings which are assumed to be frictionless, and therefore provide no moment to the connecting-rod. The connecting-rod is considered to be rigid for the purposes of this work.

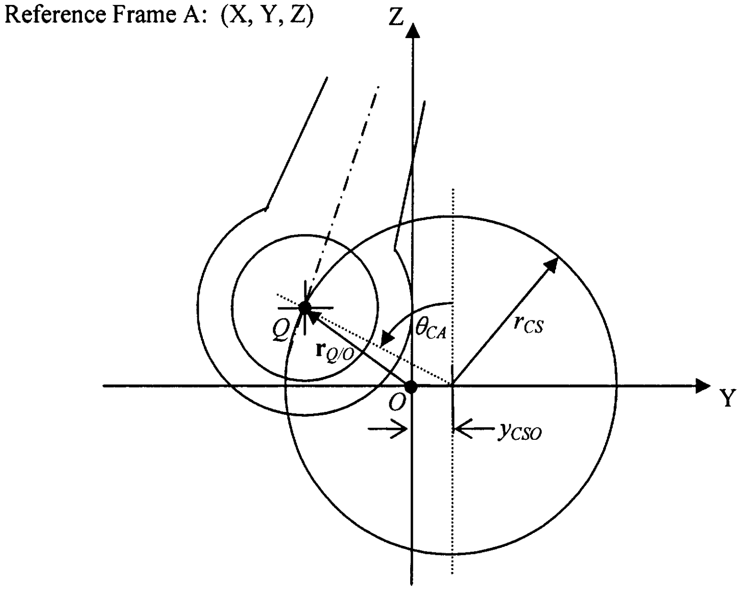

Figure A1.5: Crankshaft Dynamics

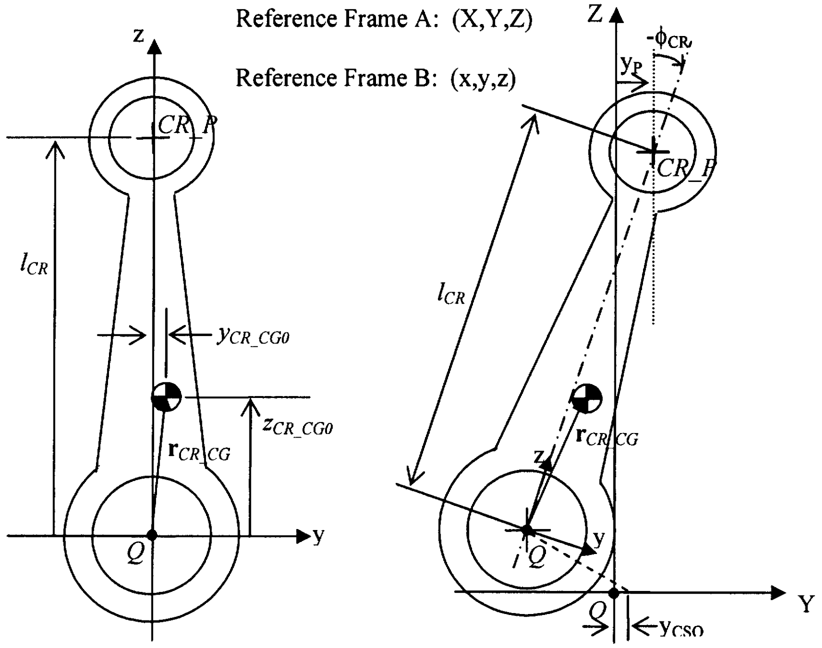

Figure A1.6: Connecting Rod Geometry and Dynamics

The motion of the large end of the connecting-rod, point *Q*, is well defined by the crankshaft motion and engine geometry:

$$\mathbf{r}_{Q/O} = \left[-r_{CS}\sin(\theta_{CA}) + y_{CSO}\right]\mathbf{j} + r_{CS}\cos(\theta_{CA})\mathbf{k}$$

$$\mathbf{v}_{Q/A} = -\dot{\theta}_{CA} r_{CS}\cos(\theta_{CA})\mathbf{j} - \dot{\theta}_{CA} r_{CS}\sin(\theta_{CA})\mathbf{k}$$

$$\mathbf{a}_{Q/A} = \left[-\ddot{\theta}_{CA} r_{CS}\cos(\theta_{CA}) + \dot{\theta}_{CA}{}^2 r_{CS}\sin(\theta_{CA})\right]\mathbf{j} - \left[\ddot{\theta}_{CA} r_{CS}\sin(\theta_{CA}) + \dot{\theta}_{CA}{}^2 r_{CS}\cos(\theta_{CA})\right]\mathbf{k}$$

The motion of the small end of the connecting-rod, point CR_*P*, can be defined by:

$$\mathbf{r}_{CR\_P/O} = \left[-r_{CS}\sin(\theta_{CA}) + y_{CSO} - l_{CR}\sin(\phi_{CR})\right]\mathbf{j} + \left[r_{CS}\cos(\theta_{CA}) + l_{CR}\cos(\phi_{CR})\right]\mathbf{k}$$

$$\mathbf{v}_{CR\_P/A} = \left[-\dot{\theta}_{CA} r_{CS}\cos(\theta_{CA}) - \dot{\phi}_{CR} l_{CR}\cos(\phi_{CR})\right]\mathbf{j} - \left[\dot{\theta}_{CA} r_{CS}\sin(\theta_{CA}) + \dot{\phi}_{CR} l_{CR}\sin(\phi_{CR})\right]\mathbf{k}$$

$$\begin{aligned}\mathbf{a}_{CR\_P/A} = {} & \left[-\ddot{\theta}_{CA} r_{CS}\cos(\theta_{CA}) + \dot{\theta}_{CA}{}^2 r_{CS}\sin(\theta_{CA}) - \ddot{\phi}_{CR} l_{CR}\cos(\phi_{CR}) + \dot{\phi}_{CR}{}^2 l_{CR}\sin(\phi_{CR})\right]\mathbf{j} \\ & - \left[\ddot{\theta}_{CA} r_{CS}\sin(\theta_{CA}) + \dot{\theta}_{CA}{}^2 r_{CS}\cos(\theta_{CA}) + \ddot{\phi}_{CR} l_{CR}\sin(\phi_{CR}) + \dot{\phi}_{CR}{}^2 l_{CR}\cos(\phi_{CR})\right]\mathbf{k}\end{aligned}$$

If we assume that there is no relative displacement between the small end of the connecting-rod, the wrist-pin and the piston, at point *P*, then the connecting-rod angle, ϕ_{CR}, and its time derivatives can be defined in terms of the lateral motion of the piston.

$$x_{Py} = -r_{CS}\sin(\theta_{CA}) + y_{CSO} - l_{CR}\sin(\phi_{CR})$$

$$\phi_{CR} = \arcsin\left[\frac{y_{CSO}}{l_{CR}} - \frac{r_{CS}}{l_{CR}}\sin(\theta_{CA}) - \frac{x_{Py}}{l_{CR}}\right]$$

The effect of lateral motion, x_{Py}, on the connecting-rod angle, only becomes significant for very small values of both crankshaft offset, y_{CSO}, and $\sin(\theta_{CA})$, at which point we can linearise arcsin to estimate this effect:

$$\phi_{CR} \sim \frac{y_{CSO}}{l_{CR}} - \frac{r_{CS}}{l_{CR}}\sin(\theta_{CA}) - \frac{x_{Py}}{l_{CR}}$$

$$\Delta\phi_{CR}(x_{Py}) \sim \frac{x_{Py}}{l_{CR}} \sim 10^{-3}$$

The lateral motion of point *P* does not significantly impact the connecting-rod angle, but the resulting changes to the connecting-rod angular acceleration, and the corresponding connecting-rod, wrist-pin and piston inertia terms, are important. The time derivatives of the connecting-rod angle are defined by:

$$\dot{\phi}_{CR} = -\frac{\dot{u}}{\sqrt{1-u^2}}$$

$$\ddot{\phi}_{CR} = -\frac{\ddot{u}}{\sqrt{1-u^2}} + \frac{u\dot{u}^2}{\left(1-u^2\right)^{3/2}}$$

where

$$u \equiv \frac{r_{CS}}{l_{CR}}\sin(\theta_{CA}) - \frac{y_{CS0}}{l_{CR}} + \frac{x_{PY}}{l_{CR}}$$

$$\dot{u} = \frac{r_{CS}}{l_{CR}}\dot{\theta}_{CA}\cos(\theta_{CA}) + \frac{\dot{x}_{PY}}{l_{CR}}$$

$$\ddot{u} = \frac{r_{CS}}{l_{CR}}\ddot{\theta}_{CA}\cos(\theta_{CA}) - \frac{r_{CS}}{l_{CR}}\dot{\theta}_{CA}{}^{2}\sin(\theta_{CA}) + \frac{\ddot{x}_{PY}}{l_{CR}}$$

Given that there are significant clearances between the connecting-rod, wrist-pin and piston at the pin bearings, and that the lubrication conditions in these bearings are not well defined, there is significant uncertainty in the relative displacement of these components. As a first approximation, we assume there is no relative motion, expecting that this results in an underestimation of the lateral accelerations experienced by the connecting-rod and wrist-pin.

The resulting equations for the motion of the small end of the connecting-rod, point CR_*P*, are:

$$\mathbf{r}_{CR\_P/O} = x_{Py}\mathbf{j} + \left[r_{CS}\cos(\theta_{CA}) + l_{CR}\cos(\phi_{CR})\right]\mathbf{k}$$

$$\mathbf{v}_{CR\_P/A} = \dot{x}_{Py}\mathbf{j} - \left[\dot{\theta}_{CA} r_{CS}\sin(\theta_{CA}) + \dot{\phi}_{CR} l_{CR}\sin(\phi_{CR})\right]\mathbf{k}$$

$$\mathbf{a}_{CR\_P/A} = \ddot{x}_{Py}\mathbf{j} - \left[\ddot{\theta}_{CA} r_{CS}\sin(\theta_{CA}) + \dot{\theta}_{CA}{}^{2} r_{CS}\cos(\theta_{CA}) + \ddot{\phi}_{CR} l_{CR}\sin(\phi_{CR}) + \dot{\phi}_{CR}{}^{2} l_{CR}\cos(\phi_{CR})\right]\mathbf{k}$$

As described in our review of rigid body motion in Section A1.1.1, the motion of an arbitrary point, P_1, on a rigid body can be defined by the fixed relative position of P_1 with respect to another arbitrary point P_2, the angular motion of the rigid body, and the motion of point P_2.

$$\mathbf{r}_{P_1/O} = \mathbf{r}_{P_1/P_2} + \mathbf{r}_{P_2/O}$$

$$\mathbf{v}_{P_1/A} = \mathbf{v}_{P_2/A} + \left[(\dot{\phi}_{CR}\mathbf{i}) \times \mathbf{r}_{P_1/P_2}\right]$$

$$\mathbf{a}_{P_1/A} = \mathbf{a}_{P_2/A} + \left[(\ddot{\phi}_{CR}\mathbf{i}) \times \mathbf{r}_{P_1/P_2}\right] + (\dot{\phi}_{CR}\mathbf{i}) \times \left[(\dot{\phi}_{CR}\mathbf{i}) \times \mathbf{r}_{P_1/P_2}\right]$$

The motion of the centre of gravity of the connecting-rod can therefore be expressed in terms of the crankshaft motion and engine geometry:

$$\begin{aligned}\mathbf{r}_{CR\_CG/O} &= \mathbf{r}_{Q/O} + \mathbf{r}_{CR\_CG/Q}\\ &= \left[-r_{CS}\sin(\theta_{CA}) + y_{CSO}\right]\mathbf{j} + r_{CS}\cos(\theta_{CA})\mathbf{k} + \mathbf{r}_{CR\_CG/Q}\end{aligned}$$

$$\begin{aligned}\mathbf{v}_{CR\_CG/A} &= \mathbf{v}_{Q/A} + \left[(\dot{\phi}_{CR}\mathbf{i}) \times \mathbf{r}_{CR\_CG/Q}\right]\\ &= -\dot{\theta}_{CA} r_{CS}\cos(\theta_{CA})\mathbf{j} - \dot{\theta}_{CA} r_{CS}\sin(\theta_{CA})\mathbf{k} + \left[(\dot{\phi}_{CR}\mathbf{i}) \times \mathbf{r}_{CR\_CG/Q}\right]\end{aligned}$$

$$
\begin{aligned}
\mathbf{a}_{CR\_CG/A} &= \mathbf{a}_{Q/A} + \left[\left(\ddot{\phi}_{CR}\mathbf{i}\right)\times\mathbf{r}_{CR\_CG/Q}\right] + \left(\dot{\phi}_{CR}\mathbf{i}\right)\times\left[\left(\dot{\phi}_{CR}\mathbf{i}\right)\times\mathbf{r}_{CR\_CG/Q}\right] \\
&= \left[-\ddot{\theta}_{CA}r_{CS}\cos(\theta_{CA})+\dot{\theta}_{CA}{}^{2}r_{CS}\sin(\theta_{CA})\right]\mathbf{j} - \left[\ddot{\theta}_{CA}r_{CS}\sin(\theta_{CA})+\dot{\theta}_{CA}{}^{2}r_{CS}\cos(\theta_{CA})\right]\mathbf{k} \\
&\quad + \left[\left(\ddot{\phi}_{CR}\mathbf{i}\right)\times\mathbf{r}_{CR\_CG/Q}\right] + \left(\dot{\phi}_{CR}\mathbf{i}\right)\times\left[\left(\dot{\phi}_{CR}\mathbf{i}\right)\times\mathbf{r}_{CR\_CG/Q}\right]
\end{aligned}
$$

where the position of the centre of gravity, of the connecting-rod, relative to point Q, $\mathbf{r}_{CR\_CG/Q}$, is defined as:

$$\mathbf{r}_{CR\_CG/Q} = x_{CR\_CG0}\mathbf{i} + \left[\cos(\phi_{CR}) - z_{CR\_CG0}\sin(\phi_{CR})\right]\mathbf{j} + \left[y_{CR\_CG0}\sin(\phi_{CR}) + z_{CR\_CG0}\cos(\phi_{CR})\right]\mathbf{k}$$

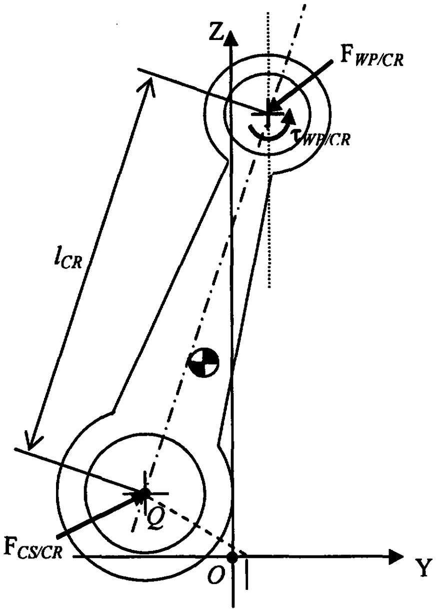

Figure A1.7: Connecting Rod Force and Moment Balance

As shown in Figure A1.7, the connecting-rod is subject to external forces from the interfaces it shares with the crankshaft and wrist-pin, $\mathbf{F}_{CS/CR}$ and $\mathbf{F}_{WP/CR}$ respectively, and due to gravity. The calculation of these forces is described in Sections 2.3 and 2.4. Conservation of linear momentum for the connecting-rod yields the following equation:

$$\mathbf{F}_{CS/CR} + \mathbf{F}_{WP/CR} + m_{CR}\mathbf{g} = m_{CR}\mathbf{a}_{CR\_CG/A}$$

Assuming that the large end bearing is a frictionless pin-joint, and therefore $\mathbf{M}_{CS/Q}$ is equal to zero, conservation of angular momentum for the connecting-rod, about the point Q, yields the following equations:

$$\frac{d\mathbf{H}_{CR\_CG}}{dt} = \mathbf{M}_{CS/Q} + \mathbf{M}_{WP/Q} + \mathbf{r}_{CR\_CG/Q}\times m_{CR}\mathbf{g} - \mathbf{r}_{CR\_CG/Q}\times m_{CR}\mathbf{a}_{CR\_CG/A}$$

$$\frac{d\mathbf{H}_{CR\_CG}}{dt} = \boldsymbol{\tau}_{WP/CR} + \mathbf{r}_{CR\_P/Q}\times\mathbf{F}_{WP/CR} + \mathbf{r}_{CR\_CG/Q}\times m_{CR}\mathbf{g} - \mathbf{r}_{CR\_CG/Q}\times m_{CR}\mathbf{a}_{CR\_CG/A}$$

The motion of the connecting-rod is assumed to be two-dimensional, and therefore the angular motion of the connecting-rod can be described by a single angle, ϕ_{CR}, thereby reducing the above equation to:

$$
\begin{aligned}
I_{CR\_XX}\ddot{\phi}_{CR} = {} & \tau_{WP/CRX} + r_{CR\_P/Q_Y} F_{WP/CRZ} - r_{CR\_P/Q_Z} F_{WP/CRY} + r_{CR\_CG/Q_Y} m_{CR} g_Z \\
& - r_{CR\_CG/Q_Z} m_{CR} g_Y - r_{CR\_CG/Q_Y} m_{CR} a_{CR\_CG/A_Z} + r_{CR\_CG/Q_Z} m_{CR} a_{CR\_CG/A_Y}
\end{aligned}
$$

Rearranging this equation, we can express that angular motion of the connecting-rod in terms of known quantities, and the three unknown forces and moments acting at the connecting-rod – wrist-pin interface:

$$
F_{WP/CRY} = \frac{\tau_{WP/CRX}}{r_{CR\_P/Q_Z}} + \frac{1}{r_{CR\_P/Q_Z}} \begin{bmatrix} r_{CR\_P/Q_Y} F_{WP/CRZ} + r_{CR\_CG/Q_Y} m_{CR} g_Z - r_{CR\_CG/Q_Z} m_{CR} g_Y \\ - r_{CR\_CG/Q_Y} m_{CR} a_{CR\_CG/A_Z} + r_{CR\_CG/Q_Z} m_{CR} a_{CR\_CG/A_Y} - I_{CR\_XX}\ddot{\phi}_{CR} \end{bmatrix}
$$

The axial force acting at the connecting-rod – wrist-pin interface can be defined by axial force balances on the piston and wrist-pin, leaving the lateral force and moment to be solved for simultaneously from the above equation and the simple bearing model described in Section 2.3.2.

A1.2.3. Wrist-Pin Dynamics and Equations of Motion

The wrist-pin connects the connecting-rod to the piston, allowing the piston to rotate relative to the connecting-rod. It can be fixed to the connecting-rod, fixed to the piston, or able to rotate independently of both the connecting-rod and piston (floating pin). For the purposes of this project we assume that the wrist-pin is rigid, and that there is no relative displacement between the wrist-pin, piston and small end of the connecting-rod at point *P*.

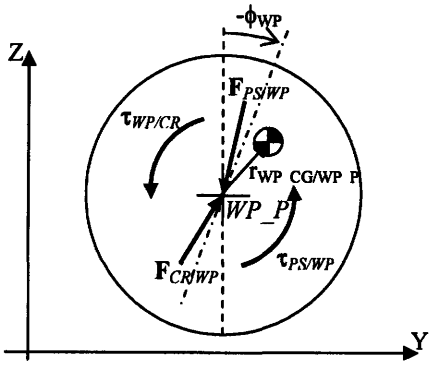

Figure A1.8: Piston Pin Dynamics

The motion of the ideal centre of the wrist-pin, point *WP_P*, is therefore given by:

$$\mathbf{r}_{WP\_P/O} = x_{Py}\mathbf{j} + \left[r_{CS}\cos(\theta_{CA}) + l_{CR}\cos(\phi_{CR})\right]\mathbf{k}$$

$$\mathbf{v}_{WP\_P/A} = \dot{x}_{Py}\mathbf{j} - \left[\dot{\theta}_{CA}r_{CS}\sin(\theta_{CA}) + \dot{\phi}_{CR}l_{CR}\sin(\phi_{CR})\right]\mathbf{k}$$

$$\mathbf{a}_{WP\_P/A} = \ddot{x}_{Py}\mathbf{j} - \left[\ddot{\theta}_{CA}r_{CS}\sin(\theta_{CA}) + \dot{\theta}_{CA}^{\,2}r_{CS}\cos(\theta_{CA}) + \ddot{\phi}_{CR}l_{CR}\sin(\phi_{CR}) + \dot{\phi}_{CR}^{\,2}l_{CR}\cos(\phi_{CR})\right]\mathbf{k}$$

As described in our review of rigid body motion in Section A1.1.1, the motion of an arbitrary point, P_1, on a rigid body can be defined by the fixed relative position of P_1 with respect to another arbitrary point P_2, the angular motion of the rigid body, and the motion of point P_2.

$$\mathbf{r}_{P_1/O} = \mathbf{r}_{P_1/P_2} + \mathbf{r}_{P_2/O}$$

$$\mathbf{v}_{P_1/A} = \mathbf{v}_{P_2/A} + \left[\left(\dot{\phi}_{CR}\mathbf{i}\right)\times\mathbf{r}_{P_1/P_2}\right]$$

$$\mathbf{a}_{P_1/A} = \mathbf{a}_{P_2/A} + \left[\left(\ddot{\phi}_{CR}\mathbf{i}\right)\times\mathbf{r}_{P_1/P_2}\right] + \left(\dot{\phi}_{CR}\mathbf{i}\right)\times\left[\left(\dot{\phi}_{CR}\mathbf{i}\right)\times\mathbf{r}_{P_1/P_2}\right]$$

The motion of the centre of gravity of the wrist-pin can therefore be expressed as:

$$\begin{aligned}\mathbf{r}_{WP\_CG/O} &= \mathbf{r}_{WP\_P/O} + \mathbf{r}_{WP\_CG/WP\_P}\\ &= x_{Py}\mathbf{j} + \left[r_{CS}\cos(\theta_{CA}) + l_{CR}\cos(\phi_{CR})\right]\mathbf{k} + \mathbf{r}_{WP\_CG/WP\_P}\end{aligned}$$

$$\begin{aligned}\mathbf{v}_{WP\_CG/A} &= \mathbf{v}_{WP\_P/A} + \left[\left(\dot{\phi}_{WP}\mathbf{i}\right)\times\mathbf{r}_{WP\_CG/WP\_P}\right]\\ &= \dot{x}_{Py}\mathbf{j} - \left[\dot{\theta}_{CA}r_{CS}\sin(\theta_{CA}) + \dot{\phi}_{CR}l_{CR}\sin(\phi_{CR})\right]\mathbf{k} + \left[\left(\dot{\phi}_{WP}\mathbf{i}\right)\times\mathbf{r}_{WP\_CG/WP\_P}\right]\end{aligned}$$

$$\begin{aligned}\mathbf{a}_{WP\_CG/A} &= \mathbf{a}_{WP\_P/A} + \left[\left(\ddot{\phi}_{WP}\mathbf{i}\right)\times\mathbf{r}_{WP\_CG/WP\_P}\right] + \left(\dot{\phi}_{WP}\mathbf{i}\right)\times\left[\left(\dot{\phi}_{WP}\mathbf{i}\right)\times\mathbf{r}_{WP\_CG/WP\_P}\right]\\ &= \ddot{x}_{Py}\mathbf{j} - \left[\ddot{\theta}_{CA}r_{CS}\sin(\theta_{CA}) + \dot{\theta}_{CA}^{\,2}r_{CS}\cos(\theta_{CA}) + \ddot{\phi}_{CR}l_{CR}\sin(\phi_{CR}) + \dot{\phi}_{CR}^{\,2}l_{CR}\cos(\phi_{CR})\right]\mathbf{k}\\ &\quad + \left[\left(\ddot{\phi}_{WP}\mathbf{i}\right)\times\mathbf{r}_{WP\_CG/WP\_P}\right] + \left(\dot{\phi}_{WP}\mathbf{i}\right)\times\left[\left(\dot{\phi}_{WP}\mathbf{i}\right)\times\mathbf{r}_{WP\_CG/WP\_P}\right]\end{aligned}$$

where the position of the centre of gravity, of the wrist-pin, relative to point *WP_P*, $\mathbf{r}_{WP\_CG/WP\_P}$, is defined as:

$$\begin{aligned}\mathbf{r}_{WP\_CG/WP\_P} &= x_{WP\_CG0}\mathbf{i} + \left[y_{WP\_CG0}\cos(\phi_{WP}) - z_{WP\_CG0}\sin(\phi_{WP})\right]\mathbf{j}\\ &\quad + \left[y_{WP\_CG0}\sin(\phi_{WP}) + z_{WP\_CG0}\cos(\phi_{WP})\right]\mathbf{k}\end{aligned}$$

The wrist-pin is subject to external forces from the interfaces it shares with the connecting-rod and piston, $\mathbf{F}_{CR/WP}$ and $\mathbf{F}_{PS/WP}$ respectively, and due to gravity. The calculation of these forces is described in Sections 2.3 and 2.4. Conservation of linear momentum for the wrist-pin yields the following equation:

$$\mathbf{F}_{PS/WP} + \mathbf{F}_{CR/WP} + m_{WP}\mathbf{g} = m_{WP}\mathbf{a}_{WP\_CG/A}$$

Conservation of angular momentum for the wrist-pin, about the centre-line yields the following equation:

$$\frac{d\mathbf{H}_{WP\_CG}}{dt} = \mathbf{M}_{PS/WP\_P} + \mathbf{M}_{CR/WP\_P} + \mathbf{r}_{WP\_CG/WP\_P} \times m_{WP}\mathbf{g} - \mathbf{r}_{WP\_CG/WP\_P} \times m_{WP}\mathbf{a}_{WP\_CG/A}$$

$$\frac{d\mathbf{H}_{WP\_CG}}{dt} = \boldsymbol{\tau}_{PS/WP} + \boldsymbol{\tau}_{CR/WP} + \mathbf{r}_{WP\_CG/WP\_P} \times m_{WP}\mathbf{g} - \mathbf{r}_{WP\_CG/WP\_P} \times m_{WP}\mathbf{a}_{WP\_CG/A}$$

The motion of the wrist-pin is assumed to be two-dimensional, thereby reducing the above equation to:

$$\begin{aligned} I_{WP\_XX}\ddot{\phi}_{WP} = {} & \tau_{PS/WPX} + \tau_{CR/WPX} + r_{WP\_CG/WP\_P_Y} \times m_{WP}g_Z - r_{WP\_CG/WP\_P_Z} \times m_{WP}g_Y \\ & - r_{WP\_CG/WP\_P_Y} \times m_{WP}a_{WP\_CG/A_Z} + r_{WP\_CG/WP\_P_Z} \times m_{WP}a_{WP\_CG/A_Y} \end{aligned}$$

A1.2.4. Piston Dynamics and Equations of Motion

The piston is connected to the wrist-pin and constrained by the cylinder bore. During combustion the pressure force pushes the piston along the cylinder bore, thereby converting the chemical energy in the fuel into kinetic energy. The piston also carries the ring pack, which act to seal the combustion gases and control the transport of lubricating oil along the cylinder bore. The piston rotates relative to the wrist-pin, but it is assumed for the purposes of this model that there is no relative displacement between the two components at point *P*. The motion of the ideal centre of the pin-bore, point *PS_P*, is therefore identical to that of the same point on the wrist-pin, point *WP_P*, and is given by:

$$\mathbf{r}_{PS\_P/O} = x_{Py}\mathbf{j} + \left[r_{CS}\cos(\theta_{CA}) + l_{CR}\cos(\phi_{CR})\right]\mathbf{k}$$

$$\mathbf{v}_{PS\_P/A} = \dot{x}_{Py}\mathbf{j} - \left[\dot{\theta}_{CA}r_{CS}\sin(\theta_{CA}) + \dot{\phi}_{CR}l_{CR}\sin(\phi_{CR})\right]\mathbf{k}$$

$$\mathbf{a}_{PS\_P/A} = \ddot{x}_{Py}\mathbf{j} - \left[\ddot{\theta}_{CA}r_{CS}\sin(\theta_{CA}) + \dot{\theta}_{CA}^{2}r_{CS}\cos(\theta_{CA}) + \ddot{\phi}_{CR}l_{CR}\sin(\phi_{CR}) + \dot{\phi}_{CR}^{2}l_{CR}\cos(\phi_{CR})\right]\mathbf{k}$$

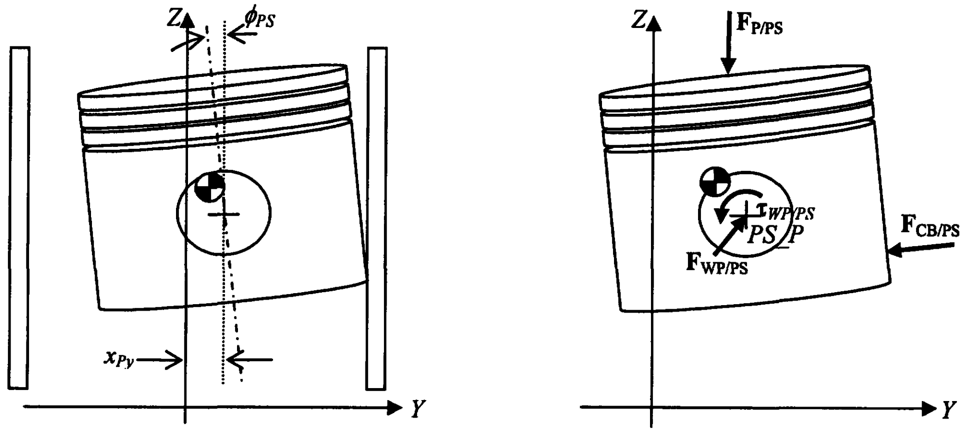

Figure A1.9: Piston Geometry and Dynamics

As described in our review of rigid body motion in Section A1.1.1, the motion of an arbitrary point, P_1, on a rigid body can be defined by the fixed relative position of P_1 with respect to another arbitrary point P_2, the angular motion of the rigid body, and the motion of point P_2.

$$\mathbf{r}_{P_1/O} = \mathbf{r}_{P_1/P_2} + \mathbf{r}_{P_2/O}$$

$$\mathbf{v}_{P_1/A} = \mathbf{v}_{P_2/A} + \left[\left(\dot{\phi}_{CR}\mathbf{i}\right)\times \mathbf{r}_{P_1/P_2}\right]$$

$$\mathbf{a}_{P_1/A} = \mathbf{a}_{P_2/A} + \left[\left(\ddot{\phi}_{CR}\mathbf{i}\right)\times \mathbf{r}_{P_1/P_2}\right] + \left(\dot{\phi}_{CR}\mathbf{i}\right)\times\left[\left(\dot{\phi}_{CR}\mathbf{i}\right)\times \mathbf{r}_{P_1/P_2}\right]$$

The motion of the centre of gravity of the piston can therefore be expressed as:

$$\begin{aligned}\mathbf{r}_{PS\_CG/O} &= \mathbf{r}_{PS\_P/O} + \mathbf{r}_{PS\_CG/PS\_P}\\ &= x_{P_y}\mathbf{j} + \left[r_{CS}\cos(\theta_{CA}) + l_{CR}\cos(\phi_{CR})\right]\mathbf{k} + \mathbf{r}_{PS\_CG/PS\_P}\end{aligned}$$

$$\begin{aligned}\mathbf{v}_{PS\_CG/A} &= \mathbf{v}_{PS\_P/A} + \left[\left(\dot{\phi}_{PS}\mathbf{i}\right)\times \mathbf{r}_{PS\_CG/PS\_P}\right]\\ &= \dot{x}_{P_y}\mathbf{j} - \left[\dot{\theta}_{CA}r_{CS}\sin(\theta_{CA}) + \dot{\phi}_{CR}l_{CR}\sin(\phi_{CR})\right]\mathbf{k} + \left[\left(\dot{\phi}_{PS}\mathbf{i}\right)\times \mathbf{r}_{PS\_CG/PS\_P}\right]\end{aligned}$$

$$\begin{aligned}\mathbf{a}_{PS\_CG/A} &= \mathbf{a}_{PS\_P/A} + \left[\left(\ddot{\phi}_{PS}\mathbf{i}\right)\times \mathbf{r}_{PS\_CG/PS\_P}\right] + \left(\dot{\phi}_{PS}\mathbf{i}\right)\times\left[\left(\dot{\phi}_{PS}\mathbf{i}\right)\times \mathbf{r}_{PS\_CG/PS\_P}\right]\\ &= \ddot{x}_{P_y}\mathbf{j} - \left[\ddot{\theta}_{CA}r_{CS}\sin(\theta_{CA}) + \dot{\theta}_{CA}{}^2 r_{CS}\cos(\theta_{CA}) + \ddot{\phi}_{CR}l_{CR}\sin(\phi_{CR}) + \dot{\phi}_{CR}{}^2 l_{CR}\cos(\phi_{CR})\right]\mathbf{k}\\ &\quad + \left[\left(\ddot{\phi}_{PS}\mathbf{i}\right)\times \mathbf{r}_{PS\_CG/PS\_P}\right] + \left(\dot{\phi}_{PS}\mathbf{i}\right)\times\left[\left(\dot{\phi}_{PS}\mathbf{i}\right)\times \mathbf{r}_{PS\_CG/PS\_P}\right]\end{aligned}$$

where the position of the centre of gravity, of the piston, relative to point *PS_P*, $\mathbf{r}_{PS\_CG/PS\_P}$, is defined as:

$$\begin{aligned}\mathbf{r}_{PS\_CG/PS\_P} &= x_{PS\_CG0}\mathbf{i} + \left[y_{PS\_CG0}\cos(\phi_{PS}) - z_{PS\_CG0}\sin(\phi_{PS})\right]\mathbf{j}\\ &\quad + \left[y_{PS\_CG0}\sin(\phi_{PS}) + z_{PS\_CG0}\cos(\phi_{PS})\right]\mathbf{k}\end{aligned}$$

The piston is subject to external forces from the interfaces it shares with wrist-pin and cylinder bore, $\mathbf{F}_{WP/PS}$ and $\mathbf{F}_{CB/PS}$ respectively, and due to combustion chamber pressure, $\mathbf{F}_{P/PS}$, and gravity. The calculation of these forces is described in Sections 2.3 and 2.4. Conservation of linear momentum for the piston yields the following equation:

$$\mathbf{F}_{WP/PS} + \mathbf{F}_{CB/PS} + \mathbf{F}_{P/PS} + m_{PS}\mathbf{g} = m_{PS}\mathbf{a}_{PS\_CG/A}$$

Conservation of angular momentum for the piston, about the ideal centre of the pin bore, *PS_P*, yields the following equation:

$$\frac{d\mathbf{H}_{PS\_CG}}{dt} = \mathbf{M}_{WP/PS\_P} + \mathbf{M}_{CB/PS\_P} + \mathbf{M}_{P/PS\_P} + \mathbf{r}_{PS\_CG/PS\_P}\times m_{PS}\mathbf{g} - \mathbf{r}_{PS\_CG/PS\_P}\times m_{PS}\mathbf{a}_{PS\_CG/A}$$

$$\frac{d\mathbf{H}_{PS\_CG}}{dt} = \boldsymbol{\tau}_{WP/PS} + \mathbf{r}_{CB/PS\_P}\times\mathbf{F}_{CB/PS} + \mathbf{r}_{P/PS\_P}\times\mathbf{F}_{P/PS} + \mathbf{r}_{PS\_CG/PS\_P}\times m_{PS}\mathbf{g} - \mathbf{r}_{PS\_CG/PS\_P}\times m_{PS}\mathbf{a}_{PS\_CG/A}$$

The motion of the piston is assumed to be two-dimensional, thereby reducing the above equation to:

$$I_{PS\_XX}\ddot{\phi}_{PS} = \tau_{WP/PSX} + \left\{ \begin{array}{l} \mathbf{r}_{CB/PS\_P} \times \mathbf{F}_{CB/PS} + \mathbf{r}_{P/PS\_P} \times \mathbf{F}_{P/PS} \\ + \mathbf{r}_{PS\_CG/PS\_P} \times m_{PS}\mathbf{g} - \mathbf{r}_{PS\_CG/PS\_P} \times m_{PS}\mathbf{a}_{PS\_CG/A} \end{array} \right\}_X$$

A1.3. Contact Model: Blunt Wedge Against a Flat Plane

For an elastic half-space, loaded over the range $-b < x < a$, by a distributed normal pressure $p(x)$ only (neglecting friction), the displacement at the surface, u_z, is given by [32]:

$$u_z = -\frac{2(1-\nu^2)}{\pi E} \int_{-b}^{a} p(s) \ln|x-s| \, ds + C_2$$

where ν is the Poisson's Ratio of the material, E is the Young's Modulus, and C_2 is an integration constant to be determined from boundary conditions.

For a blunt wedge, against a flat plane, the total surface displacement is given by [32]:

$$u_{z1} + u_{z2} = \delta - \cot\alpha . |x| \qquad -a < x < a$$

where δ is the nominal overlap of the two surfaces, at the tip of the wedge, and α is the half angle of the wedge, as shown in Figure A1.10.

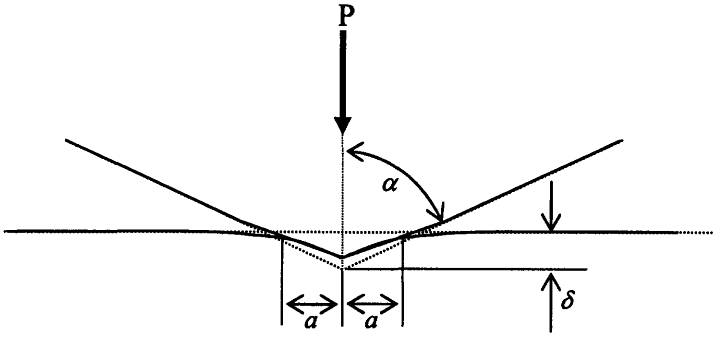

Figure A1.10: Blunt Wedge Against a Flat Plane

Using the above equation for the surface displacement of an elastic half space, under a distribution load, the surface overlap, δ, can therefore be defined by:

$$\begin{aligned}\delta &= u_{z1}\big|_{x=0} + u_{z2}\big|_{x=0} \\ &= -\frac{2}{\pi E^*}\int_{-a}^{a} p(s)\ln|s|\,ds + 2C_2\end{aligned}$$

$$E^* = \left[\frac{\left(1-\nu_1^2\right)}{E_1} + \frac{\left(1-\nu_2^2\right)}{E_2}\right]^{-1}$$

where E^* is the composite Young's Modulus of the two surfaces.

For $p(x) = 0$, $\delta = 0$, and therefore $C_2 = 0$.

The corresponding pressure distribution, $p(x)$, and total load, P, are given by [32]:

$$p(x) = \frac{E^* \cot\alpha}{\pi}\cosh^{-1}\left(\frac{a}{x}\right)$$

$$P = aE^* \cot\alpha$$

Rearranging the equation for the total load, P, the width of the contact area, a, can be defined in terms of the total load, surface geometry, and composite Young's Modulus:

$$a = \frac{P\tan\alpha}{E^*}$$

Substituting the pressure distribution, p, into the equation defining surface overlap, δ, we obtain:

$$\begin{aligned}\delta &= -\frac{2\cot\alpha}{\pi^2}\int_{-a}^{a}\cosh^{-1}\left(\frac{a}{s}\right)\ln|s|\,ds \\ &= -\frac{2a\cot\alpha}{\pi^2}\int_{-1}^{1}\cosh^{-1}\left(\frac{1}{s}\right)\ln|as|\,ds \\ &= -\frac{4a\cot\alpha}{\pi^2}\left[\int_{0}^{1}\cosh^{-1}\left(\frac{1}{s}\right)\ln(s)\,ds + \ln(a)\int_{0}^{1}\cosh^{-1}\left(\frac{1}{s}\right)ds\right]\end{aligned}$$

Numerical evaluation of the above integrals, and substitution of the contact width, a, into the above equation results in:

$$\delta = \frac{P}{E^*}\left[1.0779 - 0.6366\ln\left(\frac{P\tan\alpha}{E^*}\right)\right]$$

The wavelength averaged pressure is given by:

$$p_{asp} = \frac{P}{\lambda}$$

The nominal overlap of the two surfaces, in terms of the wavelength averaged pressure, is therefore:

$$\delta = \frac{\lambda p_{asp}}{E^*}\left[0.6366\left(\ln(\cot\alpha) - \ln\left(\frac{\lambda p_{asp}}{E^*}\right)\right) + 1.0779\right]$$

The above equation can be re-expressed in terms of the triangular tooling mark wave height, Ω, nominal clearance of the surface, *h*, and tooling mark wavelength λ:

$$\frac{\Omega}{2} - h = \left(\frac{\lambda p_{asp}}{E^*}\right)\left[0.6366\left(\ln\left(\frac{2\Omega}{\lambda}\right) - \ln\left(\frac{\lambda p_{asp}}{E^*}\right)\right) + 1.0779\right], \quad \mathrm{h} \le \frac{\Omega}{2}$$

For the lubricated model, with a very fine grid for calculating effect of tooling marks on elastohydrodynamic lubrication via direct numerical simulation, the grid spacing is smaller than the wavelength of the tooling marks. It is therefore more appropriate to use a grid averaged contact pressure, rather than a wavelength average one:

$$\frac{\Omega}{2} - h = \left(\frac{dz\, p_{asp}}{E^*}\right)\left[0.6366\left(\ln\left(\frac{2\Omega}{\lambda}\right) - \ln\left(\frac{dz\, p_{asp}}{E^*}\right)\right) + 1.0779\right], \quad \mathrm{h} \le \frac{\Omega}{2}$$

where *dz* is the axial grid spacing.

A2. Fluid Model Equations and Results

This appendix contains:

- Detailed derivation of the equations governing lubrication flow.
- Quasi-steady hydrodynamic lubrication model results for a range of simple 2D lubrication flows.

A2.1. Derivation of Lubrication Flow Equations

It is assumed that the fluid is an incompressible, Newtonian fluid with constant viscosity, and that the flow is laminar.

A2.1.1. Mass Conservation

Considering a fixed control volume, the rate of increase of mass inside the volume must be equal to the rate of mass flow into the volume [47].

$$\frac{d}{dt}\int_V \rho dV = \int_V \frac{\partial \rho}{\partial t} dV = -\int_A \rho \mathbf{u} \bullet \mathbf{dA}$$

Using the divergence theorem [47]:

$$\int_A \rho \mathbf{u} \bullet \mathbf{dA} = \int_V \nabla \bullet (\rho \mathbf{u}) dV$$

$$\int_V \frac{\partial \rho}{\partial t} + \nabla \bullet (\rho \mathbf{u}) dV = 0$$

Since the integral form of the general mass conservation equation applies for any fixed volume, the integrand must vanish at every point. The differential form of the general mass conservation equation, often referred to as the ‘continuity equation’, is therefore given by:

$$\frac{\partial \rho}{\partial t} + \nabla \bullet (\rho \mathbf{u}) = 0$$

The total derivative of a quantity, ϕ, is defined as [47]:

$$\frac{D\phi}{Dt} = \frac{\partial \phi}{\partial t} + \mathbf{u} \bullet \nabla \phi$$

The continuity equation can therefore be re-written in the following form:

$$\frac{1}{\rho}\frac{D\rho}{Dt} + \nabla \bullet \mathbf{u} = 0$$

The first of these two terms is the rate of change of density following a fluid particle. For an incompressible fluid, this term is zero and the continuity equation reduces to:

$$\nabla \bullet \mathbf{u} = 0$$

In Cartesian coordinates, for an incompressible fluid, the local mass conservation, or continuity, equation is therefore given by:

$$\frac{\partial u}{\partial x} + \frac{\partial v}{\partial y} + \frac{\partial w}{\partial z} = 0$$

A2.1.2. Momentum Conservation

Applying Newton's law of motion to an infinitesimal fluid element, we require that the net force on the element, due to both body and surface forces, must equal the element's mass multiplied by the acceleration of the element. The acceleration of an element is given by the total derivative of its velocity. The resulting equation is often referred to as 'Cauchy's equation of motion' [47].

$$\rho \frac{Du_i}{Dt} = \rho g_i + \frac{\partial \tau_{ij}}{\partial x_j}$$

The constitutive equation (relating stress and deformation) for a Newtonian fluid is given by [47]:

$$\tau_{ij} = -\left(p + \frac{2}{3}\mu \nabla \bullet \mathbf{u}\right)\delta_{ij} + 2\mu e_{ij}$$

$$e_{ij} = \frac{1}{2}\left(\frac{\partial u_i}{\partial x_j} + \frac{\partial u_j}{\partial x_i}\right)$$

Combining these equations, we can obtain the general form of the Navier-Stokes equation:

$$\rho \frac{Du_i}{Dt} = \rho g_i + \frac{\partial}{\partial x_j}\left(-\left(p + \frac{2}{3}\mu \nabla \bullet \mathbf{u}\right)\delta_{ij} + \mu\left(\frac{\partial u_i}{\partial x_j} + \frac{\partial u_j}{\partial x_i}\right)\right)$$

Assuming that we have an incompressible fluid, the conservation of momentum can be reduced to:

$$\rho \frac{Du_i}{Dt} = -\frac{\partial p}{\partial x_i} + \rho g_i + \frac{\partial}{\partial x_j}\left(\mu\left(\frac{\partial u_i}{\partial x_j} + \frac{\partial u_j}{\partial x_i}\right)\right)$$

If we also assume that viscosity is constant throughout the fluid, this can be further reduced to:

$$\rho \frac{Du_i}{Dt} = -\frac{\partial p}{\partial x_i} + \rho g_i + \mu \nabla^2 u_i$$

In vector notation, conservation of momentum, for an incompressible, constant viscosity, Newtonian fluid is therefore given by:

$$\rho \frac{D\mathbf{u}}{Dt} = -\nabla p + \rho \mathbf{g} + \mu \nabla^2 \mathbf{u}$$

A2.1.3. Lubrication Flow Approximation

For thin fluid films, such as the oil film between the piston and cylinder bore, where the Reynolds number is significantly smaller than the ratio of the film thickness to the film length in the sliding direction, the inertia terms in the Navier-Stokes equation can be neglected, reducing the equations of motion to:

$$0 = -\frac{\partial p}{\partial x} + \mu \frac{\partial^2 u}{\partial y^2}$$

$$0 = \frac{\partial p}{\partial y}$$

$$0 = -\frac{\partial p}{\partial z} + \mu \frac{\partial^2 w}{\partial y^2}$$

Considering the reduced equation for conservation of momentum in the y-direction, it is clear that pressure is a function of x, z, and t only.

$$p = p(x, z, t)$$

The remaining two conservation of momentum equations can then be integrated directly, in terms of y, in order to express the fluid velocity profiles in terms of the pressure distribution, surface heights and surface velocities. Assuming that we know the velocities of the solid surfaces at $y = h_1(x,z,t)$ and $y = h_2(x,z,t)$, and that there is no slip or fluid penetration at these surfaces, the following boundary conditions apply:

$$
\begin{aligned}
u(x, y = h_1, z, t) &= U_1(x, z, t)\\
u(x, y = h_2, z, t) &= U_2(x, z, t)\\
w(x, y = h_1, z, t) &= W_1(x, z, t)\\
w(x, y = h_2, z, t) &= W_2(x, z, t)
\end{aligned}
$$

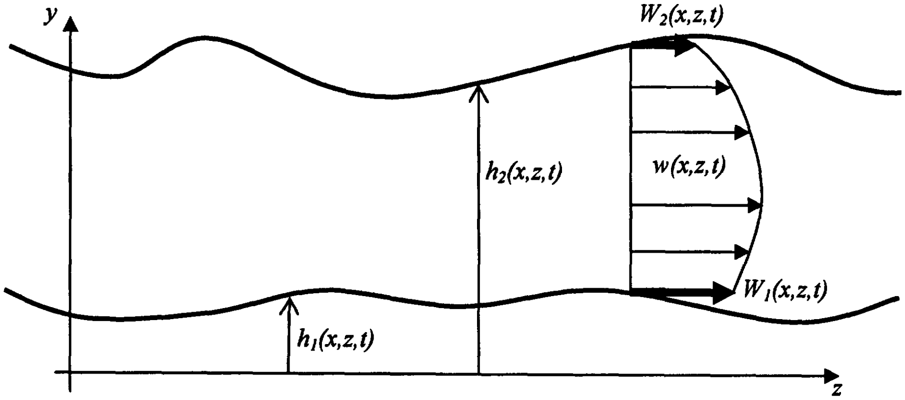

Figure A2.1: Lubrication Flow

The resulting velocity profiles are:

$$u(x,y,z,t) = -\frac{1}{2\mu}\left(-\frac{\partial p}{\partial x}\right)\left[y^2 - (h_1 + h_2)y + h_1h_2\right] + \left(\frac{U_2 - U_1}{h_2 - h_1}\right)y + \left(\frac{U_1h_2 - U_2h_1}{h_2 - h_1}\right)$$

$$w(x,y,z,t) = -\frac{1}{2\mu}\left(-\frac{\partial p}{\partial z}\right)\left[y^2 - (h_1 + h_2)y + h_1h_2\right] + \left(\frac{W_2 - W_1}{h_2 - h_1}\right)y + \left(\frac{W_1h_2 - W_2h_1}{h_2 - h_1}\right)$$

For the case where $h_1 = 0$ and $h_2 = h$, the velocity profiles reduce to the more familiar form:

$$u(x,y,z,t) = -\frac{h^2}{2\mu}\left(-\frac{\partial p}{\partial x}\right)\left[\frac{y}{h} - 1\right]\frac{y}{h} + (U_2 - U_1)\frac{y}{h} + U_1$$

$$w(x,y,z,t) = -\frac{h^2}{2\mu}\left(-\frac{\partial p}{\partial z}\right)\left[\frac{y}{h} - 1\right]\frac{y}{h} + (W_2 - W_1)\frac{y}{h} + W_1$$

A2.2. Quasi-Steady Hydrodynamic Lubrication Model Results:

In order to test the accuracy of the fluid models a set of simple 2D problems, for which analytical solutions are well defined, were simulated. For each test case it was confirmed that:

- the correct pressure distribution is generated,

- the calculated volume flow rates, shear stress, normal force and friction force are accurate, and
- mass is conserved for each control volume.

A2.2.1. Plane Poiseuille Flow:

Steady, laminar flow between two parallel plates, driven by a pressure difference across the plates is known as Plane Poiseuille Flow. The mass flow rate is driven by the pressure difference, and limited by the friction force generated at the solid boundaries. Since this is a quasi-steady, two-dimensional flow, mass conservation requires that the mass flow rate is a constant, and therefore that the pressure gradient is a constant. The flow has the following detailed characteristics:

- The pressure varies linearly from the high pressure boundary to the low pressure boundary.
- The normal force generated is proportional to the average pressure and the axial length of the flow.
- The velocity distribution is a symmetric parabola with zero velocity at the solid boundaries, and is constant with respect to axial position.
- The mass flow rate is proportional to the pressure gradient, the gap height cubed, and the inverse of the dynamic viscosity.
- The shear stress on each surface is constant with respect to axial position and proportional to the pressure gradient and the gap height.
- The friction forces generated at the two surfaces are equal and proportional to the pressure difference and the gap height.

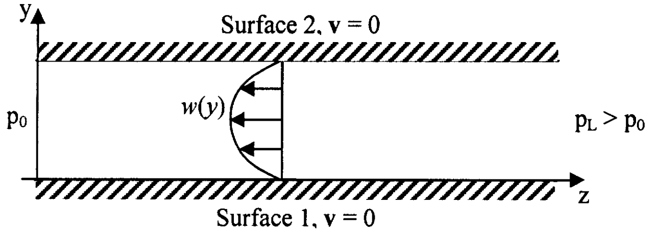

Figure A2.2: Plane Poiseuille Flow

The equations for this flow are:

$$p(z) = p_0 + \frac{p_L - p_0}{L} z \qquad \rightarrow \quad F_{N1}' = -\int_0^L p(z) dz \mathbf{i}_y = -\frac{(p_L + p_0)L}{2} \mathbf{i}_y$$

$$w(y) = -\frac{h^2}{2\mu}\left(-\frac{p_L - p_0}{L}\right)\left(\frac{y}{h} - 1\right)\frac{y}{h} \rightarrow Q' = \frac{h^3}{12\mu}\left(-\frac{p_L - p_0}{L}\right)$$

$$\tau_{yz}(y = 0) = \frac{h}{2}\left(-\frac{p_L - p_0}{L}\right)\mathbf{i}_z \qquad \rightarrow \quad F_{F1}' = \int_0^L \tau_{yz}(y = 0) dz \mathbf{i}_z = -\frac{h(p_L - p_0)}{2} \mathbf{i}_z$$

For the following parameter values, we obtain a simplified set of equations:

$$p_0 = 1\times10^5\,\text{Pa},\ p_L = 11\times10^5\,\text{Pa},\ h = 1\times10^{-5}\,\text{m},\ L = 0.1\,\text{m},\ \mu = 0.01\,\text{Pas}$$

$$p(z) = (1+100z)\times10^5 \quad \rightarrow \quad F_{N1}' = -60\mathbf{i}_y\ \text{kN/m}$$

$$w(y) = 5\times10^{-2}\left(\frac{y}{10^{-5}}-1\right)\frac{y}{10^{-5}} \quad \rightarrow \quad Q' = -83.33\times10^{-3}\ \text{mm}^2\text{/s}$$

$$\tau_{yz}(y=0) = -50\mathbf{i}_z \quad \rightarrow \quad F_{F1}' = -5\mathbf{i}_z\ \text{N/m}$$

The following simulation results were achieved using the quasi-steady fluid model.

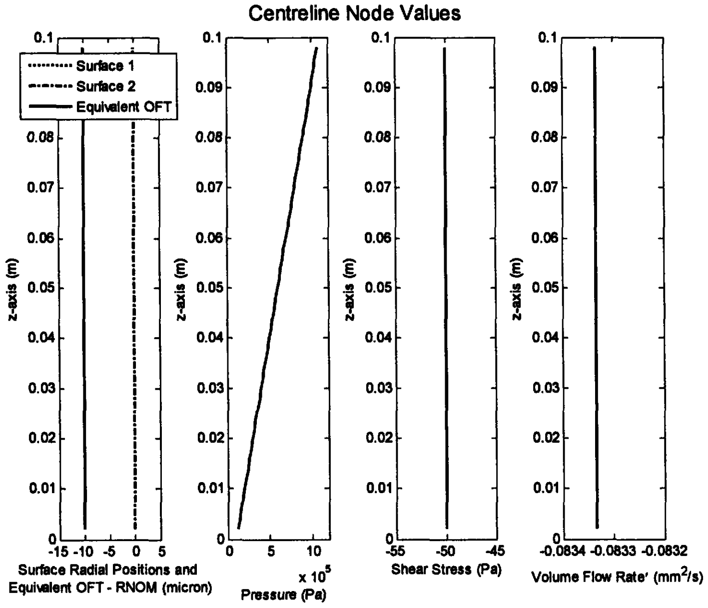

Figure A2.3: Plane Poiseuille Flow – Centreline Results

As shown in Figure A2.3, for this set of parameters, the numerical flow simulation results confirm that:

- the flow is fully flooded, with the equivalent oil film thickness being equal to the surface 1 location,
- the pressure varies linearly from 1 bar to 11 bar,
- the shear stress is constant at -50 Pa, and
- the volume flow rate, per unit width, is constant at -83.33×10^{-3} mm^2/s.

Other results produced by the model also confirmed that:

- the circumferentially averaged values are equal to those along the centerline,
- circumferentially there is no variation in any of these quantities,
- the axially averaged pressure, and the pressure at $z = 0.05$, are both equal to 6 bar,
- the total normal force generated by this flow, per unit width is -60 kN/m, and
- the total hydrodynamic friction force generated by this flow, per unit width, is -5 N/m.

For this set of parameters, the model results match the analytical results with sufficient accuracy. The model was then tested over a range of parameter values, in order to check that the more general trends and dependencies are correctly described. These results are shown in Figures A2.4-A2.6.

As required by the analytical equations, Figure A2.4 shows that the normal force, per unit width, generated by the flow is linearly proportional to the Axial Length, Base Pressure and Pressure Difference, and independent of Viscosity or Gap Height.

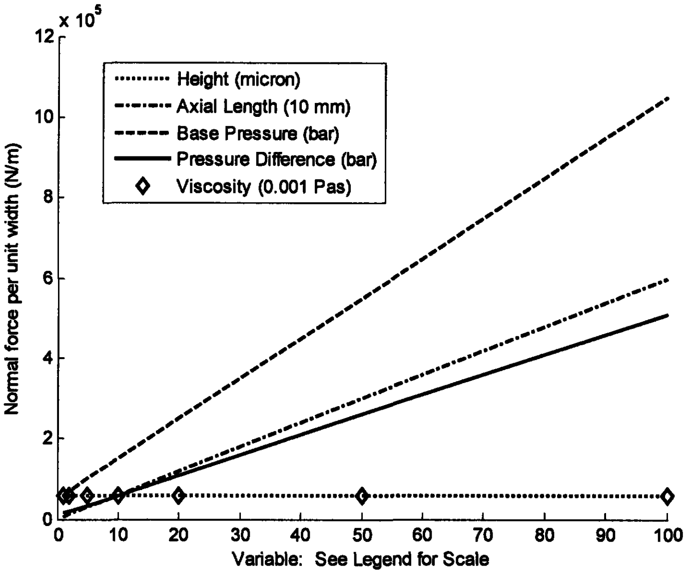

Figure A2.4: Plane Poiseuille Flow - Normal Force

The friction force generated, per unit width, is linearly proportional to the pressure difference and the gap height, and independent of the Axial Length, Base Pressure or Viscosity. This may seem counterintuitive, since the only friction generated is due to shear stress at the fluid-solid boundary, which we generally expect to be of the form:

$$\tau = \mu \frac{\partial w}{\partial y}$$

In this case though, our velocity gradient is defined by a force balance between the pressure difference and the shear force, and it is the pressure difference that drives and defines this flow.

$$\text{Friction Force} = \mu \frac{\partial w}{\partial y} L = (P_L - P_0)h$$

$$\rightarrow \frac{\partial w}{\partial y} = \frac{(P_L - P_0)h}{\mu L}$$

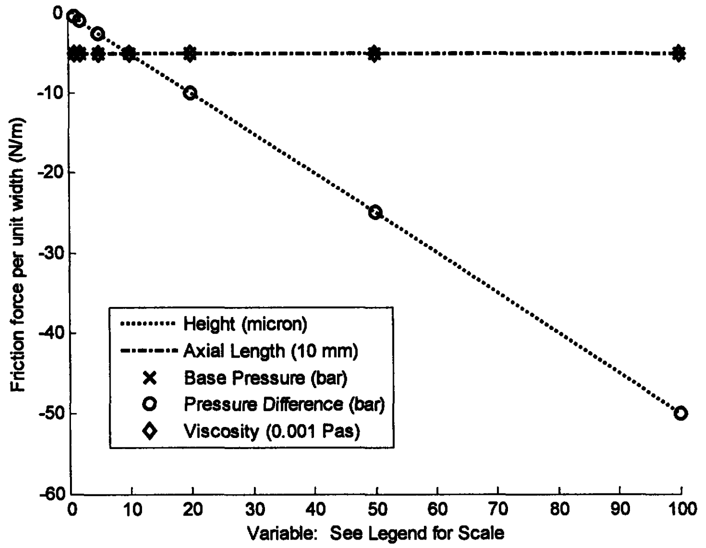

Figure A2.5: Plane Poiseuille Flow – Friction Force

In the log-log plot shown in Figure A2.6, we can clearly see that the volume flow rate is linearly proportional to the pressure difference, inversely proportional to oil viscosity and axial length, and proportional to the cube of the separation height. It is independent of the base pressure.

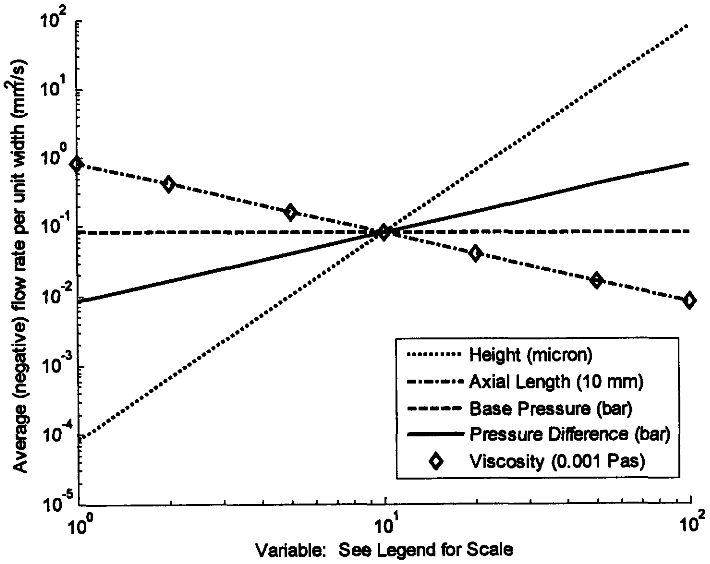

Figure A2.6: Plane Poiseuille Flow – Flow Rate

Negative pressure gradients were also tested:

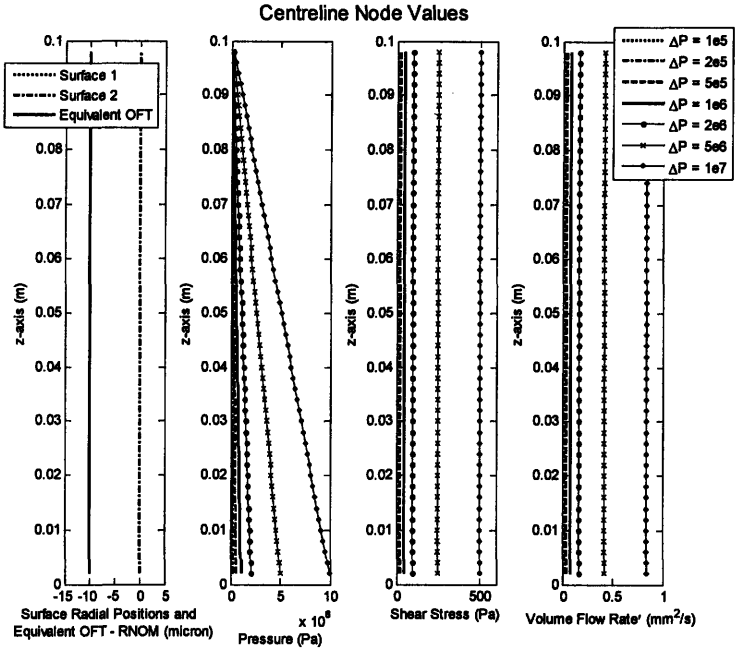

Figure A2.7: Plane Poiseuille Flow – Negative Pressure Gradients

It was also tested and confirmed that the pressure distribution and gradient are independent of the separation height (for constant separation height) and oil viscosity, and that the pressure is constant, and no flow occurs, when there is no pressure difference applied.

A2.2.2. Plane Couette Flow

Steady, laminar flow between two parallel plates, caused by relative motion of the plates is known as Plane Couette Flow. In this case the mass flow rate is determined by the average velocity of the two plates, and the gap height between them. Once again, since this is a quasi-steady, two-dimensional flow, mass conservation requires that the mass flow rate is a constant, and therefore that the pressure gradient is a constant. The pressure gradient in this case is therefore zero. The flow has the following detailed characteristics:

- The pressure is constant at the boundary pressure.
- The normal force generated is proportional to the boundary pressure and the axial length of the flow.
- The velocity distribution across the gap is linear, matching the solid velocities at the boundaries, and is constant with respect to axial position.
- The mass flow rate is proportional to the average solid velocity and the gap height.
- The shear stress is constant throughout the flow, and proportional to the velocity difference and viscosity, and to the inverse of the gap height.

- The friction forces generated at the two surfaces are equal in magnitude, and opposite in direction. They are proportional to the velocity difference, viscosity and axial length, and to the inverse of the gap height.

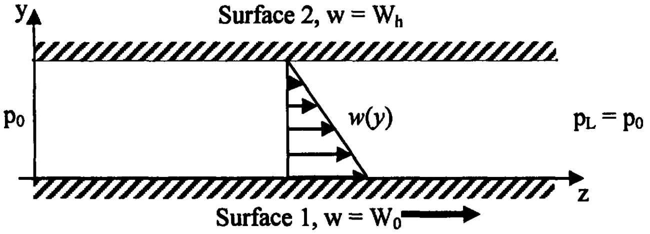

Figure A2.8: Plane Couette Flow

The equations for this flow are:

$$p(z)=p_0 \quad \rightarrow \quad F_{N1}' = -\int_0^L p(z)dz\mathbf{i}_y = -p_0 L\mathbf{i}_y$$

$$w(y)=(W_h - W_0)\frac{y}{h}+W_0 \quad \rightarrow \quad Q' = h\frac{(W_h + W_0)}{2}$$

$$\tau_{yz}(y=0)=\mu\frac{(W_h - W_0)}{h}\mathbf{i}_z \quad \rightarrow \quad F_{F1}' = \int_0^L \tau_{yz}(y=0)dz\mathbf{i}_z = \mu\frac{(W_h - W_0)}{h}L\mathbf{i}_z$$

For the following parameter values, we obtain a simplified set of equations:

$p_0 = p_L = 1\times10^6$ Pa, $h = 1\times10^{-5}$ m, $L = 0.1$ m, $\mu = 0.01$ Pas, $W_0 = 1$ m/s, $W_h = 0$

$$p(z)=10^6 \quad \rightarrow \quad F_{N1}' = -\int_0^L p(z)dz\mathbf{i}_y = -100\mathbf{i}_y \text{ kN/m}$$

$$w(y)=1-10^5 y \quad \rightarrow \quad Q' = 5\text{ mm}^2/\text{s}$$

$$\tau_{yz}(y=0)=-10^3\mathbf{i}_z \quad \rightarrow \quad F_{F1}' = \int_0^L \tau_{yz}(y=0)dz\mathbf{i}_z = -100\mathbf{i}_z \text{ N/m}$$

The following simulation results were achieved using the quasi-steady fluid model. Equivalent results were obtained with the Unsteady and Elastohydrodynamic models.

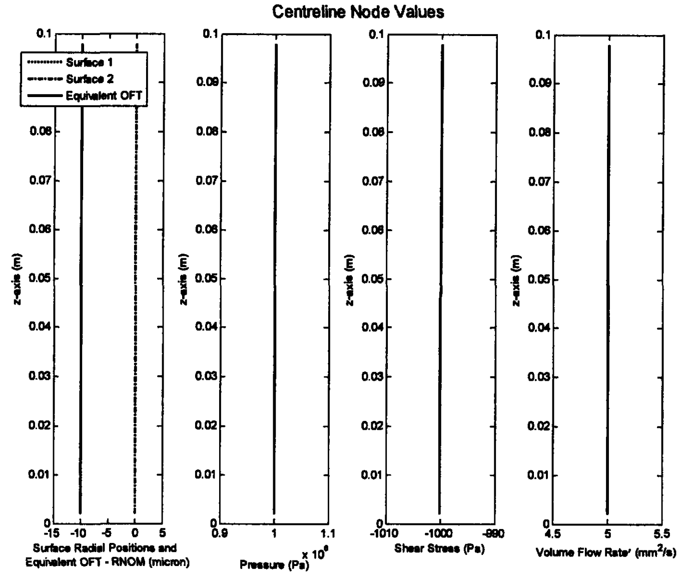

Figure A2.9: Plane Couette Flow – Centreline Results

As shown in Figure A2.9, for this set of parameters, the numerical flow simulation results confirm that:

- the flow is fully flooded, with the equivalent oil film thickness being equal to the surface 1 location,
- the pressure is constant at 10 bar,
- the shear stress is constant at -1000 Pa, and
- the volume flow rate, per unit width, is constant at 5 mm^2/s.

Other results produced by the model also confirmed that:

- the circumferentially averaged values are equal to those along the centerline,
- circumferentially there is no variation in any of these quantities,
- the total normal force generated by this flow, per unit width is -100 kN/m, and
- the total hydrodynamic friction force generated by this flow, per unit width, is -100 N/m.

For this set of parameters, the model results match the analytical results with sufficient accuracy. The model was then tested over a range of parameter values, in order to check that the more general trends and dependencies are correctly described. These results are shown in Figure A2.10-A2.12.

As required by the analytical equations, Figure A2.10 shows that the normal force, per unit width, generated by the flow is linearly proportional to the axial length and base pressure, and independent of velocity, viscosity and gap height.

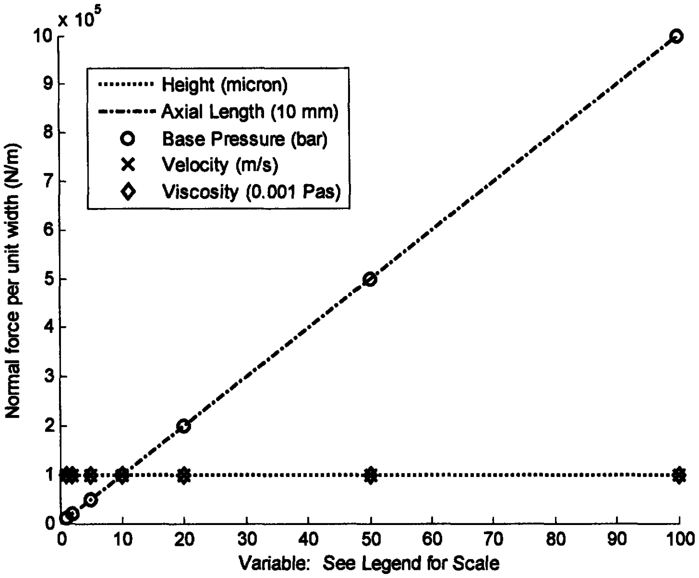

Figure A2.10: Plane Couette Flow – Normal Force

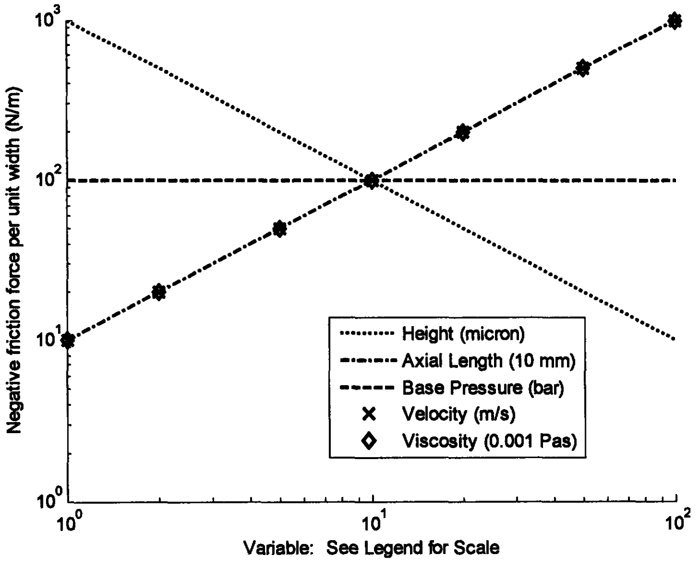

Figure A2.11: Plane Couette Flow – Friction Force

As shown by the log-log plot in Figure A2.11, the friction force generated, per unit width, is linearly proportional to the axial length, velocity and viscosity, inversely proportional to the gap height, and independent of the base pressure. We should note that for these simulations only the surface 1 velocity was varied. The friction force is proportional to the velocity gradient at the surface, and therefore defined for this flow by the difference between the two surface velocities only, and unaffected by adding the same velocity to both surfaces.

The volume flow rate is linearly proportional to the gap height and the velocity, and independent of the axial length, base pressure and viscosity. This is due to the fact that it is the solid surface motion driving this flow, and so the volume of fluid moved by the surfaces is only dependent upon the surface velocities and the size of the gap between them (as long as body forces are negligible). Once again we note that during these simulations only the surface 1 velocity was varied, and that the volume flow rate is actually proportional to the average surface velocity (so adding the velocity to both surface does change the volume flow rate).

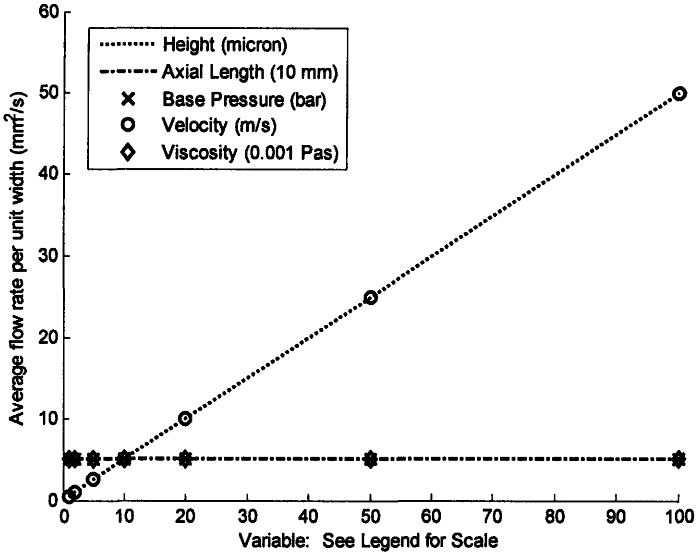

Figure A2.12: Plane Couette Flow – Flow Rate

Negative sliding velocities were also tested:

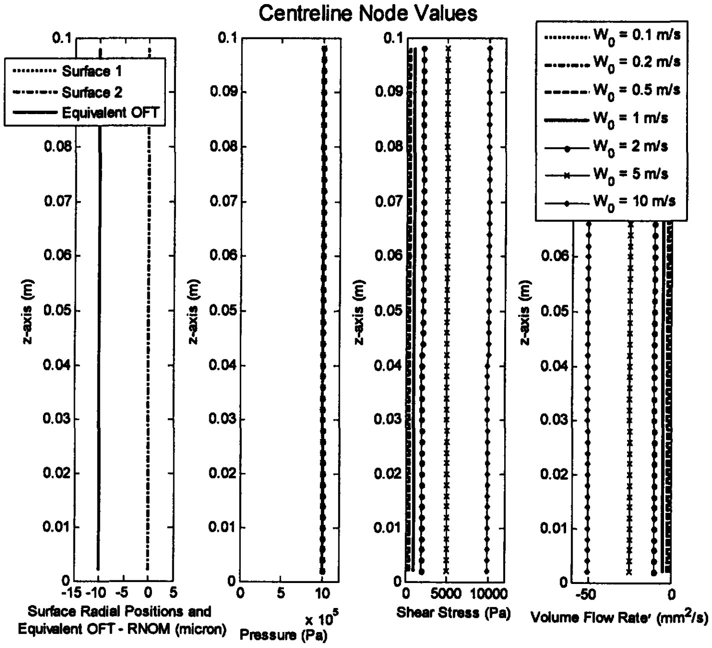

Figure A2.13: Plane Couette Flow - Negative Sliding Velocities

A2.2.3. Squeeze Flow:

Although not strictly quasi-steady, it is possible to solve a single instant in time of a squeeze flow as a quasi-steady flow. For a fully flooded squeeze flow between two parallel plates, the flow is driven by changes in the separation height of the two plates, as shown in Figure A2.14.

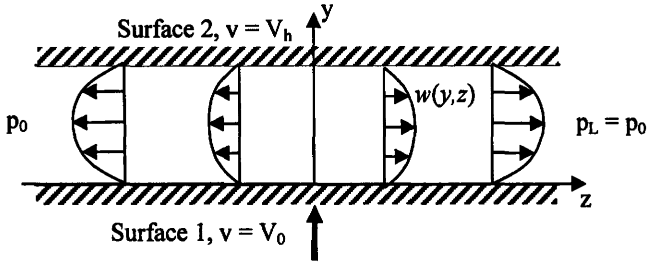

Figure A2.14: Squeeze Flow

Assuming that we have a laminar lubrication flow, the velocity is given by:

$$w(y,z,t) = -\frac{h(t)^2}{2\mu}\left(-\frac{dp}{dz}\right)\left(\frac{y}{h(t)}-1\right)\frac{y}{h(t)}$$

Considering conservation of mass, for a symmetric, fully flooded flow (no cavitation or separation), the volume flow rate, per unit width, as a function of axial position is given by:

$$Q'(z,t) = -z\frac{dh}{dt} = -z(V_h - V_0)$$

The flow rate can also be described as a function of velocity. Comparing these two expressions it is possible to define the pressure gradient as a function of surface height and axial position.

$$Q'(z,t) = \int_0^h w(y,z,t)dy = \frac{h(t)^3}{12\mu}\left(-\frac{dp}{dz}\right) = -z(V_h - V_0)$$

$$\left(\frac{dp}{dz}\right) = \frac{12\mu}{h(t)^3}(V_h - V_0)z$$

Integrating and applying the pressure boundary condition we obtain:

$$p(z,t) = \frac{6\mu}{h(t)^3}(V_h - V_0)\left(z^2 - \left(\frac{L}{2}\right)^2\right) + p_0$$

Substituting the pressure gradient back into the velocity distribution we obtain the following equations describing this flow:

$$p(z,t)=\frac{6\mu}{h(t)^3}(V_h-V_0)\left(z^2-\left(\frac{L}{2}\right)^2\right)+p_0 \quad\rightarrow\quad F_{N1}'=-\int_{-L/2}^{L/2} p(z)dz\mathbf{i}_y=\frac{\mu L^3}{h(t)^3}(V_h-V_0)-p_0L\mathbf{i}_y$$

$$w(y,z,t)=\frac{6}{h(t)}(V_h-V_0)z\left(\frac{y}{h(t)}-1\right)\frac{y}{h(t)} \quad\rightarrow\quad Q'=-z(V_h-V_0)$$

$$\tau_{yz}(y=0)=-\frac{6\mu}{h(t)^2}(V_h-V_0)z\mathbf{i}_z \quad\rightarrow\quad F_{F1}'=\int_{-L/2}^{L/2}\tau_{yz}(y=0)dz\mathbf{i}_z=0$$

Note that the friction force generated by the squeeze flow is equal to zero. A squeeze flow can be considered as a pressure driven flow where the peak pressure is determined by the force required to overcome the friction force in each half of the flow.

For the following parameter values, we obtain a simplified set of equations:

$$p_0=p_L=1\times10^6\text{ Pa},\ h=1\times10^{-5}\text{ m},\ L=0.1\text{ m},\ \mu=0.01\text{ Pas},\ V_0=1\times10^{-4}\text{ m/s},\ V_h=0$$

$$p(z,t)=10^6\left[1-6\times10^3\left(z^2-2.5\times10^{-3}\right)\right] \quad\rightarrow\quad F_{N1}'=-1.1\times10^6\mathbf{i}_y\text{ N}$$

$$w(y,z,t)=60z\left(\frac{y}{10^{-5}}-1\right)\frac{y}{10^{-5}} \quad\rightarrow\quad Q'=10^{-4}z\text{ m}^2\text{/s}=100z\text{ mm}^2\text{/s}$$

$$\tau_{yz}(y=0)=-6\times10^4z\mathbf{i}_z \quad\rightarrow\quad F_{F1}'=0$$

The following simulation results were achieved using the quasi-steady fluid model. Equivalent results were obtained with the Unsteady and Elastohydrodynamic models.

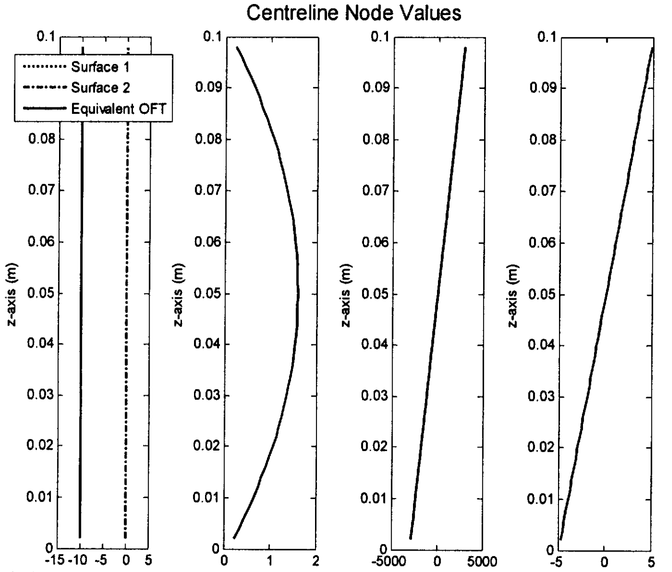

Figure A2.15: Squeeze Flow – Centreline Results

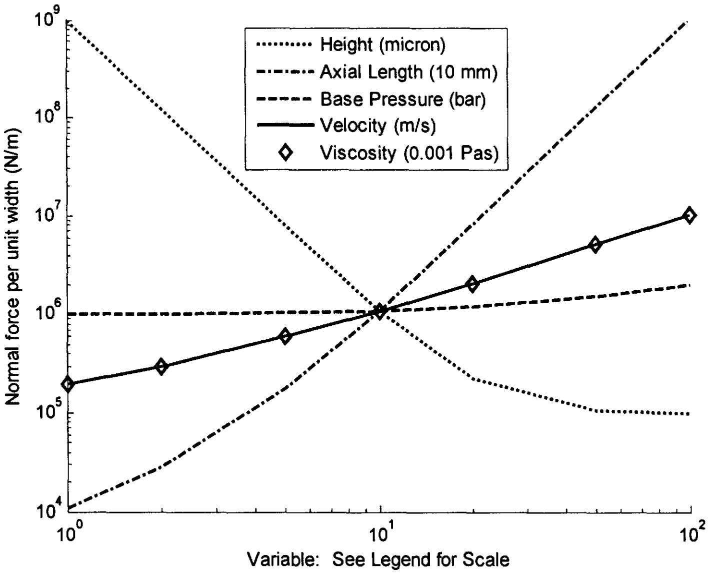

Figure A2.16: Squeeze Flow – Normal Force

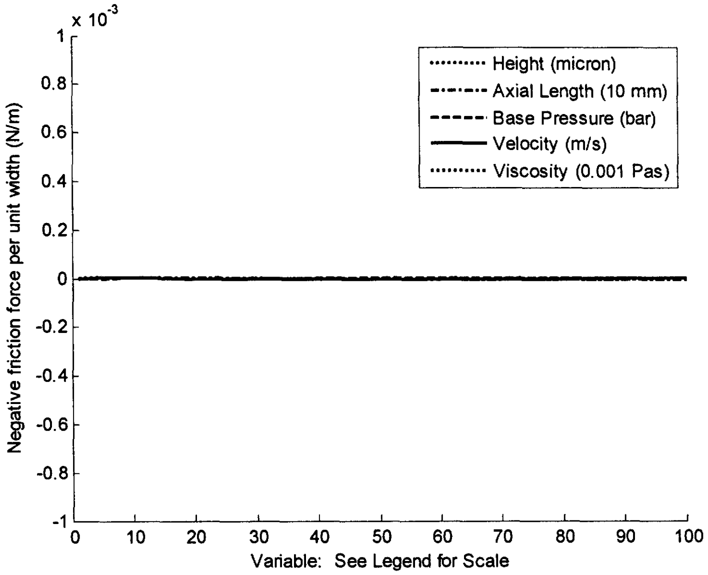

Figure A2.17: Squeeze Flow – Friction Force

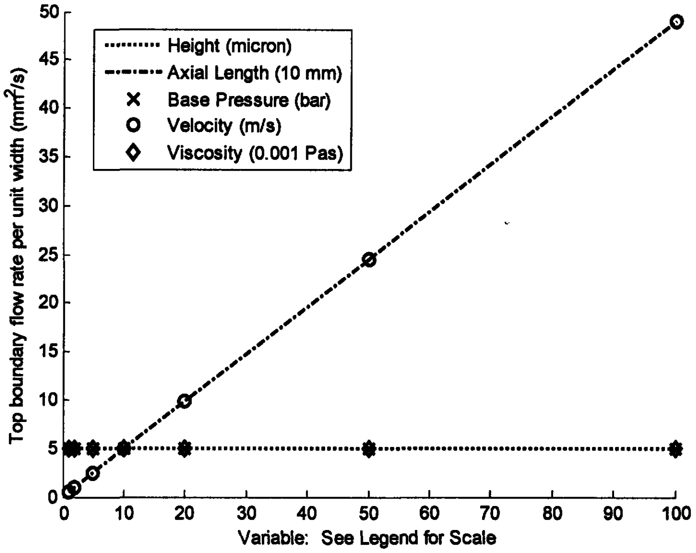

Figure A2.18: Squeeze Flow – Flow Rates

Bibliography

[1] Richardson, D.E. (2000), *Review of Power Cylinder Friction for Diesel Engines*, Journal of Engineering for Gas Turbines and Power, Transactions of the ASME, 122, 506-519.

[2] Offner, G., Herbst, H.M., Priebsch, H.H. (2001), *A Methodology to Simulate Piston Secondary Movement under Lubricated Contact Conditions*, SAE Paper 2001-01-0565.

[3] Proprietary data from sponsors.

[4] Teraguchi, S., Suzuki, W., Takiguchi, M., and Sato, D. (2001), *Effects of Lubricating Oil Supply on Reductions of Piston Slap Vibration and Piston Friction*, SAE Paper 2001-01-0566.

[5] Tian, T. (1997), *Modeling the Performance of the Piston Ring-Pack in Internal Combustion Engines*, Ph.D. Thesis, Department of Mechanical Engineering, Massachusetts Institute of Technology.

[6] Liu, L. (2005), *Modeling the Performance of the Piston Ring-Pack with Consideration of Non-Axisymmetric Characteristics of the Power Cylinder System in Internal Combustion Engines*, PhD Thesis, Department of Mechanical Engineering, Massachusetts Institute of Technology.

[7] Yilmaz, E., Thirouard, B., Tian, T., Wong, V.W., Heywood, J.B., and Lee, N. (2001), *Analysis of Oil Consumption Behaviour During Ramp Transients in a Production Spark Ignition Engine*, SAE Paper 2001-01-3544

[8] Dwyer-Joyce, R.S., Green, D.A., Harper, P., Lewis, R., Balakrishnan, S., King, P.D., Rahnejat, H., and Howell-Smith, S. (2006), *The Measurement of Liner-Piston Skirt Oil Film Thickness by an Ultrasonic Means*, SAE Paper 2006-01-0648.

[9] Griffiths, W.J. and Skorecki, J. (1964), *Some Aspects of Vibration of a Single Cylinder Diesel Engine. A: Effects of Cooling Water on Cylinder Pressure and Surface Vibration. B: Mechanics of Piston Slap.*, Journal of Sound and Vibration, 1, 345-364.

[10] Ungar, E.E. and Ross, D. (1965), *Vibrations and Noise due to Piston-Slap in Reciprocating Machinery*, Journal of Sound and Vibration, 2, 132-146.

[11] Fielding, B.J. and Skorecki, J. (1969-1970), *Identification of Mechanical Sources of Noise in a Diesel Engine: Sound Originating from Piston Slap*, Proceedings of the Institution of Mechanical Engineers, 184, 859-874.

[12] Haddad, S.D. and Pullen, H.L. (1974), *Piston Slap as a Source of Noise and Vibration in Diesel-Engines*, Journal of Sound and Vibration, 34, 249.

[13] Haddad, S.D. and Fortescue, P.W. (1977), *Simulating Piston Slap by an Analog-Computer/R*, Journal of Sound and Vibration, 52, 79-93.

[14] Knoll, G. D. and Peeken, H.J. (1982), *Hydrodynamic Lubrication of Piston Skirts*, Journal of Lubrication Technology, Transactions of the ASME, 104, 504-509.

[15] Li, D.F., Rohde, S.M. and Ezzat, H.A. (1983), *An Automotive Piston Lubrication Model*, ASLE Transactions, 26, 151-160.

[16] Oh, K.P., Li, C.H. and Goenka, P.K. (1987), *Elastohydrodynamic Lubrication of Piston Skirts*, Journal of Tribology, Transactions of the ASME, 109, 356-362.

[17] Patir, N. and Cheng, H.S. (1978), *An Average Flow model for Determining Effects of Three-Dimensional Roughness on Partial Hydrodynamic Lubrication*, Journal of Lubrication Technology, Transactions of the ASME, 100, 12-17.

[18] Zhu, D., Cheng, H., S., Arai, T. and Hamai, K. (1992), *Numerical Analysis for Piston Skirts in Mixed Lubrication. Part I: Basic Modeling*, Journal of Tribology, Transactions of the ASME, 114 (3), 553-562.

[19] Zhu, D., Hu, Y.Z., Cheng, H. S., Arai, T. and Hamai, K. (1993), *A Numerical-Analysis for Piston Skirts in Mixed Lubrication . Part II: Deformation Considerations*, Journal of Tribology, Transactions of the ASME, 115, 125-133.

[20] Dursunkaya, Z., Keribar, R. and Ganapathy, V. (1994), *A Model of Piston Secondary Motion and Elastohydrodynamic Skirt Lubrication*, Journal of Tribology, Transactions of the ASME, 116 (4), 777-785.

[21] Wong, V.W., Tian, T., Lang, H., Ryan, J.P., Sekiya, Y., Kobayashi, Y. and Aoyama, S. (1994), *A Numerical Model of Piston Secondary Motion and Piston Slap in Partially Flooded Elastohydrodynamic Skirt Lubrication*, SAE Paper 940696.

[22] McNally, C.P. (2000), *Development of a Numerical Model of Piston Secondary Motion for Internal Combustion Engines*, M.S. Thesis, Department of Mechanical Engineering, Massachusetts Institute of Technology.

[23] Duyar, M., Bell, D. and Perchanok, M. (2005), *A Comprehensive Piston Skirt Lubrication Model Using a Mass Conserving EHL Algorithm*, SAE Paper 2005-01-1640.

[24] Tripp, J.H. (1983), *Surface Roughness Effects in Hydrodynamic Lubrication: the Flow Factor Method*, Journal of Lubrication Technology, Transactions of the ASME, 105, 458-465.

[25] Harp, S.R. and Salant, R.F. (2001), *An Average Flow Model of Rough Surface Lubrication with Inter-Asperity Cavitation*, Journal of Tribology, Transactions of the ASME, 123 (1), 134-143.

[26] Prat, M., Plouraboue, F. and Letalleur, N. (2002), *Averaged Reynolds Equation for Flows Between Rough Surfaces in Sliding Motion*, Transport in Porous Media, 48 (3), 291-313.

[27] Bayada, G., Martin, S. and Vazquez, C. (2005), *An Average Flow Model of the Reynolds Roughness Including a Mass-Flow Preserving Cavitation Model*, Journal of Tribology, Transactions of the ASME, 127 (4), 793-802.

[28] Cullen, J.A. (1989), *Stress Analysis on the Piston Pin Boss for Internal Combustion Engine Considering the Hydrodynamic Oil Film Pressure*, SAE Technical Paper 890138

[29] Suhara, T. et al (1997), *Friction and Lubrication Characteristics of Piston Pin Boss Bearings of an Automotive Engine,* SAE Technical Paper 970840.

[30] Shigley, J.E. (1986), *Mechanical Engineering Design*, McGraw-Hill, Singapore.

[31] Jocsak, J. (2005), *The Effects of Surface Finish on Piston Ring-Pack Performance in Advanced Reciprocating Engine Systems*, M.S. Thesis, Department of Mechanical Engineering, Massachusetts Institute of Technology.

[32] Johnson, K.L. (1985), *Contact Mechanics*, Cambridge University Press, Cambridge.

[33] Greenwood, J.A. and Tripp, J.H. (1970-71), *The Contact of Two Nominally Flat Rough Surfaces*, Proc Instn Mech Engrs Tribology Group, 185 (48/71), 625-633.

[34] Hu, Y., Cheng, H. et al (1994), *Numerical Simulation of Piston Ring in Mixed Lubrication – A Nonaxisymmetrical Analysis*, Journal of Tribology, Transactions of the ASME, 116, 470-478.

[35] Press, W.H. et al (1992), *Numerical Recipes in Fortran 77 : The Art of Scientific Computing*, Cambridge University Press, Cambridge.

[36] Visual Numerics (1998), *IMSL Fortran 90 MP Library User's Guide.*

[37] McClure, F. (2007), *Dry Piston Secondary Motion Model User Manual*, Sloan Automotive Labortory, Massachusetts Institute of Technology.

[38] Elrod, H.G. (1981), *A Cavitation Algorithm*, Journal of Lubrication Technology, Transactions of the ASME, 103 (3), 350-354.

[39] Payvar, P. and Salant, R.F. (1992), *Computational method for cavitation in a wavy mechanical seal*, Journal of Tribology, Transactions of the ASME, 114 (1), 199-204.

[40] Letalleur, N., Plouraboue, F. and Prat, M. (2002), *Average flow model of rough surface lubrication: flow factors for sinusoidal surfaces*, Journal of Tribology, Transactions of the ASME, 124 (3), 539-46.

[41] Patir, N. and Cheng, H.S. (1979), *Application of Average Flow Model to Lubrication Between Rough Sliding Surfaces*, Journal of Lubrication Technology, Transactions of the ASME, 101, 220-230.

[42] Li, Y. (2008), Ph.D. Thesis, Department of Mechanical Engineering, Massachusetts Institute of Technology.

[43] Patankar, S.V. (1980), *Numerical Heat Transfer and Fluid Flow*, Hemisphere/McGraw-Hill, Washington DC.

[44] Saad, Y. (2005) *Sparskit Version 2*, University of Minnesota.

[45] Saad, Y. and Schultz, M. (1986) *GMRES: A Generalized Minimal Residual Algorithm for Solving Nonsymmetric Linear Systems.* SIAM J. Sci. Statist. Comput. 7, 856-869.

[46] Boresi, A.P. and Schmidt, R.J. (2001), *Engineering Mechanics: Dynamics*, Brooks/Cole, Pacific Grove, CA.

[47] Kundu, P.K. and Cohen, I.M. (2002), *Fluid Mechanics,* Academic Press, San Diego.